Doping Mechanisms and Electrical Properties of Sodium Niobate

Jordan Canton

A thesis submitted in partial fulfilment of the requirements for the degree of Doctor of Philosophy

Supervisor: Professor Derek Sinclair

The University of Sheffield
Faculty of Engineering
Department of Materials Science and Engineering

March 2024

Acknowledgments

I would like to take this opportunity to thank my supervisor Professor Derek Sinclair. His guidance, support, and encouragement over the last 4 years has been invaluable, his scientific thinking and extensive experience is the greatest resource I have ever had access to and this thesis and the research within would not have been possible without him.

I would also like to thank the EPSRC and Johnson Matthey for their funding of my studentship, allowing me to embark on this journey, and affording me the opportunity to present my research internationally. I would like to thank my industrial supervisor Dr Mark Feaviour for his help during this project and for the opportunity to use the facilities at Sonning Common.

I would also like to thank Professor John Hanna and David Bradley at the University of Warwick High-Field Solid-State NMR facility for running NMR experiments on my behalf and all their assistance with interpretation. Thank you to the Henry Royce institute for Advanced Materials for their funding for EPMA, and Mr Stuart Creasey-Gray for his assistance and insight with the data collection and analysis.

Thank you to Dr Lewis Owen for his endless enthusiasm and expertise in XRD and his assistance with any of my issues with GSAS-II.

Thanks to my fellow members of the FMD group past and present, in particular Dr Linhao Li, Dr Zhilun Lu and Dr Ge Wang, for their assistance during the early stages of this project, and Dr Thomas Hooper and James Killeen for the numerous discussions about sodium niobate.

Finally, I would like to thank my parents, for their constant support and encouragement throughout my university studies, which are finally coming to an end.

Abstract

Intermediate temperature solid oxide fuel cells (ITSOFCs) are one of many technologies attempting to decarbonise global energy production and utilise the hydrogen economy. Unfortunately, typical solid oxide electrolytes such as yttria-stabilised zirconia (YSZ) do not exhibit sufficient conductivity for operation in the intermediate temperature region (400-750 °C). As a result, many potential intermediate temperature solid oxide electrolytes have undergone investigation to replace YSZ. The goal of this project was to investigate the perovskite material $NaNbO_3$ (NN) and identify its suitability as a solid oxide electrolyte.

NN ceramics were prepared *via* solid-state reaction of mixed oxides at 900 °C, followed by sintering at temperatures in the range 1240-1350 °C. Physical properties of NN ceramics were assessed using X-Ray diffraction (XRD), Scanning Electron Microscopy (SEM), Electron Probe Micro Analysis (EPMA) and Nuclear Magnetic Resonance (NMR). Electrical properties were investigated using impedance spectroscopy to assess bulk conductivity and pO_2 dependence of the ceramics, probostat measurements have allowed for determination of oxygen ion transport numbers (t_{ion}) and the electronic band gap of NN has been determined *via* UV-Vis spectroscopy.

This project is divided into exploring the defect chemistry of NN and how it influences the electrical properties.

It has been shown that NN produced *via* solid-state synthesis varies significantly compared to hydrothermally prepared, and commercially available NN powders. The variance has been attributed to non-stoichiometry between the sodium and niobium sites caused by sodium volatility during processing. Deliberate Na:Nb non-stoichiometry in the range 0.96 – 1.22 showcases that sodium rich NN exhibits greater bulk conductivities (55:45 NN $\sigma_{500\,^{\circ}C} \approx 26$ μS cm^{-1}) and promotes ionic conductivity, compared to sodium deficient NN (49:51 NN $\sigma_{500\,^{\circ}C} \approx$ 0.13 μS cm^{-1}).

The following doping mechanisms have been used to influence the electrical properties of NN:

1. Direct substitution of sodium for calcium to generate A-site vacancies:

$$2Na^{+} = Ca^{2+}$$

2. A-site donor doping using Mg^{2+} and Ga^{3+} for the reduction of oxygen vacancies:

$$Na^{+} = Mg^{2+} + \frac{1}{2}O^{2-}$$

3. B-site donor doping using W^{6+} and Mo^{6+} for the reduction of oxygen vacancies:

$$Nb^{5+} = W^{6+} + \frac{1}{2}O^{2-}$$

4. B-site acceptor doping using Mg^{2+}, Ga^{3+} and Ti^{4+} for the generation of oxygen vacancies:

$$Nb^{5+} + O^{2-} = Ga^{3+}$$

Generation of A-site vacancies *via* calcium doping leads to an increase in bulk conductivity ($Na_{0.9}Ca_{0.05}NbO_3$ $\sigma_{500\,°C}$≈2.7 μS cm^{-1}), with low levels of ionic conductivity attributed to sodium ion conduction.

Donor doping of the A-site using Mg^{2+} or Ga^{3+} has no significant effect on the bulk conductivity ($Na_{0.99}Mg_{0.01}NbO_{3.005}$ $\sigma_{500\,°C}$ ≈ 0.24 μS cm^{-1}), however, ionic conductivity is supressed. Similarly, donor doping the B-site with W^{6+} supresses ionic conductivity without influencing bulk conductivity ($NaNb_{0.99}W_{0.01}O_{3.005}$ $\sigma_{500\,°C}$ ≈ 0.69 μS cm^{-1}). However, doping with molybdenum does not appear to be successful due to preferential formation of a molybdenum bronze.

Acceptor doping of the B-site with Ga^{3+} and Ti^{4+} promotes ionic conductivity and greatly enhances bulk conductivity ($NaNb_{0.95}Ga_{0.05}O_{2.95}$ $\sigma_{500\,°C}$ ≈ 0.08 mS cm^{-1}/$NaNb_{0.95}Ti_{0.05}O_{2.975}$ $\sigma_{500\,°C}$ ≈ 0.05 mS cm^{-1}). It has been shown that in gallium doped NN maximum conductivities are achieved at very low concentrations (<1at%) of dopant due to pinning of oxygen vacancies. Acceptor doping with Mg^{2+} appears to be unsuccessful due to a preference for A-site donor doping.

The properties of NN vary significantly according to the dopant mechanism utilised, and the Na:Nb ratio. The electronic band gap of NN appears to be unaffected by acceptor doping and remains 3.4 eV. Oxygen ion transport numbers for acceptor doped NN ceramics indicate that all variants are mixed oxide ion-electronic conductors (t_{ion}=0.2-0.7), indicating that NN based materials are unsuitable for applications as solid oxide electrolytes.

Table of Contents

Chapter 1. Literature Review

This literature review will give context to the work presented in this thesis. It will cover a background to solid oxide fuel cells (SOFCs) including general principles and the origin of various efficiency losses before moving on to address how/why intermediate temperature solid oxide fuel cells (ITSOFCs) may overcome some of the inherent issues with SOFCs and why they require additional research. Finally, it will move onto the materials of interest for the project to identify why they are promising candidates for use as solid oxide electrolyte materials.

1.1. The Problem with Fossil Fuels and an Introduction to the Hydrogen Economy

Fossil fuels have been humanities primary source of energy production since the industrial revolution.[1] In the 200 years since there has been an abundance of research into the negative environmental impacts caused by the burning of fossil fuels and the resultant global warming.[2] Pairing the environmental impact of fossil fuels with their dwindling availability it becomes increasingly evident that both energy demands, and energy production methods must change before irreparable damage to the global ecosystem is caused.[3,4] In recent years efforts to reduce the amount of fossil fuels used have been made, and various renewable energy sources have received increased attention, funding, and use globally.[5] However, typical renewable energy sources (wind, solar, hydroelectric) are reliant on environmental conditions that are not always consistent (i.e. high and low tides) paired with various issues regarding storage of renewable energy it becomes clear that typical sources of renewable energy are insufficient to meet global energy demands.[6]

Arguably the most promising method of sustainable energy production lies within a hydrogen economy.[7] The best way to utilise the hydrogen economy also means moving away from traditional combustion of fuel gases to produce energy and into a significantly more efficient, electrochemical method.

To use hydrogen as a fuel it must first be obtained. Despite being the most abundant element in the universe, pure hydrogen can be challenging to obtain. However, there are various methods of obtaining hydrogen, the most prevalent on an industrial scale is steam reforming of methane (equation 1.1).[8]

$$CH_{4_{(g)}} + H_2O_{(g)} \rightarrow 3H_{2_{(g)}} + CO_{(g)} \qquad (1.1)$$

$$\Delta H^o_{298K} = +206\ kJ\ mol^{-1} \qquad \Delta G^0_{298K} = +142\ kJ\ mol^{-1} \qquad T_{\Delta G=0} = 960\ K$$

$$CO_{(g)} + H_2O_{(g)} \rightarrow H_{2_{(g)}} + CO_{2_{(g)}} \qquad (1.2)$$

$$\Delta H^o_{298K} = -41.2\ kJ\ mol^{-1} \qquad \Delta G^0_{298K} = -55.3\ kJ\ mol^{-1} \qquad T_{\Delta G=0} = 955\ K$$

This process either generates a syngas mixture (H_2+CO) or is commonly followed by the water-gas shift reaction (equation 1.2). The conditions can be controlled to minimise the water-gas shift reaction. Alternatively, hydrogen can be extracted from water *via* electrolysis according to equation 1.3.

$$H_2O_{(l)} \rightarrow H_{2_{(g)}} + \frac{1}{2}O_{2_{(g)}} \qquad (1.3)$$

$$\Delta H^o_{298K} = +285.8\ kJ\ mol^{-1} \qquad \Delta G^0_{298K} = +237.1\ kJ\ mol^{-1} \qquad T_{\Delta G=0} = 1750\ K$$

The electrolysis process produces pure hydrogen gas; however, it requires substantial energy input (~5 kWh m^{-3} of H_2)[9] from electricity, incurring significant costs.

1.2. Solid Oxide Fuel Cells (SOFCs)

1.2.1. General Principles

SOFCs produce energy *via* the electrochemical recombination of hydrogen and oxygen to form water, rather than combustion of fuel gases. They work on the general principle shown in the equations below.

Anode Reaction: $2\mathrm{H}_{2_{(g)}} + 2\mathrm{O}^{2-} \rightarrow 2\mathrm{H}_2\mathrm{O}_{(g)} + 4\mathrm{e}^-$ (1.4)

Cathode Reaction: $\mathrm{O}_{2_{(g)}} + 4\mathrm{e}^- \rightarrow 2\mathrm{O}^{2-}$ (1.5)

Overall Reaction: $2H_{2_{(g)}} + O_{2_{(g)}} \rightarrow 2H_2O_{(g)}$ (1.6)

$$\Delta H^0_{298K} = -241.8\ kJ\ mol^{-1} \qquad \Delta G^0_{298K} = -228.5\ kJ\ mol^{-1} \qquad T_{\Delta G=0} = 5434\ K$$

This reaction is highly exothermic and releases a significant amount of energy. Figure 1.1 shows a schematic representation of a fuel cell using an oxide ion-conducting electrolyte.

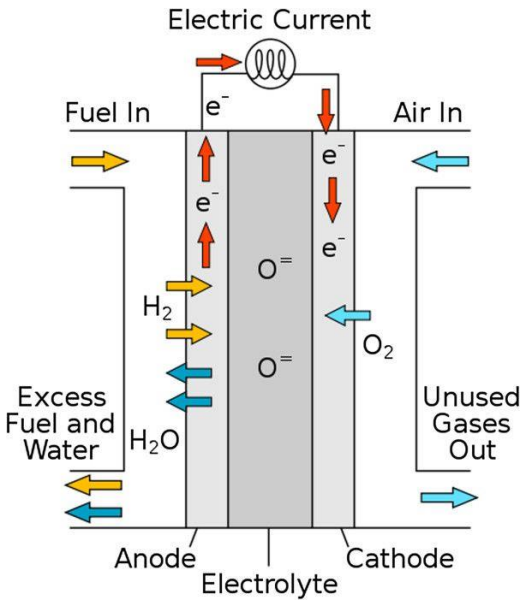

Figure 1.1: Schematic Representation of a Hydrogen Fuel Cell using an Oxide ion conducting electrolyte (Valgari et. al.)[10]

Fuel cell technology is by no means a new method of energy production. The basic principle was laid out for fuel cells in 1838 by Grove with platinum electrodes contained within tubes of hydrogen and oxygen submerged in low concentration of sulphuric acid solution.[11] The acidic solution effectively acted as a proton conducting electrolyte. Grove noted that leaving the solution with a constant flow of gases would lead to an increase in volume as a result of the reaction shown in equation 1.6. In 1842 Grove expanded upon this forming the basis for the modern phosphoric acid fuel cell.[12] An obvious weakness to this system is the use of platinum electrodes. Although platinum is very effective at facilitating the formation of hydrogen and oxide ions it does require significant purity of fuel gases to avoid poisoning the electrodes, alongside the high cost of the material.[13]

The reliance on platinum electrodes is a major drawback for alkaline fuel cells (AFCs), phosphoric acid fuel cells (PAFCs), and polymer electrolyte membrane fuel cells (PEMFCs). All of which operate at low temperatures (<200 ˚C) due to either the fuels used or liquid electrolytes. It is here that the advantages of solid oxide fuel cells begin to become clear. SOFCs typically have significant operating temperatures >800˚C, by utilising temperatures this high, fuel purity is significantly less important. Additionally, the high temperatures allow for alternative fuels to be used. Not limited by a pure hydrogen fuel requirement SOFCs often generate the fuel by internal reforming of natural gas or biogas shown in equation 1.1.[14]

The use of syngas (H_2+CO) as a fuel is somewhat desirable as it is a relatively cheap source of hydrogen, and the oxidation of carbon monoxide adds to the potential energy output of the cell (equation 1.7).

$$CO + \frac{1}{2}O_2 \rightarrow CO_2 + Energy \qquad (1.7)$$

$$\Delta H^{o}_{298K} = -283\ kJ\ mol^{-1} \qquad \Delta G^{0}_{298K} = -209\ kJ\ mol^{-1} \qquad T_{\Delta G=0} = 1136\ K$$

However, there are obvious safety concerns with storing large volumes of hydrogen, therefore the ability demonstrated for SOFCs to internally reform is not only desirable from a cost perspective[15] but the storage of natural gas or biogas is arguably safer due to the significantly smaller window for the ignition limits in air (hydrogen: 4-75%, methane: 5.3-15%).[16]

A key difference in SOFCs is their use of ceramic materials for the electrodes and electrolyte. The high operating temperatures used allow unfavourable reaction kinetics to be overcome with relative ease, allowing slightly less catalytically active, yet cheaper materials to be utilised for electrode materials (compared to platinum).[17] Due to the ability to use ceramic materials and not being limited by platinum content a wide range of ceramic SOFCs exist using a range of different materials such as perovskites, cermets, and spinel materials.[18,19] A standard SOFC utilises the oxide ion conducting yttria stabilised zirconia (YSZ) electrolyte, typically paired with a Ni-YSZ cermet anode,[20] and a cathode made of the perovskite lanthanum strontium manganite (LSM).[21]

1.2.2. SOFC Efficiency and Losses

The maximum theoretical efficiency of a solid oxide fuel cell is defined by the ratio of the Gibbs energy change to the enthalpy change shown below in equation 1.8.

$$\varepsilon_{max} = \frac{\Delta G^{0}_{298K}}{\Delta H^{0}_{298K}} \times 100 \qquad (1.8)$$

For the overall reaction between hydrogen and oxygen to form water (equation 1.6) this is 96.4% this is significantly higher than the peak theoretical efficiencies of more conventional means of energy production such as combustion engines, which are limited by the Carnot-cycle; meaning the efficiencies are limited by equation 1.9.

$$\varepsilon = \frac{W}{Q_H} \times 100 \qquad (1.9)$$

where W is the work done by the system and Q_H is the heat put into the system. Generally, the peak efficiencies of a combustion engine lie between 30 and 40%.[22]

However, fuel cells rarely meet this theoretical efficiency due to various losses. A key source of the losses within an SOFC arise at the interconnect between the electrodes. Due to the nature of a fuel cell the role of the interconnect is critical and poses a challenge from a materials perspective. In order to operate efficiently the interconnect material for an SOFC must be:

1. Electrically conductive with limited ionic transport properties.
2. Stable at high temperatures.
3. Stable in both oxidising and reducing conditions.

Naturally, the losses that arise at the interconnect are linked to the above criteria. A common material used as an interconnect in an SOFC is the perovskite $LaCrO_3$. $LaCrO_3$ is typically doped with either calcium or strontium to improve the suitability for use as an interconnect. Use of $La_{0.7}Ca_{0.3}CrO_3$ improves the sintering characteristics in air and matches the thermal expansion of the interconnect to the YSZ electrolyte. While the $La_{0.7}Ca_{0.3}CrO_3$ does improve electrical conductivity *vs* $LaCrO_3$ the chromium is reduced in the reductive atmospheres found at the anode. This reduction of Cr^{4+} to Cr^{3+} is accompanied with the generation of an oxygen vacancy and an associated expansion of the material. This expansion leads to an incompatibility with the YSZ electrolyte and places the system under significant mechanical stress. Strontium doped $LaCrO_3$ also suffers from this issue, however, co-doping with Ti^{4+} helps minimise this expansion as shown in Figure 1.2.[23]

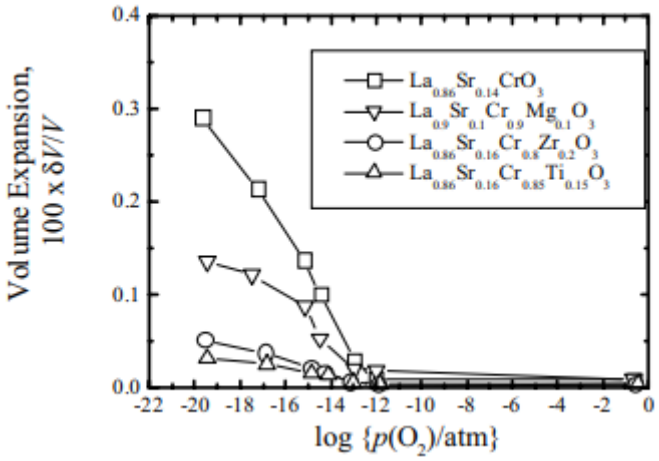

Figure 1.2: Volume Expansion of $La_{1-x}Sr_xCr_{1-y}M_yO_3$ Materials as a Function of pO_2 (Taken from Yokokawa H. et. al.)[23]

Additionally, $LaCrO_3$ based materials are susceptible to permeation of oxide ions, taking potential charge carriers/reactive O^{2-} away from the electrolyte preventing the transport to the anode and reducing the output of the cell.

Metal based interconnects have also been investigated for use in SOFCs. There are obvious advantages to using a metal interconnect such as ferritic stainless steel due to high electronic conductivity with minimal oxygen permeation. High thermal conductivity of the metal based interconnect materials allows a consistent temperature to be achieved across the cell lowering the mechanical stress placed on the components.[23] While these properties aid in minimising the efficiency losses in ceramic based interconnects at the temperatures where a typical SOFC operates (>800˚C) there is a significant mismatch between the thermal expansion coefficient of the steel interconnect and the ceramic YSZ electrolyte.[23,24] Unless operating temperatures can be reduced the usage of ferritic stainless steel will remain a challenge.

In addition to the interconnect a significant portion of the losses that occur in an SOFC arise due to polarisation of the cathode material. In order for the cell to function, the oxygen gas has to diffuse through the cathode material and undergo ionisation to move across the electrolyte. As a greater concentration of the oxide ions will be located at the interface between the cathode and the electrolyte throughout operation, a potential difference and associated polarisation will occur. This polarisation can be expressed mathematically in the following equation.

$$\eta_c = \frac{RT}{nF} \ln\left(\frac{I_e}{I_e - i}\right) \qquad (1.10)$$

$$\eta_c = Cathode\ Polarisation \quad R = Ideal\ Gas\ Constant \quad T = Temperature$$
$$n = Number\ of\ Electrons \quad F = Faraday\ Constant \quad I_e = Electrode\ Current\ Density$$
$$i = Cell\ Current$$

When the cell current is low then the polarisation of the cell has a linear relationship to the current density. As the cell current approaches the current density the polarisation increases significantly.[25] In order to limit the polarisation it is therefore desirable to use an electrode material that has a large current density. Additional methods to limit electrode polarisation include controlling the porosity of the material to aid the diffusion of oxygen gas. This must be carefully controlled as if the material is too porous there is a notable decrease in the electrical conductivity of the electrode, causing a notable increase in cathode polarisation and decrease in overall cell efficiency as shown in Figure 1.3.

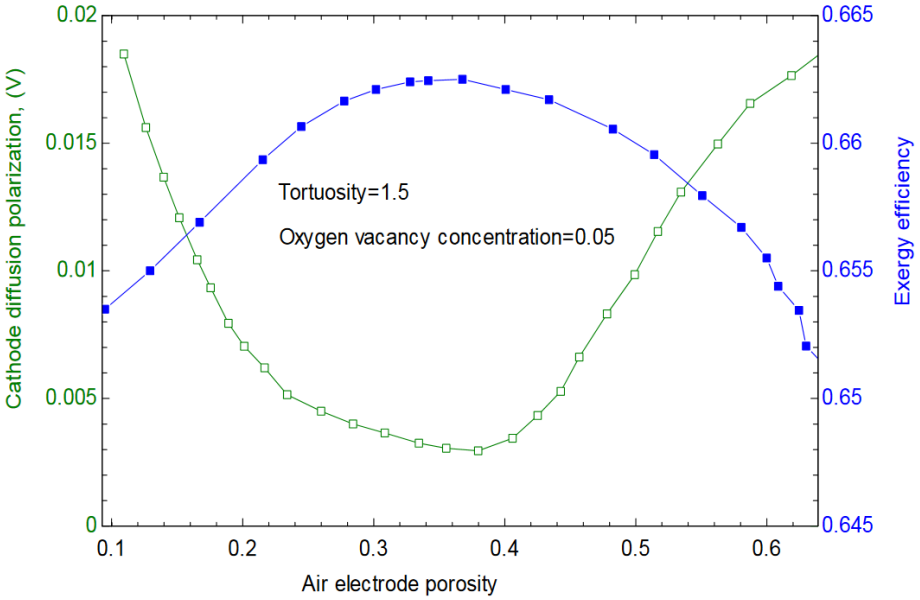

Figure 1.3: Relationship Between Porosity and Electrode Polarisation/Cell Efficiency (Taken from Zouhri et. al.)[26]

Ultimately, by increasing the porosity of the cathode material it is facilitating a higher flow rate of oxygen through the material. Similar effects may be achieved by simply increasing the flow rate of the supplied oxygen gas. This has been effectively showcased by linking cathode polarisation to pO_2.

$$\eta_c = \frac{RT}{4F} \ln\left(\frac{P_{O_2}(a)}{P_{O_2}(b)}\right) \qquad (1.11)$$

Equation 1.11 links the cathode polarisation to the ratio of oxygen pressure at the inlet to the cathode (pO_2 (a)) to the oxygen pressure at the cathode-electrolyte interface (pO_2 (b)).[27]

The polarisation of the cathode can also be reduced by increasing the operating temperature of the cell as this increases the rate of the oxygen reduction reaction (equation 1.5).[22] However, this solution is less than ideal as the already high operating temperatures of an SOFC give rise to many unfavourable side reactions. Although it is an advantage of using an SOFC system to operate at a sufficiently high temperature to internally reform their fuel, a common shortcoming of the nickel-cermet anode materials typically utilised is their susceptibility to coking.

$$CH_{4_{(g)}} \rightarrow C_{(s)} + H_{2_{(g)}} \qquad (1.12)$$

$$\Delta H^o_{298K} = +75\ kJ\ mol^{-1} \qquad \Delta G^0_{298K} = +50.7\ kJ\ mol^{-1} \qquad T_{\Delta G=0} = 926\ K$$

$$2CO_{(g)} \rightarrow C_{(s)} + CO_{2(g)} \qquad (1.13)$$

$$\Delta H^{o}_{298K} = -172.5\ kJ\ mol^{-1}\ \Delta G^{0}_{298K} = -225\ kJ\ mol^{-1} \quad T_{\Delta G=0} = 981K$$

The high temperatures present in the SOFC, while beneficial for the reforming reactions are also sufficiently high that catalytic cracking of methane can take place at the anode. This leads to a build-up of carbon on the anode, eventually leading to deactivation of the catalytic properties of the material.[28] It has been demonstrated that the nickel based cermets while catalysing the internal reforming, and the oxidation of hydrogen/carbon monoxide also catalyses the reactions shown in equations 1.12 and 1.13. In an attempt to combat this, two paths have been taken. Firstly, suppression of the undesirable reactions by addition of different precious metals to the Ni/YSZ cermet with one study demonstrating an addition of 1wt% platinum reducing carbon deposition rate by 40% while other studies have shown that ruthenium, palladium, and rhodium have similar effects while either having no effect on the electrochemical reactions, or enhancing them.[28] Secondly, investigations into alternative anode materials utilising alternative transition metals or material types; moving away from cermets and toward perovskite materials similar to those utilised for cathode materials.[29] Alternatively, as the carbon forming reactions are relatively high temperature processes, intermediate temperature solid oxide fuel cells (ITSOFCs) have been utilised to avoid the issue by operating the cell at temperatures below the point which the reactions become favourable.

1.3. Intermediate Temperature Solid Oxide Fuel Cells

Continuous operation of an SOFC at temperatures >800˚C, aside from giving rise to the deactivating reactions discussed above, also cause a significant amount of mechanical stress placed on the mechanical components required for a commercial SOFC in addition to the inherent costs in maintaining the cell at such a high temperature. Use of an intermediate temperature solid oxide fuel cell (ITSOFC) is one of the driving factors in reducing the operational costs of SOFCs, by increasing cell lifetime (suppression of deactivating reactions and alleviation of some mechanical stress) and by reducing the energy input required to reach and maintain operation temperatures.[30] ITSOFCs have operational temperatures in the range 400-750˚C. The lower temperatures are more desirable; however, they do begin to limit the ability to internally reform the fuel over the Ni/YSZ anode. It has been demonstrated that low temperature steam reforming is possible over various noble metal catalysts.[31,32] However, this has seen limited applications as anode materials in ITSOFCs typically opting for an external reforming process before feeding in the produced syngas to the anode as fuel for the cell.[33]

An additional obstacle in lowering the operational temperature is the lower conductivity of the YSZ electrolyte. A good solid oxide electrolyte is expected to maintain ionic conductivity of >1 mS cm^{-1}.[34] YSZ when operating at typical SOFC temperatures (>800˚C) displays significant oxide ion conductivity alongside its thermal stability it is obvious as to how it became the standard electrolyte. However, the conductivity decreases rapidly with temperature down to 1 µS cm^{-1} at 400˚C, the lower end of the ITSOFC operating temperature.[35–37] Due to this, significant research has been conducted into potentially appropriate electrolyte materials for ITSOFCs. In some cases, utilisation of processing techniques, such as thin or thick film processing has been shown reduce the resistance of the YSZ electrolyte and thus increase the effective power output and efficiency of the fuel cell. [35,38] Although a greater focus has been put on development of new solid oxide electrolyte materials.

Oxide ion conduction through a solid electrolyte occurs *via* two main mechanisms: oxygen vacancies, and interstitials. Conduction *via* oxygen vacancies occurs by oxide ions diffusion between vacant sites throughout the material.[39] In contrast, interstitial conduction occurs by displacement of oxide ions within the material to migrate to other interstitial sites.[40] The electrolytes discussed below all utilise oxygen vacancies.

Some of the earliest success in intermediate temperature electrolytes came from ceria-salt composites. Doping CeO_2 with various cations to generate oxygen vacancies caused oxide ion conduction to arise, then in forming a composite material with a salt (normally chlorides, fluorides, or hydroxides) would suppress the electronic conduction present, allowing for a suitably conducting electrolyte (1 – 0.01 S cm^{-1}).[41] A major drawback to using this type of electrolyte however, is the compatibility of anode/cathode materials.[42] A traditional Ni/Electrolyte cermet anode has an immediate compatibility with the electrolyte as the materials are exceedingly similar. This principal has been successfully applied to the ceria-salt composite electrolyte forming a NiO-CeO_2 electrode; however, this material has significant issues with nickel sintering leading to deactivation of the anodes electrocatalysis of hydrogen and/or carbon monoxide.[43]

An alternative type of solid oxide electrolyte for ITSOFCs is the LAMOX family of conductors, based on the material $La_2Mo_2O_9$ depicted in Figure 1.4. LAMOX displays impressive oxide-ion conductivity in the 600-800˚C temperature range after a first order phase transition. Beyond 600˚C the material displays ionic conductivity comparable to YSZ (60 mS cm^{-1}).[44] Identification of the more conductive phase as being cubic potentially offers insight into the significant jump in conductivity to compete with YSZ (also cubic) suggesting that the oxygen localisation in the lower temperature monoclinic phase inhibits the ionic conductivity.[45] Due

to this, immediate work was conducted into stabilising the more conductive cubic phase by substitution of lanthanum with neodymium, gadolinium or yttrium allowing stabilisation of the cubic phase at room temperature.[46]

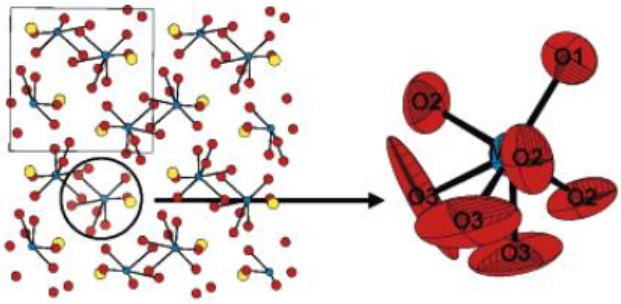

Figure 1.4: Structure of $La_2Mo_2O_9$ the Square Represents a Single Cubic Unit Cell (Taken from Evans et. al.)[47]

There are, however, additional compatibility issues in using a LAMOX electrolyte. LAMOX family conductors have a relatively high coefficient of thermal expansion causing the structural integrity of constructed fuel cells to be challenged as the temperatures rise. Additionally, for similar reasons to the ceria-salt composites the electrode/electrolyte compatibility can cause premature deactivation of the electrodes.[48]

Electrode compatibility is a significant issue in using alternative (not YSZ) electrolytes. The more similar an electrolyte is to the electrodes the greater the compatibility not only due to thermal expansion but the interface and ionic flow between the electrode and electrolyte.[49] To that end using a perovskite material as the electrolyte is understandably desirable as the compatibility between the LSM cathode and the electrolyte will be naturally high.

1.4. Introduction to Perovskites

Perovskites are a classification of ceramic material based on the structure of calcium titanate ($CaTiO_3$); they are named after Russian minerologist Lev Perovski. Figure 1.5 shows that the 'ideal' perovskite has a primitive cubic lattice (Pm-3m) with the general formula ABX_3 where A and B are cations, and X is an anion (typically O^{2-}).[50]

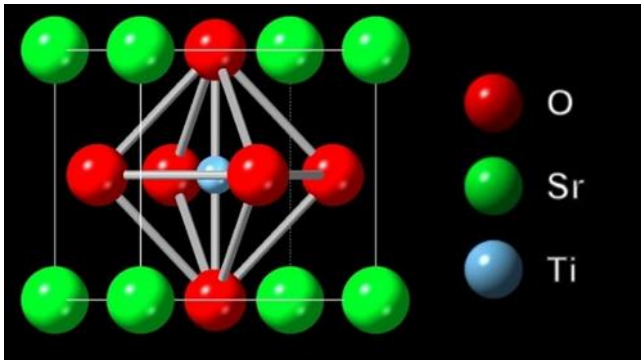

Figure 1.5: Crystal Structure of $SrTiO_3$ the "Ideal" Perovskite

The tendency of a perovskite to have an “ideal” cubic structure can be determined according to the tolerance factor (t) developed by Megaw *et. al.* The tolerance factor assesses the size agreement between A and B site cations to allow predictions of perovskite stability and room temperature symmetry systems according to the ionic radii of the constituent A, B and O ions (R_A , R_B and R_o, respectively).[51]

$$t = \frac{R_A + R_O}{\sqrt{2}(R_B + R_O)} \qquad (1.14)$$

“Ideal” cubic perovskites have a tolerance factor of 1 whereas significant deviations from 1 suggest that the perovskite material is highly unstable and will not form. Smaller deviations in tolerance factor cause adoptions of lower symmetry systems. In instances where the A-site cation is too small to fit into the B-site interstices t decreases and orthorhombic/rhombohedral symmetries are typically adopted. In instances where B site cations are too small to fill the BO_6 octahedra t increases and hexagonal/tetragonal symmetries are typically adopted.[51]

Perovskites that adopt orthorhombic symmetries have the BO_6 octahedra tilt to accommodate the mismatched ion sizes. Perovskite tilt systems have been investigated thoroughly by Glazer *et. al.* initially suggesting a possible 23 tilt systems although this has since been reduced to 15 by elimination of equivalent systems.[52] The octahedral tilt refers to the rotational distortion of octahedra relative to the ideal cubic perovskite structure based on $SrTiO_3$ about the axes of symmetry.[53] Examples of 3, 2, 1, and zero tilt systems are shown below in Figure 1.6.

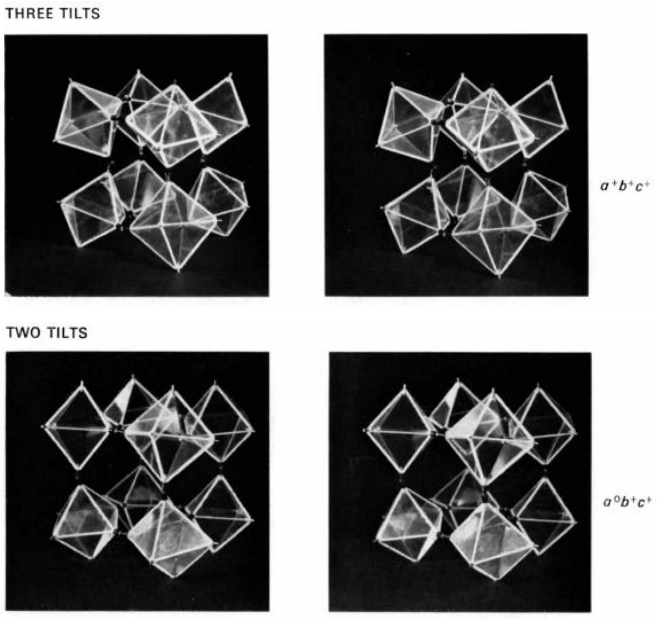

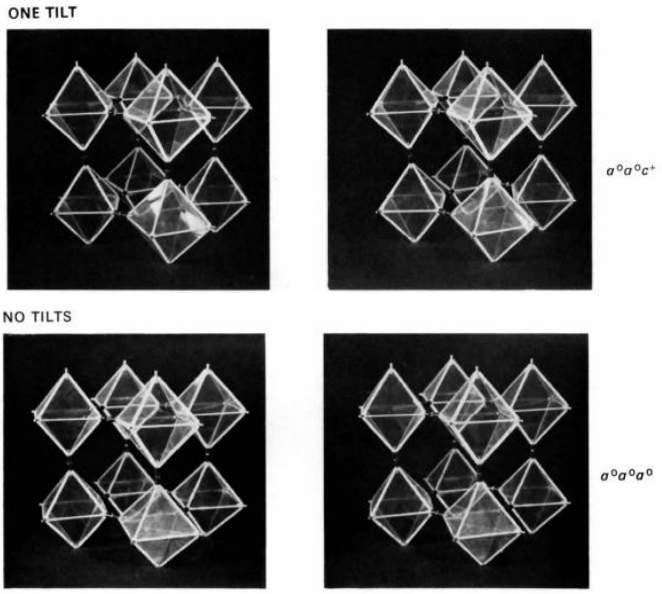

Figure 1.6: Examples of Different Tilt Systems (Taken from Glazer et.al.)[53]

Tilting within perovskites can be heavily influenced by chemical doping. When the A or B sites are occupied by multiple cations the tilting and overall symmetry of the system is influenced by the bond lengths of each cation and the ions preferred bonding environment.

1.5. Perovskites as Solid Oxide Electrolytes

A range of perovskite materials have been used as solid oxide electrolytes; however, the most widely utilised is a doped lanthanum gallate ($La_{1-x}M_xGaO_3$) developed in the early 90's.[54] Further work on this material suggested that co-doping both A and B sites of the perovskite lead to increased ionic conductivity, this led to the development of LSGM ($La_{0.9}Sr_{0.1}Ga_{0.8}Mg_{0.2}O_{3-\delta}$). This material displays significant levels of ionic conductivity at temperatures above 700˚C outperforming YSZ even at high temperatures (>900˚C).[55]

With good material compatibility between electrode materials, the LSGM perovskite is an obviously appealing electrolyte material, although it is not without its limitations. LSGM interacts with the nickel-based anode materials forming a secondary phase containing nickel ($LaSrGa(Ni)O_{4-\delta}$). This material is significantly more resistive to oxide ion conduction and significantly affects the fuel cell power output once formed.[56] While the generation of this phase can be limited by various fabrication processes this rapidly drives up the development cost of an ITSOFC using an LSGM electrolyte.[57] Although, the innate material compatibility in regards to stability and thermal expansion using a perovskite electrolyte is certainly worth pursuing.

Arguably the most promising perovskite-based electrolyte from the last decade would be (Na,Bi)TiO_3 (NBT). Both NBT ($N_{0.49}Bi_{0.51}TiO_3$) and the co-doped NBTM ($Na_{0.5}Bi_{0.49}Ti_{0.98}Mg_{0.02}O_{2.965}$) show significant oxide ion conduction arising from the polarisability of the bismuth ions alongside the hybridisation of bismuth and oxygen orbitals leading to weak Bi-O bonds of varying length; this gives rise to a somewhat distinct oxide ion diffusion pathway *via* the significant number of oxygen vacancies. The importance of bismuth-oxygen hybridisation becomes more evident in the saddle point mechanism for oxygen ion migration where bismuth-rich A-sites in a saddle point configuration have a significantly lower activation energy for oxide-ion migration than those that are sodium-rich or mixed sites. This is visualised in Figure 1.7.[58,59]

Figure 1.7: Saddle Point Mechanism and Associated Activation Energies for NBT (Taken from Yang et. Al.)[59]

Figure 1.8 shows that the more conductive NBTM shows similar levels of conductivity to LSGM and CGC electrolytes, significantly outperforming LSGM at lower temperatures.[58]

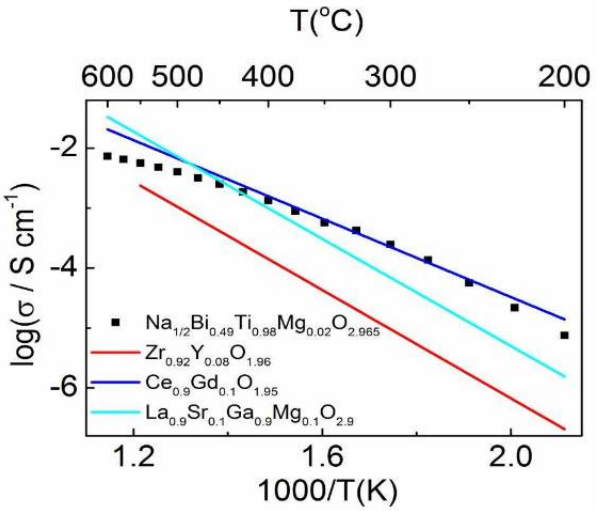

Figure 1.8: Arrhenius Plots of Bulk Conductivity for NBMT and Common Electrolyte Materials (Li et. al.)[58]

NBT and NBTM also show good compatibility with nickel and silver electrode materials, however the lower chemical stability of NBTM in reducing atmospheres causes some difficulty in the preparation of ITSOFCs using it as an electrolyte.[60] Although NBTs function

as an oxide ion conductor it opens up various suggestions as to other perovskite materials that under certain processing conditions/small compositional variations may lead to the promotion of oxide ion conductivity. As NBT was commonly used as a lead-free piezoelectric and the oxide ion conduction arises from very small changes to the level of A-site bismuth doping[58] it is interesting to see if related perovskite phases might also show high levels of ionic conductivity with modest changes in the starting composition and/or by A- and/or B-site acceptor doping.

1.6. Sodium Niobate ($NaNbO_3$)

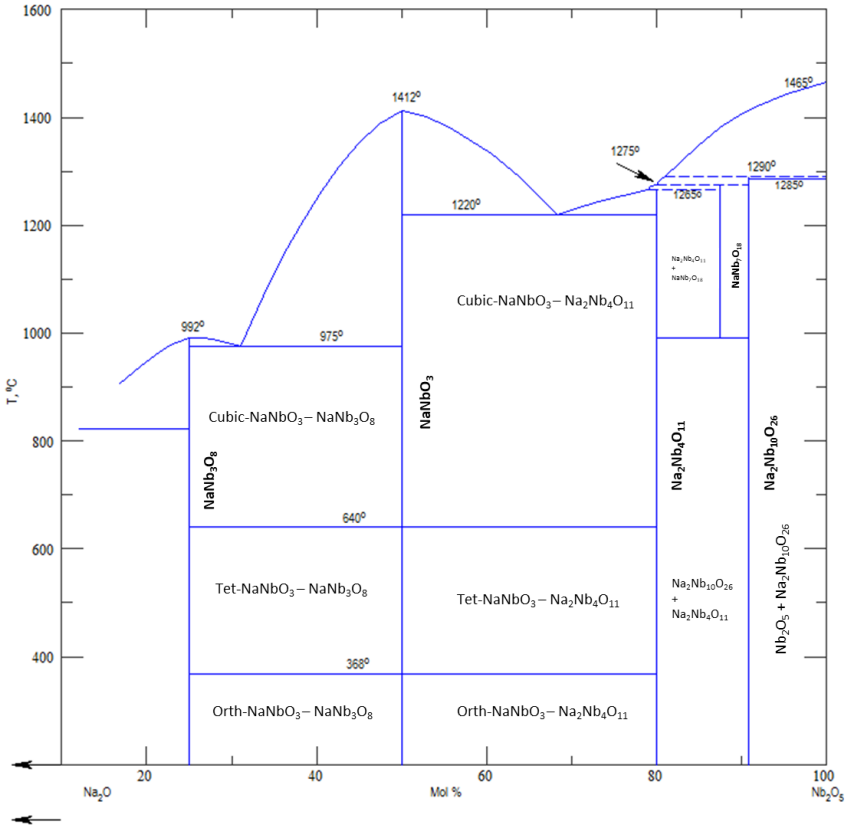

Figure 1.9: Binary Phase Diagram of Na_2O-Nb_2O_5 Adapted from Shafer et. al.[61] Obtained from ACS Phases Software

Figure 1.9 shows the binary phase diagram of Na_2O and Nb_2O_5, a stoichiometric mix leads to the formation of sodium niobate (NN), a perovskite material that has seen primary applications as a lead-free piezoelectric and dielectric material, first suggested for this use in 1959 shortly after the initial push to move away from lead zirconate titanate ($Pb[Zr_xTi_{1-x}]O_3$) (PZT) due to health concerns.[62] Sodium niobate, depicted in Figure 1.10, has been of consistent interest since then both for its significant piezoelectric properties, mainly finding applications in transducers, actuators, and sensors;[63] but also due to interest surrounding the seven successive phase transitions of the material during which the material adopts

several different tilting systems and symmetries. These are summarised in Figure 1.11.[64] The piezoelectric properties have naturally been of significant interest as a lead free material as the material displays both ferroelectric and antiferroelectric properties.[65]

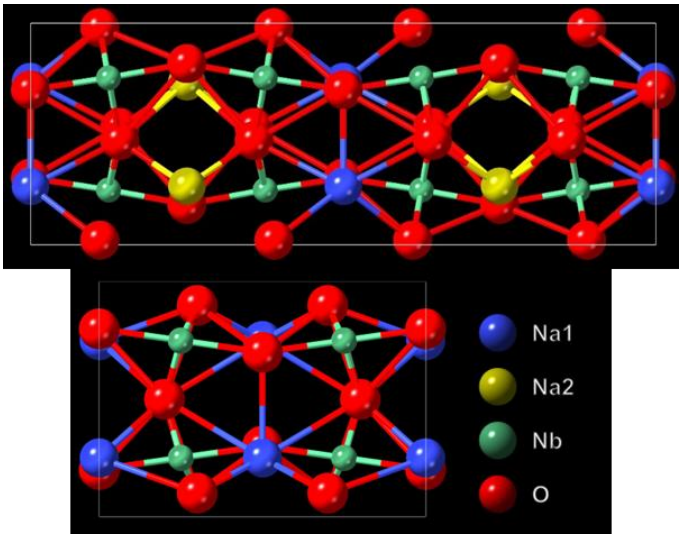

Figure 1.10: Room Temperature Phases of Sodium Niobate Unit Cells Pbma (Top) $Pmc2_1$ (Bottom)

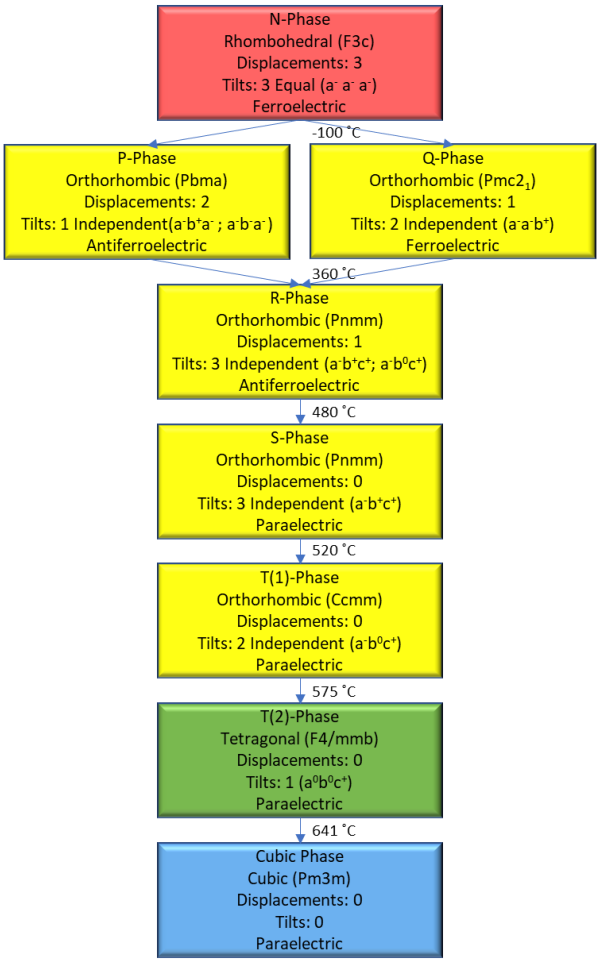

Figure 1.11: Phases of Sodium Niobate with Corresponding Ferroelectric Properties and Tilt Systems[64,66–69]

Sodium niobate moves through numerous different tilt systems as it progresses through its multiple phases.[64] Due to the significant effect of the tilting on the ferroelectric properties of each phase of sodium niobate many have found it desirable to eliminate the tilt system entirely by A-site doping with potassium which is sufficiently large enough to fill the 12-coordinated cavity of the ideal perovskite structure, thus preventing any tilting.[64] As a result potassium sodium niobate KNN ($(K,Na)NbO_3$) has become the focus of significant study at the forefront of so-called sodium niobate based ceramics, with some ceramics displaying superior piezoelectric constants compared to PZT.[70] Along with setting the stage for the subsequently expansive research into alkali niobate based ceramics.[71]

Sodium niobate has also found uses outside the traditional field of piezoelectrics (sensors, transducers, solid state memories)[72] within the field of energy storage materials. Lead-free ceramics have struggled to match the recoverable power output of their lead based counterparts, in recent years however, sodium niobate based ceramics have begun competing with the recoverable output of lead-based materials.[73,74]

One way in which NN ceramics may be suitable for this purpose is in relation to the coexistence of the antiferroelectric P-phase and the ferroelectric Q-phase at room temperature. In P-phase NN alternating layers of $a^-b^-a^-$, $a^-b^+a^-$ tilted octahedra lead to a net spontaneous polarisation of zero under application of an electric field. Q-phase NN only contains the $a^-a^-b^+$ tilt system, allowing for spontaneous polarisation giving rise to ferroelectric behaviour.[75] On application of an electric field to sodium niobate there is an irreversible phase transition to the ferroelectric Q phase.[76] Reversible AFE-FE transitions are desirable for high energy storage density although this trait is typically only observed in lead based materials.[77] It has been demonstrated that doping with $SrSnO_3$ and MnO_2 it is possible to significantly increase the recoverable energy storage density of NN by enabling the reversibility of the transition, and suppressing the conductivity of the system by addition of 1wt% MnO_2 ($0.91NaNbO_3$-$0.09SrSnO_3$ + 1wt.% Mn). This gives a significantly narrower Polarisation-Electric field (P-E) loop and affords about a 90% energy-storage efficiency. The difference in P-E loops upon modification is shown in Figure 1.12.[78]

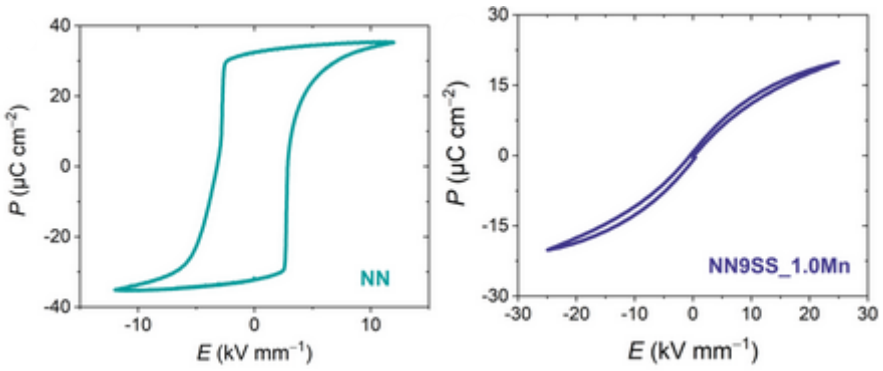

Figure 1.12: P-E loops of $NaNbO_3$ and $0.91NaNbO_3$-$0.09SrSnO_3$ + 1wt.% Mn (Taken from Zhang M. et. al.)[78]

This reversible AFE-FE transition is also observed by addition of low tolerance factor perovskite such as $CaHfO_3$. It achieves this by reducing the distortion angle of the BO_6 octahedra.[75] This methodology may be worth considering when targeting specific electrical properties within a NN based ceramics.

Recently it has been demonstrated that A site bismuth doping ($Na_{1-3x}Bi_xNbO_3$) can be used to eliminate the octahedral tilting in NN using significantly less dopant: tilting is completely eliminated at x = 0.20.[79] Electrical testing of $Na_{0.4}Bi_{0.2}NbO_3$ suggests that removing the tilting from NN affords a significant boost in oxide ion conductivity caused by increasing the oxygen vacancy concentration, and reducing the migration activation energy as shown in Figure 1.13.[80]

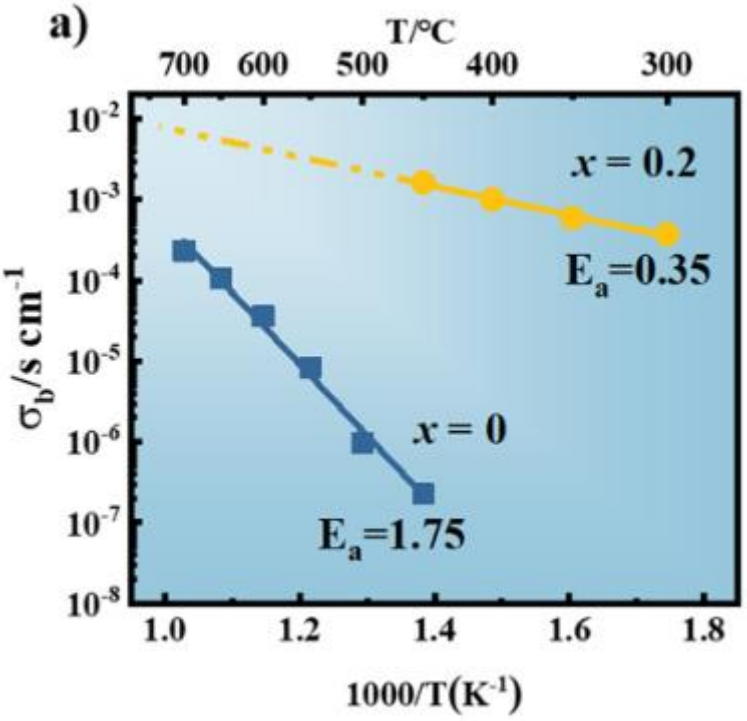

Figure 1.13: Arrhenius Plot of Bulk Conductivities of $NaNbO_3$ and $Na_{0.4}Bi_{0.2}NbO_3$ (Taken from Lei X. et. al.)[80]

Lei *et. al.* also claim that the ionic conductivity is predominantly in the form of oxide ion conductivity. Although they have not conducted experiments to clearly elucidate this, only showcasing the pO_2 dependence of the ionic response shown in Figure 1.14.[80]

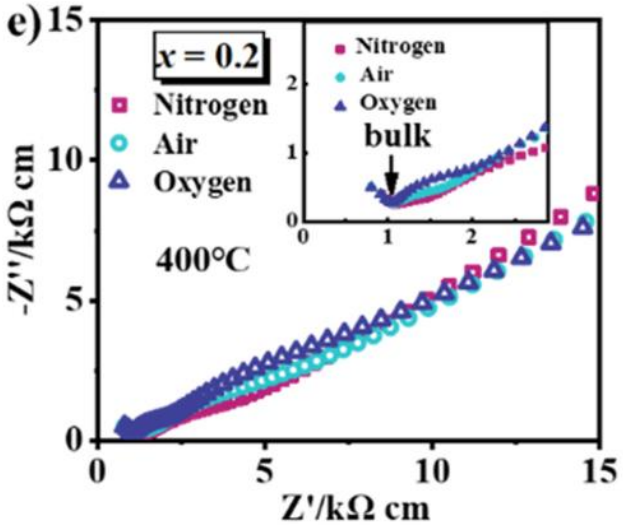

Figure 1.14: pO_2 Dependence of $Na_{0.4}Bi_{0.2}NbO_3$ (Taken from Lei X. et. Al.)[80]

It is worth noting that according to the doping mechanism proposed by Lei *et. Al.* no oxygen vacancies would be required for charge balance; therefore, the increased ionic conductivity is more likely attributed to sodium ions moving through A-site vacancies.

Titanium substituted at the B-site of NN has displayed evidence of oxide ion conduction (Figure 1.15), with undoped NN showing some sodium ion conductivity[81]

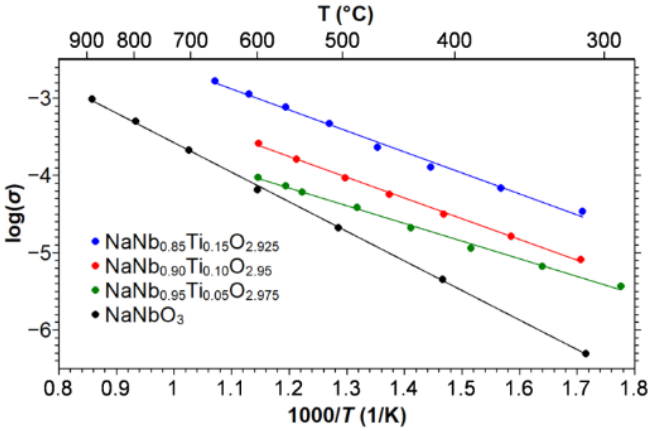

Figure 1.15: Arrhenius Plots of Bulk Conductivity of $NaNb_{1-x}Ti_xO_{3-\delta}$ (Taken from Gorget et. al.)[81]

Further studies with NN doped with up to 10% Ti^{4+} showcases the generation of oxygen vacancies, and boosts ionic conductivity according to the doping mechanism: $Nb^{5+} + ½\ O^{2-} = Ti^{4+}$. The material $NaNb_{0.9}Ti_{0.1}O_{2.95}$ displays high levels of ionic conductivity;

this has been attributed to be a mixture of Na^+ and O^{2-} conduction; dominated at low temperatures by Na^+ in a ratio of 22:3 (Na^+:O^{2-}). As temperature increases and the material passes through the S-T(1) and T(1)-T(2) phase transitions, detailed in Figure 1.11,[64] the material becomes a pure ionic conductor, and the transport numbers t_{Na+} and t_{O2-} invert, as shown in Figure 1.16 which indicates the change in t_{O2-} according to temperature, producing a purely ionic oxide ion conductor. Comparatively, the ionic conductivity of undoped sodium niobate is attributed to sodium ion conduction at all temperatures and is independent of any phase transitions.[82]

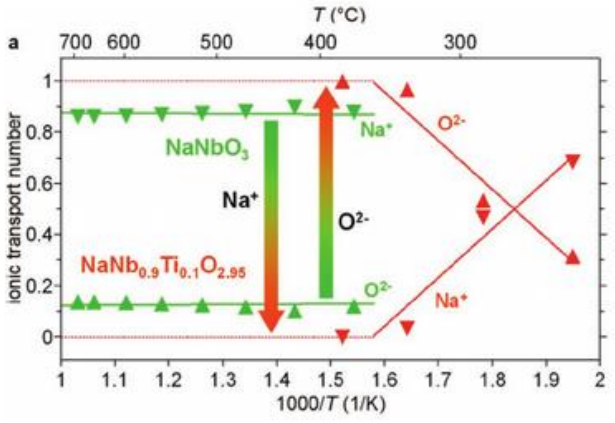

Figure 1.16: Inversion of Na^+ and O^{2-} Transport Numbers (Taken from Gouget et.al.)[82]

The ionic transport numbers shown by Gouget *et. al.* in Figure 1.16 was determined *via* a blocking layer method impedance spectroscopy. A pellet was prepared layered with 8-YSZ blocking layers and tested *via* impedance spectroscopy.

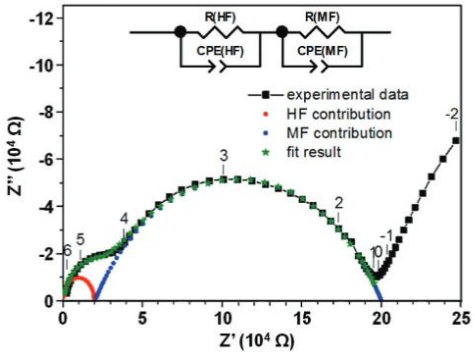

Figure 1.17: Typical Z Plot for 8-YSZ/$NaNb_{0.9}Ti_{0.1}O_{2.95}$/8-YSZ Pellet (Taken from Gouget et. al.)*[82]

According to Gouget *et. al.* the high frequency distortion is attributed to the conductivity of the 8-YSZ layers (HF contribution in Figure 1.17) the subsequent arc is then entirely attributed to the investigated sodium niobate species (MF contribution in Figure 1.17). As YSZ has an oxygen transport number of approximately 1 and negligible alkaline cation

diffusion, the following equation can be used to extract the specific conductivity of the oxide ion conducting species.

$$\frac{1}{R_{Total}} - \frac{1}{R_{YSZ}} = \sigma_{O^{2-}} \qquad (1.15)$$

The conductivity of the sodium ion conducting species was then determined by subtraction of the oxide ion conductivity from the total conductivity of the species without blocking layers.

$$\sigma_{Total\ (Non\ blocking)} - \sigma_{O^{2-}} = \sigma_{Na^{+}} \qquad (1.16)$$

The ion transport numbers are then extracted from the following equations.

$$t_{O^{2-}} = \frac{\sigma_{O^{2-}}}{\sigma_{Na^{+}} + \sigma_{O^{2-}} + \sigma_{e^{-}}} = \frac{\sigma_{O^{2-}}}{\sigma_{Total}} \qquad (1.17)$$

$$t_{Na^{+}} = \frac{\sigma_{Na^{+}}}{\sigma_{Na^{+}} + \sigma_{O^{2-}} + \sigma_{e^{-}}} = \frac{\sigma_{Na^{+}}}{\sigma_{Total}} \qquad (1.18)$$

It is worth noting that this method of determining the conductivity of the sodium ion conducting species does not successfully decouple the conductivity contributions of sodium ions and electrons.

Sodium niobate faces a range of complications as a material. Primarily during the synthesis and fabrication processes. When using a traditional solid state synthesis method, calcination and sintering temperatures frequently exceed 800˚C for calcination and 1200˚C for sintering. At temperatures this high the sodium oxide typically used in the synthesis becomes volatile leading to discrepancies in sodium content both at the surface and throughout the body of the final NN product.[83,84] The initial volatilisation may be avoided by use of alternative synthesis techniques such as sol-gel or hydrothermal routes. However, the densification into a usable ceramic remains problematic. Steps have been taken to increase density without incurring sodium loss such as adding excess soda to the green bodies[84] and sintering in low pO_2 environments which appear to minimise volatility and increase the density of the ceramic product without any sintering additives.[85]

1.7. Potassium Tantalate

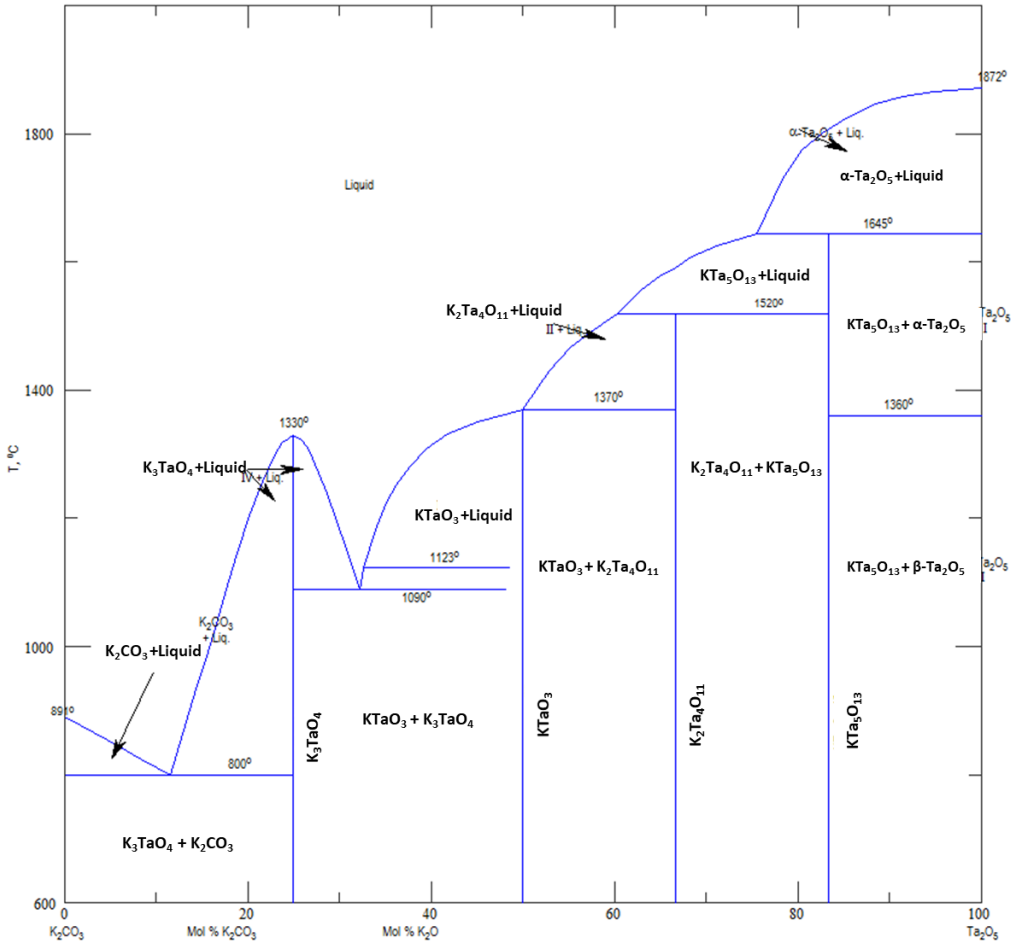

Figure 1.18: Binary Phase Diagram of K_2CO_3 – Ta_2O_5 Adapted from A. Reizman et. al. Obtained from ACS Phases Software

Figure 1.18 shows the binary phase diagram of K_2CO_3 and Ta_2O_5, a stoichiometric mix leads to the formation of the perovskite $KTaO_3$. Much of the interest in $KTaO_3$ has been in the field of superconductivity. Although this was achieved *via* electrostatic carrier doping and was utilised to highlight the limitations of chemical doping the system. While applications in this field are interesting, it is ultimately unrelated to the wider scope of the work presented in this thesis and so the following review of $KTaO_3$ focuses on its applications as a functional ceramic material.

Potassium Tantalate is an ABO_3 perovskite that has undergone quite limited investigation. Structural studies have been conducted in the past and the phase diagram shown in Figure 1.18 showcases the adjacent materials and potential solid solutions present in the K_2CO_3-Ta_2O_5 system.

$KTaO_3$ has been identified as an incipient ferroelectric. This incipient behaviour is characterised by a rapid increase in relative permittivity on cooling towards 0 K but is saturated due to quantum fluctuations.[86,87] This leads to the relative permittivity remaining constant, independent of temperature as shown below in Figure 1.19.

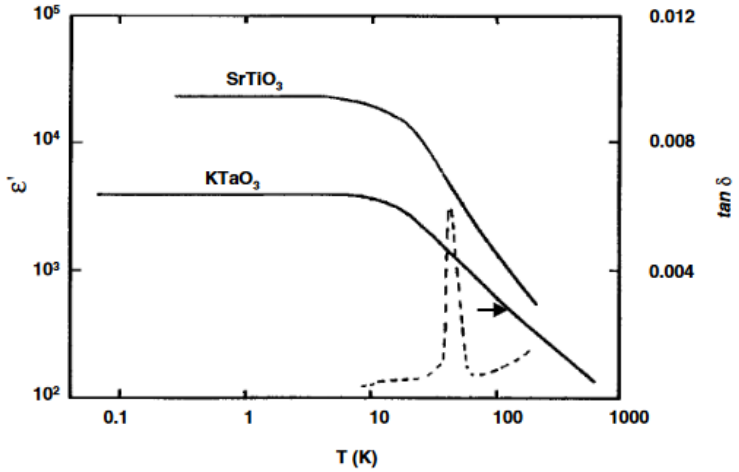

Figure 1.19: Incipient Behaviour of $KTaO_3$ and $SrTiO_3$ Ceramics and Associated Dielectric Losses (Taken from Samara G.)[87]

Where the incipient ferroelectric breaks away from traditional Curie-Weiss behaviour the Barrett equation can be used to fit the temperature dependence of the relative permittivity. The Curie-Weiss and Barrett equations are shown below in equations 1.19 and 1.20, respectively.

$$\varepsilon_r = \varepsilon_0 + \frac{C}{T - T_c} \qquad (1.19)$$

$$\varepsilon_r = \frac{M}{\left(\frac{T_1}{2}\right) coth\left(\frac{T_1}{2T}\right) - T_0} + A \qquad (1.20)$$

Where M is a constant related to the quantum fluctuations in the material, A is the permittivity at the high frequency limit, T_1 is the crossover temperature between Curie-Weiss behaviour and where quantum effects dominate and T_0 is the expected Curie temperature. When $T >> T_1$: $\left(\frac{T_1}{2}\right) coth\left(\frac{T_1}{2T}\right)$ approaches T causing the equation to reduce to the Curie-Weiss law. In the case of most ferroelectrics $T_0 > T_1$ meaning that the ferroelectric phase transition occurs before any quantum fluctuations stabilise the long-range ferroelectric order thus ensuring the paraelectric state is not stabilised. In $KTaO_3$ T_1=56.9 K and T_0=13.1 K giving rise to the incipient behaviour observed. Incipient ferroelectrics have been investigated for potential applications in microwave dielectrics however, $KTaO_3$ has been deemed unsuitable for this application due to a low permittivity at room temperature (Figure 1.19).[88,89]

$KTaO_3$ has received some interest as an ionic conductor. The novel work conducted by Yadav *et. al.* suggested that acceptor doping enhanced oxide ion conductivity within the material at temperatures above 550˚C, lending it to potential applications as an ITSOFC electrolyte material. The work focuses on the B-site co-doped material $KTa_{1-x-y}Ti_xGe_yO_{3-\delta}$.[90] Acceptor doping of the B-site according to the following mechanism to introduce oxygen vacancies and promote oxide ion conductivity.

$$2Ta^{5+} + O^{2-} = Ti^{4+} + Ge^{4+} \qquad (1.21)$$

Doping with titanium or germanium individually did not yield the same level of conductivity as the co-doped material. The reason for this disparity is not discussed; the tolerance factors for the titanium, germanium and co-doped materials are shown in the table below.

Composition	Tolerance Factor (t)
$KTaO_3$	1.06
$KTa_{0.6}Ti_{0.4}O_{2.8}$	1.07
$KTa_{0.6}Ge_{0.4}O_{2.8}$	1.09
$KTa_{0.4}Ti_{0.3}Ge_{0.3}O_{2.7}$	1.09

Table 1.1: Calculated Tolerance Factors for $KTa_{1-x-y}Ti_xGe_yO_{3-\delta}$ Materials

Although the tolerance factor increases, suggesting movement to a more disordered, likely tetragonal symmetry system, it is reported that the unit cell remains cubic with relatively unchanged lattice parameters. This has been attributed to the “rigid nature of the octahedral network” although it is worth noting that generally an increase in the vacancy concentration in a perovskite would be associated with a notable expansion or contraction of the unit cell.[91]

The reported ionic conductivity in $KTa_{0.4}Ti_{0.3}Ge_{0.3}O_{2.7}$ is comparable to several other ITSOFC electrolyte candidates including LSGM and NBT as shown in Figure 1.20.

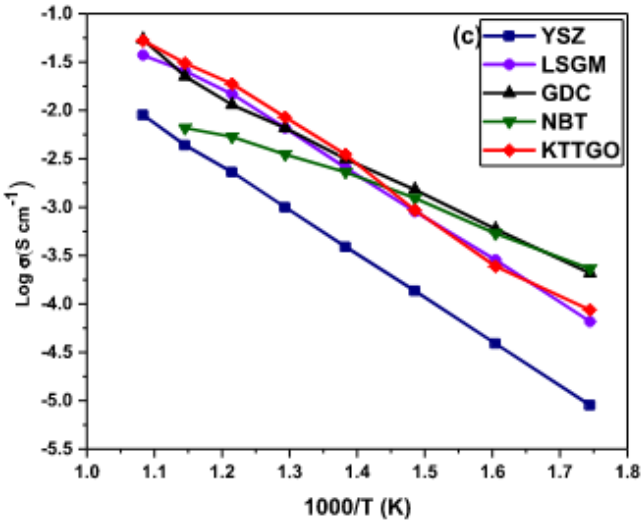

Figure 1.20: Arrhenius Plots of conductivity for $KTa_{0.4}Ti_{0.3}Ge_{0.3}O_{2.7}$ Compared to Notable Oxide Ion Conductors (Taken from Yadav et. al.)[90]

If the reported conductivity of $KTa_{0.4}Ti_{0.3}Ge_{0.3}O_{2.7}$ is accurate it may be an attractive option for ITSOFC electrolytes, although significant additional characterisation is required to assess its suitability for this application. To date there has not been a determination of ionic transport number and there is evidence at lower temperatures of p-type conductivity indicating mixed conduction.[90]

1.4. Conclusions

ITSOFCs while a desirable pursuit in the future of energy production continue to face a range of issues that must be overcome if they are to consistently match the power output and lifetime of their high temperature counterparts. Arguably, the key to overcoming many of these issues is by production of a solid electrolyte that is chemically stable within the range of operational temperatures (400-800˚C), both chemically and thermally compatible with common electrode materials, and with high interfacial ionic conductivity. The development of NBT as an oxide ion conductor suggests that other lead-free piezoelectric type perovskites with small compositional changes may also function as ionic conductors for the same purpose. By use of this alongside intelligent perovskite design with oxide ion conduction in mind;[92] it may be possible to produce electrode materials that are suitable for ITSOFCs, without the requirement for performance compromises or additional fabrication processes. The perovskites sodium niobate and potassium tantalate may be candidates for this. The ionic conductivity observed in $Na_{0.4}Bi_{0.2}NbO_3$ and $NaNb_{1-x}Ti_xO_{3-\delta}$ warrant further investigation. Both materials have been of interest for many years with some applications as dielectrics, the potential uses as ionic conductors have only become of interest recently. It is possible

that application of similar methodologies to other ‘leaky’ dielectrics may find a suitable electrolyte material.

1.5. References

1. Ritchie, H. & Roser, M. Fossil fuels. *Our World Data* (2017).

2. Maslin, M. *Global warming: a very short introduction*. (OUP Oxford, 2008).

3. Shafiee, S. & Topal, E. When will fossil fuel reserves be diminished? *Energy Policy* **37**, 181–189 (2009).

4. Iwata, H. & Okada, K. Greenhouse gas emissions and the role of the Kyoto Protocol. *Environ. Econ. Policy Stud.* **16**, 325–342 (2014).

5. Murdock, H. E. *Renewables 2019 Global Status Report Collaborative*. (2019).

6. Whittingham, M. S. History, evolution, and future status of energy storage. *Proc. IEEE* **100**, 1518–1534 (2012).

7. Marbán, G. & Valdés-Solís, T. Towards the hydrogen economy? *Int. J. Hydrogen Energy* **32**, 1625–1637 (2007).

8. Xu, J. & Froment, G. F. Methane steam reforming, methanation and water-gas shift: I. Intrinsic kinetics. *AIChE J.* **35**, 88–96 (1989).

9. Stojić, D. L., Marčeta, M. P., Sovilj, S. P. & Miljanić, Š. S. Hydrogen generation from water electrolysis - Possibilities of energy saving. *J. Power Sources* **118**, 315–319 (2003).

10. Vaghari, H., Jafarizadeh-Malmiri, H., Berenjian, A. & Anarjan, N. Recent advances in application of chitosan in fuel cells. *Sustain. Chem. Process.* **1**, 16 (2013).

11. Grove, W. R. XXIV. On voltaic series and the combination of gases by platinum . *London, Edinburgh, Dublin Philos. Mag. J. Sci.* **14**, 127–130 (1839).

12. Grove, W. R. On a gaseous voltaic battery. *J. Franklin Inst.* **35**, 277–280 (1843).

13. Sealy, C. The problem with platinum. *Mater. Today* **11**, 65–68 (2008).

14. Aguiar, P., Adjiman, C. S. & Brandon, N. P. Anode-supported intermediate temperature direct internal reforming solid oxide fuel cell. I: Model-based steady-state performance. *J. Power Sources* **138**, 120–136 (2004).

15. Pei, P., Korom, S. F., Ling, K. & Nasah, J. Cost comparison of syngas production from natural gas conversion and underground coal gasification. *Mitig. Adapt. Strateg. Glob. Chang.* **21**, 629–643 (2016).

16. Pritchard, D. F. & Rattigan, W. M. Hazards of liquid hydrogen: Position paper. Health and Safety Executive (2010).

17. Aloui, T. & Halouani, K. Analytical modeling of polarizations in a solid oxide fuel cell using biomass syngas product as fuel. *Appl. Therm. Eng.* **27**, 731–737 (2007).

18. Minh, N. Q. Ceramic fuel cells. *J. Am. Ceram. Soc.* **76**, 563–588 (1993).

19. Yang, Z., Xia, G. G., Li, X. H. & Stevenson, J. W. $(Mn,Co)_3O_4$ spinel coatings on ferritic stainless steels for SOFC interconnect applications. *Int. J. Hydrogen Energy* **32**, 3648–3654 (2007).

20. Zhu, T., Fowler, D. E., Poeppelmeier, K. R., Han, M. & Barnett, S. A. Hydrogen Oxidation Mechanisms on Perovskite Solid Oxide Fuel Cell Anodes. *J. Electrochem. Soc.* **163**, F952–F961 (2016).

21. Hibino, T., Wang, S., Kakimoto, S. & Sano, M. One-chamber solid oxide fuel cell constructed from a YSZ electrolyte with a Ni anode and LSM cathode. *Solid State Ionics* **127**, 89–98 (2000).

22. Benjamin, T. G., Camara, E. H. & Marianowski, L. G. *Handbook of fuel cell performance*. (1980).

23. Yokokawa, H., Sakai, N., Horita, T. & Yamaji, K. Recent developments in solid oxide fuel cell materials. *Fuel cells* **1**, 117–131 (2001).

24. Yang, Z., Weil, K. S., Paxton, D. M. & Stevenson, J. W. Selection and Evaluation of Heat-Resistant Alloys for SOFC Interconnect Applications. *J. Electrochem. Soc.* **150**, A1188 (2003).

25. Zouhri, K., Shinneeb, M., Chikhalsouk, M. & Cress, J. Solid oxide fuel cell cathode diffusion polarization: materials and exergy study. *Energy Convers. Manag.* **231**, 113865 (2021).

26. Zouhri, K., Shinneeb, M., Chikhalsouk, M. & Cress, J. Solid oxide fuel cell cathode diffusion polarization: materials and exergy study. *Energy Convers. Manag.* **231**, 113865 (2021).

27. Huang, K., Zampieri, A. & Ise, M. Cathode Polarizations of a Cathode-Supported Solid Oxide Fuel Cell. *J. Electrochem. Soc.* **157**, B1471 (2010).

28. Takeguchi, T., Kikuchi, R., Yano, T., Eguchi, K. & Murata, K. Effect of precious metal addition to Ni-YSZ cermet on reforming of CH_4 and electrochemical activity as SOFC anode. *Catal. Today* **84**, 217–222 (2003).

29. Tao, S. & Irvine, J. T. S. A redox-stable efficient anode for solid-oxide fuel cells. *Nat. Mater.* **2**, 320–323 (2003).

30. Zhe, Y., Qizhao, L. & Zhu, B. Thermodynamic analysis of ITSOFC hybrid system for polygenerations. *Int. J. Hydrogen Energy* **35**, 2824–2828 (2010).

31. Shen, J. P. & Song, C. Influence of preparation method on performance of Cu/Zn-based catalysts for low-temperature steam reforming and oxidative steam reforming of methanol for H_2 production for fuel cells. *Catal. Today* **77**, 89–98 (2002).

32. Basagiannis, A. C., Panagiotopoulou, P. & Verykios, X. E. Low temperature steam reforming of ethanol over supported noble metal catalysts. *Top. Catal.* **51**, 2–12 (2008).

33. Vivanpatarakij, S., Aiouache, F. & Assabumrungrat, S. Performance of an improved combination unit of Pd-membrane methane steam reformer and intermediate temperature solid oxide fuel cell (C-Pd-ITSOFC). *Int. J. Hydrogen Energy* **40**, 1894–1901 (2015).

34. Brett, D. J. L., Atkinson, A., Brandon, N. P. & Skinner, S. J. Intermediate temperature solid oxide fuel cells. *Chem. Soc. Rev.* **37**, 1568–1578 (2008).

35. Kwon, O. H. & Choi, G. M. Electrical conductivity of thick film YSZ. *Solid State Ionics* **177**, 3057–3062 (2006).

36. Sammes, N. M. & Zhihong, C. Ionic conductivity of ceria/yttria stabilized zirconia electrolyte materials. *Solid State Ionics* **100**, 39–44 (1997).

37. Han, M., Tang, X., Yin, H. & Peng, S. Fabrication, microstructure and properties of a YSZ electrolyte for SOFCs. *J. Power Sources* **165**, 757–763 (2007).

38. Jasinski, P., Petrovsky, V., Suzuki, T., Petrovsky, T. & Anderson, H. U. Electrical Properties of YSZ Films Prepared by Net Shape Technology. *J. Electrochem. Soc.* **152**, A454 (2005).

39. Ishigaki, T., Yamauchi, S., Kishio, K., Mizusaki, J. & Fueki, K. Diffusion of oxide ion vacancies in perovskite-type oxides. *J. Solid State Chem.* **73**, 179–187 (1988).

40. Esaka, T. Oxide Ion Conduction via Interstitial Sites in the Substituted Scheelite-and Spinel-type Oxides. *Electrochemistry* **78**, 16–22 (2010).

41. Zhu, B. Functional ceria-salt-composite materials for advanced ITSOFC applications. *J. Power Sources* **114**, 1–9 (2003).

42. Zhu, B., Fan, L. & Lund, P. Breakthrough fuel cell technology using ceria-based multi-functional nanocomposites. *Appl. Energy* **106**, 163–175 (2013).

43. Gil, V., Moure, C. & Tartaj, J. Sinterability, microstructures and electrical properties of Ni/Gd-doped ceria cermets used as anode materials for SOFCs. *J. Eur. Ceram. Soc.* **27**, 4205–4209 (2007).

44. Lacorre, P., Goutenoire, F., Bohnke, O., Retoux, R. & Laligant, Y. Designing fast oxide-ion conductors. *Nature* **404**, 9–11 (2000).

45. Goutenoire, F., Isnard, O., Retoux, R. & Lacorre, P. Crystal structure of $La_2Mo_2O_9$, a new fast oxide-ion conductor. *Chem. Mater.* **12**, 2575–2580 (2000).

46. Georges, S. *et al.* The LAMOX Family of Fast Oxide-Ion Conductors: Overview and Recent Results. *J. New Mater. Electrochem. Syst.* **7**, 51–57 (2004).

47. Evans, I. R., Howard, J. A. K. & Evans, J. S. O. The Crystal Structure of α-$La_2Mo_2O_9$ and the Structural Origin of the Oxide Ion Migration Pathway. *Chem. Mater.* **17**, 4074–4077 (2005).

48. Le, M. V., Tsai, D. S. & Nguyen, T. A. BSCF/GDC as a refined cathode to the single-chamber solid oxide fuel cell based on a LAMOX electrolyte. *Ceram. Int.* **44**, 1726–1730 (2018).

49. Yokokawa, H. Understanding Materials Compatibility. *Annu. Rev. Mater. Res.* **33**, 581–610 (2003).

50. Mitchell, R. H. *Perovskites Modern and Ancient*. (2002).

51. Megaw, H. D. Crystal structure of double oxides of the perovskite type. *Proc. Phys. Soc.* **58**, 133–152 (1946).

52. Howard, C. J. & Stokes, H. T. Group-theoretical analysis of octahedral tilting in perovskites. *Acta Crystallogr. Sect. B Struct. Sci.* **54**, 782–789 (1998).

53. Glazer, A. M. The classification of tilted octahedra in perovskites. *Acta Crystallogr. Sect. B Struct. Crystallogr. Cryst. Chem.* **28**, 3384–3392 (1972).

54. Ishihara, T., Matsuda, H. & Takita, Y. Doped $LaGaO_3$ Perovskite Type Oxide as a New Oxide Ionic Conductor. *J. Am. Chem. Soc.* **116**, 3801–3803 (1994).

55. Huang, P. Superior Oxygen Ion Conductivity of Lanthanum Gallate Doped with Strontium and Magnesium. *J. Electrochem. Soc.* **143**, 1644 (1996).

56. Huang, P., Horky, A. & Petric, A. Interfacial reaction between nickel oxide and lanthanum gallate during sintering and its effect on conductivity. *J. Am. Ceram. Soc.* **82**, 2402–2406 (1999).

57. Fergus, J. W. Electrolytes for solid oxide fuel cells. *J. Power Sources* **162**, 30–40 (2006).

58. Li, M. *et al.* A family of oxide ion conductors based on the ferroelectric perovskite $Na_{0.5}Bi_{0.5}TiO_3$. *Nat. Mater.* **13**, 31–35 (2014).

59. Yang, F. *et al.* Defect chemistry and electrical properties of sodium bismuth titanate perovskite. *J. Mater. Chem. A* **6**, 5243–5254 (2018).

60. Lu, Y., López, C. A., Wang, J., Alonso, J. A. & Sun, C. Insight into the structure and functional application of Mg-doped $Na_{0.5}Bi_{0.5}TiO_3$ electrolyte for solid oxide fuel cells. *J. Alloys Compd.* **752**, 213–219 (2018).

61. Shafer, M. W. & Roy, R. Phase equilibria in the system Na_2O–Nb_2O_5. *J. Am. Ceram. Soc.* **42**, 482–486 (1959).

62. Egerton, L. & Dillon, D. M. Piezoelectric and dielectric properties of ceramics in the system potassium—sodium niobate. *J. Am. Ceram. Soc.* **42**, 438–442 (1959).

63. Li, P. *et al.* Mechanism of significantly enhanced piezoelectric performance and stability in textured potassium-sodium niobate piezoelectric ceramics. *J. Eur. Ceram. Soc.* **38**, 75–83 (2018).

64. Megaw, H. D. The Seven Phases of Sodium Niobate. *Ferroelectrics* **7**, 87–89 (1974).

65. Cross, L. E. & Nicholson, B. J. LV. The optical and electrical properties of single crystals of sodium niobate. *London, Edinburgh, Dublin Philos. Mag. J. Sci.* **46**, 453–466 (1955).

66. Reznichenko, L. A. *et al.* Structural instabilities, incommensurate modulations and P

and Q phases in sodium niobate in the temperature range 300-500 K. *Crystallogr. Reports* **48**, 448–456 (2003).

67. Wang, X. B. *et al.* High temperature Raman study of phase transitions in antiferroelectric $NaNbO_3$. *J. Mol. Struct.* **385**, 1–6 (1996).

68. Glazer, A. M. & Megaw, H. D. Studies of the lattice parameters and domains in the phase transitions of $NaNbO_3$. *Acta Crystallogr. Sect. A* **29**, 489–495 (1973).

69. Zhang, M. H., Fulanović, L., Zhao, C. & Koruza, J. Review on field-induced phase transitions in lead-free $NaNbO_3$-based antiferroelectric perovskite oxides for energy storage. *J. Mater.* **9**, 1–18 (2023).

70. Liu, W., Zhao, D. & Li, S. Large electrostrain with good temperature stability in sodium niobate based ceramics. *RSC Adv.* **7**, 2550–2554 (2017).

71. Wu, J., Xiao, D. & Zhu, J. Potassium-sodium niobate lead-free piezoelectric materials: Past, present, and future of phase boundaries. *Chem. Rev.* **115**, 2559–2595 (2015).

72. Zhang, H., Yang, B., Yan, H. & Abrahams, I. Isolation of a ferroelectric intermediate phase in antiferroelectric dense sodium niobate ceramics. *Acta Mater.* **179**, 255–261 (2019).

73. Shao, T. *et al.* Potassium-sodium niobate based lead-free ceramics: novel electrical energy storage materials. *J. Mater. Chem. A* **5**, 554–563 (2017).

74. Yang, Z. *et al.* Significantly enhanced recoverable energy storage density in potassium-sodium niobate-based lead free ceramics. *J. Mater. Chem. A* **4**, 13778–13785 (2016).

75. Luo, N. *et al.* Well-defined double hysteresis loop in $NaNbO_3$ antiferroelectrics. *Nat. Commun.* **14**, 1776 (2023).

76. Zhang, M. H. *et al.* Electric-field-induced antiferroelectric to ferroelectric phase transition in polycrystalline NaNbO3. *Acta Mater.* **200**, 127–135 (2020).

77. Tan, X., Ma, C., Frederick, J., Beckman, S. & Webber, K. G. The antiferroelectric ↔ ferroelectric phase transition in lead-containing and lead-free perovskite ceramics. *J. Am. Ceram. Soc.* **94**, 4091–4107 (2011).

78. Zhang, M.-H. *et al.* Tailoring high-energy storage $NaNbO_3$-based materials from antiferroelectric to relaxor states. *Nat. Commun. 2023 141* **14**, 1–11 (2023).

79. Levin, I. *et al.* Displacive Order–Disorder Behavior and Intrinsic Clustering of Lattice Distortions in Bi-Substituted $NaNbO_3$. *Adv. Funct. Mater.* **2001840**, 1–13 (2020).

80. Lei, X. *et al.* Realizing oxygen ion conduction in perovskite structure $NaNbO_3$ by A-site Bismuth doping. *J. Alloys Compd.* **924**, 2–6 (2022).

81. Gouget, G. *et al.* High Ionic Conductivity in Oxygen-Deficient Ti-Substituted Sodium Niobates and the Key Role of Structural Features. *Chem. Mater.* **31**, 2828–2841 (2019).

82. Gouget, G. *et al.* Associating and Tuning Sodium and Oxygen Mixed-Ion Conduction in Niobium-Based Perovskites. *Adv. Funct. Mater.* **30**, 1–12 (2020).

83. Zhang, Z. T., Sridhar, S. & Cho, J. W. An investigation of the evaporation of B_2O_3 and Na_2O in f-free mold slags. *ISIJ Int.* **51**, 80–87 (2011).

84. Lee, Y. H., Cho, J. H., Kim, B. I. & Choi, D. K. Piezoelectric properties and densification based on control of volatile mass of potassium and sodium in $(K_{0.5}Na_{0.5})NbO_3$ ceramics. *Jpn. J. Appl. Phys.* **47**, 4620–4622 (2008).

85. Shimizu, H., Kobayashi, K., Mizuno, Y. & Randall, C. A. Advantages of low partial pressure of oxygen processing of alkali niobate: $NaNbO_3$. *J. Am. Ceram. Soc.* **97**, 1791–1796 (2014).

86. Ferrarelli, M. C., Nuzhnyy, D., Sinclair, D. C. & Kamba, S. Soft-mode behavior and incipient ferroelectricity in $Na_{1/2}Bi_{1/2}Cu_3Ti_4O_{12}$. *Phys. Rev. B - Condens. Matter Mater. Phys.* **81**, 1–7 (2010).

87. Samara, G. A. The relaxational properties of compositionally disordered ABO_3 perovskites. *J. Phys. Condens. Matter* **15**, (2003).

88. Kamba, S. *et al.* Ferroelectric and incipient ferroelectric properties of a novel $Sr_{9-x}Pb_xCe_2Ti_2O_{36}$(x = 0-9) ceramic system. *Chem. Mater.* **21**, 811–819 (2009).

89. Tagantsev, A. K., Sherman, V. O., Astafiev, K. F., Venkatesh, J. & Setter, N. Ferroelectric materials for microwave tunable applications. *J. electroceramics* **11**, 5–66 (2003).

90. Yadav, A., Pyare, R., Goodenough, J. B. & Singh, P. $KTa_{1-x-y}Ti_xGe_yO_{3-\delta}$: A High κ Relaxor Dielectric and Superior Oxide-Ion Electrolyte for IT-SOFC. *ACS Appl. Energy Mater.* **3**, 3205–3211 (2020).

91. Tsvetkov, D. S., Sereda, V. V., Malyshkin, D. A., Ivanov, I. L. & Zuev, A. Y. Chemical lattice strain in nonstoichiometric oxides: an overview. *J. Mater. Chem. A* **10**, 6351–6375 (2022).

92. Gao, R. *et al.* Designing Optimal Perovskite Structure for High Ionic Conduction. *Adv. Mater.* **32**, 1–9 (2020).

Chapter 2. Experimental Procedure

2.1. Materials Synthesis

2.1.1. Conventional Solid State

The majority of materials discussed in this thesis were synthesised *via* a traditional solid-state method. The reagents used were oxide (Nb_2O_5, Ga_2O_3, MgO, TiO_2, WO_3, and MoO_3), and carbonate (Na_2CO_3 and $CaCO_3$) powders dried for 8 hours at appropriate temperatures prior to being mixed in stoichiometric amounts to obtain 25 g batches of each investigated composition. The mixed powders were then suspended in isopropanol and ball milled with YSZ milling media for 6 hours at a rate of 300 rpm. The ball milled powder was then separated from the milling media and dried overnight at 80˚C to remove all the isopropanol. The dried powders were sieved through a 250 μm mesh. The dried mixture was transferred to an alumina crucible and calcined at 900 ˚C for 2 hours with a heating rate of 5˚C min^{-1}.[1] The reacted powder was ball milled, dried, and sieved again to obtain the final composition. Subsequent calcinations were carried out, if necessary, until the obtained powder was confirmed to be single phase *via* X-ray diffraction.

2.1.2. Hydrothermal

NN was also synthesised *via* a hydrothermal method. 8.1240g of Nb_2O_5 (99.9985%, Sigma Aldrich) was dissolved in 60 ml of an 8.4 M Na(OH) solution and the resultant mixture placed into a Teflon lined autoclave. The autoclave was heated to 200 °C for 72 hours. The resultant precipitate was washed 3 times using deionised water in a centrifuge and dried overnight at 180 °C to give the powders.[2]

2.1.3. Sintering

Single phase powders were uniaxially pressed under a pressure of 123 kPa in circular 10-20 mm dies to obtain green pellets. These pellets were transferred to an alumina crucible and covered in sacrificial powder of the same composition; then fired in a furnace at an appropriate temperature for 4 hours with a heating/cooling rate of 2.5˚C min^{-1} to obtain sintered ceramics.

2.2. Density Calculation and Theoretical Density

The density of sintered ceramics was calculated from its geometry and confirmed *via* use of an Archimedes balance with negligible differences observed in any sample.

Geometry:

$$\rho = \frac{m}{V} \qquad V = \pi r^2 h$$

$m = mass\ of\ sample$ $r = radius\ of\ sample\ face$ $h = sample\ thickness$

Archimedes Principle:

$$\rho = \frac{m_{air}}{m_{air} - m_{H_2O}} \times \rho_{H_2O}$$

$m_{air} = Sample\ mass\ in\ air$ $m_{H_2O} = Sample\ mass\ in\ water$

The calculated densities were compared to the maximum theoretical density to assess the quality of sintering conditions and level of porosity in the ceramic. The theoretical density was obtained *via* the following equation.

$$\rho_{max} = \frac{Mr \times N}{V_{Cell} \times N_A}$$

$Mr = Molecular\ Weight$ $N = Number\ of\ units\ in\ cell$

$V_{Cell} = Unit\ Cell\ Volume$ $N_A = Avogadros\ Number$

The unit cell volume and number of units in a cell were determined from the lattice parameters obtained from the powder X-ray diffraction data.

2.3. X-Ray Diffraction

X-ray diffraction data was utilised to perform phase analysis of synthesised powders and for determination of lattice parameters. Diffraction data was collected from the PANalytical X'Pert^3 using a Cu K_α radiation source. Powder samples were prepared by backfilling a standard round PANalytical sample holder and compressing with a glass slide to ensure a flawless incident surface.

Diffraction data was obtained in the 2θ = 10 - 90˚ range (no peaks below 20˚) using a 0.02˚ step size. Phase analysis was conducted using the PDF-4+ software and comparing the obtained diffraction patterns with literature patterns within the ICDD database.

Lattice parameters were determined *via* iterative calculations using GSAS 2.0 software and using a relevant .cif file obtained from the International Union of Crystallography (IUCr) database. A silicon standard was used to calibrate the peak positions prior to iterative calculations. The parameters iteratively solved were: histogram scale factor, sample displacement, background (chebychebev-1), micro strain, crystallite size, and unit cell. For all refined unit cells, the R_{wp}<10%.

2.4. Scanning Electron Microscopy (SEM)

SEM samples were prepared by polishing a sintered ceramic with increasingly fine grit polishing paper/diamond pastes. The ceramic would be polished to a 1 micron finish before undergoing thermal etching by firing the polished pellet at 200˚C below the sintering temperature for 20 minutes. The thermally etched samples were mounted to an Agar Scientific SEM pin stub using a carbon disk and painting the side of the pellet with silver dag to provide the SEM current route to ground and minimise sample drift and charging effects. The mounted pellet was then carbon coated using a sputter coater to provide a conductive surface.

The samples were analysed using an FEI Inspect F-50 high resolution electron microscope with spot size 3 and an accelerating voltage of 10-20 kV collecting both secondary electron (SE) and back scattered electron (BSE) images to evaluate both topographical and compositional changes. Elemental analysis was conducted using energy dispersive x-ray spectroscopy (EDS)

2.5. Electron Probe Microanalysis (EPMA)

EPMA samples were prepared in the same manner as SEM samples.

The samples were analysed using a JEOL JXA8530 equipped with 4 wavelength dispersive spectroscopy (WDS) crystal spectrometers. The microscope utilised a 100 nA current and 15 kV accelerating voltage. The standards used for the WDS quantitative analysis were MgO (magnesium), Jadeite ($NaAlSi_2O_6$, sodium), GaP (gallium), Niobium metal (niobium) and Al_2O_3 (oxygen).

WDS spectra are generated by accelerating electrons from an electron gun to the sample surface to generate characteristic X-rays. The generated X-rays are then diffracted by the crystals according to Bragg's law before reaching the detector, measuring the intensity of the X-rays as shown in Figure 2.1. The resultant intensity is then compared to the WDS spectra of the chosen standards for each element to determine the concentration of an element within the sample.

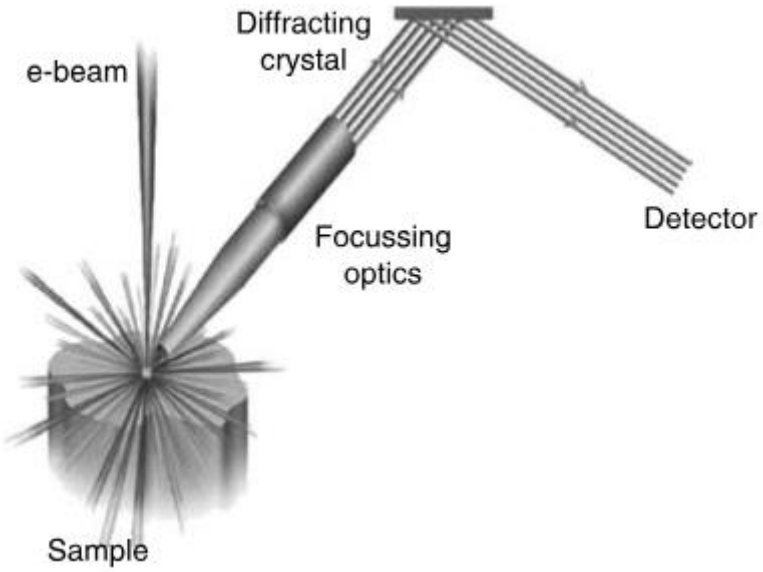

Figure 2.1: Schematic Representation of Generation of WDS Spectra (Taken from Van Hoek C. et. Al.)[3]

The position of the crystals may be adjusted to tune the spectrometer to the wavelength of a characteristic X-ray for one specific element.[3]

2.6. UV-Vis Spectroscopy

UV-Vis reflectance spectroscopy has been utilised to measure the band gap of $NaNbO_3$ and $NaNb_{0.95}Ga_{0.05}O_{2.95}$. A Shimadzu UV-2700i spectrometer with specular reflectance measurement attachment was utilised to collect the UV-Vis spectrum in the range 800-200 nm. A $BaSO_4$ standard was used to establish a baseline prior to measurement of the investigated powders. As the electronic band gap is defined as the energy required to excite an electron from the valence band to the conduction band, the wavelength of light absorbed by a sample is proportional to the band gap energy. This is indicated by a rapid decrease in the reflectance shown in Figure 2.2.

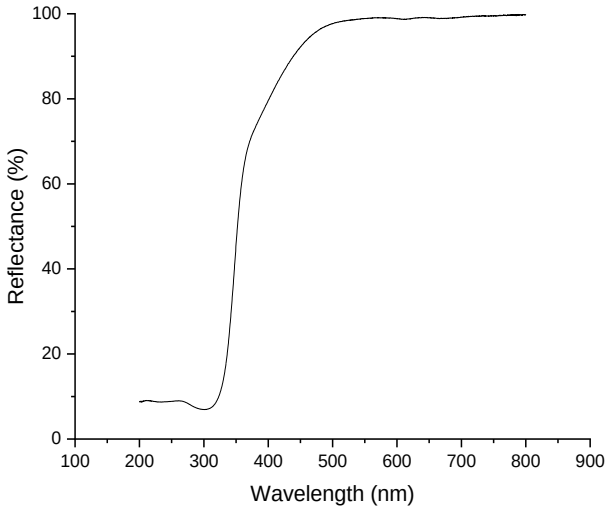

Figure 2.2: Example UV-Vis Reflectance Spectra Showcasing Onset of Absorption

The resultant reflectance spectrum was converted into a tauc-plot *via* the following equations:

$$R = \frac{\%R}{100}$$

$$k = (1 - R)^2$$

$$s = 2R$$

$$F(R) = \frac{k}{s}$$

$$E = hv$$

$$(F(R)hv)^{0.5} = \left(\frac{khv}{s}\right)^{0.5}$$

$R = Reflectance$ $k = Absorption\ Coefficient$ $s = Scattering\ Coefficient$

$h = Planks\ Constant$ $v = frequency$

$(F(R)hv)^{0.5}$ was plotted against energy in electron volts to obtain the tauc-plot shown in Figure 2.3.[4]

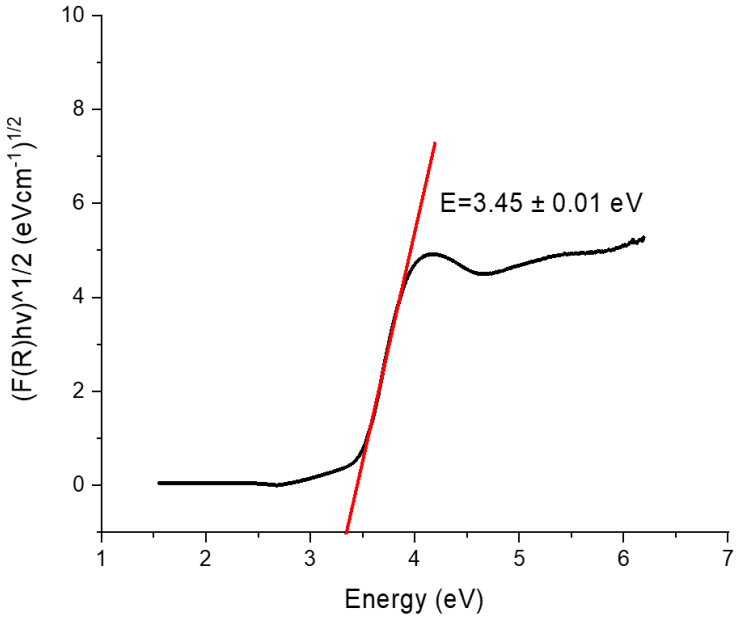

Figure 2.3: Example Tauc-plot Used for Band Gap Determination

The determined band gap is the x-intercept of the tangent to the linear region of the tauc-plot where y=mx+c:

$$E_g = \frac{-c}{m}$$

$$E_g = Band\ Gap$$

$$c = y - intercept \qquad m = slope$$

The associated error of the band gap has been determined *via* the following equation:

$$\sigma_{E_g} = \sqrt{\left(\frac{\sigma_m}{m}\right)^2 + \left(\frac{\sigma_c}{c}\right)^2}$$

$$\sigma_{E_g} = Standard\ Error\ of\ Band\ Gap \qquad \sigma_x = Standard\ Deviation\ of\ x$$

2.7. Electrical Analysis

2.7.1. Impedance Spectroscopy

Impedance spectroscopy has been utilised to determine the electrical properties of the ceramics. 10 mm sintered pellets had gold electrodes applied to each side. The pellet was loaded into a jig made in house and inserted into a tube furnace. The variables used for this project are temperature and oxygen partial pressure (pO_2).

An alternating voltage of 100 mV was then applied using an Agilent E4980A Precision LCR meter to the sample over a range of frequencies between 10^6-10^1 Hz. All measurements and data were geometry corrected according to the following equation before analysis.

$$GF = \frac{\pi r^2}{T}$$

$$r = Sample\ radius\ (cm) \qquad T = Sample\ Thickness\ (cm)$$

Impedance spectroscopy can be used to identify and characterise individual electrical components within an electroceramic according to the different time constants associated with each response. The time constant is a geometry independent parameter that may be expressed in a number of different equations linked to conductivity.

$$\tau = \frac{\varepsilon_0 \varepsilon_r}{\sigma} \qquad \tau = RC$$

$$\tau = Time\ Constant \quad \varepsilon_0 = Permittivity\ of\ Free\ Space \quad \varepsilon_r = Relative\ Permittivity$$
$$\sigma = Conductivity \qquad R = Resistance \qquad C = Capacitance$$

The time constant allows each electrical component to be ‘relaxed-out’ at different frequencies.

$$\omega_{max} RC = 1 \qquad \omega_{max} = 2\pi f_{max}$$

$$\omega_{max} = Maximum\ Angular\ Frequency \qquad f_{max} = Maximum\ Frequency\ of\ Peak$$

Each electrical component can usually be modelled as a resistor and a capacitor connected in parallel. Each ‘RC element’ will produce an arc in the Z* and M* plots where:[5]

$$Z^* = Z' - jZ''$$

$$Z^* = Complex\ Impedance \qquad j = \sqrt{-1}$$

$$Z' = Real\ impedance\ (Resistance) \qquad Z'' = Imaginary\ Impedance\ (Reactance)$$

And:

$$M^* = M' + jM''$$

$$M^* = Complex\ Electrical\ Modulus$$

$$M' = Real\ Modulus \qquad M'' = Imaginary\ Modulus$$

Figures 2.4 and 2.5 showcase how the capacitance of M'' or Z'' peaks may be extracted from $\omega_{max}RC=1$. For the purpose of this project bulk conductivities of ceramics were calculated from the imaginary modulus (M'') as the electrical modulus is dominated by the component with the lowest capacitance (typically bulk) and the conductivities of grain boundaries were determined from the imaginary impedance (Z'') as the impedance is dominated by the component with the greatest resistance (typically grain boundaries). By plotting the M'' and Z'' components against frequency the conductivity of each element may be extracted according to the following equations:

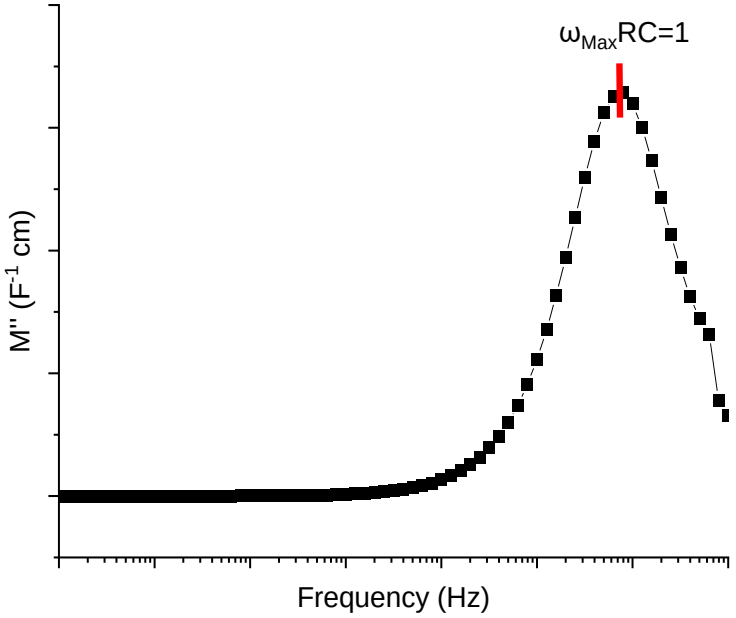

Figure 2.4: Example Frequency vs M'' Plot Used for Bulk Conductivity Determination

Bulk Conductivity:

$$C = \frac{1}{2M''}$$

$$R_B = \frac{1}{\omega_{Max} C}$$

$$\omega_{Max} \approx 2\pi f_{Max}$$

$$R_B = \frac{1}{2\pi f_{Max} \frac{1}{2M''}}$$

$$R_B = \frac{2M''}{2\pi f_{Max}}$$

$$\sigma_B = \frac{1}{R_B}$$

$$\sigma_B = \frac{\pi f_{max}}{M''}$$

Grain Boundary Conductivity:

$$R_{GB} = 2Z''$$

$$\sigma_{GB} = \frac{1}{2Z''}$$

Determination of Errors:

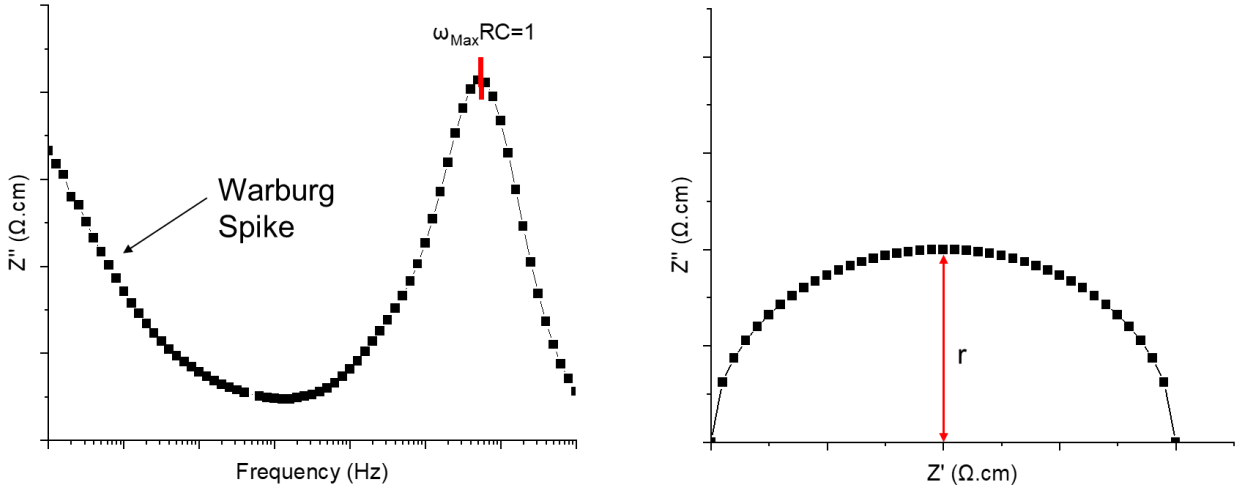

Figure 2.5: Methods of Extracting the Capacitance of Z'' Responses

Extraction of capacitance from Z'' plots utilises the following equation.

$$2\pi f_{max} RC = 1$$

$$R = 2Z''$$

$$C = \frac{1}{2\pi f_{max} 2Z''}$$

To approximate the error of this calculation the Z'' is calculated from the radius of the fitted circle of the Z* plane.

$$R = 2Z''_{max} = r$$

The difference between the calculated capacitances from the 2 methods is taken to be the error.

As M'' is a measure of capacitance the error of the value is equal to the error of the LCR meter which in this case is ±0.05%.

The Warburg spike shown in Figure 2.6b is the primary indicator of ionic conductivity within a sample.

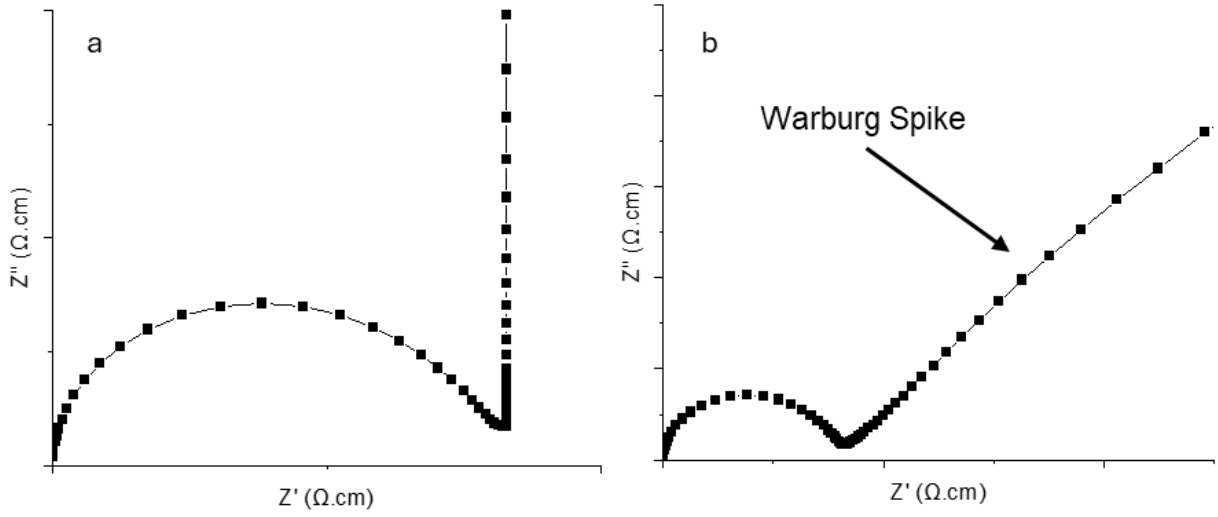

Figure 2.6: a) Idealised Electrode Response with Blocking Electrodes b) Typical Electrode Response for an Ionic Conductor

At low frequencies the Warburg response emerges in ionic conductors, representing diffusion of ions towards and away from the sample-electrode interface. In an ideal model with blocking electrodes the concentration of ions builds up at the interface and behaves as an ideal capacitor, yielding a low frequency vertical response in the Z* plane (Figure 2.6a) with an angle of exactly 90°. However, under real conditions some ions may migrate through the interface due to imperfections in the electrode surface, this may be treated as an infinite diffusion of charge carriers which conditions yield $|Z'| = |Z''|$ and therefore a 45° spike (Figure 2.6b).[6] Under experimental conditions the angle of the Warburg spike may vary from 45° based on the partially blocking properties of the electrode, identity of the charge carrier, and/or the presence of mixed conduction.

2.7.2. LCR

Samples are prepared in the same way detailed for impedance spectroscopy. An alternating voltage is then applied using an Agilent E4980A Precision LCR meter at frequencies 1 kHz , 10 kHz, 100 kHz, 250 kHz, and 1 MHz. At each frequency the capacitance and dielectric losses (tan δ) are measured. The sample is cycled twice to 850 ̊C and cooled to room temperature at a heating/cooling rate of 1 ̊C min^{-1} taking a measurement every 1 ̊C. The measured capacitance is then converted into relative permittivity *via* the following equations.

$$GF = \frac{\pi r^2}{T}$$

$$C_{Corrected} = \frac{C_{Observed}}{GF}$$

$$\varepsilon_r = \frac{C_{corrected}}{\varepsilon_0}$$

2.7.3. Oxide Ion Transport Number – Probostat

20 mm ceramic pellets are sintered according to the procedure detailed above and platinum electrodes are applied to each side of the pellet. The sample is then glued, using KeraGlas ST K03 glass sealant, to the top of a YSZ tube attached to a probostat potentiometer and configured as shown in Figure 2.7.

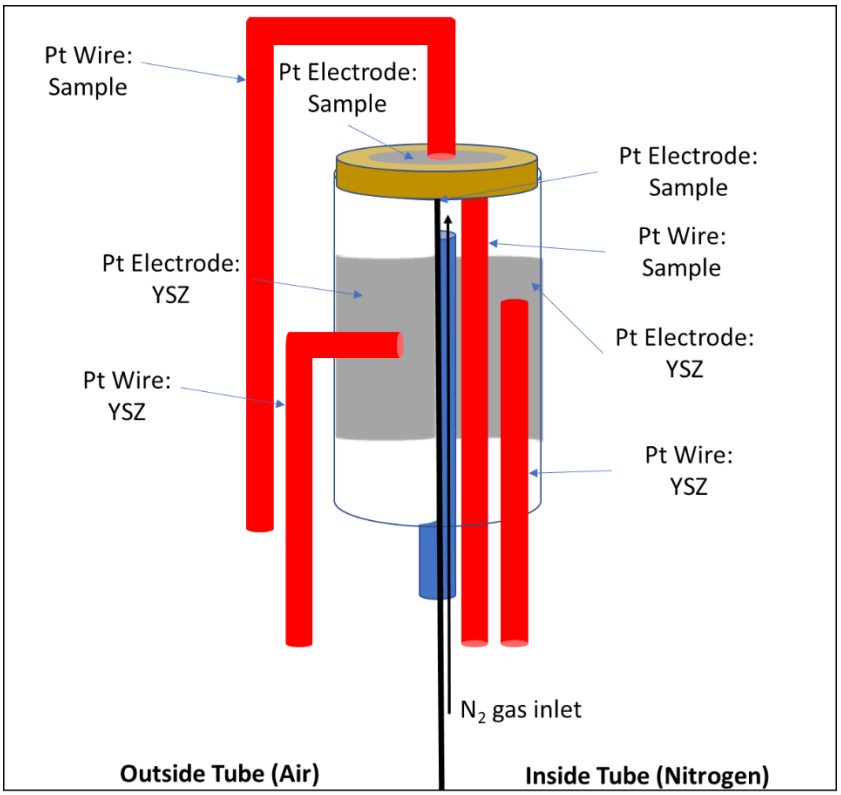

Figure 2.7: Schematic Diagram of Probostat Tube Configuration for Oxide ion Transport

Nitrogen gas flows into the YSZ tube and the outside is left exposed to air. As YSZ has an oxide ion transport number ≈ 1 the potential difference between the inside and outside of the tube is 100% attributed to oxide ion conductivity. By measuring the potential difference across the sample, the associated oxide ion transport number can be determined according to the following equation:

$$t_{O^{2-}} = \frac{V_{Sample}}{V_{YSZ}}$$

The voltages of the sample and YSZ are measured at various temperatures in the range of 500-800°C allowing the system to fully equilibrate at each temperature.

Unfortunately, this technique for oxygen transport number measurement possesses several limitations. Due to the compression required during the sealing stage any samples with poor mechanical properties cannot be measured as the sample may crack and break preventing an airtight seal/pO_2 gradient.

Additionally, the glass sealant may not always form an airtight seal; confirmation *via* leak testing is required after completion of the experiment. If this occurs the obtained transport number may not be reliable, and the experiment must be repeated.

Finally, poor electrode contact on the inner sample/YSZ electrodes (Figure 2.7) prevents measurement of the potential difference across the pO_2 gradient and cannot be resolved without removal of the sample.

As the ceramic is glued onto the YSZ tube removal of the sample usually results in fragmentation. As a result, this technique is generally considered to be a destructive measurement; and poor electrode contact/poor seal requires full preparation of a new ceramic.

2.8. Gallium NMR Spectroscopy

^{71}Ga NMR experiments were carried out at the UK High Field Solid-State NMR Facility by David Bradley and Prof. John V. Hana using a Bruker AVANCE NEO 1000 MHz NMR SPECTROMETER operating at 23.5 T. Samples were loaded into a 1.3 mm probe with 40 kHz of magic angle spinning (MAS). All experiments were referenced to an aqueous sample of gallium nitrate and processed using Topspin 4.

2.9. References

1. Fresno, F. *et al.* CO_2 reduction over $NaNbO_3$ and $NaTaO_3$ perovskite photocatalysts. *Photochem. Photobiol. Sci.* **16**, 17–23 (2017).

2. Handoko, A. D. & Goh, G. K. L. Hydrothermal synthesis of sodium potassium niobate solid solutions at 200 °C. *Green Chem.* **12**, 680–68 (2010).

3. Van Hoek, C. & Koolwijk, M. Conventional wavelength dispersive spectroscopy versus parallel beam spectroscopy - A basic overview. *Microchim. Acta* **161**, 287–293 (2008).

4. Makuła, P., Pacia, M. & Macyk, W. How To Correctly Determine the Band Gap Energy of Modified Semiconductor Photocatalysts Based on UV-Vis Spectra. *J. Phys. Chem. Lett.* **9**, 6814–6817 (2018).

5. Jonscher, A. K. Dielectric relaxation in solids. *J. Phys. D. Appl. Phys.* **32**, R57 (1999).

6. Sinclair, D. C. Characterization of Electro-materials using ac Impedance Spectroscopy. *Bol. la Soc. Esp. Ceram. y Vidr.* **65**, 55–66 (1995).

Chapter 3. Undoped and Non-Stoichiometric Sodium Niobate ($NaNbO_3$)

Sodium niobate (NN) is a tilted ABO_3 perovskite typically used as a piezoelectric material. Significant studies have been conducted to investigate the numerous successive polymorphs and phase transitions in NN. However, the electrical properties of the base-material have undergone fairly limited investigation. Additionally, due to the volatility of sodium, processing NN encounters some challenges in attaining truly stoichiometric materials after ceramic processing.

NN can be synthesised by a variety of methods, and this can influence the sodium volatility experienced in any given sample. Conventional solid-state synthesis is most susceptible to sodium volatility due to the high temperatures required for calcination and sintering (>800 °C). Utilisation of a sol-gel or hydrothermal method use significantly lower temperatures, and in the case of hydrothermal synthesis, a sealed environment.[1,2]

Deviation from a strictly stoichiometric ratio of cations has been documented to have a profound effect in some perovskite materials. Figure 3.1 shows how small changes in the stoichiometry of $BaTiO_3$ can have a significant effect on the temperature of the structural phase transition causing the change from paraelectric-ferroelectric behaviour.[3]

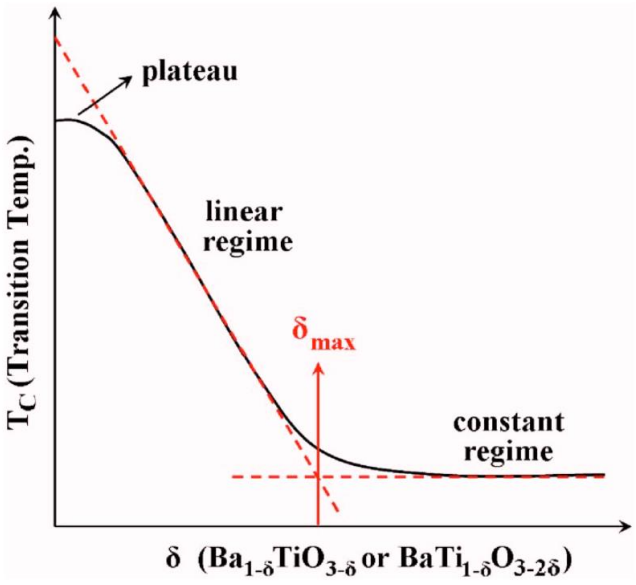

Figure 3.1: Change in Ferroelectric Phase Transition of $BaTiO_3$ According to Ba:Ti Non-Stoichiometry (Taken from Lee S. et. al.)[3]

Figure 3.1 shows that as defect concentrations increase in $BaTiO_3$ due to non-stoichiometry, the ferroelectric phase transition temperature decreases up to a maximum defect

concentration (δ_{max}) beyond which the transition temperature remains constant. The linear regime occurs due to increasing vacancy concentrations formed *via* charge compensation before δ_{max}. The change in T_c with respect to A-site vacancy concentration is expressed in equation 3.1, and with respect to B-site vacancy concentration is shown in equation 3.2 where δ=0-0.02.

$$\left(\frac{\Delta T_C^0}{\Delta \delta}\right)_{T.p(O_2)}^{Ba_{1-\delta}TiO_{3-\delta}} = -2.2 \pm 0.3\ K\ \delta^{-1} \qquad (3.1)$$

$$\left(\frac{\Delta T_C^0}{\Delta \delta}\right)_{T.p(O_2)}^{BaTi_{1-\delta}O_{3-2\delta}} = -8.2 \pm 1.6\ K\ \delta^{-1} \qquad (3.2)$$

The resultant constant regime is due to the solid solution limits of BaO and TiO_2 in $BaTiO_3$ leading to coexistence of the primary $BaTiO_3$ phase with a secondary of Ba_2TiO_4 or $BaTi_2O_5$ depending on the Ba:Ti ratio.[3]

Alternatively, non-stoichiometry in $Na_{0.5}Bi_{0.5}TiO_3$ (NBT) leads to significant changes in the conductivity and electrical properties of the material. Figure 3.2 shows how changing the bismuth content between 0.49 and 0.51 site occupancy causes significant increases or decreases in the bulk conductivity of the material.

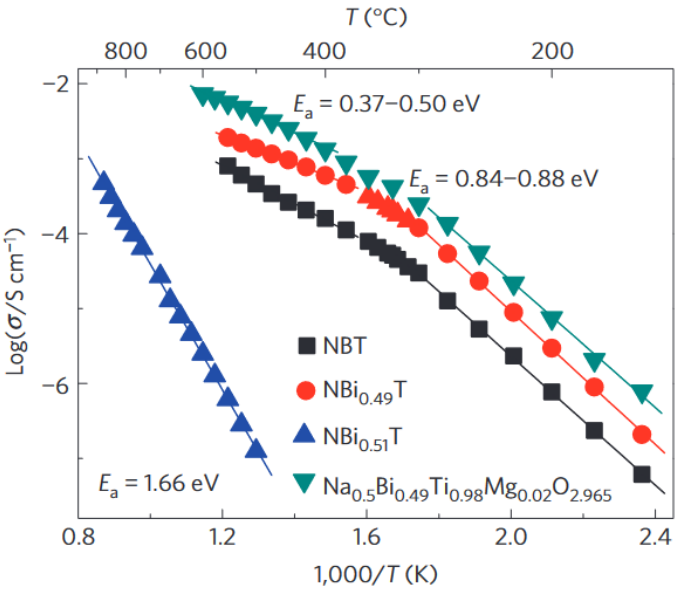

Figure 3.2: Changes in Bulk Electrical Conductivity with Low Levels of Non-Stoichiometry in NBT (Taken from Li M. et. al.)[4]

Increasing the Na:Bi ratio from 1 to 1.02 leads to excess sodium in vacant bismuth sites (due to volatility during processing) leading to a fully occupied A-site. This relatively small

increase in Na:Bi ratio leads to increased oxide ion conductivity as oxygen vacancies are generated according to the mechanism:

$$Na^{+} = Bi^{3+} + O^{2-} \qquad (3.3)$$

Conversely, decreasing in the Na:Bi ratio to 0.98 causes a reduction in bulk conductivity of ~3 orders of magnitude, due to the excess bismuth overcoming losses to volatility during processing and resulting in a stoichiometric $Na_{0.5}Bi_{0.5}TiO_3$ and exhibiting primarily intrinsic electronic conduction.[5]

Due to the inherent sodium volatility in NN, small levels of non-stoichiometry are inevitable; therefore, it is important to understand what effect deliberate changes to this stoichiometry have on the properties of undoped NN. Loss of sodium to volatility and the generation of A-site metal vacancies will cause generation of oxygen vacancies to balance the charge ($Na_{1-x}NbO_{3-0.5x}$).

$$2Na_{Na}^{X} + O_{O}^{X} \rightarrow 2V_{Na}^{\prime} + V_{O}^{\cdot\cdot} + Na_2O \qquad (3.4)$$

If by increasing the Na:Nb ratio B-site vacancies can be generated a larger increase in conductivity may be observed, as following the same charge compensation mechanism ($NaNb_{1-x}O_{3-2.5x}$) a greater number of oxygen vacancies would be generated promoting oxide ion conductivity.

$$2Nb_{Nb}^{X} + 5O_{O}^{X} \rightarrow 2V_{Nb}^{\prime\prime\prime\prime\prime} + 5V_{O}^{\cdot\cdot} + Nb_2O_5 \qquad (3.5)$$

Perovskites containing oxygen vacancies may be susceptible to moisture uptake showcased in proton conduction at lower temperatures due to the following mechanism:

$$H_2O_{(g)} + V_{O}^{\cdot\cdot} + O_{O}^{X} \leftrightarrow 2OH_{O}^{\cdot} \qquad (3.6)$$

Some preliminary studies into non-stoichiometry in NN exist; conducted by Ruf *et al.* who suggest that changes to the stoichiometric Na:Nb ratio in the range of 0.92-1.08, can have a notable effect on the electrical conductivity and permittivity of ceramics.[6] Increasing the Na:Nb ratio causes an increase in bulk electrical conductivity, however, it is worth noting that all electrical characterisation was over a narrow temperature window (25-450 ̊C).The influence of non-stoichiometry on the bulk conductivity of NN reported by Ruf *et.al.* is shown in Figure 3.3.

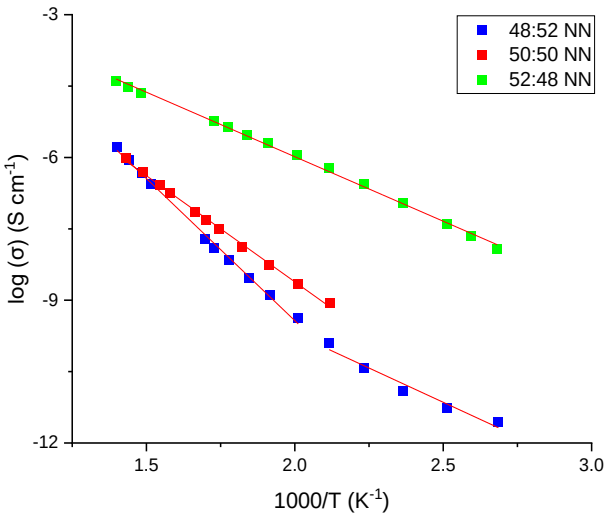

Figure 3.3: Arrhenius Plots of Bulk Conductivity for Non-Stoichiometric NN (Adapted from Reference 6)

Figure 3.3 shows how increasing the Na:Nb leads to an increase in bulk conductivity through the ceramic in the low-intermediate temperature region. This chapter expands upon the initial work conducted by Ruf *et al.* and compares the properties of stoichiometric NN in an attempt to understand how nominally identical compositions may significantly vary in physical and electrical properties.

3.1. Undoped $NaNbO_3$

In order to understand how subtle changes in Na:Nb stoichiometry may have an effect on the properties of NN it is important to first establish the properties of nominally stoichiometric 1:1 Na:Nb $NaNbO_3$. Additionally, considering how different synthesis routes and purity of starting reagents may influence the properties of the materials. Table 3.1 summarises 4 different undoped NN samples investigated in this study.

Composition	Synthesis Technique	Reagents	Conditions Required for Single Phase Powders
Lower Purity NN (LP NN)	Conventional Solid State	Na_2CO_3 (99.98%) Nb_2O_5 (99.85%)	Calcined 900 °C 2 Hours Sintered 1350 °C 4 Hours
High Purity NN (HP NN)	Conventional Solid State	Na_2CO_3 (99.98%) Nb_2O_5 (99.9985%)	Calcined 900 °C 2 Hours Sintered 1350 °C 4 Hours
Hydrothermal NN (HT NN)	Hydrothermal	Na(OH) (8.4M) Nb_2O_5 (99.9985%)	Hydrothermal 200 °C 72 Hours Sintered 1240 °C 4 Hours
Industry NN (I NN)	Unknown	Unknown	As Received from Kyocera-AVX Ltd. Sintered 1350 °C 4 Hours

Table 3.1: Compositions of Undoped NN with Reagents and Reaction Conditions

3.1.1 Phase purity and Crystal Structure

X-ray diffraction (XRD) was used to determine phase purity and unit cell parameters of NN powders and compare any differences between the various processing conditions and/or reagents. The obtained patterns are shown below in Figure 3.4.

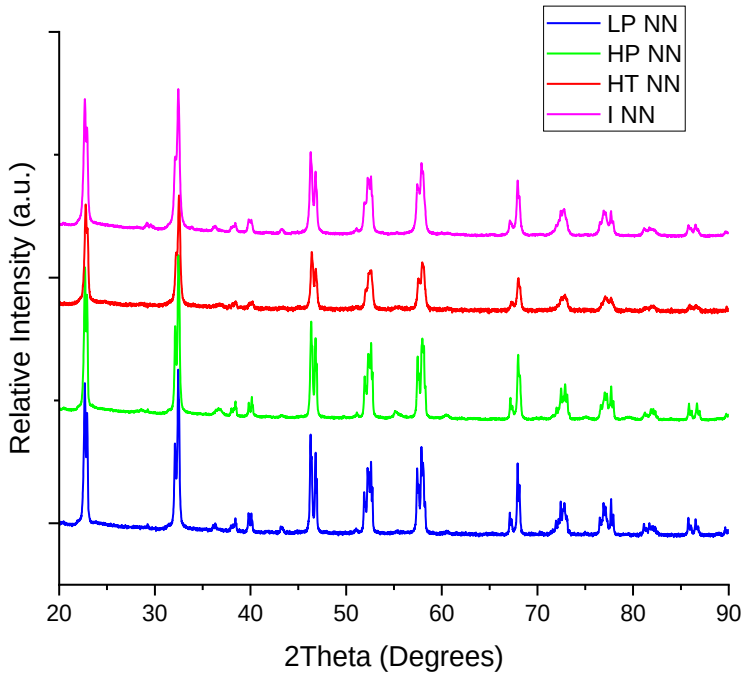

Figure 3.4: X-Ray Diffraction Patterns of Undoped NN Powders as detailed in Table 3.1

NN powders appear to be a mixture of the P (Pbma) and Q (Pmc21) phases after a single calcination.

To assess if any structural changes occur during the sintering of the ceramics diffraction patterns have been collected and compared to their respective powders. Figure 3.5 shows the diffraction patterns of the LP NN powder compared to the sintered ceramic.

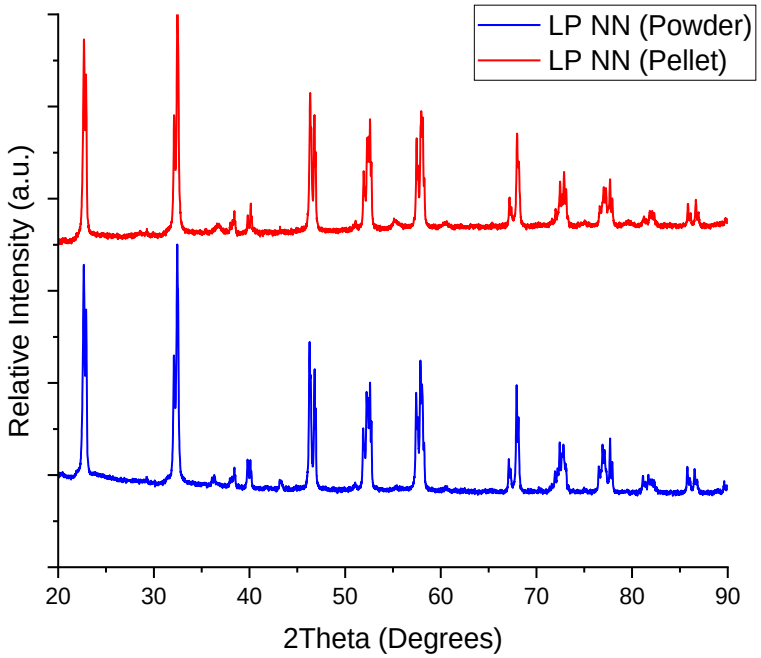

Figure 3.5: Comparison of 'LP NN' Powder and Pellet XRD Patterns

There are no notable changes to the diffraction patterns before and after sintering. This is consistent across all stoichiometric NN ceramics. For clarity only the LP NN ceramic is included in the following results although the trend is the same with all stoichiometric NN ceramics.

Rietveld refinements have been conducted on the NN powders and sintered ceramics. An example refinement on the LP NN powder is shown below in Figure 3.6, and the details from each refinement are tabulated in table 3.2.

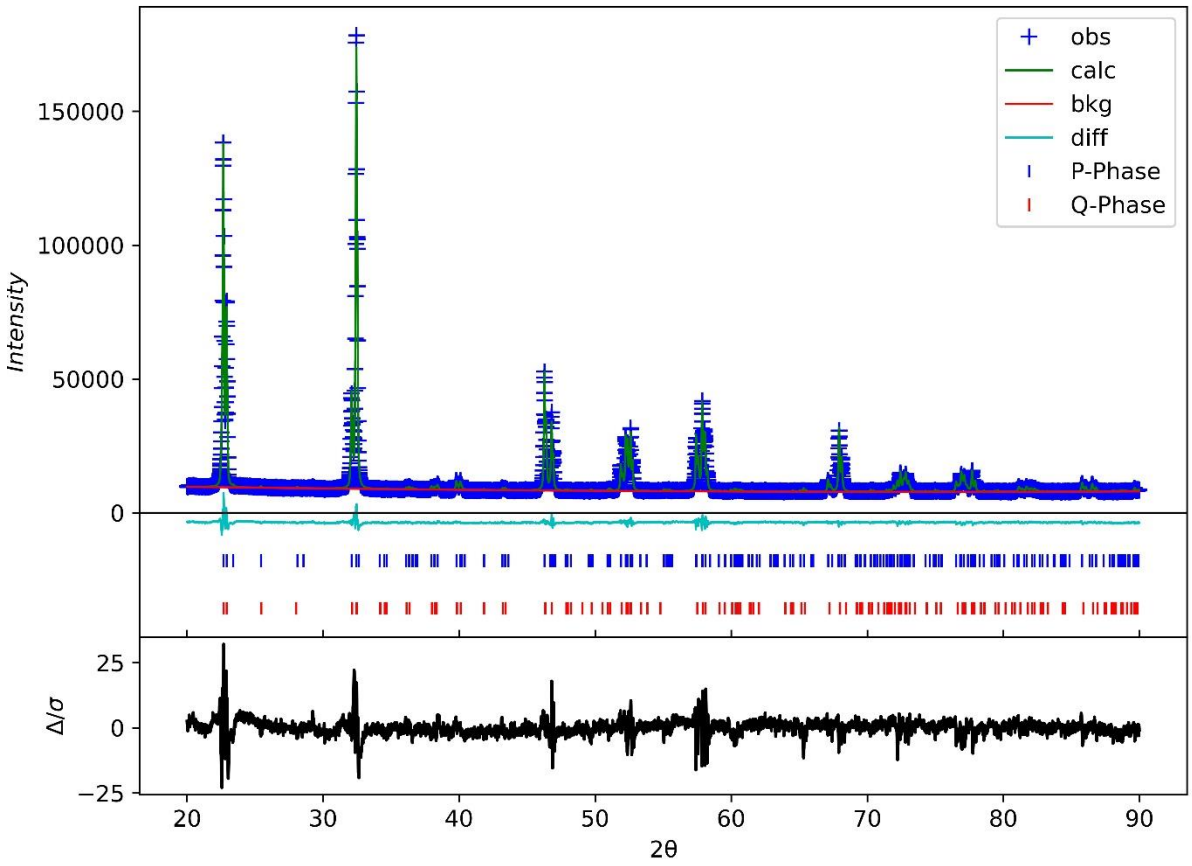

Figure 3.6: Example Rietveld Refinement of 'LP NN' Powder

	Parameters	LP NN	HP NN	HT NN	I NN	LP NN Pellet
P Phase (Pbma)	a / Å	5.57450(6)	5.56743(7)	5.56467(21)	5.57198(9)	5.56947(13)
	b / Å	15.51670(17)	15.51433(18)	15.5366(7)	15.51976(23)	15.5164(4)
	c / Å	5.51674(7)	5.50361(7)	5.50971(24)	5.51438(11)	5.50604(13)
	Cell Volume / Å^3	477.18611(2)	475.37402(2)	476.34777(7)	476.86038(2)	475.82164(4)
	Phase Fraction	0.655(9)	0.73(5)	0.762(21)	0.917(4)	0.651(15)
Q Phase (Pmc21)	a / Å	7.75949(26)	7.76124(20)	7.7672(15)	7.8642(15)	7.75952(22)
	b / Å	5.56788(22)	5.57189(17)	5.5719(9)	5.517(3)	5.56615(14)
	c / Å	5.51122(22)	5.51237(19)	5.5190(11)	5.518(4)	5.50222(14)
	Cell Volume / Å^3	238.1062(7)	238.3812(5)	238.85162(16)	239.40831(1)	238.1062(7)
	Phase Fraction	0.345(9)	0.27(5)	0.238(21)	0.083(4)	0.349(15)
Residuals	R_w / %	2.935	2.440	1.945	2.193	3.07
	χ^2	8.95	17.17	2.39	13.66	7.68

Table 3.2: Summary of Rietveld Refinements for Stoichiometric NN Variants

The ratio of P:Q phases in each sample has been determined *via* Rietveld refinements and are shown below in Figure 3.7.

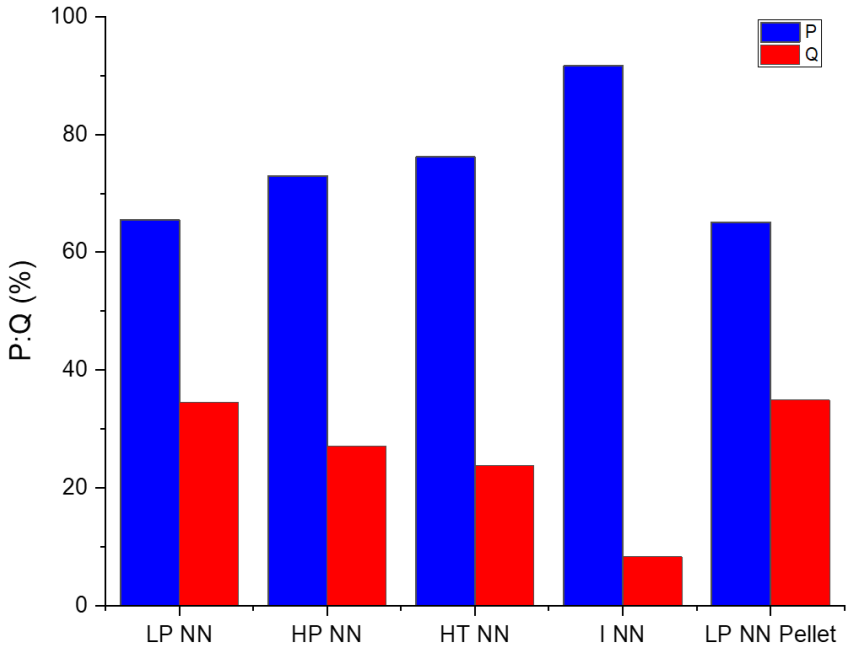

Figure 3.7: Ratio of P:Q Phases in NN Powders Obtained from Rietveld Refinement

All variants of stoichiometric NN show a preference for the P-phase, I NN shows the greatest preference for the P-phase. The P:Q ratio of stoichiometric NN ceramics is unaffected by the sintering process.

The Rietveld refinements also allowed for determination of unit cell parameters, the calculated cell volume for each variant is shown in Figure 3.8.

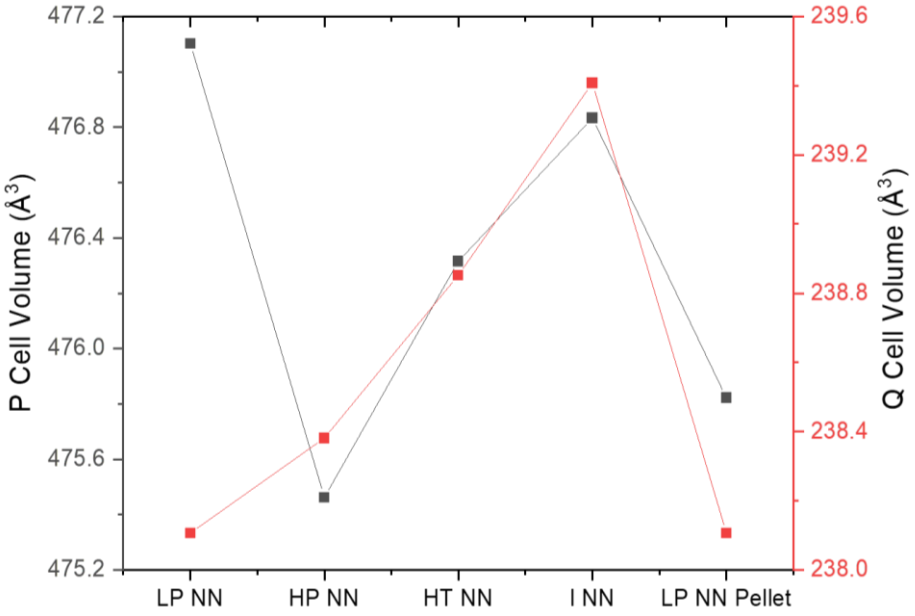

Figure 3.8: Unit Cell Volume Changes of Undoped NN Powders

The P and Q phase unit cells exhibit variance of approximately 1.5 $Å^3$ according to processing technique. This variance is reasonably small; however, it does indicate that some variance of these polymorphic phases occurs according to the processing technique.

The Q-phase unit cell appears to increase as the relative concentration of the Q-phase decreases. The P-phase unit cell does not follow any particular trend. On sintering of all NN ceramics the P-phase appears to contract slightly, while the Q-phase is unaffected, however, this contraction is still within the observed P-phase cell variance indicating that the sintering process has no significant effect on the underlying polymorphism and crystal structures in stoichiometric NN.

All subsequent variants of NN discussed in this thesis showcase comparable unit cell variations, suggesting that non-stoichiometry and doping of NN have no significant effect on unit cell volume.

3.1.2. Microstructure

Sintered ceramics of stoichiometric NN were thermally etched and have undergone SEM analysis to assess the microstructure. The density for all stoichiometric NN ceramics lies in the range of 79-95% of the theoretical density (4.500 g cm^{-3}). Figure 3.9 shows a general overview of the microstructure and associated grain sizes and distributions for each of the NN ceramics.

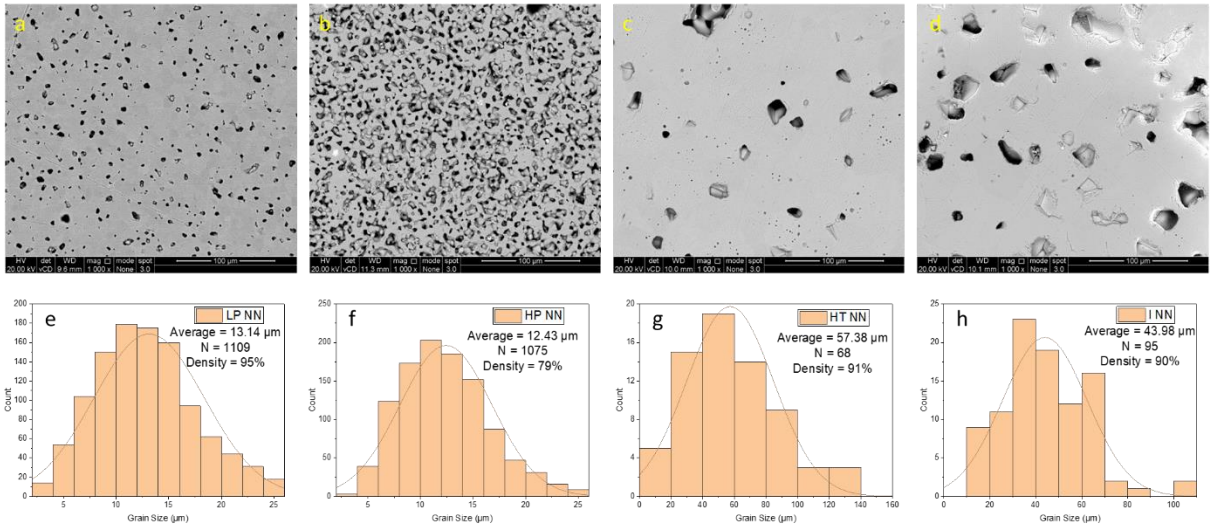

Figure 3.9: BSE Images of a) LP NN b) HP NN c) HT NN d) I NN and Associated Grain Size Evaluations e) LP NN f) HP NN g) HT NN and h) I NN

Although there is a reasonable size agreement between LP and HP NN the HT and I variants have a significantly larger average grain size. EDS analysis of each sample has

been conducted to assess the elemental distribution throughout the ceramics, this is shown in Figures 3.10-3.13.

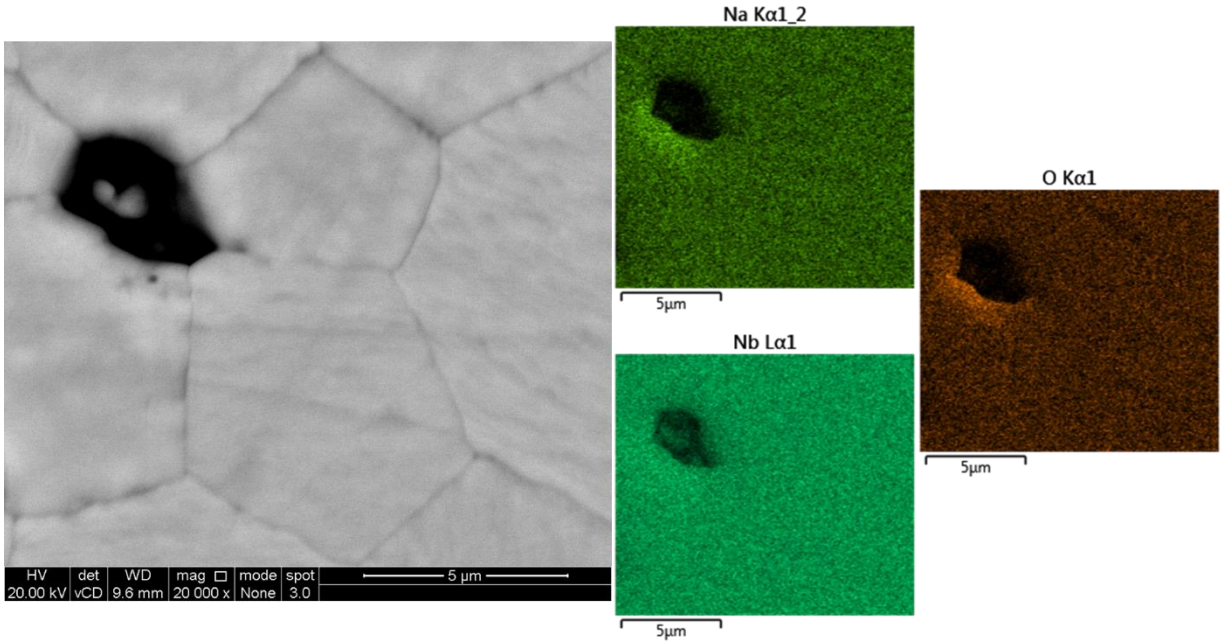

Figure 3.10: EDS Map of 'LP NN'

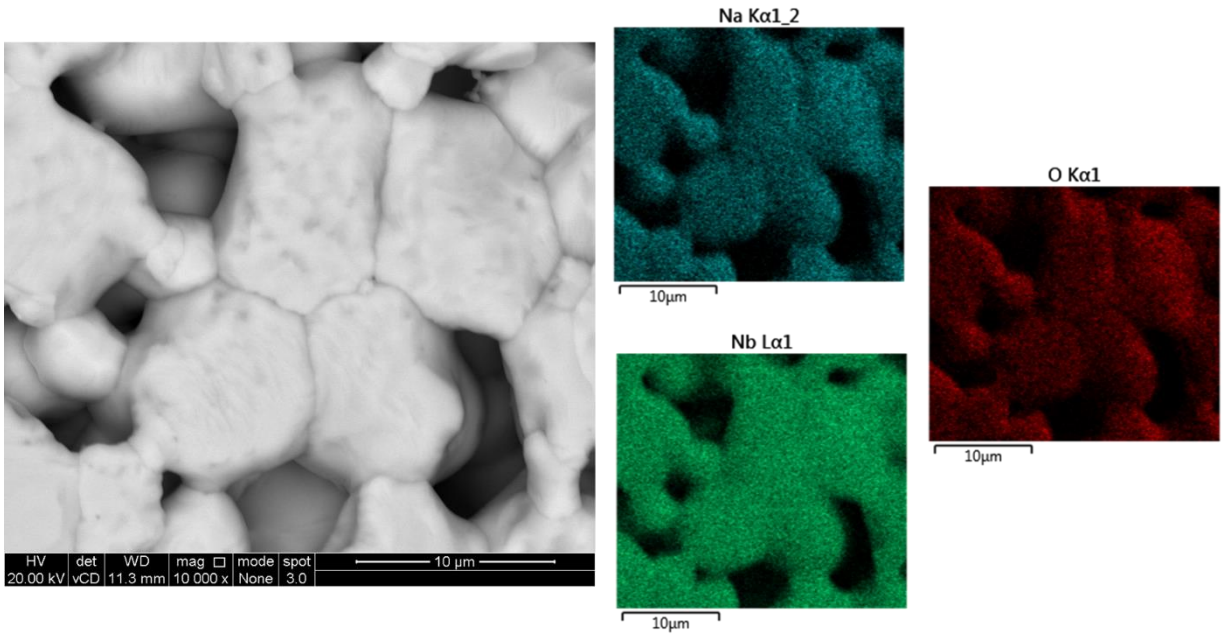

Figure 3.11: EDS Map of 'HP NN'

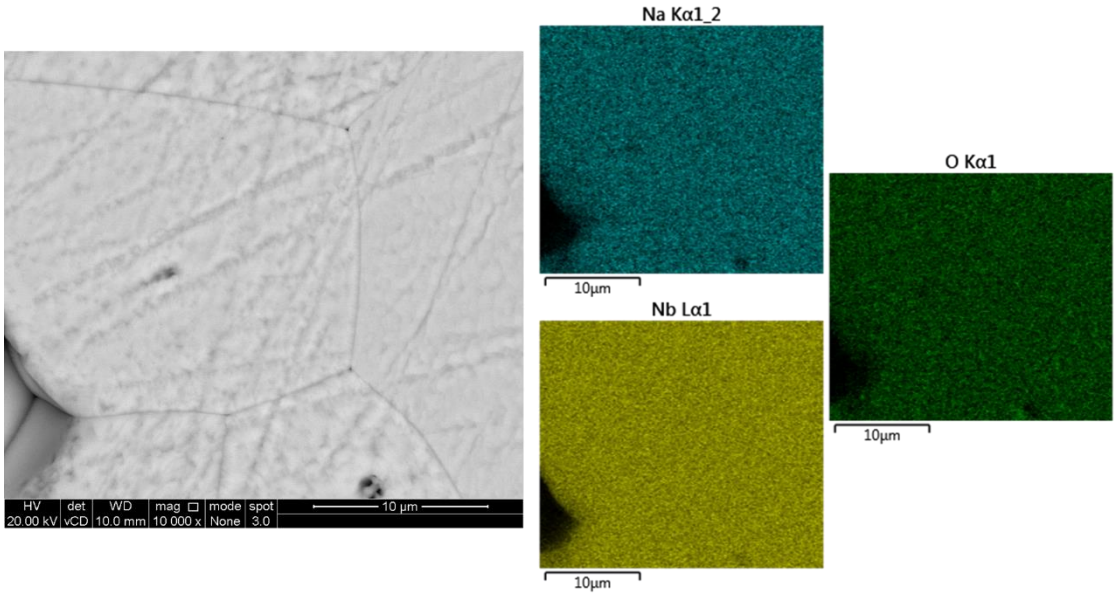

Figure 3.12: EDS Map of 'HT NN'

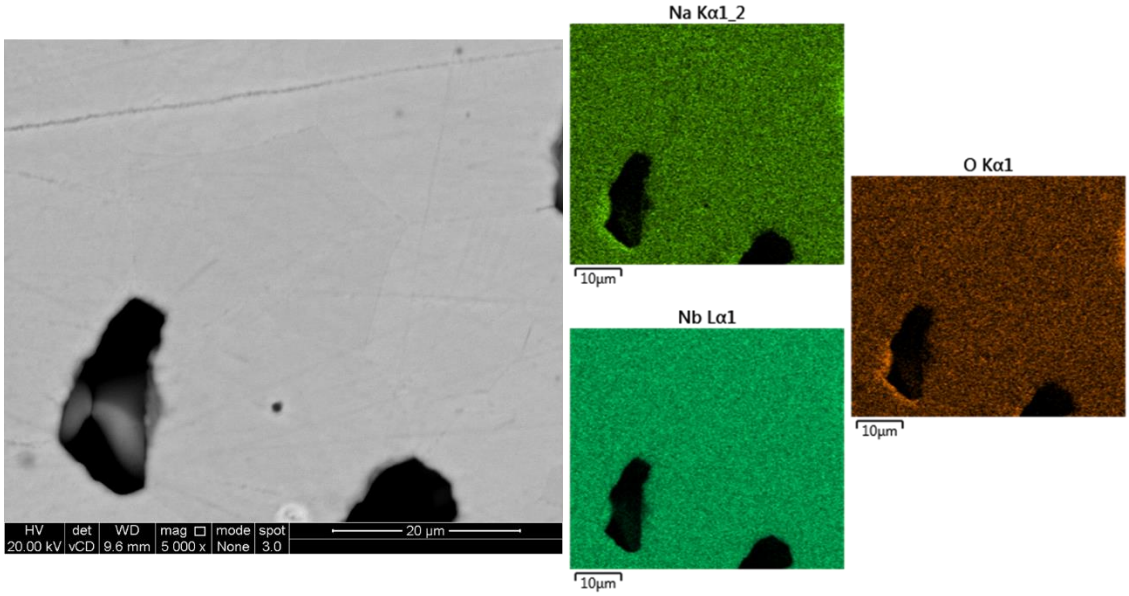

Figure 3.13: EDS Map of 'I NN'

EDS maps of the ceramics show that there is no significant variation of elemental distribution between grains and grain boundaries in the LP, HT and I NN ceramics. The HP NN ceramic (Figure 3.11) showcases a slight sodium deficiency along the grain boundaries. Additionally, spot analysis of each sample indicates that the sodium content of each ceramic is lower than anticipated in both the grains and grain boundaries. Results from the spot analysis are shown in table 3.3 and compared to the expected concentrations.

	Grains			Grain Boundaries		
Composition	**Na / wt%**	**Nb / wt%**	**O / wt%**	**Na / wt%**	**Nb / wt%**	**O / wt%**
LP NN	12.59 ± 0.03	61.03 ± 0.01	26.37 ± 0.03	12.38 ± 0.06	62.96 ± 0.01	24.67 ± 0.03
HP NN	13.97 ± 0.01	57.30 ± 0.01	28.77 ± 0.02	12.20 ± 0.01	62.55 ± 0.01	25.25 ± 0.02
HT NN	13.00 ± 0.02	60.31 ± 0.02	26.67 ± 0.03	12.37 ± 0.04	64.11 ± 0.01	23.57 ± 0.03
I NN	12.49 ± 0.03	61.99 ± 0.01	25.52 ± 0.03	12.40 ± 0.02	61.66 ± 0.01	25.93 ± 0.02
Theoretical NN	14.00	57.00	29.00			

Table 3.3: Average Grain and Grain Boundary compositions of Stoichiometric NN ceramics

Use of higher purity reagents generally yields ceramics with close to ideal sodium contents in the grains. Whereas ceramics with lower than anticipated bulk sodium content appear to have more homogenous grains and grain boundaries.

3.1.3. Relative Permittivity and Dielectric Losses

The temperature dependence of the relative permittivity for each of the NN ceramics has been determined and compared over 2 heating and cooling cycles. The overall ε_r – T for 100 kHz is shown in Figure 3.14.

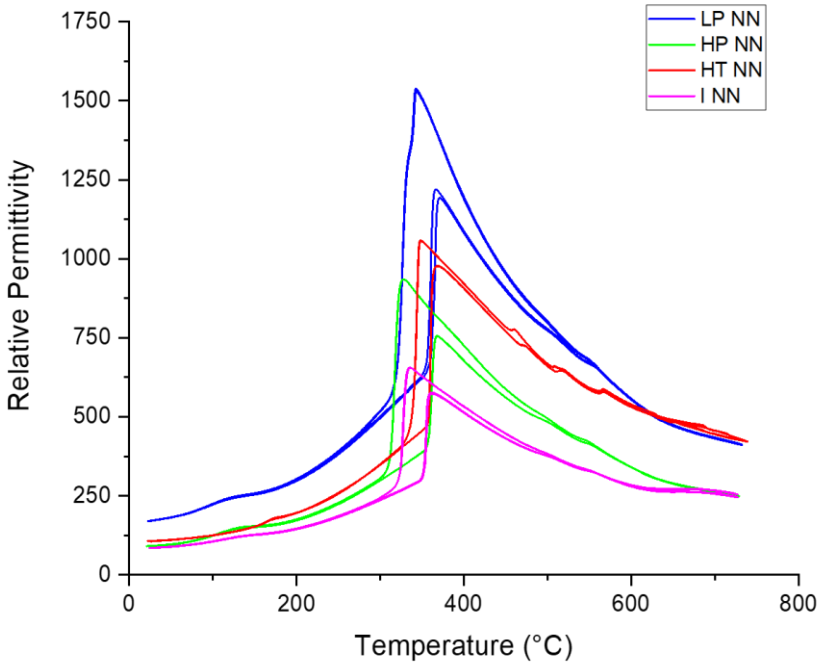

Figure 3.14: Relative Permittivity of NN Ceramics at 100 kHz

ε_r – T plots of NN ceramics vary significantly according to the processing technique. The LP NN sample clearly exhibits the largest permittivity whereas 'I NN' exhibits the smallest. All ceramics are stable over 2 heating/cooling cycles with permittivity remaining consistent

between cycles. The main hysteresis observed occurs around the characteristic peak at the P-R phase transition (~360 °C).

The dielectric losses of each ceramic were also assessed and are compared below in Figure 3.15 (also at 100 kHz).

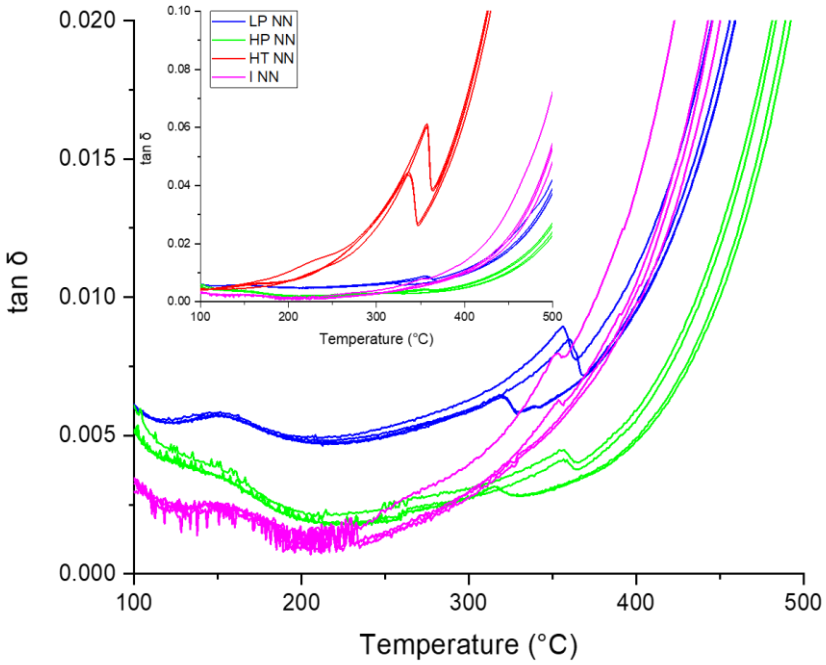

Figure 3.15: Dielectric Losses of NN ceramics at 100 kHz

As observed in Figure 3.14, the T_{Max} of the P-R phase transition for stoichiometric NN ceramics is ~360 °C. Up to this temperature the observed dielectric losses are generally low and interpretable. Beyond T_{Max}, space charge effects begin to dominate, and the dielectric losses increase rapidly beyond ~400 °C.

The losses observed in NN ceramics appear to be consistent over heating/cooling cycles with the main observed hysteresis occurring around the P-R phase transition. The maximum losses occurring around the phase transition are generally less than 1%, with the exception of HT NN which exhibits greater losses of up to 6% on heating.

At ~150 °C a notable peak in the tan δ plot arises, this is also seen in the ε_r – T plot in Figure 3.14. This peak is most likely attributed to the Q phase present in the ceramic transforming into the more abundant P phase.[7]

3.1.4. Electrical Properties

The electrical properties of the NN ceramics have been investigated *via* impedance spectroscopy to determine what electrical differences may arise from the small differences in polymorphic assemblage and microstructure. Overlaid M''/Z'' plots for the NN ceramics are shown in Figure 3.16 at a comparable temperature (600 °C) to identify the types of electrical responses present and to assess the electrical homogeneity of the ceramics.

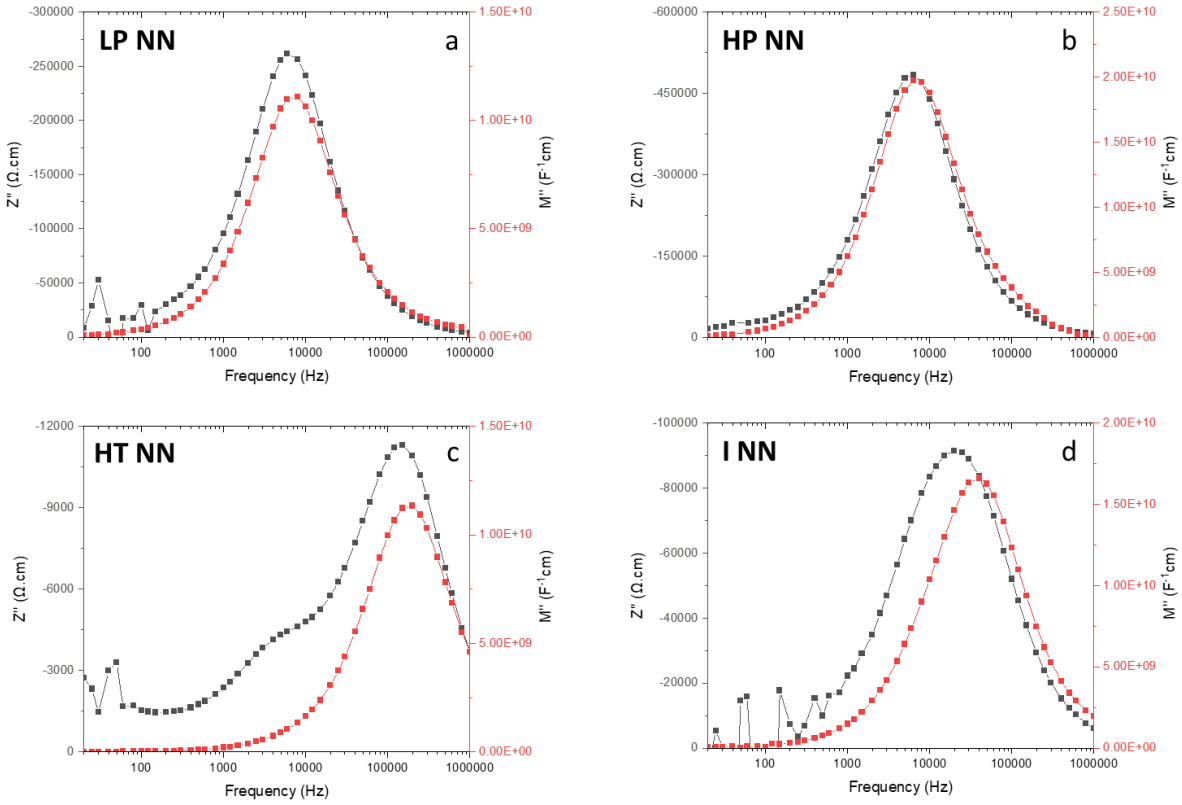

Figure 3.16: M'' Z'' Plots of a) LP b) HP c) HT and d) I NN Ceramics at 600°C

Composition	Capacitance (Z'') / F cm^{-1}	Capacitance (M'') / F cm^{-1}	F_{max}(M'') / kHz	Corresponding Response
LP NN	$5.1(4) \times 10^{-11}$	$4.5(2) \times 10^{-11}$	8.00	Bulk
HP NN	$2.6(2) \times 10^{-11}$	$2.5(1) \times 10^{-11}$	6.30	Bulk
HT NN 1	$4.7(8) \times 10^{-11}$	$4.4(2) \times 10^{-11}$	200	Bulk
HT NN 2	$3.0(14) \times 10^{-9}$	-	-	Grain Boundary
I NN	$4.4(13) \times 10^{-11}$	$3.0(1) \times 10^{-11}$	40.0	Bulk

Table 3.4: Tabulated Capacitances Extracted from M'' and Z'' Responses in Figure 3.16

The LP and HP NN ceramics show a single response in both M'' and Z'' plots indicating that both samples have a single RC element relating to the bulk electrical response.[8] The I NN ceramic shows a single response in the M'' plot, however, in the Z'' plot there is a very broad peak. This is likely due to 2 RC elements (bulk and grain boundary) with similar time constants coalescing into a single peak. HT NN ceramic shows a single response in the M''

plot. In the Z'' plot there are 2 distinct responses corresponding to the bulk (high frequency) and the grain boundary (low frequency) responses. Although the ceramics show little change in the low frequency Z'' response the capacitance of the ceramics does increase at low frequencies, although this is far more pronounced in the C' vs frequency plots shown in Figure 3.17.

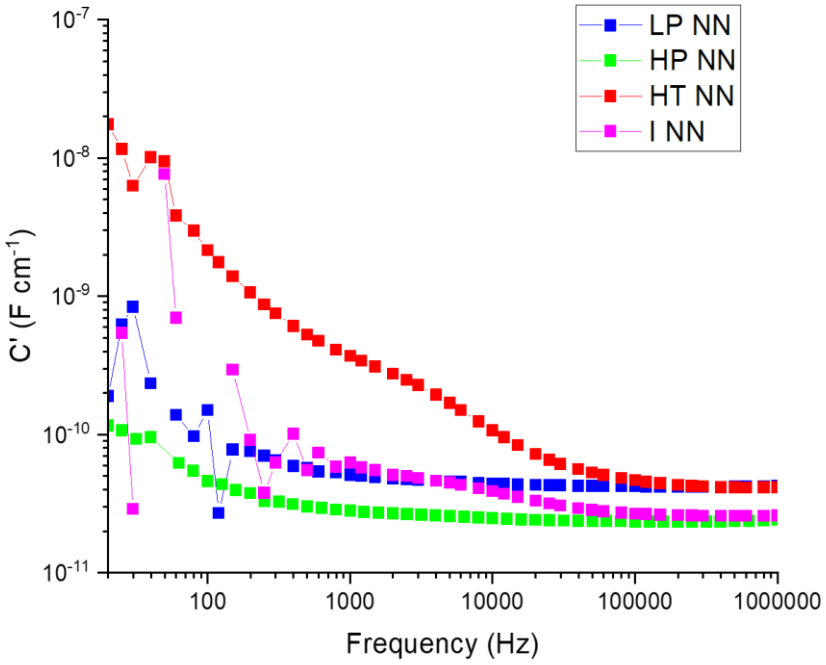

Figure 3.17: C' vs Frequency Plot of NN Ceramics at 600°C

All ceramics show a slight increase in capacitance at low frequencies that might be associated with ionic conductivity. The most rapid increase in capacitance is observed in the HT NN sample, which also shows an additional plateau corresponding to the grain boundary response observed in the Z'' plane.

The Arrhenius plots of bulk conductivity are shown below in Figure 3.18.

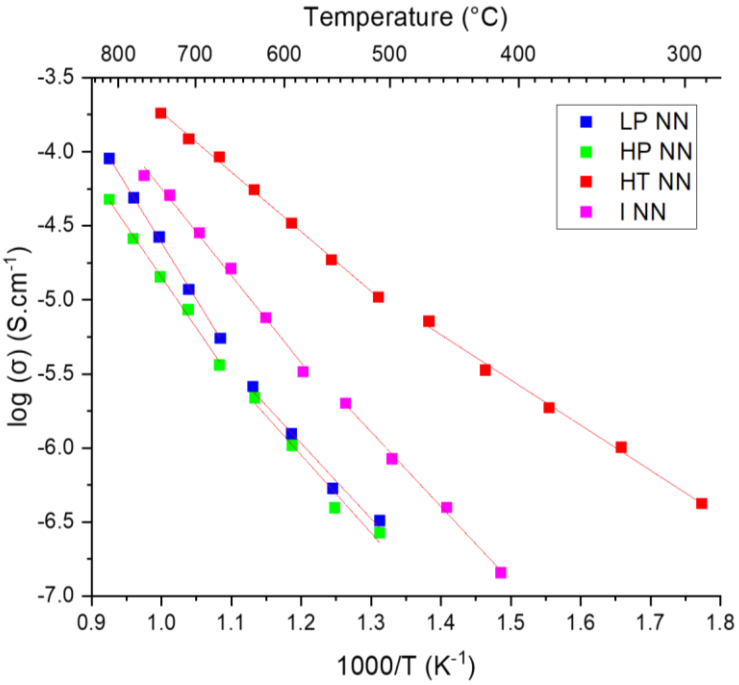

Figure 3.18: Arrhenius Plots of Bulk Conductivity for NN Ceramics

The bulk conductivity (σ_B) of the ceramics has been determined as the inverse of bulk resistance (R_B) determined from the calculated capacitances for M'' peaks. The bulk conductivities of undoped NN ceramics vary by as much as 1.5 orders of magnitude. Two distinct regions exist within each Arrhenius plot with changes in associated activation energies. The distinct linear regions have been identified visually in the first instance to find an approximate crossover point. The data ranges are then adjusted to achieve linear regression values (R^2) of ~1, this methodology has been utilised throughout this thesis. The activation energies associated with each sample are shown in table 3.5.

Composition	Low Temperature Ea /eV	High Temperature Ea / eV	Crossover Temperature / °C
LP NN	1.01 ± 0.10	1.52 ± 0.02	636
HP NN	1.04 ± 0.13	1.37 ± 0.05	636
HT NN	0.61 ± 0.03	0.80 ± 0.01	468
I NN	1.00 ± 0.04	1.17 ± 0.05	543

Table 3.5: Activation Energies of NN Ceramics Extracted from Arrhenius Plots of Bulk Conductivity

With the exception of HT NN, the NN ceramics exhibit comparable low temperature activation energies. However, in the high temperature domain significantly more variance is introduced. Additionally, the change in activation energy between domains decreases as bulk conductivity increases.

HT NN shows a significantly greater bulk conductivity with a much lower activation energy at both high and low temperatures.

The pO_2 dependence of each ceramic at 600 °C has also been assessed, the complex impedance plots (Z*) and M'' plots are shown in Figures 3.19-3.22. LP, HP and I NN ceramics show high frequency spikes in the M'' plots, this spike is associated with a jig effect and may be ignored.

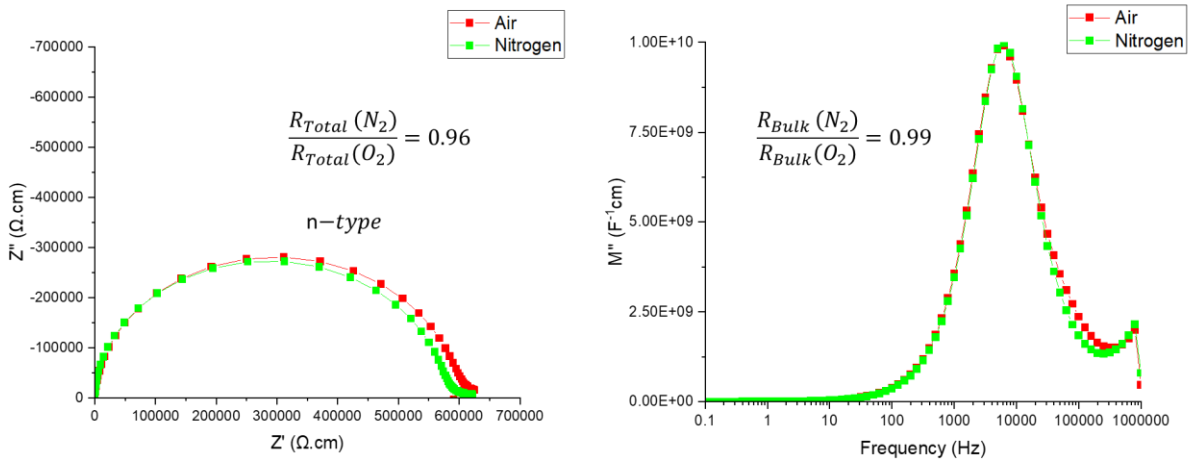

Figure 3.19: pO_2 Dependence of LP NN ceramics. Complex Impedance (Left) and M'' vs Frequency Plot (Right) at 600 °C

LP NN ceramics exhibit slightly n-type behaviour in regard to the total conductivity of the sample. However, the M'' plot shows no indication of pO_2 dependence within the bulk conductivity, i.e. f_{max} of the M'' Debye peak is independent of pO_2. This Indicates that any effects on the overall pO_2 dependence arise from extrinsic effects, which are not clearly observable in the bulk response.

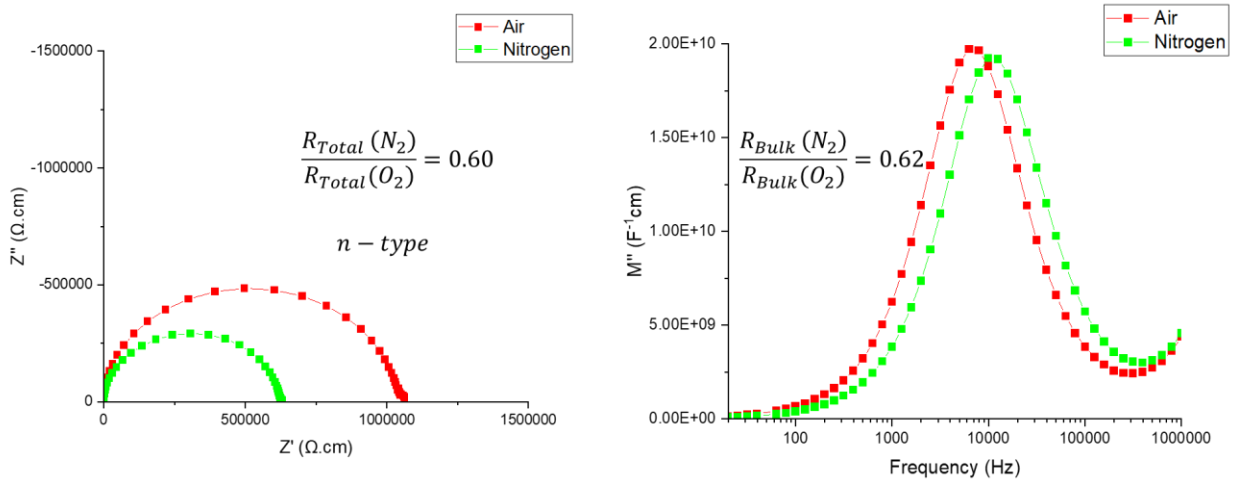

Figure 3.20: pO_2 Dependence of HP NN ceramics. Complex Impedance (Left) and M'' Response (Right) at 600°C

HP NN shows significant pO_2 dependence compared to LP NN. The total resistivity decreases significantly as pO_2 is lowered and n-type conductivity is observed. Unlike the

response observed for LP NN the drop in resistivity is attributed to the bulk conductivity of the ceramic as the f_{max} of the M'' bulk response increases as pO_2 decreases. This is associated with a decrease in resistance comparable to the observed Z* response.

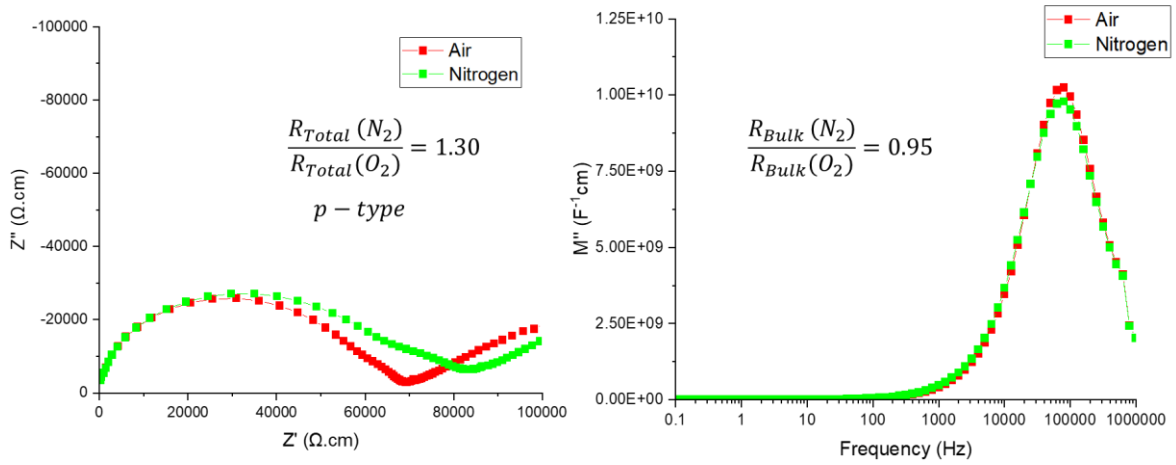

Figure 3.21: pO_2 Dependence of HT NN Complex Impedance (Left) and M'' Response (Right) at 600°C

HT NN ceramics show an increase in total resistance based on Z* plots as pO_2 decreases, giving rise to an overall observed p-type response. However, the pO_2 dependence of the bulk conductivity appears to be independent as the observed resistance is unchanged with pO_2. This indicates that there are extrinsic effects present (such as grain boundaries) in the ceramic that exhibit notable p-type conductivity.

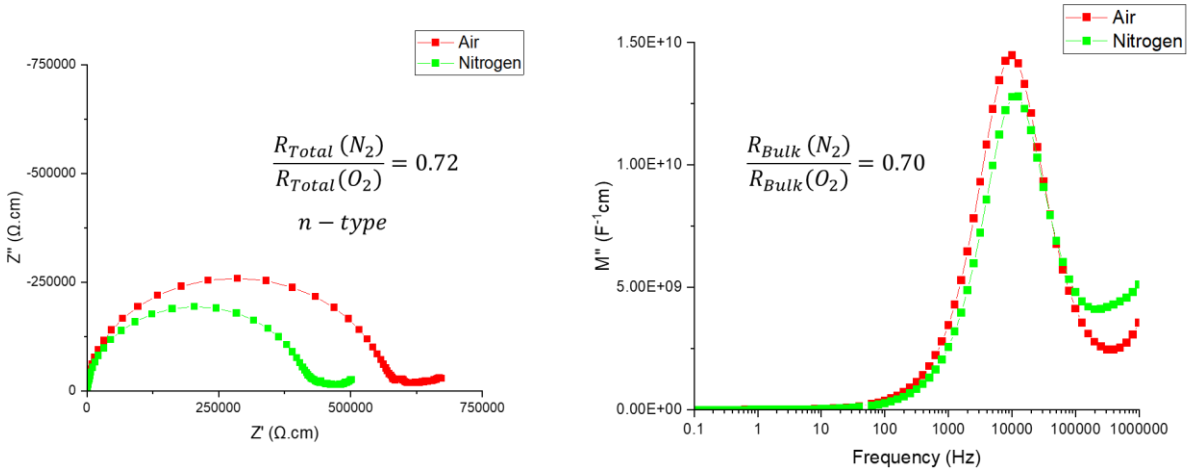

Figure 3.22: pO_2 Dependence of I NN ceramics. Complex Impedance (Left) and M'' Response (Right) at 600°C

I NN exhibits pO_2 dependence in the Z* plane showcasing a notable decrease in resistance with pO_2. This lower resistance is attributed to pO_2 dependence of the bulk electrical

response due to a drop in capacitance in a nitrogen atmosphere leading to the observed n-type conductivity.

3.1.5. Oxide Ion Transport Number

The oxide ion transport number (t_{O2-}) of the NN variants has been determined *via* use of a probostat potentiometer (detailed in section 2.7.3.). The results of which are shown below in Figure 3.23.

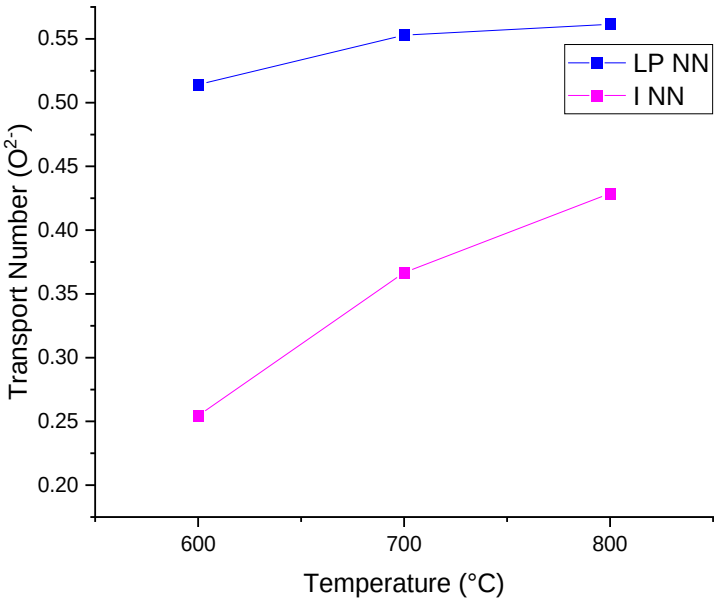

Figure 3.23: Oxygen Transport Numbers of 'LP NN' and 'I NN' As a Function of Temperature

Both measured NN variants showcase an increase in oxygen transport as temperatures increase. The LP NN ceramic showcasing a maximum t_{O2-} of 0.56 compared to the I NN lower t_{o2-} of 0.43. This shows that the ionic conductivity observed in stoichiometric NN in this temperature range may be attributed to oxide ions. Due to the lower density of the HP NN ceramic, it was not possible to acquire reliable transport number measurements.

3.1.6. Band Gap Determination

The UV-Vis spectrum of 'LP NN' has been acquired and converted into a tauc-plot for determination of the electronic band gap. The raw data and associated tauc-plot are shown Figure 3.24a and b.

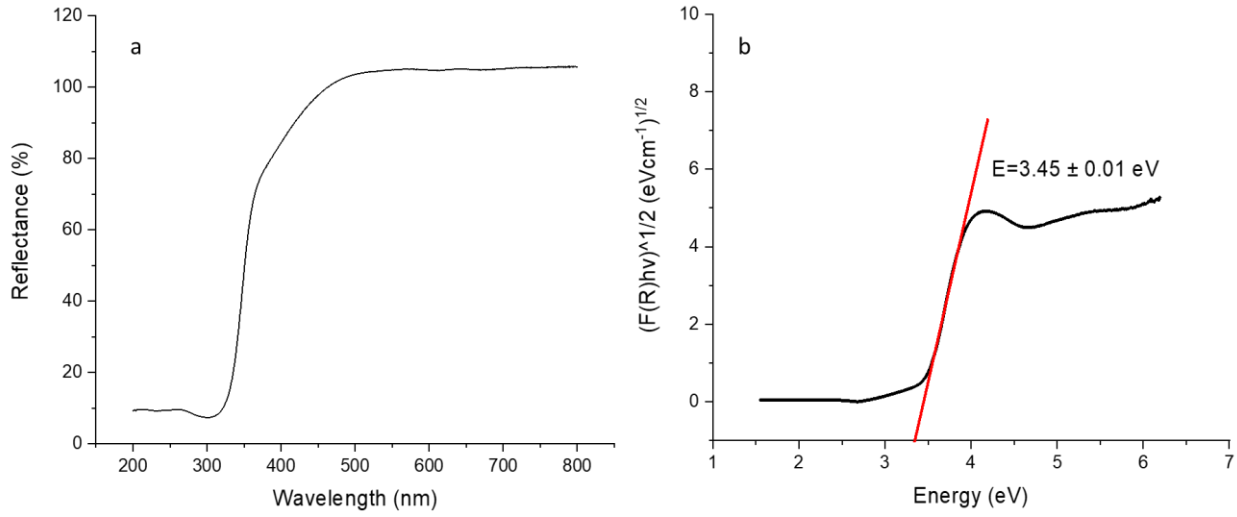

Figure 3.24: a) UV-Vis Spectrum of 'LP NN' Powder using a $BaSO_4$ Standard and b) Tauc-Plot of LP NN showcasing X-intercept of Linear Region.

The UV-Vis spectrum of 'LP NN' shows a sharp increase in reflectance at ~350 nm. Conversion of UV-Vis reflectance into a tauc-plot allows for determination of the band gap of NN. The x-intercept of the linear region presented in the tauc-plot is equal to the band gap in electron volts.[9] For LP NN the calculated band gap has been determined to be 3.45 ± 0.01 eV.

3.2. Non-Stoichiometric $NaNbO_3$

Deliberate changes to the Na:Nb ratio in NN have been made to investigate the effects of non-stoichiometry. By investigating the influence of non-stoichiometry, the goal is to provide some explanation to the large variance observed in undoped NN ceramics and to confirm that any changes in properties arising from doping NN (chapters 4-6) are due to the dopant rather than changing of the Na:Nb ratios.

Based on the results reported above on the variance of the properties in NN according to processing technique the following results will be compared to LP NN as the processing conditions were similar based on reagents used and technique.

The non-stoichiometric variants of NN to be discussed are as follows:

1. 49:51 $NaNbO_3$ – Sodium Deficient NN
2. 51:49 $NaNbO_3$ } Sodium Rich NN
3. 55:45 $NaNbO_3$ }

Changing the Na:Nb in non-stoichiometric NN will lead to a change in the associated tolerance factor in the ceramics. The associated tolerance factors of the discussed non-stoichiometric NN variants are shown in table 3.6.

Na:Nb Ratio	Adjusted Tolerance Factor
49:51	0.943
1:1	0.967
51:49	0.983
55:45	1.048

Table 3.6: Tolerance Factors for Non-Stoichiometric NN Variants

The tolerance factor of NN ceramics increases as Na:Nb ratio increases. It has been demonstrated that decreasing the tolerance factor of NN favours the formation of the P phase.[10]

3.2.1. Phase Purity and Crystal Structure

The phase purity of the non-stoichiometric NN ceramics has been investigated *via* XRD, the results are shown in Figure 3.25. LP NN is included for comparison with a nominally stoichiometric composition.

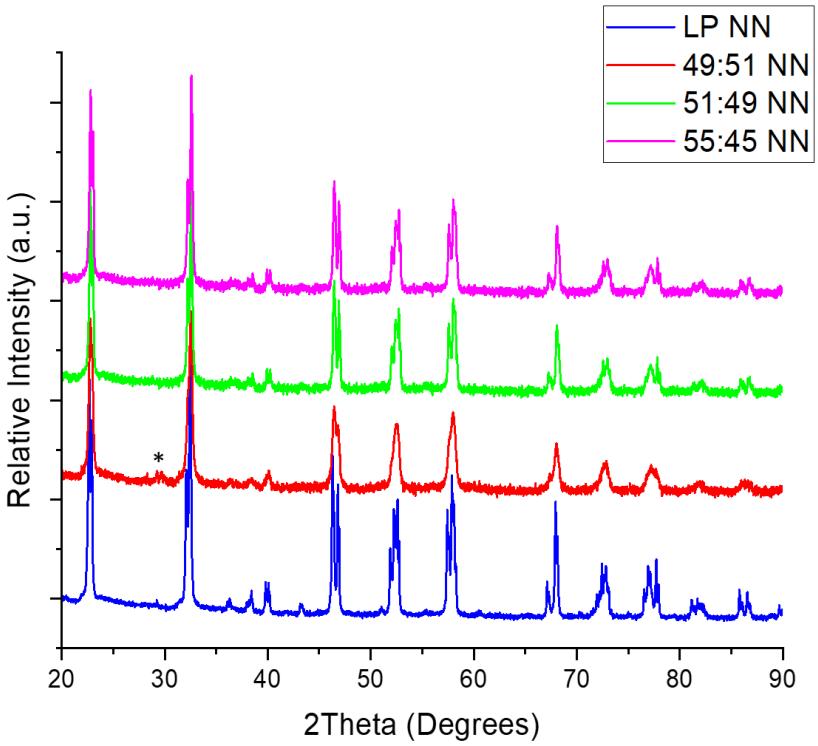

Figure 3.25: X-Ray Diffraction Patterns of Non-Stoichiometric NN Powders Compared to LP NN

After a single calcination the non-stoichiometric powders appear to be a mixture of the P (Pbma) and Q (Pmc21). A small amount of Na_3NbO_4 is detected as a secondary phase in 49:51 NN (indicated by a *), no secondary phases are observed in the sodium rich variants.

The obtained diffraction patterns for the non-stoichiometric powders were processed and refined in the same manner as the stoichiometric patterns in Figure 3.4. An example refinement on the sodium deficient 49:51 NN is shown in Figure 3.26 and the details of each refinement are tabulated in table 3.7.

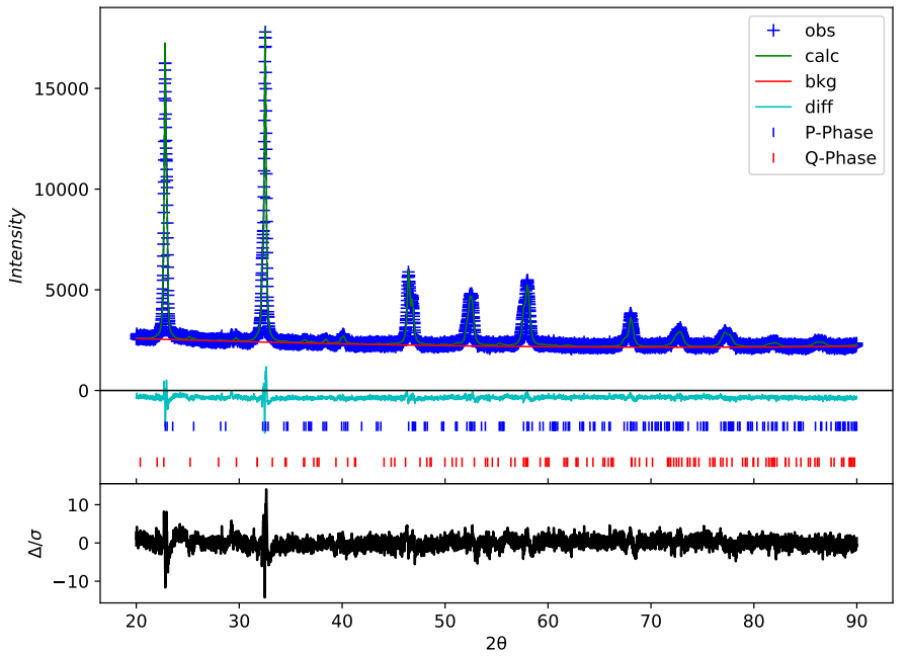

Figure 3.26: Example Rietveld Refinement of 49:51 NN Powder

	Parameters	LP NN	49:51 NN	51:49 NN	55:45 NN
P Phase (Pbma)	a / Å	5.57450(6)	5.51457(25)	5.56665(14)	5.56799(8)
	b / Å	15.51670(17)	15.5467(5)	15.5124(4)	15.51396(22)
	c / Å	5.51674(7)	5.55943(29)	5.50429(14)	5.50445(8)
	Cell Volume / Å^3	477.18611(2)	476.62864(8)	475.30701(4)	475.48306(2)
	Phase Fraction	0.655(9)	0.9304(30)	0.477(9)	0.524(4)
Q Phase (Pmc21)	a / Å	7.75949(26)	7.805(4)	7.76081(24)	7.76206(22)
	b / Å	5.56788(22)	5.5563(31)	5.57190(17)	5.57321(17)
	c / Å	5.51122(22)	5.5760(26)	5.51394(20)	5.51436(19)
	Cell Volume / Å^3	238.1062(7)	241.8395(9)	238.43631(6)	238.54896(5)
	Phase Fraction	0.345(9)	0.0696(30)	0.523(9)	0.476(4)
Residuals	R_w / %	2.935	3.103	3.159	2.71
	χ^2	8.95	2.50	2.63	7.51

Table 3.7: Summary of Rietveld Refinements for Non-Stoichiometric NN Powders

The changes to unit cell volume and the ratio of P:Q phases has been determined *via* Rietveld refinements. The determined ratios are shown in Figure 3.27.

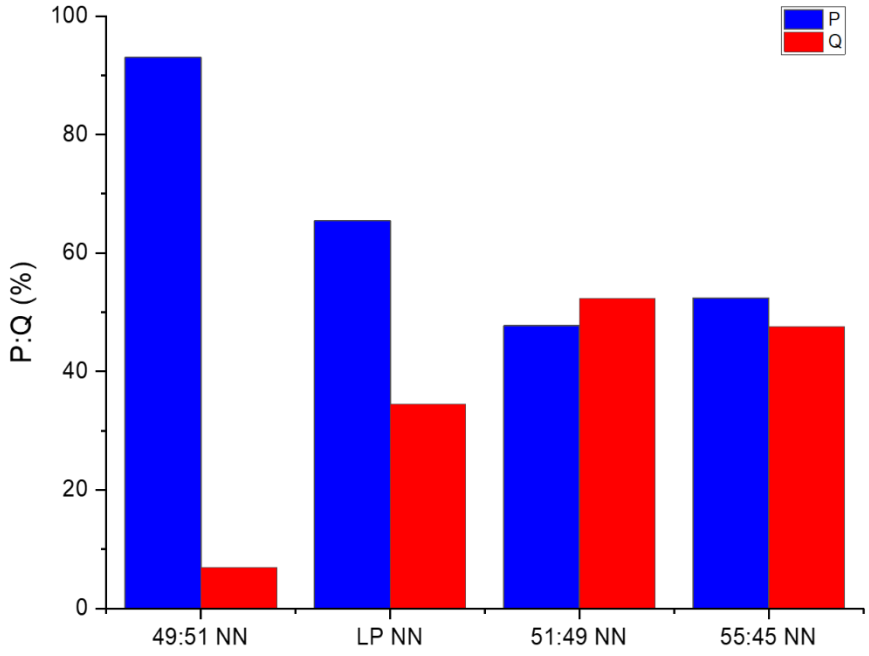

Figure 3.27: Ratio of P:Q Phases in Non-Stoichiometric NN Powders Obtained from Rietveld Refinement

The sodium deficient 49:51 NN appears almost exclusively P phase, whereas the sodium-rich variants show a significant increase in the amount of Q phase present compared to the stoichiometric LP NN.

3.2.2. Microstructure

The sintered ceramics have undergone a thermal etch and have been investigated *via* SEM-EDS. The grain structure and associated sizes have been evaluated and are shown in Figure 3.28.

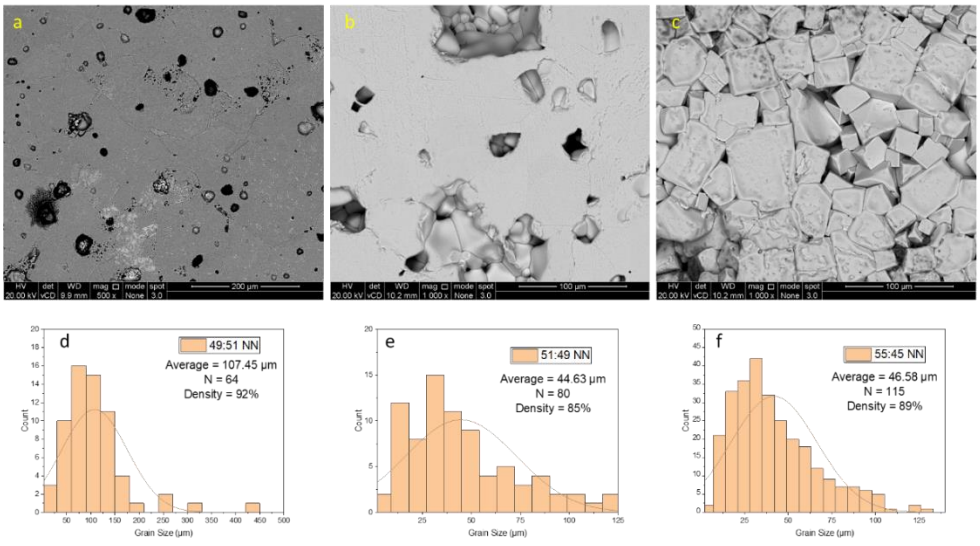

Figure 3.28: BSE Images of a) 49:51 NN b) 51:49 NN c) 55:45 NN and Associated Grain Size Evaluations d) 49:51 NN e) 51:49 NN and f) 55:45 NN

Moving away from a 1:1 Na:Nb ratio causes significant grain growth in all samples. The sodium deficient 49:51 NN samples have the largest level of grain growth. Additionally, Figure 3.28a shows the 49:51 NN ceramic contains an obviously ‘lighter’ region in the BSE image along the grain boundaries and some of the bulk indicating the presence of a secondary phase that has a lower Mr than NN segregating throughout the ceramic.

The sodium rich 51:49 and 55:45 NN ceramics showcase similar grain sizes. However, while the 51:49 NN ceramic exhibits a grain structure comparable to other NN ceramics, the 55:45 ceramic showcases a significant change in grain shape, appearing as a matrix of geometric cuboids, Figure 3.28c.

The elemental distribution throughout grains/grain boundaries have been determined *via* EDS and the obtained elemental maps are shown in Figures 3.29-3.31.

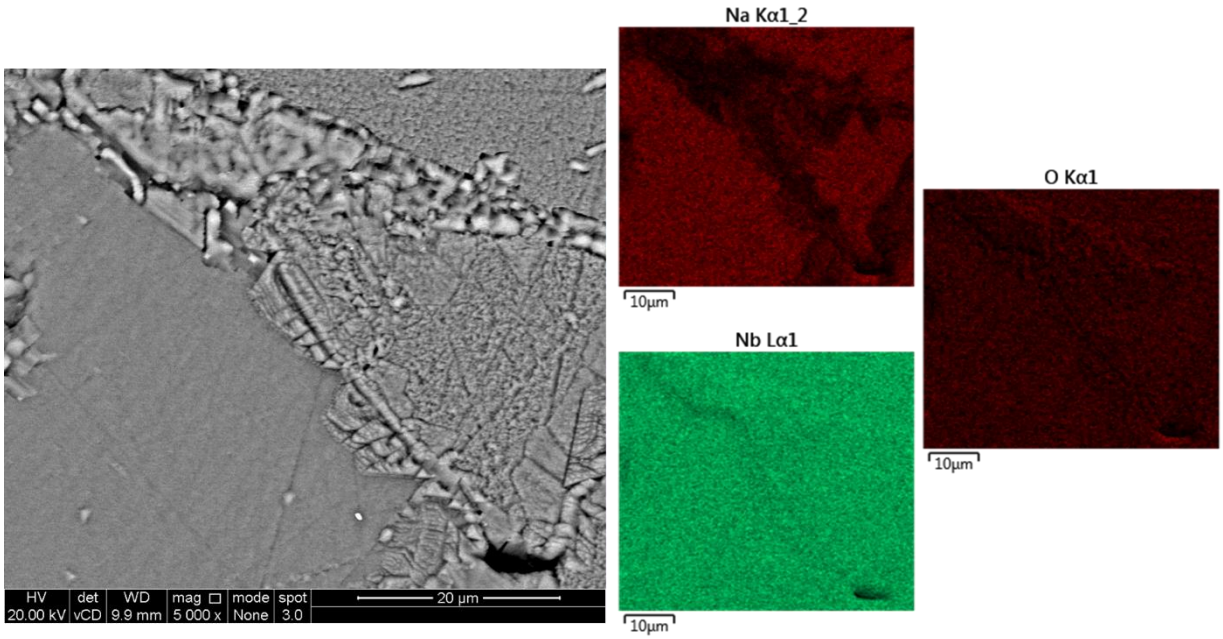

Figure 3.29: EDS Map of 49:51 NN

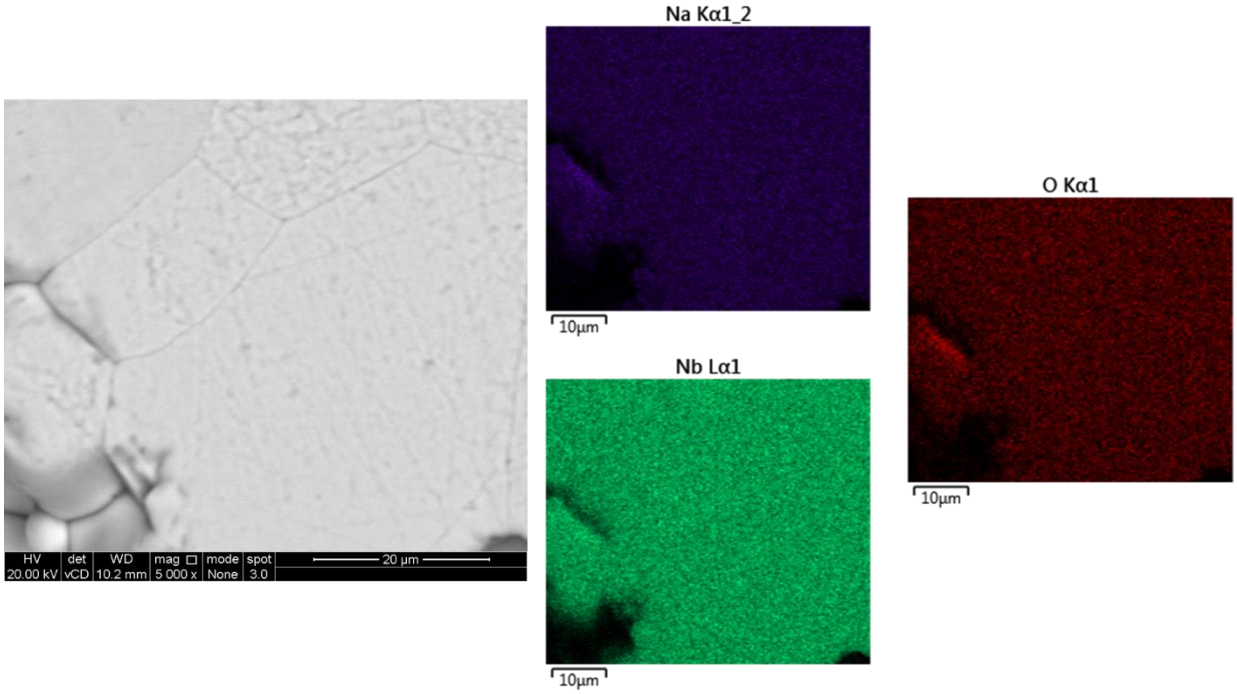

Figure 3.30: EDS Map of 51:49 NN

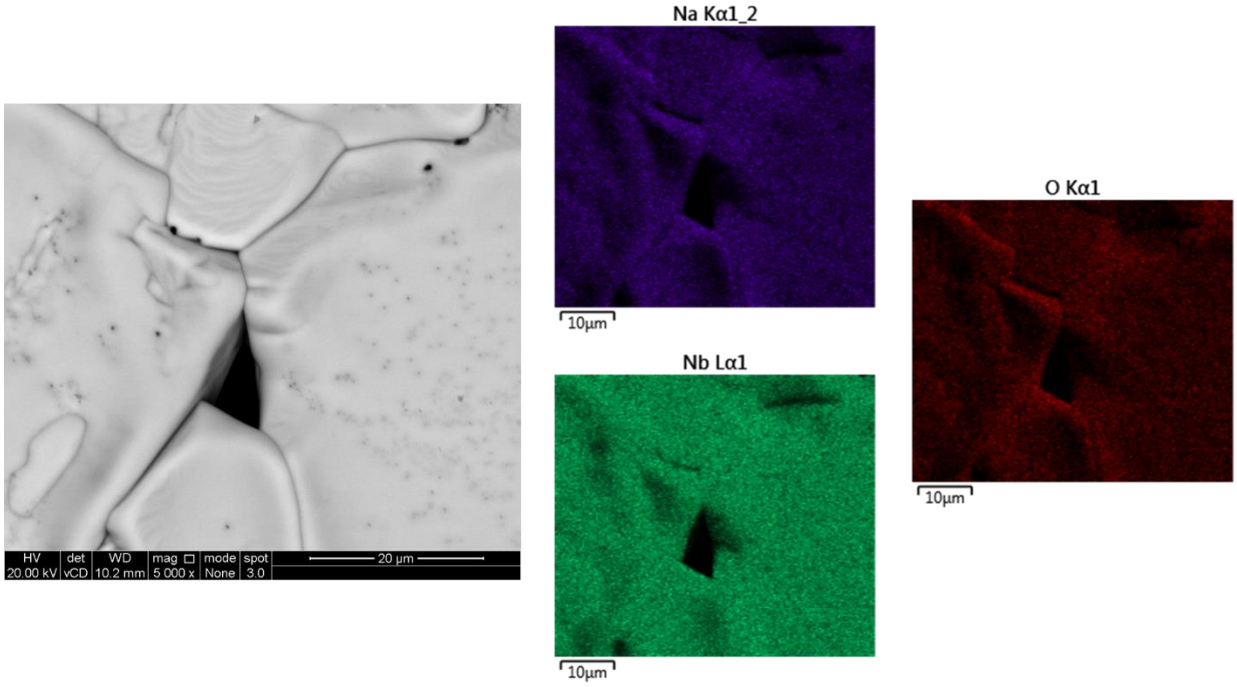

Figure 3.31: EDS Map of 55:45 NN

Figure 3.29 shows that 49:51 NN ceramics have a significant sodium deficiency along the grain boundary regions. The concentrations of niobium in the grain boundary regions increase by ~7 wt% compared with the rest of the ceramic. The sodium rich 51:49 NN (Figure 3.30) ceramic appears compositionally homogenous across the grains and grain boundaries whereas the 55:45 NN ceramic (Figure 3.31) appears to have slight sodium

deficiencies along the grain boundaries. Spot analysis has been used to determine the composition in each region of the tested ceramics. The results for the spot analysis are reported below in table 3.8 and compared to the theoretical stoichiometry for each ceramic.

	Theoretical			Grains			Grain Boundaries		
Composition	**Na / wt%**	**Nb / wt%**	**O / wt%**	**Na / wt%**	**Nb / wt%**	**O / wt%**	**Na / wt%**	**Nb / wt%**	**O / wt%**
49:51 NN	13.42	57.09	29.15	12.38 ± 0.02	63.65 ± 0.01	23.95 ± 0.01	6.10 ± 0.04	71.30 ± 0.01	22.67 ± 0.02
LP NN	14.00	57.00	29.00	12.59 ± 0.03	61.03 ± 0.01	26.37 ± 0.03	12.38 ± 0.06	62.96 ± 0.01	24.67 ± 0.03
51:49 NN	14.43	56.03	29.54	13.05 ± 0.02	60.40 ± 0.01	26.55 ± 0.02	12.83 ± 0.02	59.38 ± 0.01	27.75 ± 0.02
55:45 NN	16.12	53.29	30.59	12.18 ± 0.03	62.40 ± 0.01	25.08 ± 0.03	11.78 ± 0.04	63.32 ± 0.01	24.90 ± 0.03

Table 3.8: Average Grain and Grain Boundary compositions of Non-Stoichiometric NN ceramics Compared to LP NN

The sodium content of each of the ceramics is lower than expected throughout. However, the sodium content at the grain boundaries are slightly lower than in the bulk suggesting sodium may be lost to volatilisation through the grain boundaries. The 49:51 NN ceramic shows the most substantial sodium deficiency at the large grain boundaries.

3.2.3. Relative Permittivity and Dielectric Losses

The relative permittivity and dielectric losses of non-stoichiometric NN ceramics have been determined. The overall ε_r – T plots are shown in Figure 3.32.

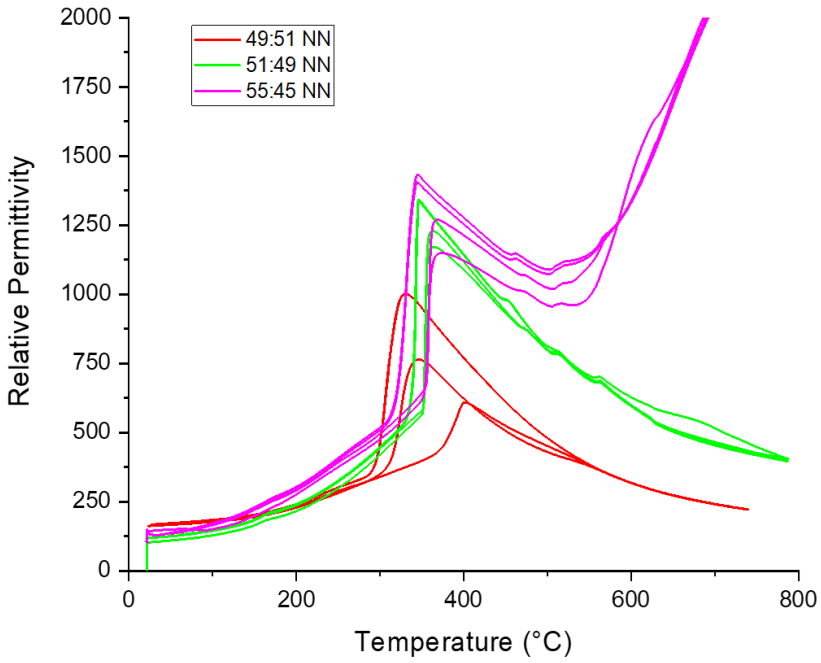

Figure 3.32: Relative Permittivity of Non-Stoichiometric NN Ceramics (Taken at 100 kHz)

The non-stoichiometric variants of NN also showcase a characteristic peak in permittivity around the P-R phase transition. However, unlike stoichiometric variants of NN the permittivity is not always consistent over subsequent heating/cooling cycles. This is shown below in Figure 3.33 for the sodium deficient 49:51 and sodium rich 51:49 ceramics.

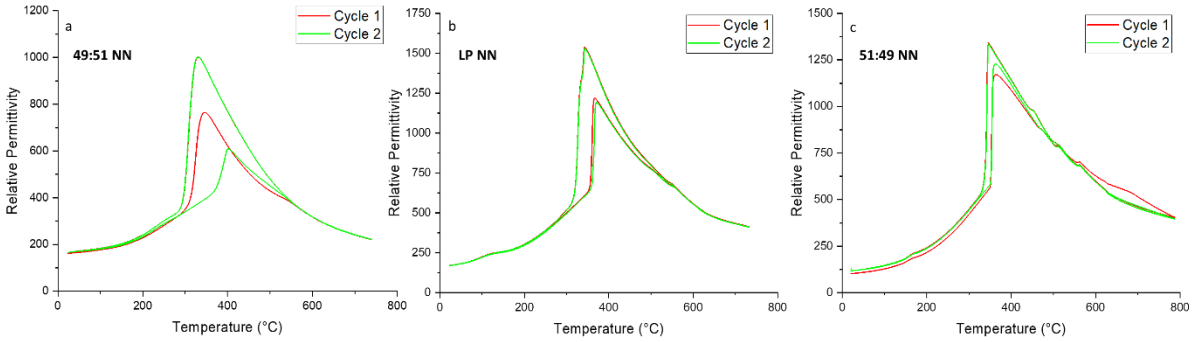

Figure 3.33: Relative Permittivity Plots of a) 49:51 NN and b) LP NN and c) 51:49 NN Ceramics over 2 Heating/Cooling Cycles

The sodium deficient ceramic experiences slight differences over subsequent heating cycles; however, it remains consistent during cooling cycles. Between heating cycle 1 and 2 the P-R phase transition has shifted to a higher temperature with a notable drop in permittivity. Conversely in the stoichiometric LP NN and sodium rich 51:49 NN ceramics, the P-R phase transition is unaffected over successive cycles.

The lower temperature, Q-P transition is also unaffected over subsequent heating/cooling cycles. However, as the stoichiometric ratio changes this transition temperature changes. In the sodium deficient 49:51 NN ceramic this transition occurs at ~250 °C, whereas in the stoichiometric LP NN and sodium rich 51:49 NN ceramics it occurs below 200 °C.

The dielectric losses for non-stoichiometric NN are shown below in Figure 3.34.

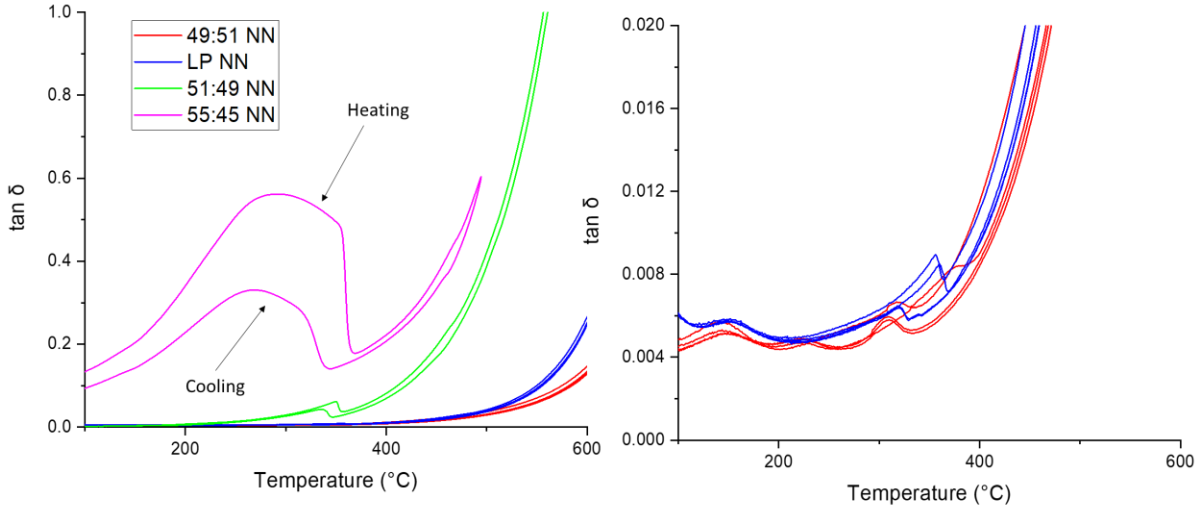

Figure 3.34: Dielectric Losses of Non-Stoichiometric NN ceramics at 100 kHz Compared to 'LP NN'

The sodium deficient 49:51 NN shows very low dielectric losses of less than 1% losses before 400 °C; as observed with stoichiometric NN the losses increase rapidly as space charge effects begin to dominate the response. As the Na:Nb ratio increases the losses increase significantly, with the 55:45 NN ceramic showcasing maximum losses of ~60% on heating around the P-R phase transition. As observed in the relative permittivity, the losses showcase a slight reduction over subsequent heating/cooling cycles.

3.2.4. Electrical Properties

The electrical properties of the non-stoichiometric NN ceramics have been evaluated *via* impedance spectroscopy to establish the effect of a variable Na:Nb ratio on the overall conductivity of the ceramics. To assess the electrical homogeneity of the ceramics the overlaid M''/Z'' at 600 °C are shown in Figure 3.35.

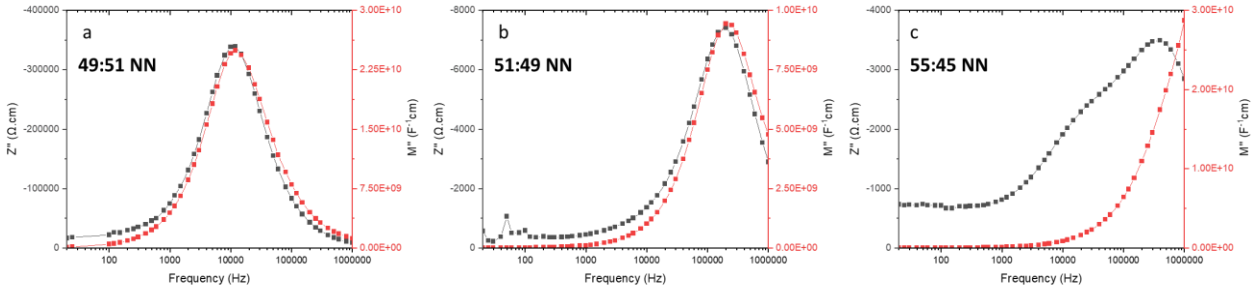

Figure 3.35: M'' Z'' Plots of a) 49:51 NN b) 51:49 NN and c) 55:45 NN Ceramics at 600°C

Composition	Capacitance (Z'') / F cm^{-1}	Capacitance (M'') / F cm^{-1}	F_{max} (M'') / kHz	Corresponding Response
49:51 NN	$1.9(1) \times 10^{-11}$	$2.0(1) \times 10^{-11}$	12	Bulk
LP NN	$5.1(4) \times 10^{-11}$	$4.5(2) \times 10^{-11}$	8.00	Bulk
51:49 NN	$5.4(6) \times 10^{-11}$	$5.3(3) \times 10^{-11}$	200	Bulk
55:45 NN 1	$5.7(25) \times 10^{-11}$	-	-	Bulk
55: 45 NN 2	$1.1(9) \times 10^{-9}$	-	-	Grain Boundary

Table 3.9: Tabulated Capacitances Extracted from M'' and Z'' Responses in Figure 3.35 Compared to LP NN

As the Na:Nb ratio increases the imaginary impedance (Z'') becomes increasingly distorted, indicating the presence of 2 or more RC elements. All observable M'' peaks show a single response related to the bulk conductivity. As observed with the stoichiometric NN variants there is not a notable increase in the Z'' response at low frequencies, suggesting that ionic conductivity is minimal. However, there is a notable increase in capacitance towards μF cm^{-1} in the C' vs frequency plot shown in Figure 3.36.

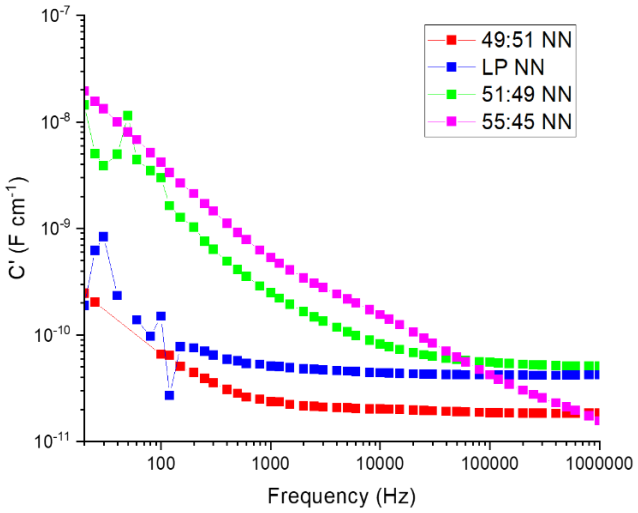

Figure 3.36: C' vs Frequency Plot of Non-Stoichiometric NN Ceramics Compared to LP NN at 600°C

The capacitance for the sodium deficient 49:51 NN ceramic remains relatively consistent before a slight increase below 100 Hz. Conversely the sodium rich ceramics showcase a consistent and rapid increase in capacitance as frequency decreases suggesting the presence of ionic conductivity.

The bulk conductivity of the non-stoichiometric NN ceramics has been calculated from the capacitance extracted from the M'' plots. The Arrhenius plots of bulk conductivity are shown below in Figure 3.37 and compared to LP NN ceramics showcased in section 3.1.3.

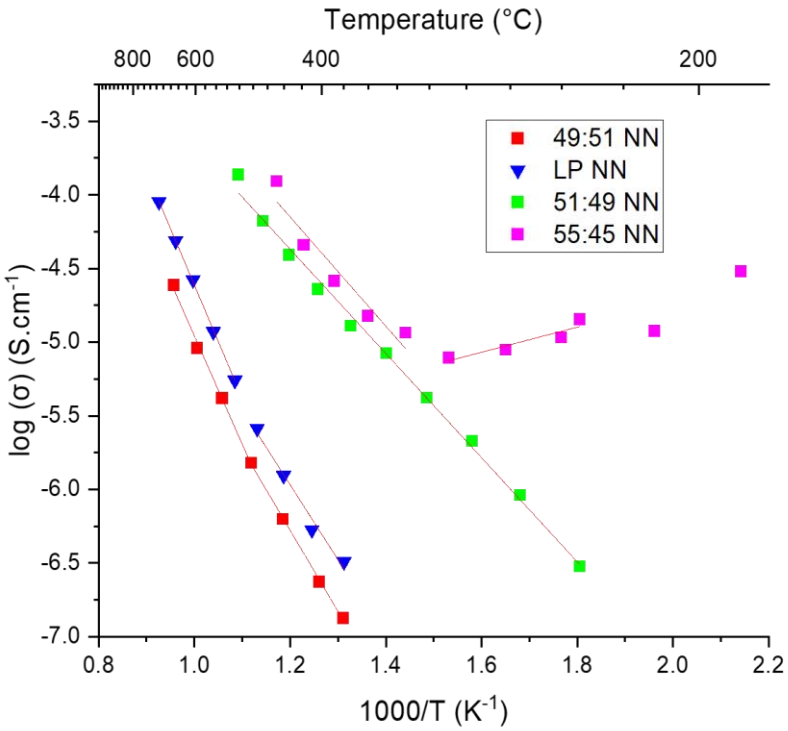

Figure 3.37: Arrhenius Plots of Bulk Conductivities for Non-Stoichiometric NN Variants Compared to Stoichiometric LP NN

The bulk conductivity of NN materials decreases slightly as the Na:Nb ratio decreases. As the ratio increases the bulk conductivity of the ceramics increase by approximately 1.5 orders of magnitude. All sodium rich materials appear to have similar bulk conductivities above 500 °C. Generally, conductivities are increasing consistently with temperature. However, the 55:45 NN ceramic shows a slight decrease in conductivity as temperature increases in the region 200-500 °C. This is likely a result of proton conduction being eliminated as water in the sample is removed.

The effect of proton conduction is more prominent at lower temperatures shown in the room temperature M''/Z'' plots in Figure 3.38 and the extended Arrhenius plot in Figure 3.39.

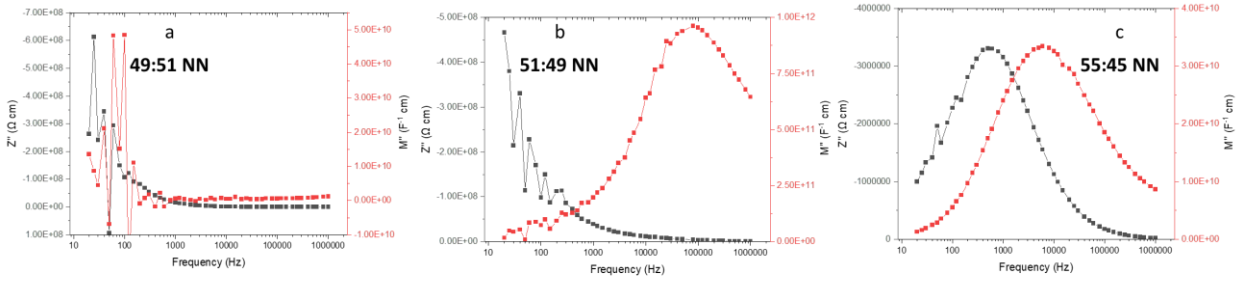

Figure 3.38: M'' Z'' Plots of a) 49:51 NN b) 51:49 NN and c) 55:45 NN Ceramics at Room Temperature

Composition	Capacitance (Z'') / F cm^{-1}	Capacitance (M'') / F cm^{-1}	F_{max} (M'') / kHz	Corresponding Response
49:51 NN	-	-	-	Bulk
51:49 NN	-	$5.2(3) \times 10^{-13}$	80.0	Edge/Grain Boundary
55:45 NN	$4.8(20) \times 10^{-11}$	$1.5(1) \times 10^{-11}$	6.00	Bulk

Table 3.10: Tabulated Capacitances Extracted from M'' and Z'' Responses in Figure 3.38

At room temperature the sodium deficient 49:51 NN ceramic is too resistive to analyse *via* impedance spectroscopy, conversely, the sodium rich ceramics exhibit broad M'' peaks. The 55:45 ceramic showcasing a bulk electrical response, however, the pF capacitance of the 51:49 ceramic is indicative of a short circuit in the measurement, likely as a consequence of moisture down the sides of the pellet or throughout the grain boundaries. As the Na:Nb ratio increases the room temperature bulk conductivity increases before gradually decreasing with temperature as proton conduction is eliminated.

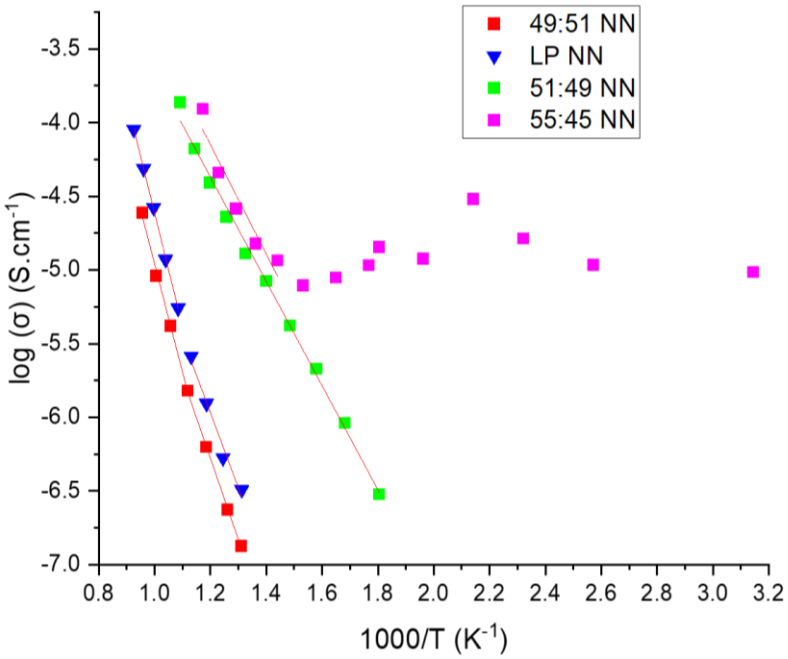

Figure 3.39: Arrhenius Plots of Bulk Conductivities for Non-Stoichiometric NN and LP NN over a Larger Temperature Range

The activation energies for each region have been extracted from the slopes of each Arrhenius plot and are shown below in table 3.11.

Composition	Low Temperature Ea /eV	High Temperature Ea / eV	Crossover Temperature / °C
49:51 NN	1.09 ± 0.02	1.46 ± 0.06	628
LP NN	1.01 ± 0.10	1.52 ± 0.02	636
51:49 NN	0.70 ± 0.05	-	-
55:45 NN	0.12 ± 0.02	0.56 ± 0.08	352

Table 3.11: Activation Energies Extracted from Arrhenius Plots of M'' Spectra (Figure 3.37)

All variants except 51:49 NN showcase a change in slope at higher temperatures, leading to a greater activation energy. 51:49 NN maintains a single activation energy throughout the Arrhenius plot. The sodium deficient 49:51 NN shows similar activation energies to LP NN, however, as the Na:Nb ratio increases the activation energy of each ceramic decreases at all temperatures, possibly indicating a change in conduction mechanism(s) in these samples.

To help understand the origins of the n-type and p-type conductivities observed in stoichiometric NN ceramics the pO_2 dependence of the non-stoichiometric NN ceramics was assessed and the results shown in Figures 3.40-3.42.

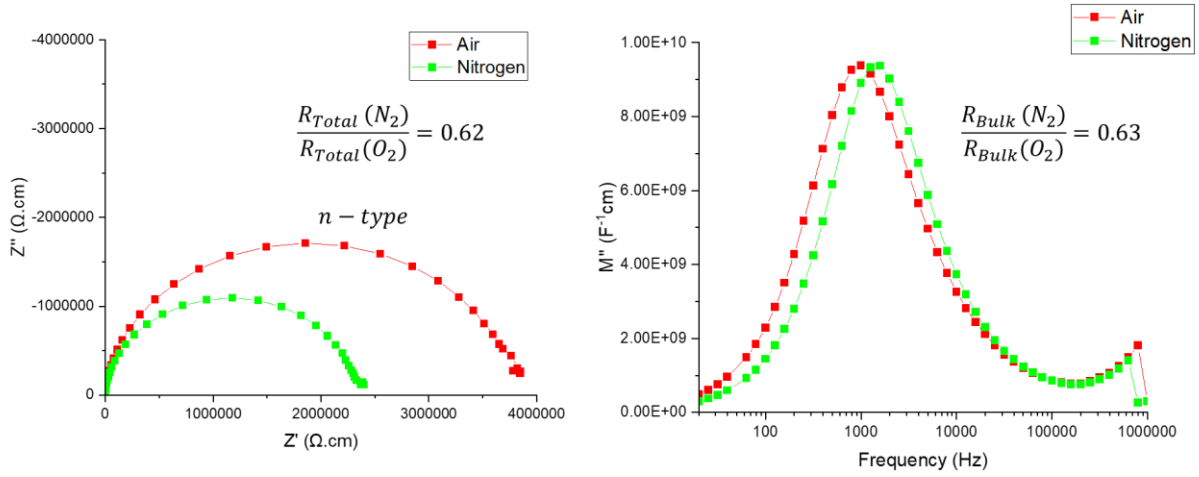

Figure 3.40: pO_2 Dependence of 49:51 NN Ceramics. Complex Impedance (Left) and M'' Response (Right) at 500 °C

Sodium deficient 49:51 NN ceramics exhibit a decrease in total resistivity as pO_2 decreases indicating the presence of n-type conductivity. This n-type conductivity is attributed to the bulk response of the ceramic as f_{max} shifts to higher frequencies. The increase in capacitance at high frequencies is attributed to a jig effect and may be ignored.

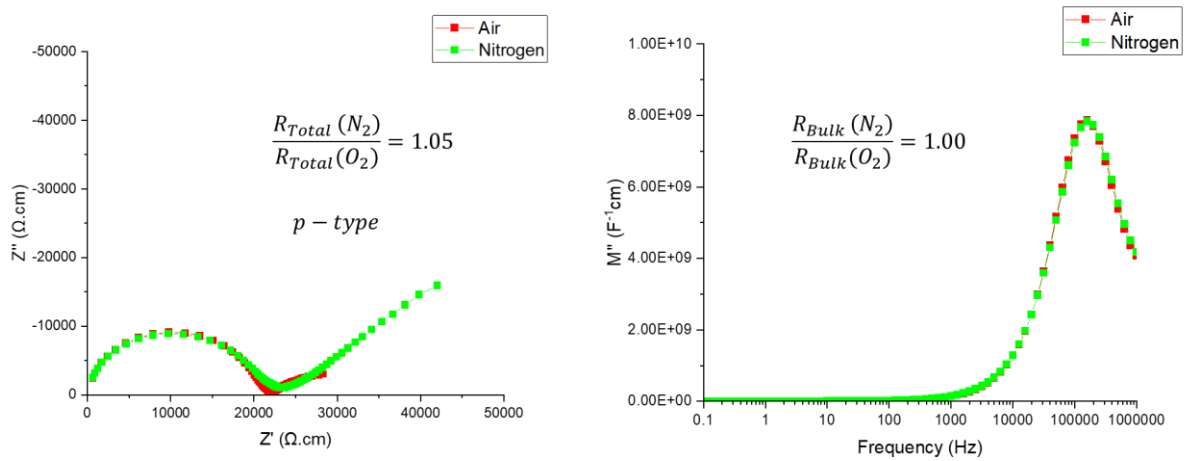

Figure 3.41: pO_2 Dependence of 51:49 NN Ceramics. Complex Impedance (Left) and M'' Response (Right) at 600 °C

The 51:49 NN ceramic shows a slight increase in resistivity as pO_2 decreases, however, the bulk electrical response is not affected, indicating the slight increase in resistivity is attributable to extrinsic effects.

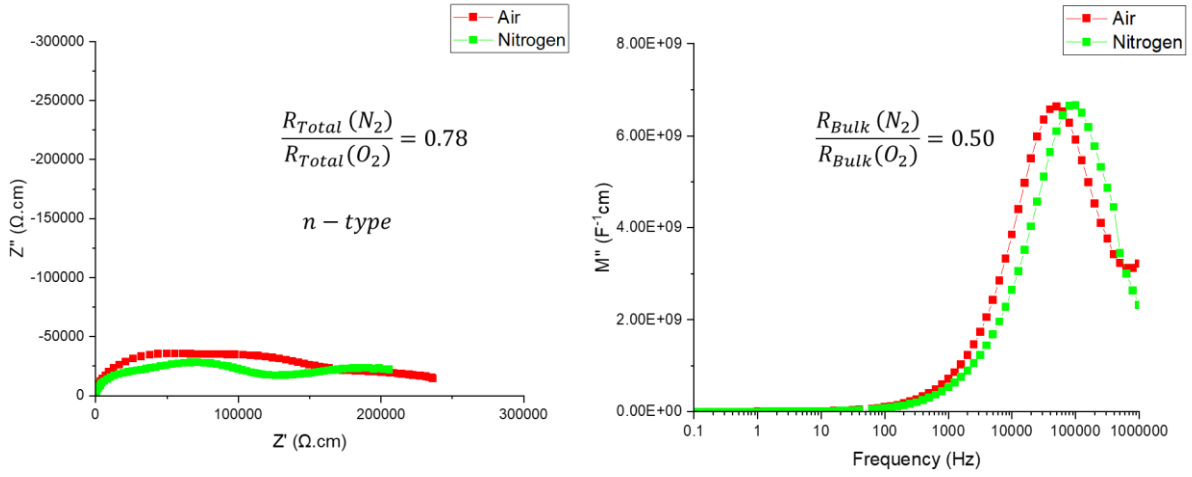

Figure 3.42: pO_2 Dependence of 55:45 NN Ceramics. Complex Impedance (Left) and M'' Response (Right) at 500°C

The 55:45 NN ceramic shows a slight decrease in total resistivity as pO_2 decreases indicating n-type conductivity. This is primarily due to the bulk response as f_{max} shifts to higher frequencies. However, the n-type behaviour observed in the bulk response is significantly greater than what is observed in the Z* plane. This is partially due to the grain boundary response exhibiting less pO_2 dependence ($\frac{R_{GB}(N_2)}{R_{GB}(O_2)} = 0.81$). However, this does not fully account for the difference indicating the presence of extrinsic effects exhibiting p-type conductivity.

3.2.5. Oxide Ion Transport Number

The oxide ion transport number (t_{O2-}) has been determined for the 49:51 NN ceramic and compared against 'LP' and 'I NN' in Figure 3.43.

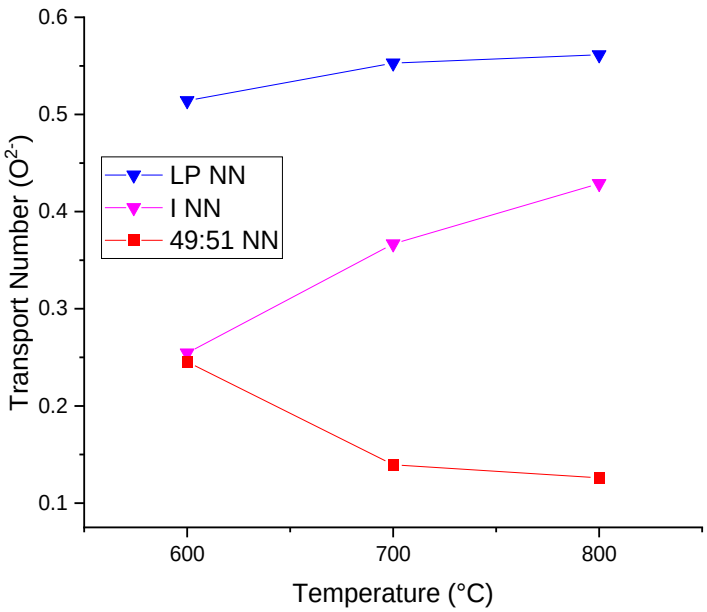

Figure 3.43: Transport Number of 49:51 NN as a Function of Temperature Compared to LP and I NN

The determined transport t_{O2-} for 49:51 NN is significantly lower than the stoichiometric counterparts at high temperatures with a value of 0.13 at 800 °C. t_{O2-} appears to increase at lower temperatures in the 49:51 NN ceramic. However, this is more likely an artefact of the measurement due to the rapidly increasing resistance of YSZ with decreasing temperature.

The sodium rich 51:49 and 55:45 NN ceramics were unable to undergo testing due to the larger diameter ceramics required for the measurements becoming too brittle to withstand the applied compression during the sealing process. (Section 2.7.3.).

3.3. Discussion

The physical and electrical properties of NN materials vary significantly based on reaction conditions. In order to understand the origin of the variance, the changes observed in non-stoichiometric variants may be useful.

3.3.1. Microstructure and Phase Purity

The presence of any secondary phases such as the sodium-rich Na_3NbO_4 or the niobium-rich phases of $Na_2Nb_4O_{11}$ and $NaNb_3O_8$ have previously been attributed to some of the observed differences in non-stoichiometric variances.[6] However, the electrical properties of these phases have undergone limited investigation, the most notable findings for the

potential secondary phases are: the low observed permittivity of $Na_2Nb_4O_{11}$ and room temperature impedance showcasing low conductivity of approximately 1 μS cm^{-1}.[11,12]

As shown in the phase diagram (literature review Figure 1.9) the sodium rich phase Na_3NbO_4 and NN can coexist. If there is an incomplete calcination of NN and unreacted Na_2CO_3 remains, the equilibrium shown in equation 3.7 dictates that the sodium rich Na_3NbO_4 phase will form. As a result of this equilibrium electrical testing of Na_3NbO_4 is dominated by the effects of NN and specific investigations in inert atmospheres have not taken place.[13]

$$NaNbO_3 + Na_2CO_3 \rightleftharpoons Na_3NbO_4 + CO_2 \qquad (3.7)$$

Additionally, if these phases are present within the discussed compositions the concentrations are below the detection limits of XRD. The 49:51 NN ceramic showcases a region of significant sodium deficiency along the large grain boundary, as shown in Figure 3.29. The Na:Nb ratio in this region is approximately 1:3 which corresponds to the $NaNb_3O_8$ phase. Additionally, the formation of this phase along the grain boundaries is consistent with previous literature that suggests liquid secondary phases form at the boundaries of larger grains.[14] As per the Na_2O-Nb_2O_5 phase diagram shown in the literature review (Figure 1.9) the melting point of $NaNb_3O_8$ is 992 °C.[15] When a significant level of sodium deficiency is present in the NN system near stoichiometric NN, $NaNb_3O_8$ therefore forms a minor secondary phase. During sintering the $NaNb_3O_8$ segregates to the grain boundaries and melts, this solid/liquid interface may lead to the abnormal grain growth as observed with $BaTiO_3$.[16] None of the other investigated ceramics show sodium or niobium deficiencies significant enough to be attributed to either the $NaNb_3O_8$ or Na_3NbO_4 phases.

HT NN ceramics showcase the largest grain sizes of the undoped ceramics. However, this enlargement of grain sizes is unlikely to be a result of sodium volatility. While the sodium content is slightly lower than the theoretical amount, as shown in table 3.3, it is not sufficiently low to promote the formation of the $NaNb_3O_8$ phase. It is more likely that the increased grain size in the ceramics is a consequence of a smaller particle size of the powder used to prepare ceramics compared to the NN variants synthesised *via* solid state method.[2]

3.3.2. Relative Permittivity, Dielectric Losses, and Polymorphism

The effect of Na:Nb non-stoichiometry appears to have a significant effect on the P-R phase transition observed in the permittivity-temperature plots. The hysteresis on heating/cooling can be used to evaluate the stability of the P and R phases of NN. Figure 3.44 and table

3.12 show the temperature where ε_r is at a maximum (T_{max}) on heating and cooling as well as the difference between the observed temperatures. All T_{max} values were extracted from cycle 2 to ensure the influence of any moisture on the electrical properties had been completely eliminated.

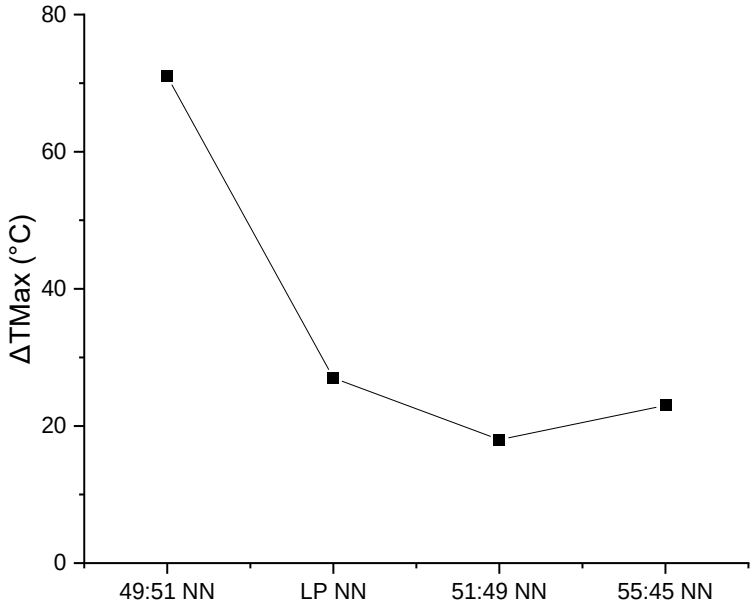

Figure 3.44: Change in ΔT_{Max} with Increasing Na:Nb Ratio

Composition	T_{max} (Heating) / °C	T_{max} (Cooling) / °C	ΔT_{Max} / °C	P-Phase / %	Q-Phase / %
LP NN	371	344	27	66	34
HP NN	368	328	40	73	27
HT NN	369	348	21	76	24
I NN	362	356	6	92	8
49:51 NN	402	331	71	93	7
51:49 NaNbO3	363	345	18	48	52
55:45 NaNbO3	367	344	23	52	48

Table 3.12: Comparison of T_{Max} on Heating and Cooling in NN Ceramics (σ_T = ±0.5°C)

As the Na:Nb ratio increases ΔT_{Max} decreases notably. With a slight sodium deficiency in 49:51 NN the A-site vacancies cause stabilisation of the lower temperature P phase on heating shifting the phase transition to higher temperatures, on cooling however, the P phase is destabilised shifting the transition lower and widening the hysteresis. As the ceramics become sodium rich in 51:49 and 55:45 NN ΔT_{Max} does not significantly vary beyond stoichiometric NN, suggesting that either:

1. B-site vacancies have no significant effect on the P-R phase transition.
2. The sodium rich ceramics are closer to stoichiometric NN than targeted due to sodium volatility.

As previously discussed, some sodium volatility is expected under the processing conditions, and the significant observed effect on the phase transition with A-site vacancies suggests that the ceramics are closer to stoichiometric NN.

The stoichiometric NN samples show some variance in the P-R phase transition. According to Megaw *et. Al.* the P-R phase transition of stoichiometric undoped NN occurs at 360 °C.[17] On heating the ceramic with the greatest agreement is I NN with very little variance in the transition on thermal cycling. This resistance to cycling and the associated narrow hysteresis may be a consequence of the relatively small amount of Q-phase NN present in the ceramic. As Q-phase concentrations increase in the other stoichiometric NN variants ΔT_{Max} increases. T_{max} on heating increases in all ceramics, and T_{max} on cooling decreases in all ceramics. This divergence of T_{max} indicates a destabilisation of the phase transition, as observed with A-site vacancies. Small amounts of sodium will be lost during calcination and sintering of NN ceramics. The utilisation of hydrothermal synthesis limits the amount of sodium loss during processing by elimination of the initial calcination of Na_2CO_3 and Nb_2O_5.

As shown in Figure 3.34, the dielectric losses of non-stoichiometric NN increase with increasing Na:Nb ratio with ceramics becoming progressively 'leakier'. A-site metal vacancies cause the dielectric losses to decrease to <1%. This low magnitude of dielectric losses is in line with the losses observed with stoichiometric NN ceramics. The exception in this case is the HT NN which showcases significant dielectric losses more in line with the sodium rich 51:49 NN ceramic, as shown in Figure 3.45.

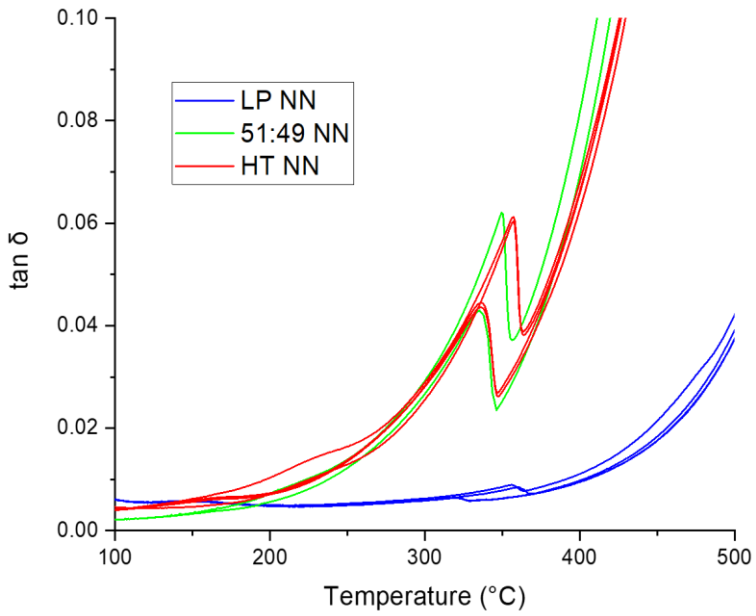

Figure 3.45: Dielectric Losses of 51:49 NN Compared to HT and LP NN

This is likely a consequence of the sodium rich environment in the processing conditions. In the conventionally processed ceramics (LP and HP NN) Na_2CO_3 and Nb_2O_5 are mixed in a stoichiometric ratio. In HT NN Nb_2O_5 is mixed dissolved in an 8.4 M solution of Na(OH).[2] This sodium rich synthesis environment is most likely responsible for the increased dielectric losses.

3.3.3. Impedance Spectroscopy

The bulk conductivity of stoichiometric and non-stoichiometric NN ceramics scale with the observed dielectric losses. As the ceramic becomes increasingly 'leaky' the bulk conductivity increases. The low temperature regions (<400 °C) of NN ceramics are dominated by extrinsic effects and proton conduction. This leads to low temperature activation energies being difficult to interpret and compare. However, in the higher temperature region of the Arrhenius plots the non-stoichiometric NN activation energies decrease with increasing Na:Nb ratio or increasing losses (Figures 3.34 and 3.37).

The bulk conductivity and associated activation energy of the sodium deficient 49:51 NN is in line with the 2 conventionally processed stoichiometric NN as shown in the Arrhenius plot below.

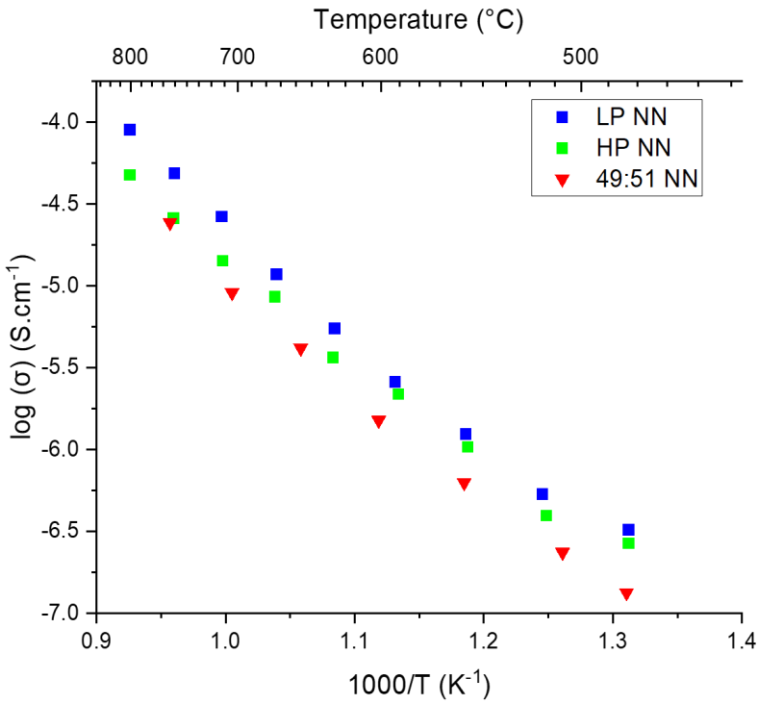

Figure 3.46: Arrhenius Plots of Bulk Conductivity of LP, HP, and 49:51 NN Ceramics

The most likely reason for the associated increase in conductivity with increasing Na:Nb ratio is the generation of additional oxygen vacancies. Re-defining the non-stoichiometric

ceramics into a conventional formula shown in table 3.13 shows how the vacancy concentration may increase significantly.

Na:Nb Ratio	Conventional Formula
48.75:51.25	$Na_{0.95}NbO_{2.975}$
51:49	$NaNb_{0.96}O_{2.90}$
55:45	$NaNb_{0.82}O_{2.55}$

Table 3.13: Conversion of Na:Nb Ratio to Conventional Formula
N.B.: 48.75:51.25 has been rounded to 49:51 for clarity throughout this chapter

Within this context Figure 3.37 shows that ceramic bulk conductivity increases with vacancy concentration indicating that contributions from oxide ion conductivity are increasing. Additionally, the activation energy decreases, indicating a changing conduction mechanism. The determined band gap for LP NN is 3.45 eV. For purely intrinsic electrical conduction effects, the activation energy for bulk conductivity should be approximately half of the band gap, 1.73 eV. The observed bulk activation energy for LP NN and 49:51 NN are 1.52 eV and 1.46 eV, respectively. This indicates that some extrinsic effects remain in the high temperature region. In both cases this effect is most likely related to low levels of oxide ion conduction demonstrated by the transport numbers of 0.56 and 0.13, respectively (Figure 3.43).

As oxygen vacancy concentrations increase throughout the samples, the activation energy lowers gradually to the region of 0.56 eV which is typically representative of fast oxide ion conduction in perovskites.[18] However, transport number measurements on the 'leakier' ceramics were unable to be collected due to the poor mechanical properties of the ceramics, the more brittle ceramics resulting from the increased Na:Nb ratio is likely a consequence of the increased moisture sensitivity showcased by the proton conduction at lower temperatures (Figures 3.38 and 3.39). Additionally, the ceramics with the greatest bulk conductivity contain the greatest concentration of the Q-phase (Figure 3.27 and 3.37). It has previously been demonstrated that oxygen vacancies in NN may be responsible for increased formation of the Q-phase, which appears to be observed in this case.[7]

3.3.4. pO_2 Dependence

The pO_2 dependence for the ceramics shown in sections 3.1.3 and 3.2.4 are summarised in table 3.14.

Composition	$\frac{R_{Total}(N_2)}{R_{Total}(O_2)}$	Total Observed Response	$\frac{R_{Bulk}(N_2)}{R_{Bulk}(O_2)}$	Bulk Observed Response
LP NN	0.96	n	0.99	Independent
HP NN	0.60	n	0.62	n
HT NN	1.30	p	0.95	Independent
I NN	0.72	n	0.70	n
49:51 NN	0.62	n	0.63	n
51:49 NN	1.05	p	1.00	Independent
55:45 NN	0.78	n	0.50	n

Table 3.14: Summarised pO_2 Dependency of NN Ceramics

The pO_2 dependence of the bulk electrical response of the tested NN ceramics is primarily weak n-type, most likely as a consequence of oxygen loss and consequent reduction of the niobium ions:

$$O^{2-} \rightarrow \frac{1}{2}O_{2_{(g)}} + 2e^- \qquad (3.8)$$

$$2Nb^{5+} + 2e^- \rightarrow 2Nb^{4+} \qquad (3.9)$$

In stoichiometric NN the bulk pO_2 dependence varies between independent (LP and HT NN) and n-type (HP and I NN). This variable pO_2 dependence is likely a consequence of reagent purity, comparing the LP and HP NN ceramics where processing conditions were identical, the resultant bulk conductivity is comparable (Figure 3.18) but the pO_2 dependence of the ceramic made from higher purity reagents is slightly n-type. A potential reason for this would be the presence of donor ions in LP NN as impurities that contribute to filling the oxygen vacancies, indicating that pO_2 dependence in NN is heavily linked with processing conditions.

3.3.5. Mixed Conductivity and Oxygen Transport Numbers

The observed pO_2 dependence in the bulk responses, while process dependent, does show that there is a mixed component to the conductivity of NN. Combined with the transport number measurements showing a contribution from oxide ions (Figure 3.43) the NN system is typically a mixed electronic (n-type) and ionic conductor. Gouget *et. Al.* claim NN is a mixed sodium/oxide ion conductor; however, as discussed in the literature review (section 1.6) the methodology used fails to eliminate the contributions from electronic conduction.[19] While the methodology used in this work does not explicitly eliminate sodium ion conduction, the likelihood of mixed electronic (n-type) and ionic conductivity due to both sodium and oxide ions is low.

3.4. Conclusions

The synthesis of stoichiometric undoped NN poses a notable challenge. Sodium volatility during synthesis, calcination, and potentially high temperature operation of NN ceramics leads to the generation of A-site metal vacancies, and in turn oxygen vacancies. The presence of oxygen vacancies in undoped NN is responsible for the low levels of ionic conductivity observed and the notable dielectric losses.

If sodium content is sufficiently low, the niobium-rich $NaNb_3O_8$ phase may form in the ceramics along grain boundaries, causing significant microstructural effects such as enlargement of grain size. Additionally, sodium deficiency may be responsible for the destabilisation around the P-R phase transition.

Utilisation of a slightly sodium-rich processing environment eliminates pO_2 dependence of the bulk electrical response. But in turn this environment produces an increasingly 'leaky' dielectric material with poor mechanical properties. This suggests that in terms of dielectric performance some sodium deficiency may be tolerated, but any potential advantages of increased sodium content to overcome volatility can have too much of an impact on dielectric performance to be worthwhile for this application.

The 'leakier' the observed dielectric response the greater the observed bulk conductivity due to suspected increased contributions from oxide ion conduction *via* oxygen vacancies. As oxygen vacancy concentrations increase the susceptibility to proton conduction also increases due to increased availability of oxygen sites in the lattice allowing for hydration of the ceramic according to equation 3.6. However, the effects of proton conduction are eliminated before the temperature range most relevant to potential ITSOFC electrolyte applications.

NN ceramics with the greatest concentrations of Q-phase NN exhibit the greatest bulk conductivities. While this may indicate that Q-phase NN is more conductive than P-phase NN it has been previously reported that oxygen vacancies in NN may cause increased formation of the Q phase.[7] This suggests that the more conductive NN ceramics contain more Q-phase, because of higher vacancy concentrations.

The significant variance in stoichiometric NN may be addressed by selection of suitable dopant ions to enhance or diminish desired traits in the ceramics. This will be discussed in chapters 4 and 5, Chemical Doping of Sodium Niobate.

3.5. References

1. Brunckova, H., Medvecký, L. & Hvizdoš, P. Effect of substrate on phase formation

and surface morphology of sol-gel lead-free $KNbO_3$, $NaNbO_3$, and $K_{0.5}Na_{0.5}NbO_3$ thin films. *Chem. Pap.* **66**, 748–756 (2012).

2. Handoko, A. D. & Goh, G. K. L. Hydrothermal synthesis of sodium potassium niobate solid solutions at 200 °C. *Green Chem.* **12**, 680–68 (2010).

3. Lee, S., Liu, Z. K., Kim, M. H. & Randall, C. A. Influence of nonstoichiometry on ferroelectric phase transition in $BaTiO_3$. *J. Appl. Phys.* **101**, 1–8 (2007).

4. Li, M. *et al.* A family of oxide ion conductors based on the ferroelectric perovskite $Na_{0.5}Bi_{0.5}TiO_3$. *Nat. Mater.* **13**, 31–35 (2014).

5. Yang, F. *et al.* Defect chemistry and electrical properties of sodium bismuth titanate perovskite. *J. Mater. Chem. A* **6**, 5243–5254 (2018).

6. Ruf, T. *et al.* The influence on sintering and properties of sodium niobate ($NaNbO_3$) ceramics by “non-stoichiometric” precursor compositions. *Mater. Chem. Phys.* **229**, 437–447 (2019).

7. Shakhovoy, R. A. *et al.* Ferroelectric Q and antiferroelectric P phases’ coexistence and local phase transitions in oxygen-deficient $NaNbO_3$ single crystal: Micro-Raman, dielectric and dilatometric studies. *J. Raman Spectrosc.* **43**, 1141–1145 (2012).

8. Irvine, J. T. S., Sinclair, D. C. & West, A. R. Electroceramics: Characterization by Impedance Spectroscopy. *Adv. Mater.* **2**, 132–138 (1990).

9. Makuła, P., Pacia, M. & Macyk, W. How To Correctly Determine the Band Gap Energy of Modified Semiconductor Photocatalysts Based on UV-Vis Spectra. *J. Phys. Chem. Lett.* **9**, 6814–6817 (2018).

10. Guo, H., Shimizu, H., Mizuno, Y. & Randall, C. A. Strategy for stabilization of the antiferroelectric phase (Pbma) over the metastable ferroelectric phase (P21ma) to establish double loop hysteresis in lead-free (1-x)$NaNbO_3$ - x$SrZrO_3$ solid solution. *J. Appl. Phys.* **117**, 214103 (2015).

11. Masó, N., Woodward, D. I., Várez, A. & West, A. R. Polymorphism, structural characterisation and electrical properties of $Na_2Nb_4O_{11}$. *J. Mater. Chem.* **21**, 12096–12102 (2011).

12. Romeu, M. C. *et al.* Impedance spectroscopy study of TiO_2 addition on the ceramic matrix $Na_2Nb_4O_{11}$. *J. Mater. Sci. Mater. Electron.* **24**, 4993–4999 (2013).

13. Näfe, H., Amin, R. & Aldinger, F. Thermodynamic Characterization of the Eutectic Phase Mixture $NaNbO_3/Na_3NbO_4$. II: Solid-State Electrochemical Investigation. *J. Am. Ceram. Soc.* **90**, 3227–3232 (2007).

14. Liu, W. Dielectric and sintering properties of $NaNbO_3$ ceramic prepared by Pechini method. *J. Electroceramics* **31**, 376–381 (2013).

15. Shafer, M. W. & Roy, R. Phase equilibria in the system $Na_2O–Nb_2O_5$. *J. Am. Ceram. Soc.* **42**, 482–486 (1959).

16. Lee, B.-K., Chung, S.-Y. & Kang, S.-J. L. Grain boundary faceting and abnormal grain growth in $BaTiO_3$. *Acta Mater.* **48**, 1575–1580 (2000).

17. Megaw, H. D. The Seven Phases of Sodium Niobate. *Ferroelectrics* **7**, 87–89 (1974).

18. Lacorre, P., Goutenoire, F., Bohnke, O., Retoux, R. & Laligant, Y. Designing fast oxide-ion conductors. *Nature* **404**, 9–11 (2000).

19. Gouget, G. *et al.* Associating and Tuning Sodium and Oxygen Mixed-Ion Conduction in Niobium-Based Perovskites. *Adv. Funct. Mater.* **30**, 1–12 (2020).

Chapter 4. Chemically Doped Sodium Niobate Part 1 – A-Site

Chemical doping of perovskite materials can be utilised to help tailor the electrical properties. In the context of this work doping has typically been utilised to increase oxide ion conductivity in $NaNbO_3$ (NN).

Chemical doping of NN to increase oxide ion conductivity has previously been conducted *via* 2 alternative methods discussed in the literature review (chapter 1).

1. Doping of the A-site with bismuth – Lei *et. al.*[1]
2. Doping of the B-site with titanium – Gouget *et. al.*[2]

In both cases it is claimed that the chemical doping increases the concentration of oxygen vacancies in the ceramic. However, the doping mechanism utilised by Lei *et. al.* is one of A-site substitution where the charge is balanced and an increase in oxygen vacancies is not required:

$Na_{1-3x}Bi_xNbO_3$ – Mechanism: $3Na^+ = Bi^{3+}$

Figure 4.1 (a) shows how bismuth doped NN becomes a more regular perovskite compared to undoped NN as the octahedral tilting is eliminated. This elimination of the octahedral tilts is accompanied by a significant increase in bulk conductivity and a lowering of the activation energy associated with the conduction, Figure 4.1 (b).

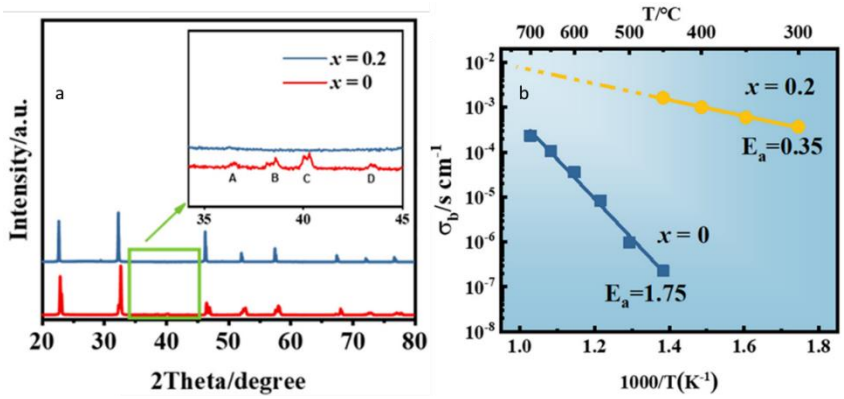

Figure 4.1: a) Elimination of Octahedral Tilting and b) Associated Increase in Bulk Conductivity in $Na_{1-3x}Bi_xO_3$ (Adapted from Lei et. Al.)[1]

Other studies on bismuth doped NN confirm the elimination of octahedral tilting in $Na_{0.4}Bi_{0.2}NbO_3$ and additionally showcase an associated drop in relative permittivity and increase in dielectric losses as the bismuth concentration increases up to x = 0.20 as shown in Figure 4.2.[3]

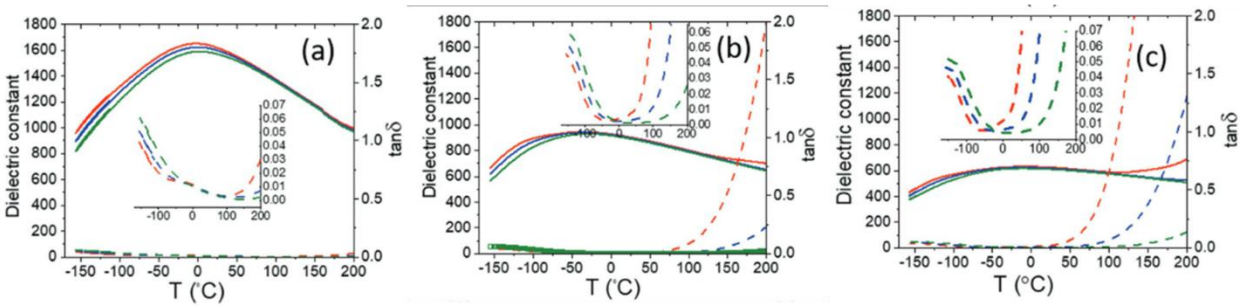

Figure 4.2: Influence of Bismuth Concentration on Dielectric Constant and losses in $Na_{1-3x}Bi_xO_3$ a) x=0.1 b) x=0.15 c) x=0.20 (Taken from Levin I et. al.)[3]

This suggests that any increases in ionic conductivity are resultant from the elimination of the octahedral tilting, the A-site metal vacancies, or a combination of both.[1,3]

The generation of A-site vacancies in NN has been investigated *via* calcium doping of the A-site *via* a similar method as bismuth shown above. It has been demonstrated that up to 20% of the A-site may be occupied by calcium ions. Below 10% calcium doping the antiferroelectric P-phase is stabilised (compared to the ferroelectric Q-phase) at room temperature. As the doping concentration increases the recoverable energy storage density increases, however the energy efficiency of the system decreases. Figure 4.3 shows the effect of increasing calcium content on the bipolar P-E loops.[4]

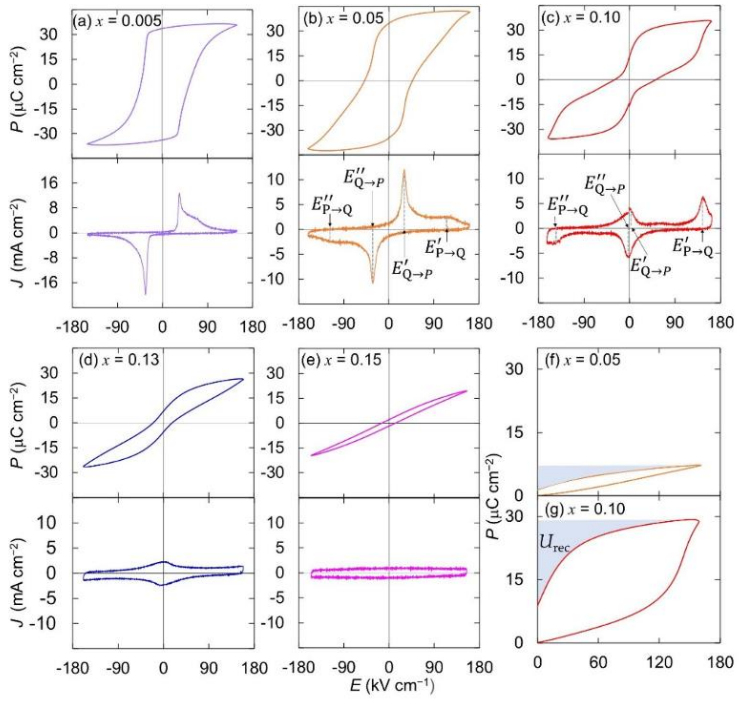

Figure 4.3: Bipolar P-E loops of $Na_{1-x}Ca_xNbO_3$ Ceramics (Taken from Aso S et. Al.)[4]

As the dopant concentration increases beyond x = 0.10 the antiferroelectric R-phase becomes stabilised at room temperature, minimising the P-Q AFE-FE phase transition utilised for energy storage.[4]

This chapter further explores how A-site doping influences the properties of NN ceramics.

4.1. A-Site Doped Sodium Niobate

The previous chapter detailed the effects of non-stoichiometry and metal vacancies on the physical and electrical properties of NN. However, any change to the stoichiometry in NN is also accompanied by a change in oxygen vacancy concentration.

2 Different mechanisms of A-site doping have been investigated:

Direct substitution of sodium with calcium:

$$2Na^{+} = Ca^{2+} \qquad (4.1)$$

1. 2.5% Ca NN - $Na_{0.95}Ca_{0.025}NbO_3$ – Na:Nb Ratio consistent with 49:51 NN
2. 5% Ca NN - $Na_{0.9}Ca_{0.05}NbO_3$ – Metal vacancy concentration consistent with 49:51 NN

Donor doping:

3. 1% Mg NN - $Na_{0.99}Mg_{0.01}NbO_{3+\delta}$

   Targeted Mechanism: $Na^{+} = Mg^{2+} + \frac{1}{2}O^{2-}$ (4.2)

4. 1% Ga NN - $Na_{0.99}Ga_{0.01}NbO_{3+\delta}$

   Targeted Mechanism: $Na^{+} = Ga^{3+} + O^{2-}$ (4.3)

The reagents used for each of the discussed compositions and their associated processing conditions are shown in table 1. All A-site doped NN variants were processed *via* a conventional solid-state method.

Composition	Reagents	Conditions Required for Single Phase Powders
2.5% Ca NN	Na_2CO_3 (99.98%) Nb_2O_5 (99.85%) $CaCO_3$ (>99%)	Calcined 900 °C 2 Hours Sintered 1350 °C 4 Hours
5% Ca NN	Na_2CO_3 (99.98%) Nb_2O_5 (99.85%) $CaCO_3$ (>99%)	Calcined 900 °C 2 Hours Sintered 1350 °C 4 Hours
1% Ga NN	Na_2CO_3 (99.98%) Nb_2O_5 (99.85%) Ga_2O_3 (>99.99%)	Calcined 900 °C 2 Hours Sintered 1240 °C 4 Hours
1% Mg NN	Na_2CO_3 (99.98%) Nb_2O_5 (99.85%) MgO (>99%)	Calcined 900 °C 2 Hours Sintered 1240 °C 4 Hours

Table 4.1: Compositions of A-Site Doped NN Variants with Reagents and Processing conditions

Doping *via* these methods will also allow for some understanding of the effects of ion size on the various properties of NN. The relevant ionic radii are shown below in table 4.2.

Ion	Ionic Radii / pm	Adjusted Tolerance Factor
Na^+	139	NN-0.967
Ca^{2+}	134	2.5% Ca NN - 0.955 5% Ca NN - 0.942
Mg^{2+}	89*	1% Mg NN – 0.965
Ga^{3+}	62*	1% Ga NN – 0.964

Table 4.2: Ionic Radii of Investigated Ions Extracted from R.D. Shannon[5] and Associated Tolerance Factors for NN Variants

*N.B.: Ionic Radii is Influenced by Coordination Number. If 12 Coordinate Radius is Unavailable the Highest Available Coordination Number has been Used as an Approximation. (Denoted by *)*

Although the size agreement between Na^+ and Mg^{2+}/Ga^{3+} ions is poor, there is existing evidence that A-site doping by an intermediate, rather than a large ion can occur in perovskites. An example of this phenomenon is manganese doping of $SrTiO_3$, where it is

well documented that up to 3 at% of Mn^{2+} ions dope onto the A-site despite poor size agreements (Sr^{2+}≈144 pm, Mn^{2+}≈96 pm)[5]. Even small amounts of the Mn^{2+} ion being incorporated onto the A-site leads to notable changes in the magnetism, dielectric properties, and incipient ferroelectric behaviour.[6–8]

As the A-site is doped with smaller ions the tolerance factor will decrease. Various scenarios can arise. Doping can lead to a change in room temperature polymorphism, variations in polymorphic phase transition temperatures and ultimately to instability of the perovskite phase. It has been demonstrated that decreasing the tolerance factor in NN favours the formation of the P-phase.[9]

4.1.1. Phase Purity and Crystal Structure

X-Ray Diffraction (XRD) has been used to assess the phase purity and polymorphism of A-site doped NN variants. For comparison the 'LP NN' powder discussed in chapter 3 is utilised. The XRD patterns for A-site doped variants are shown below in Figure 4.4.

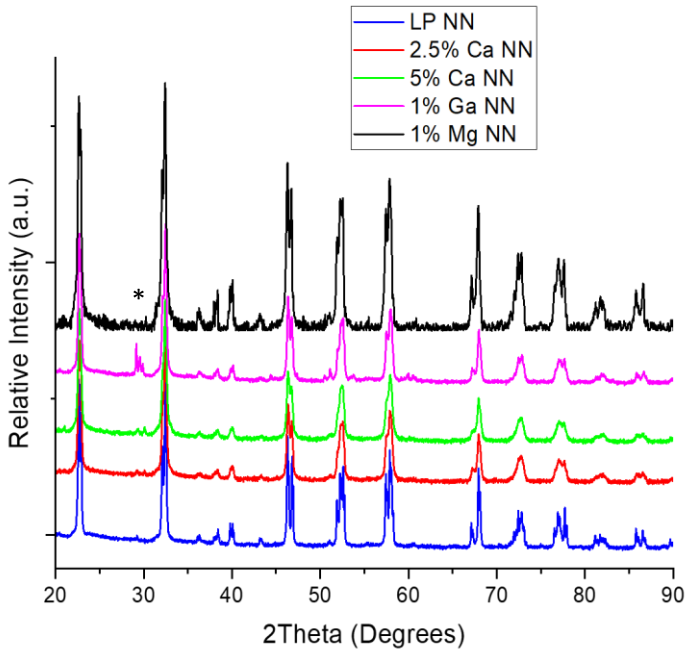

Figure 4.4: X-ray diffraction patterns of A-Site Doped NN Materials Compared to 'LP NN'.

A-site doped NN variants all appear as a mixture of the P (Pbma) and Q ($Pmc2_1$) phases of NN. After a single calcination the 5% Ca NN and 1% Ga NN materials show the presence of the niobium-rich secondary phase $Na_2Nb_4O_{11}$ (indicated by *). This secondary phase is eliminated during the sintering process without any significant changes to the unit cell. The XRD patterns of 1% Ga NN as a powder and sintered pellet are compared in Figure 4.5.

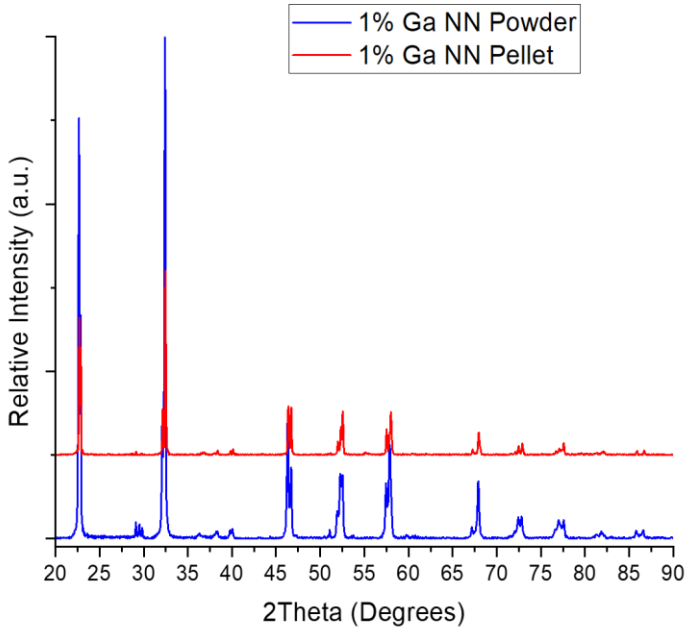

Figure 4.5: Comparison of X-Ray Diffraction Patterns for 1% Ga NN

The obtained XRD patterns have undergone Rietveld refinements to determine unit cell parameters and the ratio of P and Q phases. An example refinement of the 5% Ca NN XRD data is shown in Figure 4.6 and the refinement data for all A-site doped variants are tabulated below.

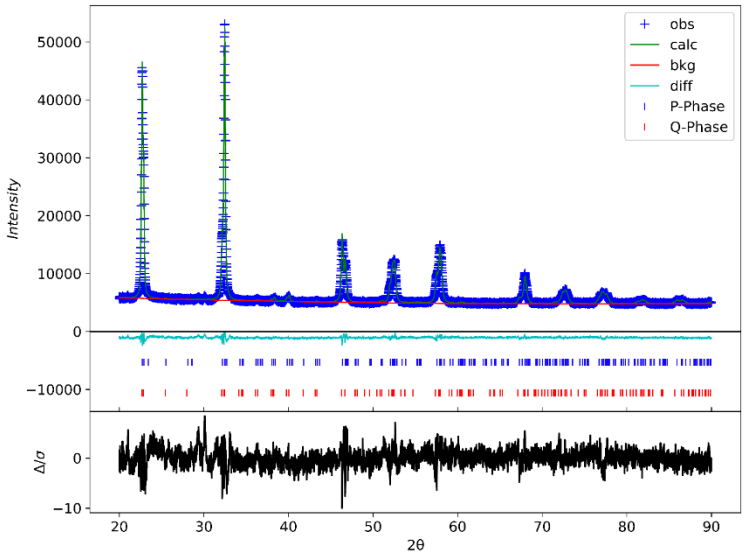

Figure 4.6: Example Rietveld Refinement of 5% Ca NN

	Parameters	LP NN	2.5% Ca NN	5% Ca NN	1% Ga NN	1% Mg NN
P Phase (Pbma)	a / Å	5.57450(6)	5.56680(19)	5.56047(25)	5.56412(17)	5.57055(19)
	b / Å	15.51670(17)	15.5274(4)	15.5344(6)	15.5298(4)	15.5344(5)
	c / Å	5.51674(7)	5.51144(18)	5.50861(26)	5.50679(18)	5.51113(21)
	Cell Volume / Å^3	477.18611(2)	476.39746(5)	475.82582(8)	475.83991(5)	476.90647(6)
	Phase Fraction	0.655(9)	0.833(6)	0.846(9)	0.906(8)	0.870(5)
Q Phase (Pmc21)	a / Å	7.75949(26)	7.7818(6)	7.7825(9)	7.7893(22)	7.7858(26)
	b / Å	5.56788(22)	5.5463(4)	5.5759(7)	5.5177(20)	5.5537(22)
	c / Å	5.51122(22)	5.5072(4)	5.5159(7)	5.5715(17)	5.5198(20)
	Cell Volume / Å^3	238.1062(7)	237.6918(1)	239.3594(2)	239.4576(5)	238.6761(6)
	Phase Fraction	0.345(9)	0.167(6)	0.154(9)	0.094(8)	0.130(5)
Residuals	R_w / %	2.935	2.180	2.163	3.812	11.818
	χ^2	8.95	2.91	2.81	15.23	2.69

Table 4.3: Summary of Rietveld Refinements for A-Site Doped NN Variants

The ratio of P and Q phases have been determined *via* the Rietveld refinements of the XRD data. This ratio is plotted below in Figure 4.7.

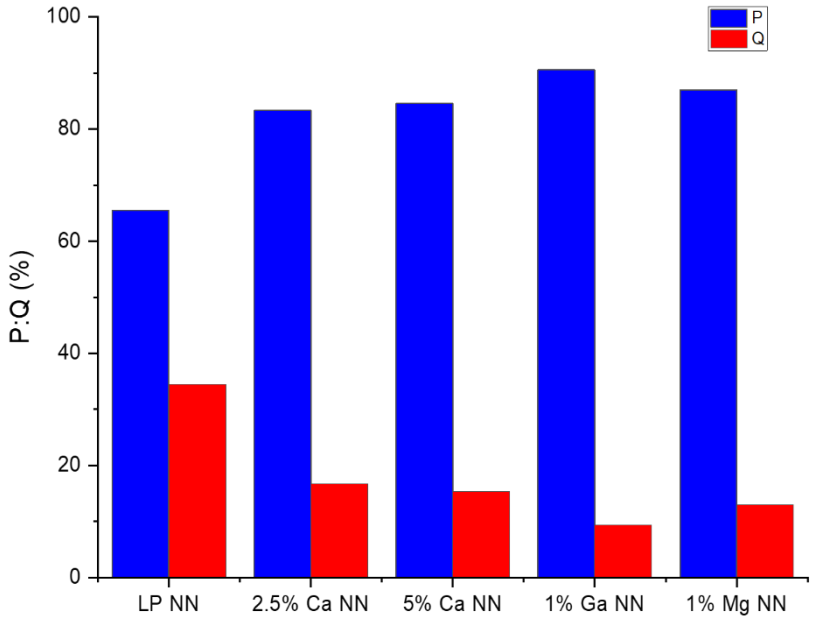

Figure 4.7: Ratio of P and Q Phases in A-Site Doped NN Variants Compared to 'LP NN'.

All A-site doped materials show a significant preference for P-phase NN with approximately 90% P-phase forming. As stated in the introduction to this chapter, the lower tolerance factor showcased by the calcium doped NN variants may be responsible for the increased formation of the P-phase.[9]

4.1.2. Microstructure

Sintered ceramics of each material have been investigated using SEM to understand the effects of various dopants on the observed ceramic microstructure. Where possible, average grain sizes and distributions have been determined. These results are shown below in Figure 4.8.

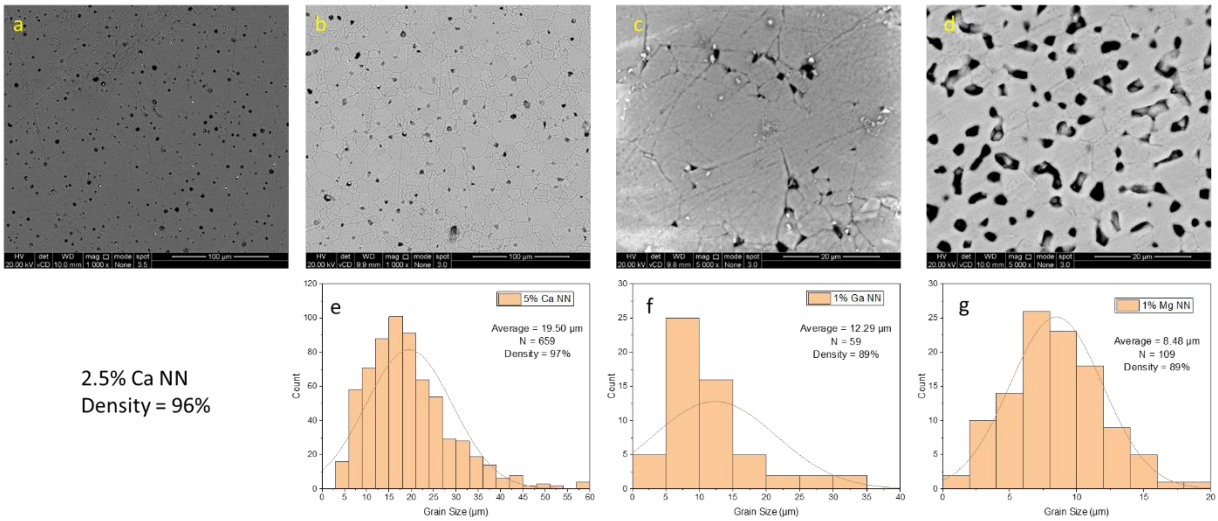

Figure 4.8: BSE Images of a) 2.5% Ca NN b) 5% Ca NN c) 1% Ga NN d) 1% Mg NN and Associated Grain Size Evaluations e) 5% Ca NN f) 1% Ga NN and g) 1% Mg NN

There is reasonable grain size agreement between 'LP NN' and the A-site donor doped ceramics (1% Ga/Mg NN) where magnesium doping delivered a slight decrease in grain size. Conversely, the 2.5% and 5% Ca NN ceramics appear to have a slight increase in grain size. The 2.5% Ca NN ceramic appears to have large grain sizes; however, the grain boundaries are not sufficiently defined to allow for formal analysis.

Calcium doped NN ceramics showcase the highest densities of >95% of the theoretical density, whereas the donor doped Ga/Mg NN ceramics exhibited densities more in line with the undoped NN ceramics discussed in the previous chapter (3.1.2.).

Both 1% Ga and 1% Mg NN ceramics appear to have flecks of a significantly lighter phase present distributed across the surfaces of the ceramics. EDS analysis of each sample has been used to assess the elemental distribution throughout the ceramics, this is shown in Figures 4.9-4.12.

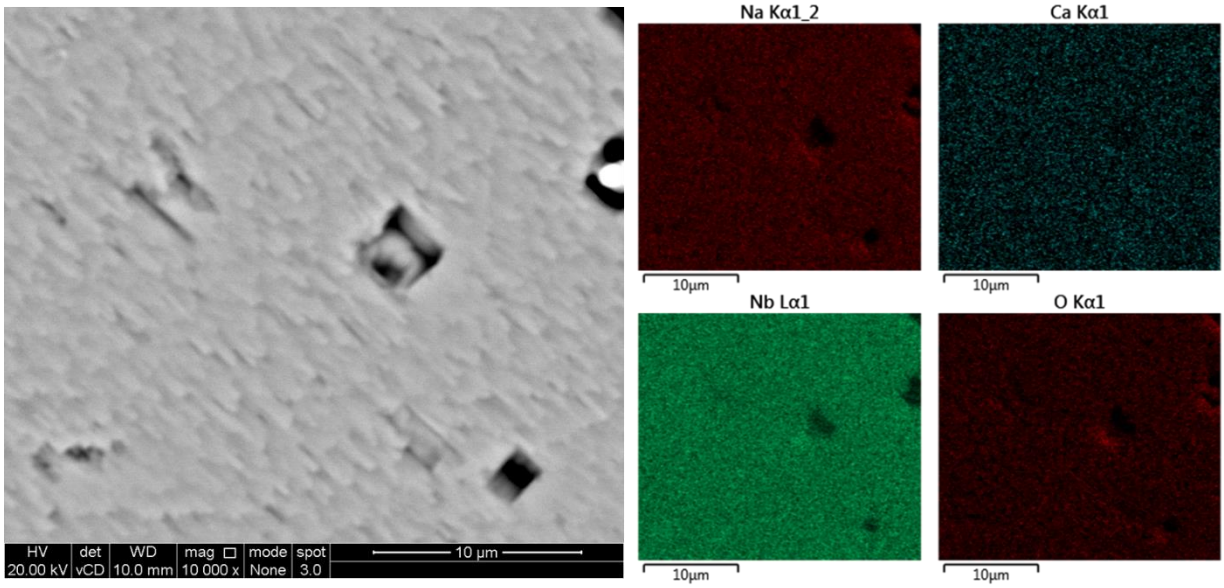

Figure 4.9: EDS Map of 2.5% Ca NN

The 2.5% Ca NN sintered ceramic shows a generally uniform distribution of all elements throughout the material. Any regions of the EDS map that appear to be deficient in elements can be attributed to a pore in the ceramic surface.

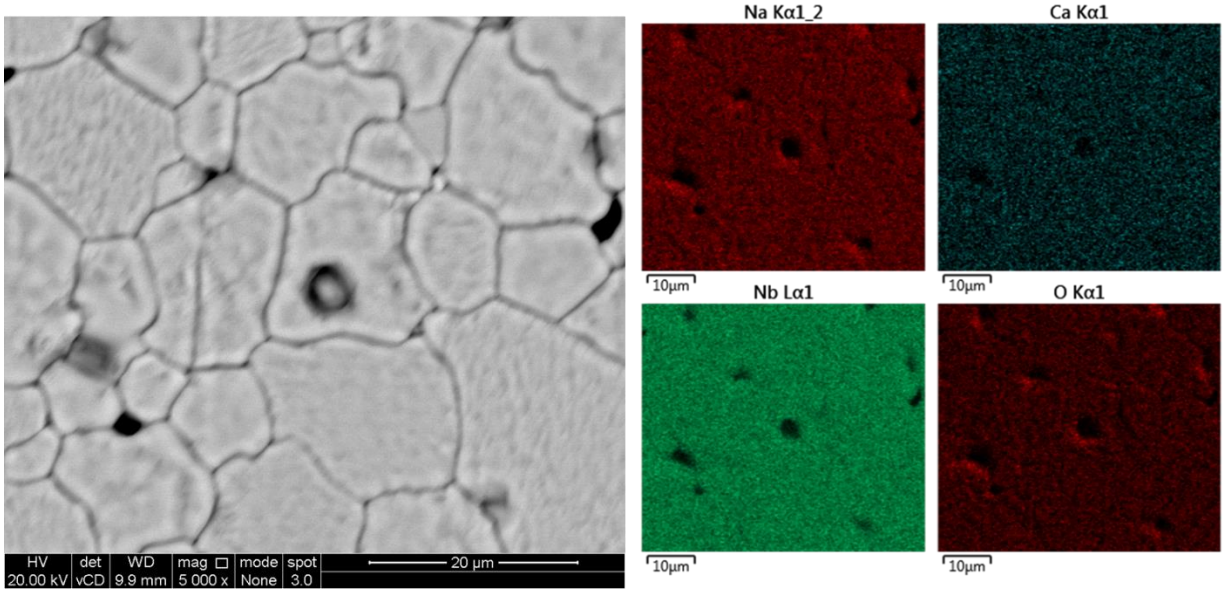

Figure 4.10: EDS Map of 5% Ca NN

The 5% Ca NN ceramic shows slight sodium deficiencies along some grain boundaries, likely attributed to sodium volatility during the sintering process. Other elements appear uniform across the entire ceramic.

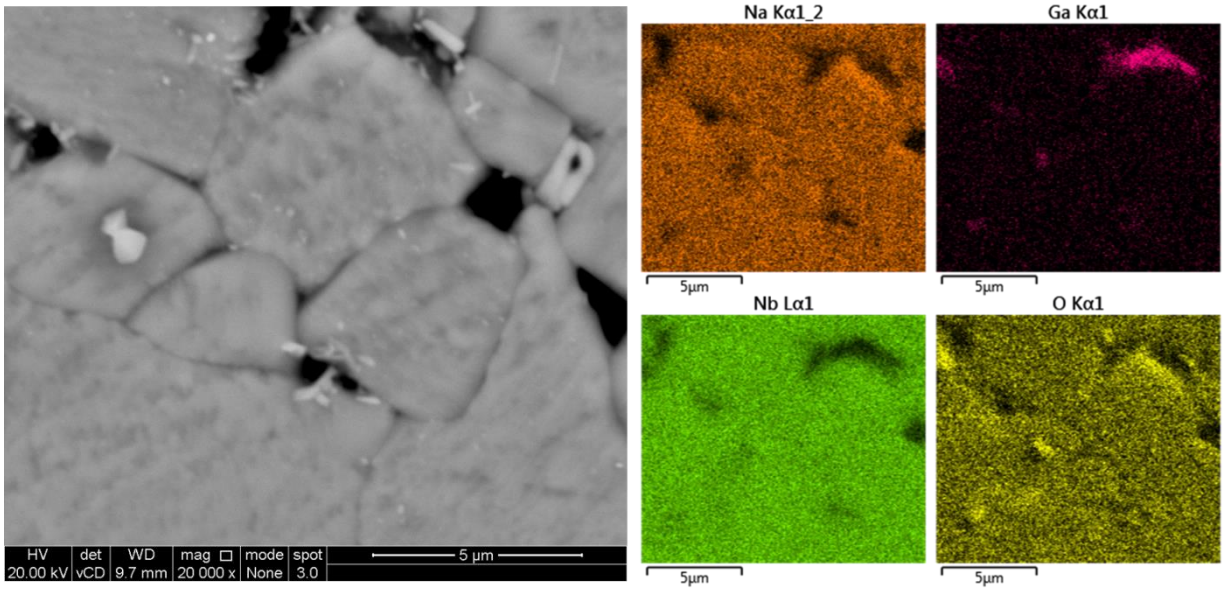

Figure 4.11: EDS Map of 1% Ga NN

The 1% Ga NN ceramic appears to have 2 different phases present. Sodium and niobium content appears consistent across the ceramic; however, gallium and oxygen have coinciding rich areas present in the map. The gallium and oxygen rich areas coincide with the 'lighter' areas in the BSE image. The lighter regions are attributed to unreacted Ga_2O_3 remaining on the surface of the ceramic.

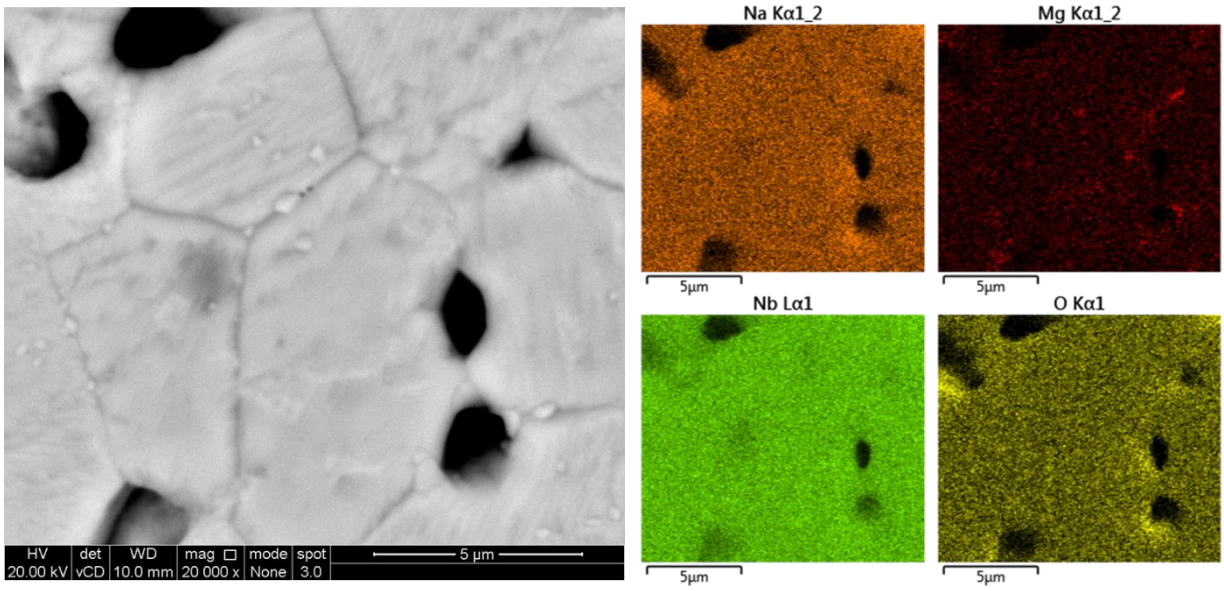

Figure 4.12: EDS Map of 1% Mg NN

The 1% Mg NN ceramic contains 2 different phases. Sodium and niobium content is consistent throughout the ceramic; however, as observed in 1% Ga NN there are magnesium and oxygen rich regions throughout the ceramic, the rich areas coincide with the

'lighter' areas in the BSE image, indicating they are due to unreacted MgO remaining on the surface of the ceramic.

Spot analysis has been conducted on grains and grain boundaries of the ceramics to determine compositional changes between grains and grain boundaries. The results of the spot analysis are summarised in table 4.4.

	Theoretical				Grain				Grain Boundary			
Composition	**Na / wt%**	**X / wt%**	**Nb / wt%**	**O / wt%**	**Na / wt%**	**X / wt%**	**Nb / wt%**	**O / wt%**	**Na / wt%**	**X / wt%**	**Nb / wt%**	**O / wt%**
LP NN	14.00	-	57.00	29.00	12.59 ± 0.03	-	61.03 ± 0.01	26.37 ± 0.03	12.38 ± 0.06	-	62.96 ± 0.01	24.67 ± 0.03
2.5% Ca NN	13.34	0.61	56.74	29.31	11.82 ± 0.02	0.68 ± 0.00	63.80 ± 0.01	23.83 ± 0.02	-	-	-	-
5% Ca NN	12.65	1.22	56.79	29.34	11.62 ± 0.02	1.32 ± 0.00	62.28 ± 0.01	24.82 ± 0.02	10.80 ± 0.02	1.28 ± 0.11	62.85 ± 0.01	25.03 ± 0.02
1% Ga NN	13.83	0.42	56.47	29.27	13.90 ± 0.01	0.00 ± 0.00	55.80 ± 0.01	30.25 ± 0.01	14.00 ± 0.1	0.00 ± 0.00	55.30 ± 0.30	30.70 ± 0.30
1% Mg NN	13.88	0.15	56.65	29.32	13.45 ± 0.01	0.15 ± 0.00	57.40 ± 0.01	29.00 ± 0.01	13.30 ± 0.10	0.00 ± 0.00	60.00 ± 0.30	26.70 ± 0.30

Table 4.4: Average Elemental Compositions of Grains and Grain Boundaries of A-Site Doped NN Ceramics (X=Ca/Ga/Mg)

Spot analysis of calcium doped variants of NN revealed the sodium content is notably lower than anticipated. This is most likely a consequence of sodium volatility during calcination/sintering of the ceramics. The variance observed in the bulk is somewhat in line with the sodium deficient ceramic 49:51 NN discussed in chapter 3. However, it is worth noting that the difference in sodium content between grains and grain boundaries in the calcium doped variants are significantly lower than the variance in the non-stoichiometric ceramic. Calcium content appears slightly greater than expected from the stoichiometry.

Spot analysis of the donor doped NN variants shows the sodium content is generally in line with the expected stoichiometries.

In 1% Ga NN the gallium content in grains and grain boundaries appears to be zero indicating that if any gallium has been integrated into the crystal structure it is below the detection limit for SEM-EDS analysis. The composition of the grains and grain boundaries in 1% Ga NN is consistent.

Conversely, the 1% Mg NN ceramic showcases the magnesium content in grains is as expected from the target stoichiometry. In grain boundaries however, the magnesium content appears to be zero. All other stoichiometries in the ceramic are as expected and consistent between grains and grain boundaries.

4.1.3. Relative Permittivity and Dielectric Losses

The temperature dependence of the relative permittivity and dielectric losses of A-site doped NN variants have been determined and compared against the 'LP NN' ceramic. The relative permittivity plots versus temperature are shown in Figure 4.13.

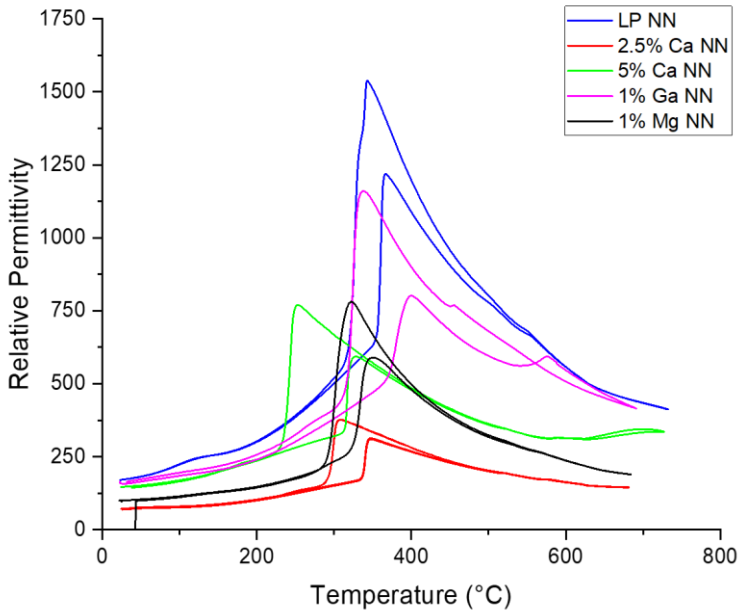

Figure 4.13: Relative Permittivity of A-Site Doped NN Variants Compared to 'LP NN' (Taken at 100 kHz)

The relative permittivity of A-site doped NN continues to show the characteristic peak in permittivity around the P-R phase transition. As observed with non-stoichiometric variants, the temperature of the transition shifts significantly with small changes in composition. The observed maximum permittivity of all A-site doped variants is significantly lower than 'LP NN' with calcium doped NN showcasing the lowest permittivity's.

Table 4.5 shows the change in T_{Max} on heating and cooling and the maximum permittivity for each of the A-site doped NN variants.

Composition	T_{max} (Heating) / °C	$\varepsilon_{r_{Max}}$(Heating)	T_{max} (Cooling) / °C	$\varepsilon_{r_{Max}}$(Cooling)	Ionic Radii of Dopant
LP NN	371	1219	344	1538	-
2.5% Ca NN	347	313	307	376	134
5% Ca NN	326	593	252	770	134
1% Ga NN	399	801	337	1160	62*
1% Mg NN	349	590	322	782	89*

Table 4.5: Change in T_{Max} on Heating and Cooling with Associated Maximum Permittivity (ε_r) Compared to Size of A-Site Dopant

Increasing the amount of the dopant calcium causes a notable shift to lower T_{Max} on both heating and cooling indicating stabilisation of the higher temperature R-phase.

The NN ceramics with comparable dopant concentrations (2.5% Ca, 1% Mg/Ga) do not showcase a significant shift in the hysteresis, however the maximum permittivity does showcase significant variance, with the permittivity increasing as the dopant ions radius decreases.

The dielectric losses of A-site doped NN variants are shown in the Figure 4.14.

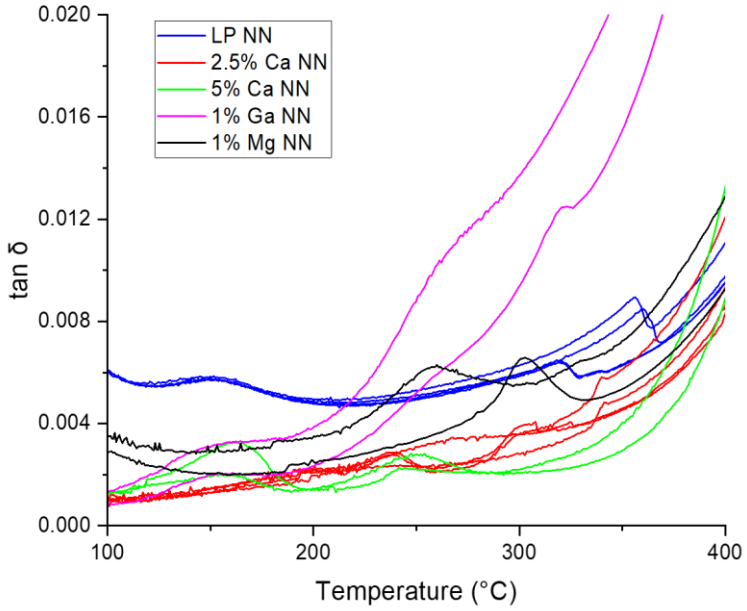

Figure 4.14: Dielectric Losses of A-Site Doped NN Variants Compared to 'LP NN' (Taken at 100 kHz)

The dielectric losses for A-site doped NN variants are generally very low and do not increase compared to LP NN with maximum losses occurring around the P-R phase transition of <1%. Beyond 400 °C space charge effects begin to dominate, and losses increase rapidly.

The exception to this is the 1% Ga NN ceramic, the losses initially start low, and in line with other A-site doped NN variants and showcases the characteristic bump indicating the conversion between Q and P phase around 150 °C. After this conversion the dielectric losses increase steadily and quickly overtake LP NN although no significant peak is observed around the P-R phase transition.

4.1.4. Impedance Spectroscopy

The electrical properties of A-site doped NN variants have been investigated *via* impedance spectroscopy to determine the effects of varying vacancy concentrations and microstructural changes on conductivity in the ceramic. The overlaid M''/Z'' plots for the investigated ceramics are shown in Figure 4.15.

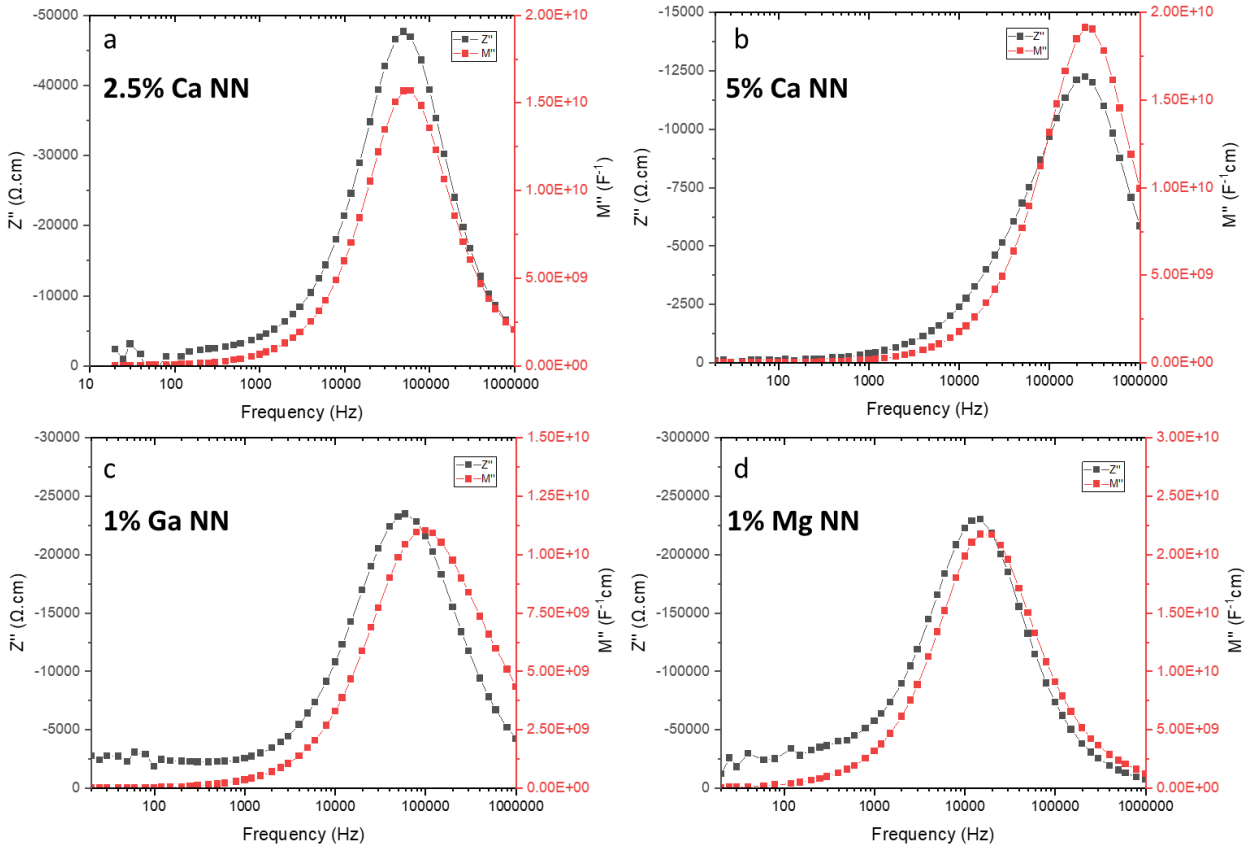

Figure 4.15: M'' Z'' Plots of a) 2.5% Ca NN b) 5% Ca NN c) 1% Ga NN and d) 1% Mg NN Ceramics at ~620°C

Composition	Capacitance (Z'') / F cm^{-1}	Capacitance (M'') / F cm^{-1}	F_{max}(M'') / kHz	Corresponding Response
LP NN	$5.1(4) \times 10^{-11}$	$4.5(2) \times 10^{-11}$	8.00	Bulk
2.5% Ca NN	$3.3(2) \times 10^{-11}$	$3.2(2) \times 10^{-11}$	60.0	Bulk
5% Ca NN	$2.6(2) \times 10^{-11}$	$2.6(1) \times 10^{-11}$	250	Bulk
1% Ga NN	$6(1) \times 10^{-11}$	$4.5(2) \times 10^{-11}$	100	Bulk
1% Mg NN	$2.3(2) \times 10^{-11}$	$2.3(1) \times 10^{-11}$	15.0	Bulk

Table 4.6: Tabulated Capacitances Extracted from M'' and Z'' Responses in Figure 4.15

All investigated A-site doped ceramics show single peaks in the M'' and Z'' plots generally corresponding to a single RC element, with capacitance indicative of a bulk electrical response.[10] The exception is 5% Ca NN which contains a slight 'shoulder' in the Z'' response, indicating the presence of a second RC element. Accurate determination of f_{max}

for this secondary response is challenging due to poor resolution of the peak. An additional plateau is observed in the C' vs frequency plot shown in Figure 4.16.

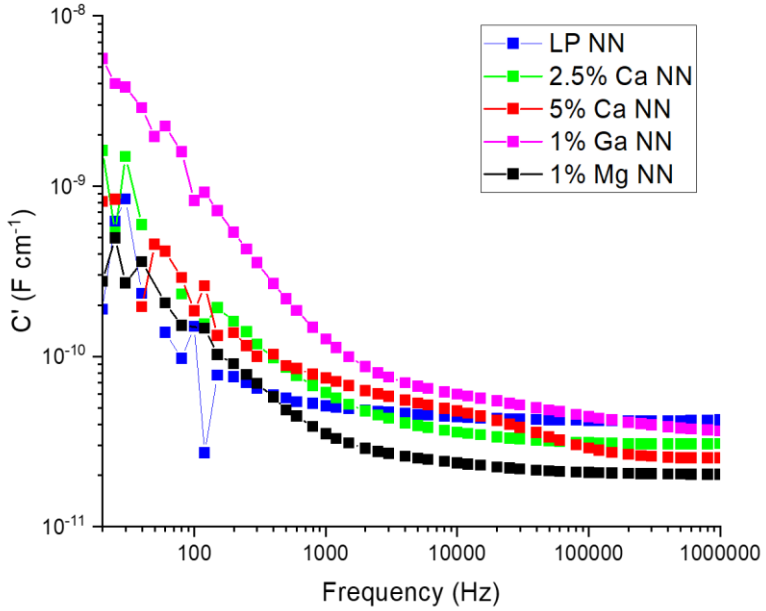

Figure 4.16: C' vs Frequency Plot of A-Site Doped NN Ceramics at ~620 °C

5% Ca and 1% Ga NN ceramics showcase additional plateaus in the C' plot, suggesting the presence of a second RC element, most likely due to a slightly more resistive grain boundary response that is poorly resolved due to similar time constants.

All A-site doped ceramics, despite showing no significant increase in low frequency response in the Z'' plane, there is an obvious increase in capacitance at low frequencies indicating low levels of ionic conductivity.

The bulk conductivities of A-site doped ceramics have been extracted from the M'' peaks and are shown in the Arrhenius plot in Figure 4.17.

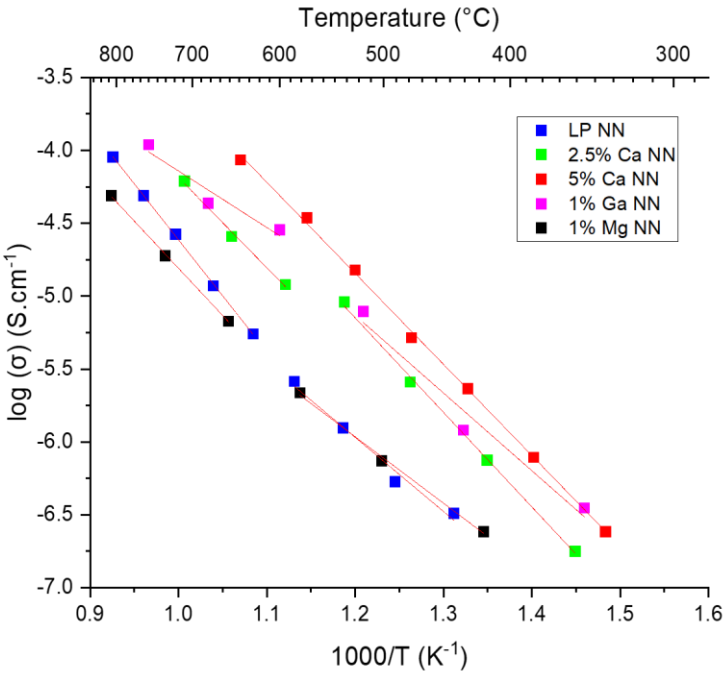

Figure 4.17: Arrhenius Plots of Bulk Conductivity for A-Site Doped NN Variants

A-site doped NN ceramics generally show a slight increase in conductivity compared to the 'LP NN' ceramic. The only exception to this is the magnesium doped variant which exhibits near identical conductivity to the 'LP NN' ceramic. The activation energies have been extracted from the Arrhenius plots of bulk conductivity and are shown in table 4.7.

Composition	Low Temperature Ea /eV	High Temperature Ea / eV
LP NN	1.01 ± 0.10	1.52 ± 0.02
2.5% Ca NN	1.29 ± 0.03	1.23 ± 0.10
5% Ca NN	1.24 ± 0.02	-
1% Ga NN	1.06 ± 0.18	0.77 ± 0.21
1% Mg NN	0.90 ± 0.05	1.29 ± 0.03

Table 4.7: Activation Energies Extracted from Arrhenius Plots of Bulk Conductivity (Figure 4.17)

The calcium doped NN ceramics exhibit very similar activation energies that are generally consistent at high and low temperatures.

The pO_2 dependence of A-site doped NN ceramics has been assessed and is shown below in Figures 4.18 and 4.19.

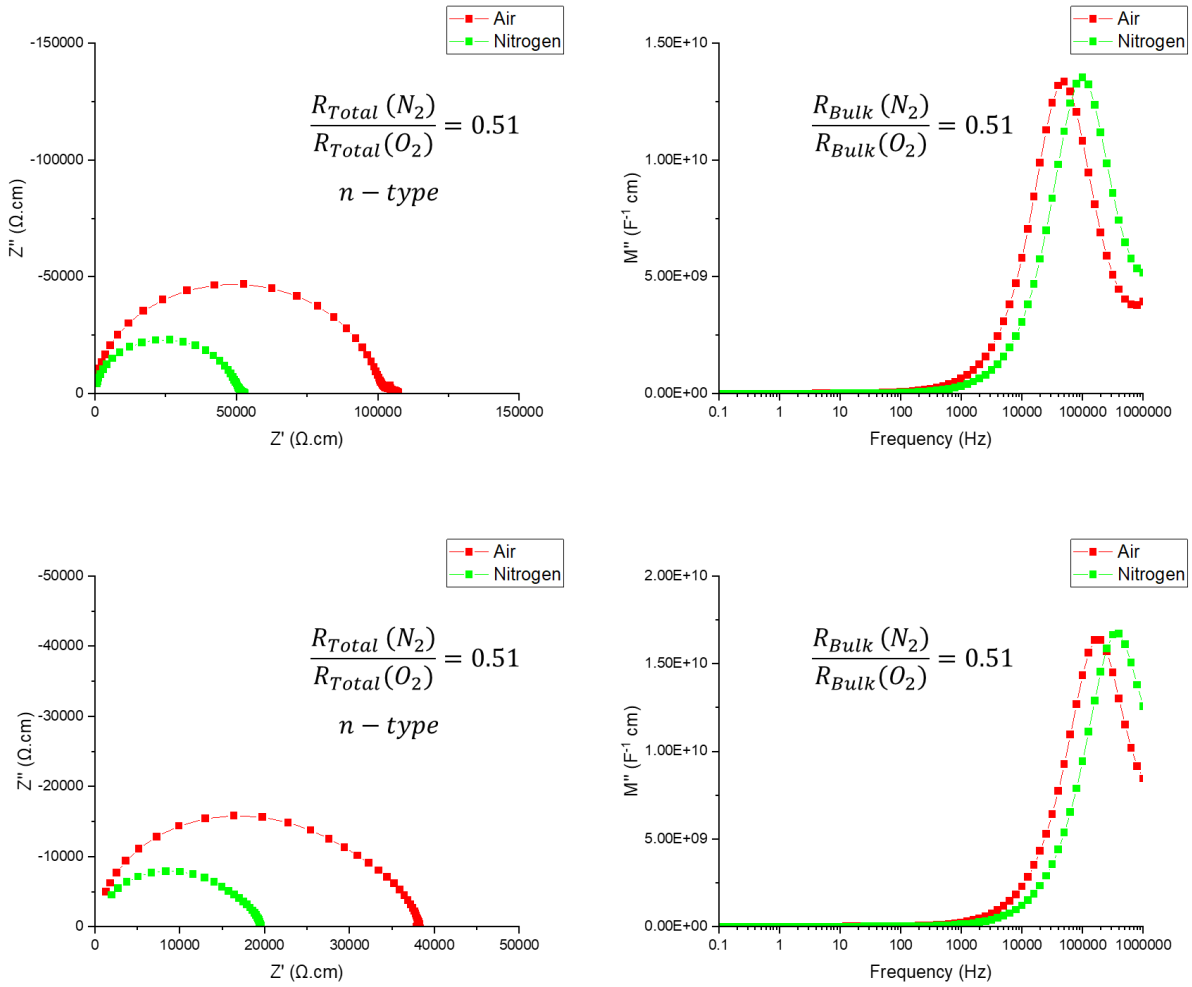

Figure 4.18: pO_2 Dependence of 2.5% Ca NN (Top) and 5% Ca NN (Bottom) Ceramics at 600 °C

The resistivity of the calcium doped ceramics decreases with pO_2 indicating the presence of n-type conductivity. In both cases this effect is fully attributed to the bulk electrical response as f_{max} shifts to higher frequencies as pO_2 decreases. The magnitude of the n-type conductivity is consistent between both ceramics.

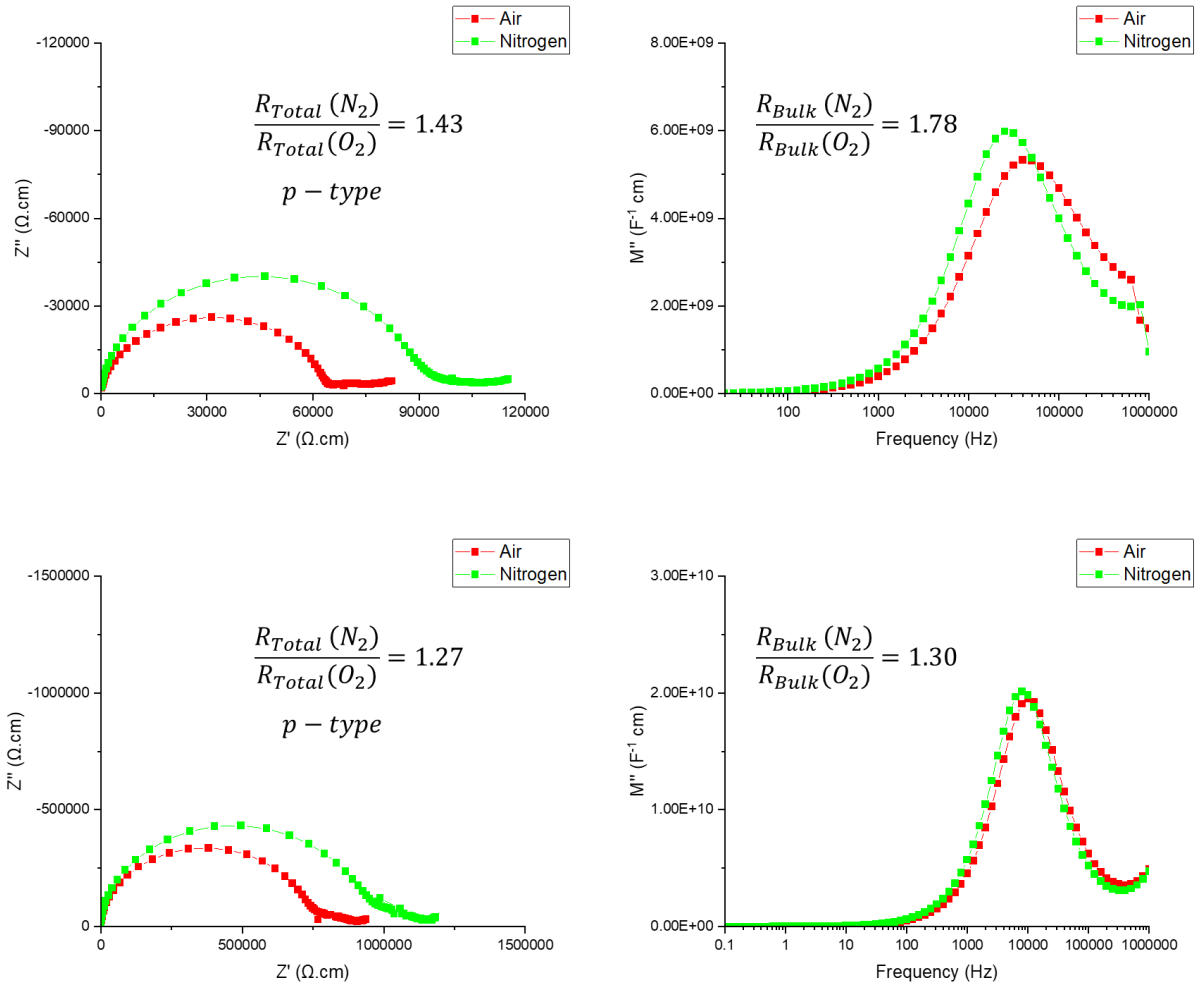

Figure 4.19: pO_2 Dependence of 1% Ga NN (Top) and 1% Mg NN (Bottom) Ceramics at 600 °C

In the A-site donor doped NN ceramics the total resistivity increases as the pO_2 decreases, indicating that the ceramics exhibit p-type conductivity. This pO_2 dependence is attributed to the bulk electrical response in each. The gallium doped ceramic exhibits a greater degree of p-type conductivity compared to the magnesium doped ceramic in the bulk response.

4.2. Discussion

4.2.1. Effects of A-Site Doping on Polymorphism and Microstructure

Figure 4.7 showcases a notable decrease in the concentration of the Q-phase in all A-site doped NN variants. This is consistent with existing literature indicating that decreasing the tolerance factor of NN causes the AFE P-phase to be stabilised.[4,9] However, as shown in table 4.2 the tolerance factor for the Ga/Mg Doped NN variants decreases by ~0.001, which is unlikely to have any meaningful impact on the phase stability of NN. It is therefore likely that the decrease in Q-phase concentration is a consequence of the doping mechanism reducing the amount of oxygen vacancies present in the ceramics.[11]

The microstructure of calcium doped NN showcases a notable improvement compared to undoped NN variants with a density increase of ~5% compared to the stoichiometric variants discussed in chapter 3. EDS spot analysis has been used to evaluate the elemental composition of the A-site doped NN variants. Table 4.4 shows that calcium and magnesium contents of the grains are approximately in line with the expected stoichiometry, whereas the 1% Ga NN ceramic appears to have very little gallium present outside of unreacted Ga_2O_3 (Figure 4.11) suggesting that if any gallium has been incorporated into the crystal structure, the limits of the solid solution are less than 1% for A-site doping.

4.2.2. Effects of A-Site Doping on Permittivity

The effect of A-site doping on the relative permittivity of NN ceramics is significantly more pronounced than what was observed with Na:Nb non-stoichiometry (discussed in chapter 3). Figure 4.20 and table 4.8 show the change in temperature where ε_r is at a maximum (T_{Max}) on heating and cooling.

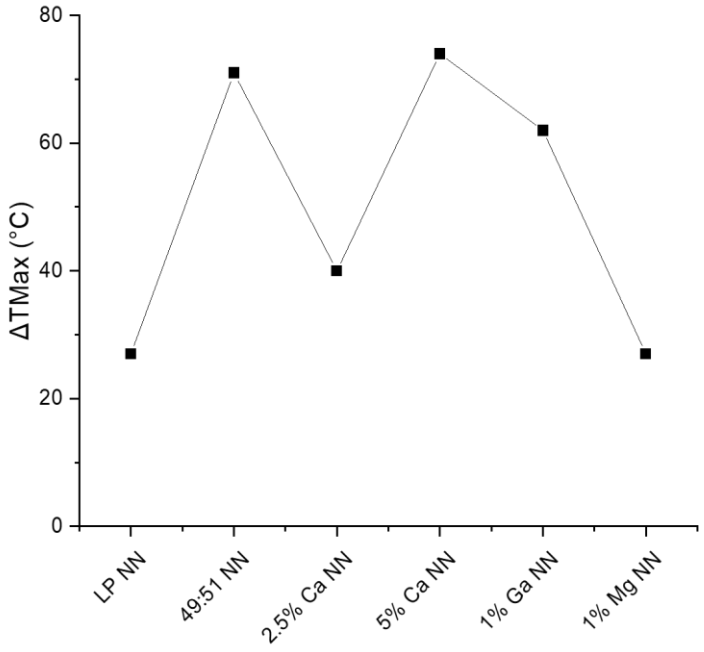

Figure 4.20: Change in ΔT_{Max} of A-Site Doped NN Ceramics

Composition	T_{max} (Heating) / °C	T_{max} (Cooling) / °C	ΔT_{Max} / °C	P-Phase / %	Q-Phase / %
LP NN	371	344	27	66	34
49:51 NN	402	331	71	93	7
2.5% Ca NN	347	307	40	83	17
5% Ca NN	326	252	74	85	15
1% Ga NN	399	337	62	91	9
1% Mg NN	349	322	27	87	13

Table 4.8: Comparison of T_{Max} on Heating and Cooling in A-Site Doped NN Ceramics (σ_T = ±0.5°C)

All A-site doped variants of NN exhibit a greater ΔT_{Max} than LP NN with the exception of 1% Mg NN where the change is identical, indicating that A-site doping of NN leads to some broadening of the hysteresis (shown in Figure 4.13).

The calcium doped variants as stated in the introduction of this chapter were selected to maintain the Na:Nb ratio (2.5% Ca) and maintain the concentration of A-site vacancies in the ceramic (5% Ca). Figure 4.20 shows that the primary cause for the broadening of the hysteresis in A-site deficient NN is due to the concentration of A-site vacancies. As the concentration of A-site vacancies decreases the hysteresis narrows. The larger hysteresis exhibited by the 1% Ga NN system is indicative of the unreacted Ga_2O_3 distributed through the ceramic (shown in Figure 4.11) and in turn the higher concentration of A-site vacancies than initially targeted.

The 1% Mg NN ceramic, exhibits no change in the hysteresis compared to LP NN, suggesting that there is no significant change in the A-site vacancy concentration.

All A-site doped NN ceramics additionally showcase a shift in the P-R phase transition. Calcium doped NN ceramics display the most notable shift to lower temperatures particularly on cooling, indicating a stabilisation of the higher temperature R-phase. This is consistent with existing literature that shows the R-phase to be fully stabilised at room temperature in calcium doped NN where calcium concentrations exceed 13%.[4] To a lesser extent this R-phase stabilisation is observed in the 1% Mg NN ceramic. Conversely, the 1% Ga NN ceramic showcases a shift to higher temperatures indicating a stabilisation of the lower temperature P-phase on heating, with minimal impact on cooling.

4.2.3 Effects of A-Site Metal Vacancies (Calcium Doped NN)

Substitution of the A-site sodium for calcium has been conducted to further evaluate the effects of A-site metal vacancies beyond the non-stoichiometric NN work presented in the previous chapter. The goal was to insert calcium for charge balance to minimise oxygen vacancies in the ceramic while maintaining the same Na:Nb ratio/concentration of A-site vacancies as the 49:51 NN ceramic discussed in chapter 3. The Arrhenius plot shown in Figure 4.21 compares calcium doped NN to the sodium deficient 49:51 NN ceramic.

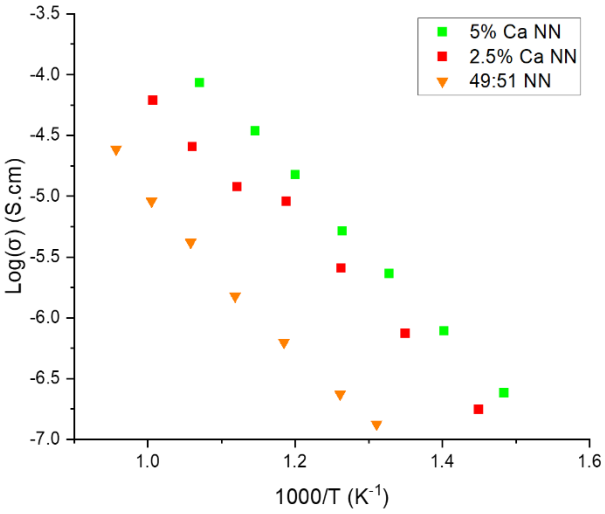

Figure 4.21: Arrhenius Plots of Bulk Conductivity for A-site Deficient NN Ceramics

Substitution of calcium to the system causes an increase in bulk conductivity compared to a non-stoichiometric approach, this is in spite of utilising a doping mechanism to minimise the concentrations of oxygen vacancies. Additionally, the low frequency capacitance spikes remain in the C' *vs* frequency plot shown in Figure 4.22.

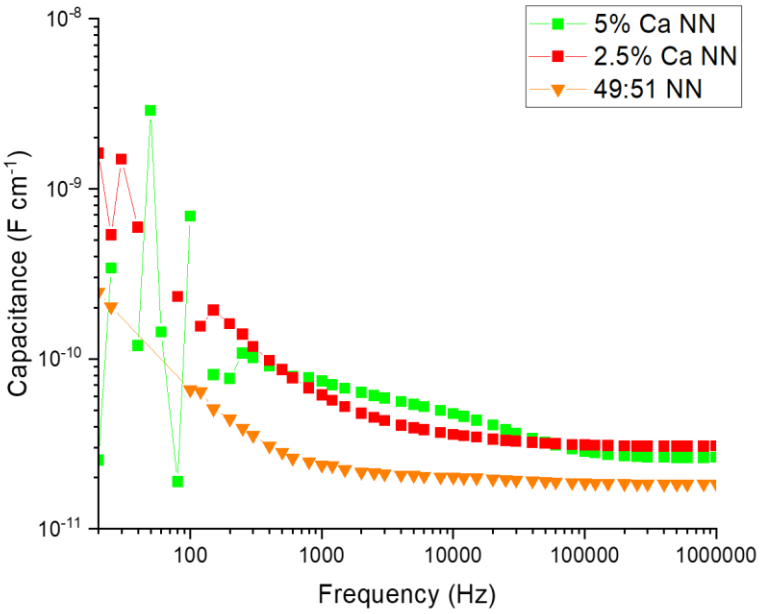

Figure 4.22: C' vs Frequency Plot of A-Site Deficient Ceramics at ~600 °C

The increasing capacitance at lower frequencies indicates that all A-site deficient ceramics maintain some level of ionic conductivity. This may be due to sodium ion conductivity

through the vacant A-sites or alternatively it may be due to minimal oxygen vacancies remaining in the material. This may occur based on an alternative doping mechanism:

1. Targeted generation of A-site vacancies: $2Na^{+} = Ca^{2+}$ (4.4)
2. Alternative filling of oxygen vacancies: $Na^{+} = Ca^{2+} + \frac{1}{2}O^{2-}$ (4.5)

Mechanism 2 would result in some oxygen vacancies remaining in the material for charge balance due to non-stoichiometry. As previously discussed in chapter 3 and existing literature, the generation of the Q-phase may be somewhat indicative of a greater concentration of oxygen vacancies within the material.[11] Figure 4.23 compares the P:Q ratios of the A-site deficient NN ceramics.

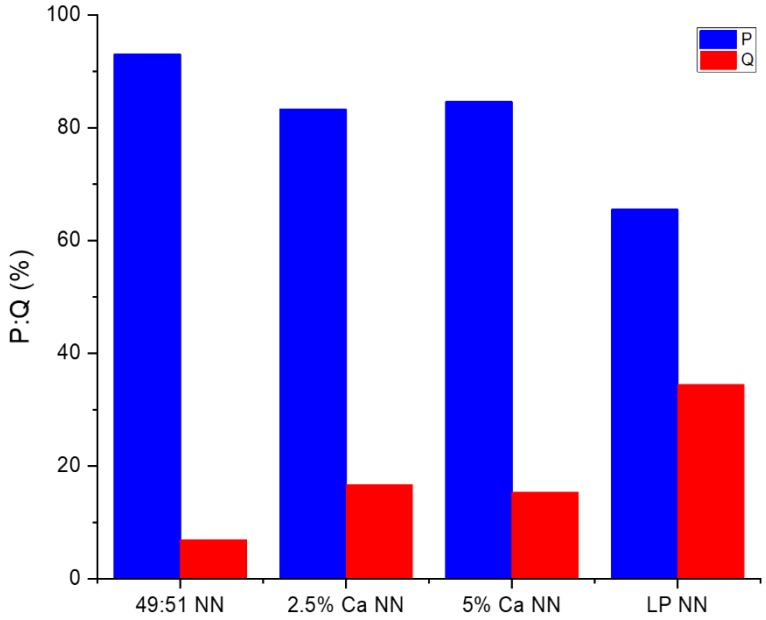

Figure 4.23: P:Q Ratios of A-Site Deficient NN Ceramics

The P:Q ratio of calcium doped NN is significantly greater than observed in the stoichiometric LP NN ceramic. However, the 49:51 NN ceramic showcases an even greater preference for the P-phase. This may occur due to either, a greater concentration of oxygen vacancies in the ceramic (compared to 49:51 NN) causing increased generation of the Q phase.[11] Alternatively, as discussed in the introduction this may be a result of the change in polymorphic phase stability due to decreased tolerance factor. As table 4.2 shows the tolerance factors for 2.5% Ca and 5% Ca NN ceramics are 0.955 and 0.942, respectively. The tolerance factor for the 49:51 NN ceramic is 0.943, the lower tolerance factors are reflected in greater stabilisation of the P phase.

The activation energy of conductivity for the calcium doped NN ceramics at high temperatures is lower than for 49:51 NN indicating a change in conduction mechanism. As the transport number for the 49:51 NN ceramic was generally very low, the change in conduction mechanism and increased conductivity of the calcium doped NN is likely due to increased contributions from ionic (presumably sodium) ion conduction.

4.2.4. Effects of A-Site Donor Doping (Gallium/Magnesium Doped NN)

The magnesium doped NN ceramic exhibited no significant change in the lower temperature conductivity as the LP NN ceramic, as shown in Figure 4.17, although in the higher temperature domain (>600 °C) the activation energy decreases indicating that the conduction mechanism has changed. This may be indicative of the lessened contribution from oxide ions due to filling of the oxygen vacancies according to the target mechanism:

$$Na^{+} = Mg^{2+} + \frac{1}{2}O^{2-} \qquad (4.6)$$

Although this mechanism would suggest an increase in activation energy as the system moves towards intrinsic electrical conduction. As there is good evidence for the incorporation of magnesium into the ceramic structure, in particular from the SEM spot analysis and the change in T_{Max} from the LCR data, it is possible that magnesium doping has led to a reduction of the band gap. This could be further investigated *via* UV-Vis spectroscopy as demonstrated in section 3.1.5.

Doping with gallium leads to a slight increase in conductivity compared to LP NN with a notable drop in activation energy in the higher temperature region of the Arrhenius plot (table 4.6). This increase in conductivity is likely a consequence of the increased dielectric losses shown in Figure 4.14. However, the target mechanism should show similar results as the magnesium doping.

$$Na^{+} = Ga^{3+} + O^{2-} \qquad (4.7)$$

The observed increase in conductivity is likely a consequence of A-site vacancies caused by a low solid solution limit. Table 4.4 showcases that the gallium content within the ceramic is significantly lower than expected, with unreacted Ga_2O_3 remaining on the surface of the ceramic. Therefore, due to the targeted stoichiometry there will likely be an increase in A-site vacancies leading to a gain in conductivity similar to calcium doped NN as shown in Figure 4.17.

4.2.5. pO_2 Dependence of A-Site Doped NN

The pO_2 dependence of A-site doped NN ceramics shown in Figures 4.18 and 4.19 are summarised in table 4.9 and compared to LP NN and 49:51 NN ceramics discussed in chapter 3.

Composition	$\frac{R_{Total}(N_2)}{R_{Total}(O_2)}$	Total Observed Response	$\frac{R_{Bulk}(N_2)}{R_{Bulk}(O_2)}$	Bulk Observed Response
LP NN	0.96	n	0.99	Independent
49:51 NN	0.62	n	0.63	n
2.5% Ca NN	0.51	n	0.51	n
5% Ca NN	0.51	n	0.51	n
1% Ga NN	1.43	p	1.78	p
1% Mg NN	1.27	p	1.30	p

Table 4.9: Summarised pO_2 Dependence of A-Site Doped NN Ceramics

The calcium doped NN ceramics showcase the exact same pO_2 dependence, furthermore this dependence is in line with the sodium deficient 49:51 NN ceramic where n-type conductivity is observed. As stated in chapter 3, this n-type conductivity is likely a consequence of oxygen loss and subsequent reduction of the niobium ions:

$$O^{2-} \rightarrow \frac{1}{2}O_2 + 2e^- \qquad (4.8)$$

$$2Nb^{5+} + 2e^- \rightarrow 2Nb^{4+} \qquad (4.9)$$

The presence of A-site vacancies in the ceramics may encourage oxygen loss in NN as a mechanism for charge balance as sodium volatility increases.

The 1% Ga/Mg NN ceramics exhibit p-type conductivity, with the 1% Ga NN ceramic showcasing a greater pO_2 dependence. P-type conductivity indicates oxidation of an ion within the NN ceramic, as sodium (+1), niobium (+5), and both dopant metals exist in their highest oxidation states in NN the p-type conductivity must be a consequence of either:

1. Extrinsic effects/Impurities within the ceramic
2. Holes on the oxygen sites

As the p-type conductivity in 1% Mg NN is linked to the bulk response it is likely that it originates from holes on the oxygen sites:[12]

$$O^{2-} + h^+ \rightarrow O^- \qquad (4.10)$$

The pO_2 dependence of the 1% Ga NN is likely also linked to this mechanism. The greater disparity between the total pO_2 dependence and the bulk pO_2 dependence is likely a consequence of increased secondary phase in the ceramic in the form of unreacted Ga_2O_3 as observed in the SEM images in Figure 4.11.

4.3. Conclusions

The A-site of NN has been successfully doped according to 2 distinct mechanisms. A-site calcium doping of NN is well documented[4,9] and the work presented in this chapter builds on the existing literature. Calcium doped NN variants show significant stabilisation of the higher temperature R-phase with increasing dopant concentration. Additionally, as A-site vacancies increase with calcium content the bulk conductivity increases. Ionic conductivity is present in the ceramics. Given the target mechanism, the concentration of oxygen vacancies should be negligible suggesting that the most likely origin of the ionic conductivity is sodium ions through the vacant A-sites.[13]

The incorporation of an ion as small as Mg^{2+} into NN is not currently reported in the literature. However, as stated in the introduction, the incorporation of low levels of Mn^{2+} on the significantly larger Sr^{2+} sites in $SrTiO_3$ has undergone significant investigation.[7] Although the low temperature conductivity of 1% Mg NN is generally consistent with the stoichiometric LP NN ceramic, the high temperature activation energy decreases. The low temperature Arrhenius plot is unchanged, indicating that the more extrinsic conduction mechanism shown at lower temperatures remains consistent; however, the decrease in the higher temperature activation energy is attributed to a decrease in the band gap, although further investigation is required to confirm this suggestion.

As the tolerance factor of gallium and magnesium doped NN ceramics are generally consistent with undoped NN, the increased preference for the P-phase is likely indicative of successful donor doping to reduce the concentration of oxygen vacancies in NN.[11]

While the evidence presented in this chapter for successful A-site doping with gallium is tenuous, there is further evidence of A-site gallium doping discussed in chapter 6. Where the doping mechanism of NN are explored further by targeting the B-site.

4.4. References

1. Lei, X. *et al.* Realizing oxygen ion conduction in perovskite structure $NaNbO_3$ by A-site Bismuth doping. *J. Alloys Compd.* **924**, 2–6 (2022).

2. Gouget, G. *et al.* High Ionic Conductivity in Oxygen-Deficient Ti-Substituted Sodium Niobates and the Key Role of Structural Features. *Chem. Mater.* **31**, 2828–2841

(2019).

3. Levin, I. *et al.* Displacive Order–Disorder Behavior and Intrinsic Clustering of Lattice Distortions in Bi-Substituted $NaNbO_3$. *Adv. Funct. Mater.* **2001840**, 1–13 (2020).

4. Aso, S., Matsuo, H. & Noguchi, Y. Reversible electric-field-induced phase transition in Ca-modified $NaNbO_3$ perovskites for energy storage applications. *Sci. Rep.* **13**, 1–10 (2023).

5. Shannon, R. D. Revised effective ionic radii and systematic studies of interatomic distances in halides and chalcogenides. *Acta Crystallogr. Sect. A Cryst. physics, diffraction, Theor. Gen. Crystallogr.* **32**, 751–767 (1976).

6. Valant, M. *et al.* The origin of magnetism in Mn-doped $SrTiO_3$. *Adv. Funct. Mater.* **22**, 2114–2122 (2012).

7. Choudhury, D. *et al.* Tuning of dielectric properties and magnetism of $SrTiO_3$ by site-specific doping of Mn. *Phys. Rev. B - Condens. Matter Mater. Phys.* **84**, (2011).

8. Tkach, A., Vilarinho, P. M. & Kholkin, A. L. Polar behavior in Mn-doped $SrTiO_3$ ceramics. *Appl. Phys. Lett.* **86**, 1–3 (2005).

9. Guo, H., Shimizu, H., Mizuno, Y. & Randall, C. A. Strategy for stabilization of the antiferroelectric phase (Pbma) over the metastable ferroelectric phase (P21ma) to establish double loop hysteresis in lead-free (1-x)$NaNbO_3$ -x $SrZrO_3$ solid solution. *J. Appl. Phys.* **117**, 214103 (2015).

10. Irvine, J. T. S., Sinclair, D. C. & West, A. R. Electroceramics: Characterization by Impedance Spectroscopy. *Adv. Mater.* **2**, 132–138 (1990).

11. Shakhovoy, R. A. *et al.* Ferroelectric Q and antiferroelectric P phases' coexistence and local phase transitions in oxygen-deficient $NaNbO_3$ single crystal: Micro-Raman, dielectric and dilatometric studies. *J. Raman Spectrosc.* **43**, 1141–1145 (2012).

12. Ren, P. *et al.* Mixed oxide ion and proton conduction and p-type semiconduction in $BaTi_{0.98}Ca_{0.02}O_{2.98}$ ceramics. *J. Mater. Chem. C* **1**, 2426–2432 (2013).

13. Gouget, G. *et al.* Associating and Tuning Sodium and Oxygen Mixed-Ion Conduction in Niobium-Based Perovskites. *Adv. Funct. Mater.* **30**, 1–12 (2020).

Chapter 5. Chemically Doped Sodium Niobate Part 2 – B-Site

The previous chapter established the effects of doping the A-site of $NaNbO_3$ (NN) according to 2 different doping mechanisms. The goal of this chapter is to investigate how doping of the B-site influences the physical and electrical properties of NN.

Acceptor doping of NN has previously been explored by Gouget *et. al.* using titanium to introduce oxygen vacancies according to the mechanism:[1,2]

$NaNb_{1-x}Ti_xO_{3-0.5x}$ – Mechanism: $Nb^{5+} + \frac{1}{2}O^{2-} = Ti^{4+}$

Acceptor doping of the B-site with titanium indicated a notable increase in total conductivity, the Arrhenius plots of titanium doped NN samples are shown in Figure 5.1.

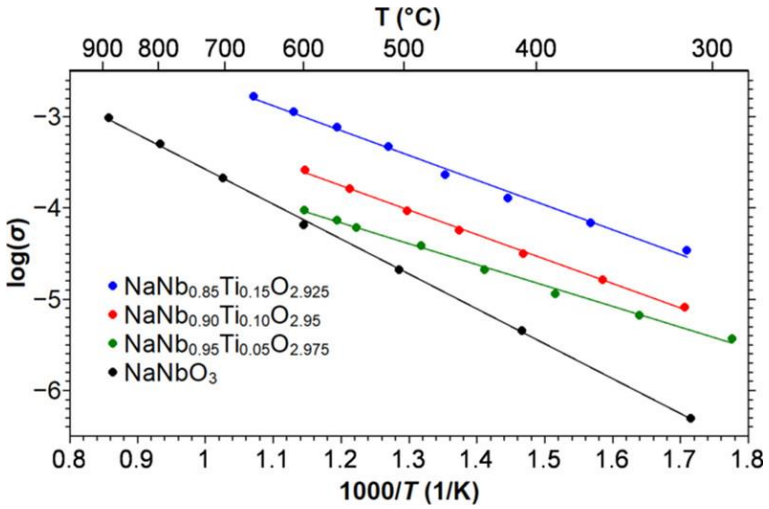

Figure 5.1: Arrhenius Plots of Total Conductivity of Ti-Doped NN (Taken from Gouget et. al.)[1]

Figure 5.1 shows that with increasing titanium concentrations, the total conductivity increases, Gouget et. al. additionally report this increase in total conductivity is exclusively due to oxide ion conduction showcasing a high temperature transport number of 1, as shown in Figure 5.2.[2] As discussed in the literature review the methodology behind the claim that ionic transport inverts between Na^+ and O^{2-} fails to exclude electronic contributions from the Na^+ measurements.

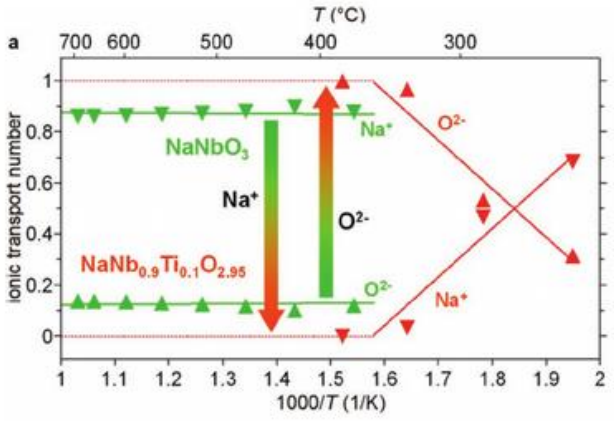

Figure 5.2: Inversion of Na+ and O2- Transport Numbers (Taken from Gouget et.al.)[2]

Section 5.1 will expand upon this work and investigate the effects of B-site acceptor doping in NN using titanium, gallium, and magnesium.

DFT calculations have shown that electronic donor doping of the B-site of NN with molybdenum and tungsten leads to hybridisation of the Mo 4d and Nb 4d orbitals/W 5d and Nb 4d orbitals, leading to a reduction of the band gap as shown in Figure 5.3.[3]

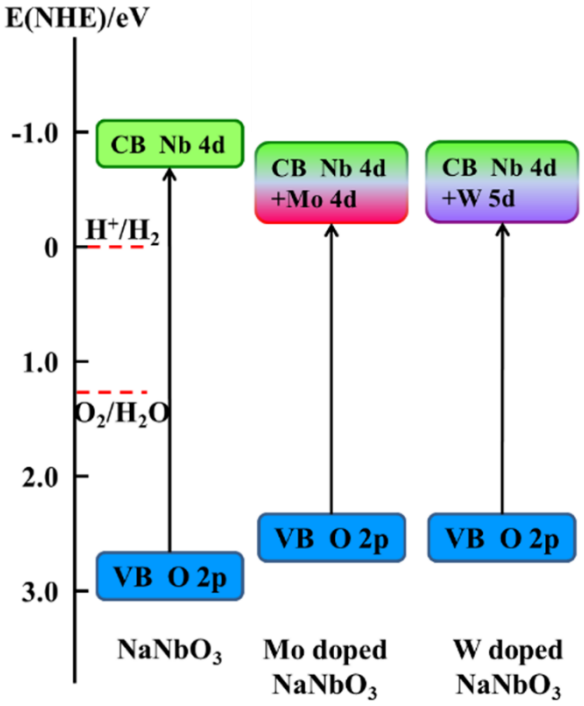

Figure 5.3: Variance of the Calculated Valence, and Conduction Bands of Donor Doped NN with Respect to Normal Hydrogen Electrode (NHE) (Taken from Shi H. et. al.)[3]

Chapter 4 showcased that donor doping of the A-site with magnesium may lead to a reduction of the band gap. Section 5.2. will expand on the DFT work presented with an experimental investigation of B-site donor doped NN ceramics.

When evaluating the B-site donor doping mechanisms it may be important to consider any potential side reactions and the secondary phases that may be generated. WO_3 and Nb_2O_5 may react together to form many phases with various Nb:W ratios, the binary phase diagram showing this is shown in Figure 5.4.

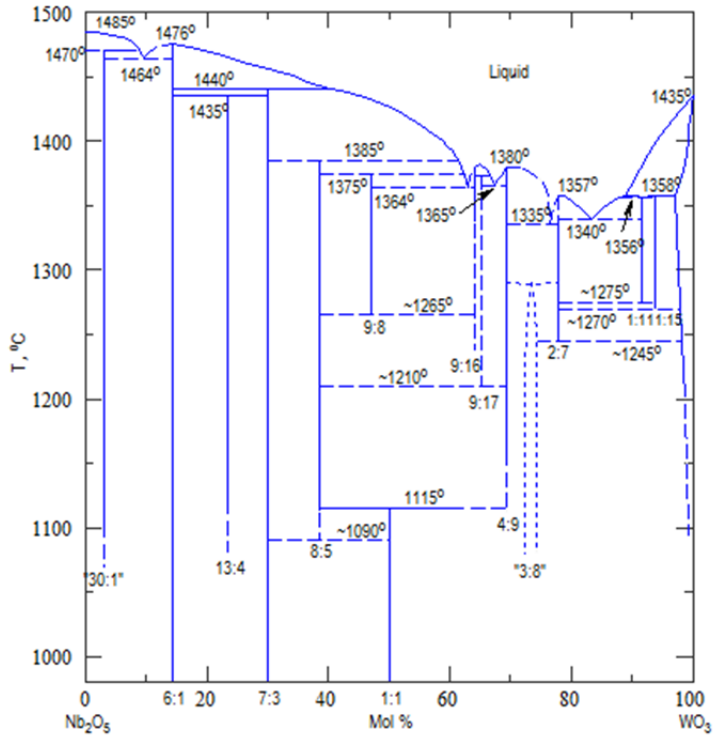

Figure 5.4: Nb_2O_5-WO_3 Binary Phase Diagram (Taken from Roth R. et. Al.)[4] Obtained from ACS Phases Software

Figure 5.4 shows that there are many tungsten bronzes that may potentially form under the conditions required to calcine/sinter NN ceramics. If any of the phases in Figure 5.4 were to form it is likely that sodium would be incorporated and may form the tungsten bronzes:[5]

$$Na_xW_x^VW_{1-x}^{VI}O_3 \qquad \text{or} \qquad Na_xNb_x^VW_{1-x}^{VI}O_3$$

This series of tungsten bronzes vary notably with x. When x is low they exhibit semiconducting properties, as x increases the properties become more metallic, with high conductivities at room temperature ($Na_{0.49}WO_3$=9.5 kS cm^{-1}).[5,6]

Similar observations may occur with the potential formation of molybdenum bronzes, which are generally very similar; although they exhibit notably lower conductivities ($Na_{0.93}Mo_{5.9}O_{17}$ = 3.85 S cm^{-1} at 60°C).[7]

5.1. B-Site Acceptor Doped Sodium Niobate

The ultimate goal of the PhD project is to develop an oxide ion conducting ceramic electrolyte suitable for ITSOFCs. In order to enhance the oxide ion conductivity in NN the B-site has been acceptor doped with various elements in attempts to generate oxygen vacancies.

The acceptor doped variants to be discussed are as follows:

1. 1% Mg NN - $NaNb_{0.99}Mg_{0.01}O_{2.985}$

   Target Mechanism: $Nb^{5+} + \frac{3}{2}O^{2-} \rightarrow Mg^{2+}$ (5.1)

2. 5% Ga NN - $NaNb_{0.95}Ga_{0.05}O_{2.95}$

   Target Mechanism: $Nb^{5+} + O^{2-} \rightarrow Ga^{3+}$ (5.2)

3. 5% Ti NN - $NaNb_{0.95}Ti_{0.05}O_{2.975}$

   Target Mechanism: $Nb^{5+} + \frac{1}{2}O^{2-} \rightarrow Ti^{4+}$ (5.3)

The reagents used for each of the above compositions and the associated processing conditions are shown in table 5.1. All acceptor doped NN variants were processed *via* a conventional solid-state method.

Composition	Reagents	Conditions Required for Single Phase Powders
1% Mg NN	Na_2CO_3 (99.98%) Nb_2O_5 (99.85%) MgO (>99%)	Calcined 900 °C 2 Hours Sintered 1240 °C 4 Hours
5% Ga NN	Na_2CO_3 (99.98%) Nb_2O_5 (99.85%) Ga_2O_3 (>99.99%)	Calcined 900 °C 2 Hours Sintered 1240 °C 4 Hours
5% Ti NN	Na_2CO_3 (99.98%) Nb_2O_5 (99.85%) TiO_2 (>99.99%)	Calcined 900 °C 2 Hours Sintered 1240 °C 4 Hours

Table 5.1: Compositions of B-Site Acceptor Doped NN Variants with Reagents and Processing Conditions

As discussed in chapter 4, decreasing the tolerance factor of NN induces stabilisation of the P-phase.[8] In this chapter, doping the B-site with smaller ions should increase the tolerance

factor of NN. Table 5.2 lists the ionic radii of the dopant ions and their adjusted tolerance factor.

Ion	Ionic Radii / pm	Adjusted Tolerance Factor
Nb^{5+}	64	NN-0.967
Mg^{2+}	72	1% Mg NN – 0.967
Ga^{3+}	62	5% Ga NN – 0.968
Ti^{4+}	60.5	5% Ti NN – 0.968

Table 5.2: Ionic Radii of Investigated Ions Extracted from R.D. Shannon[9] and Associated Tolerance Factors for NN Variants

The selected ions have a very good size agreement with Nb^{5+}, additionally the dopant levels chosen are low. As a consequence, the tolerance factor of B-site acceptor doped NN variants is largely unaffected.

5.1.1. Phase Purity and Crystal Structure

The phase purity of acceptor doped NN variants has been investigated *via* XRD, the obtained diffraction patterns are shown in Figure 5.5.

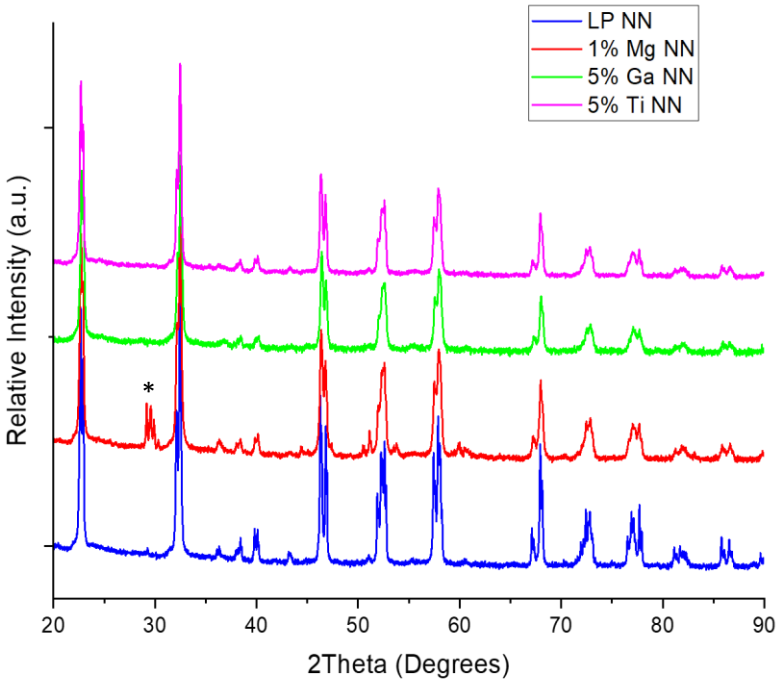

Figure 5.5: X-Ray Diffraction Patterns of Acceptor Doped NN Variants Compared to 'LP NN'.

After a single calcination, gallium and titanium doped variants appear to be a mix of P and Q phases. Between all sintered variants no significant shifting of the peaks occurs. 1% Mg NN

contains the additional secondary phase $Na_2Nb_4O_{11}$ (indicated by *). This secondary phase is eliminated during sintering, as shown in Figure 5.6.

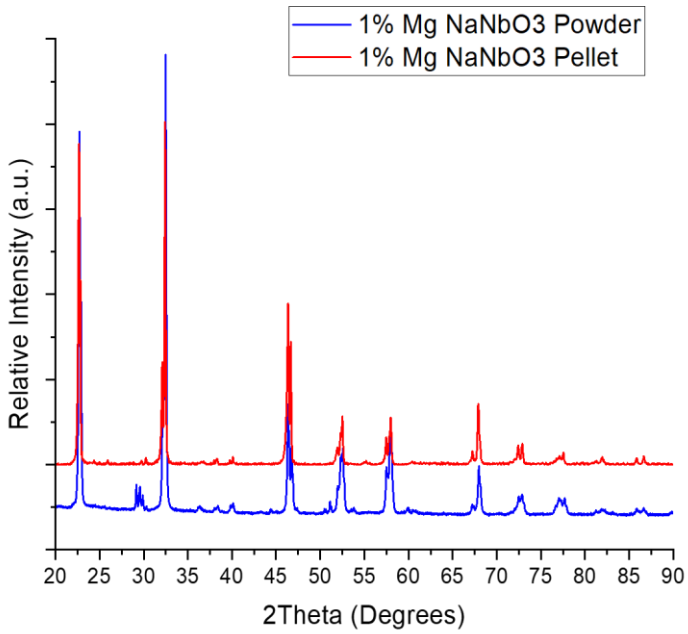

Figure 5.6: Comparison of 1% Mg NN Powder vs Pellet XRD

On sintering the secondary phase is eliminated, however, the rest of the XRD pattern is generally unaffected by the sintering process.

The obtained XRD patterns have undergone Rietveld refinement to determine the unit cell parameters and the ratio of P and Q phases. An example refinement is shown in Figure 5.7 and the associated parameters tabulated below.

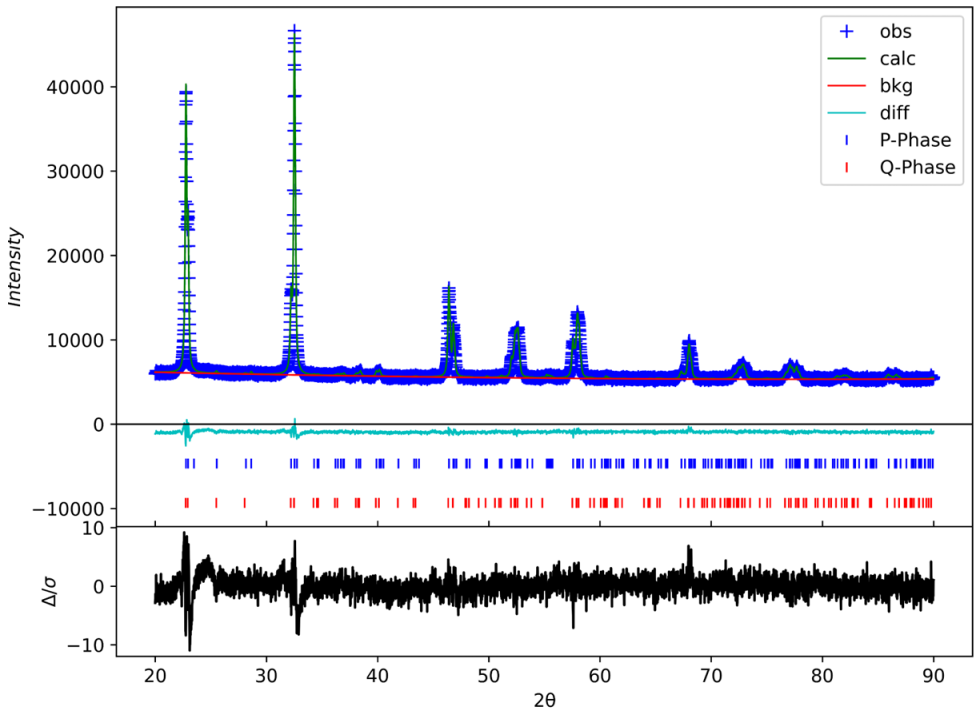

Figure 5.7: Example Rietveld Refinement of 5% Ga NN

	Parameters	LP NN	1% Mg NN	5% Ga NN	5% Ti NN
P Phase (Pbma)	a / Å	5.57450(6)	5.56633(22)	5.56278(23)	5.56205(18)
	b / Å	15.51670(17)	15.5267(5)	15.5292(6)	15.5180(4)
	c / Å	5.51674(7)	5.5075(22)	5.50785(24)	5.50626(17)
	Cell Volume / Å^3	477.18611(2)	475.99525(6)	475.79850(7)	475.25572(5)
	Phase Fraction	0.655(9)	0.735(15)	0.528(21)	0.425(9)
Q Phase (Pmc21)	a / Å	7.75949(26)	7.7797(23)	7.7727(5)	7.76606(23)
	b / Å	5.56788(22)	5.5473(23)	5.5700(4)	5.51502(20)
	c / Å	5.51122(22)	5.5207(2)	5.5167(5)	5.56983(18)
	Cell Volume / Å^3	238.1062(7)	238.2532(6)	238.8397(1)	238.55569(6)
	Phase Fraction	0.345(9)	0.265(15)	0.472(21)	0.575(9)
Residuals	R_w / %	2.935	4.247	2.033	2.105
	χ^2	8.95	18.90	2.61	6.49

Table 5.3: Summary of Rietveld Refinements for Acceptor Doped NN Powders

The determined P:Q ratio for each acceptor doped variants are shown in Figure 5.8.

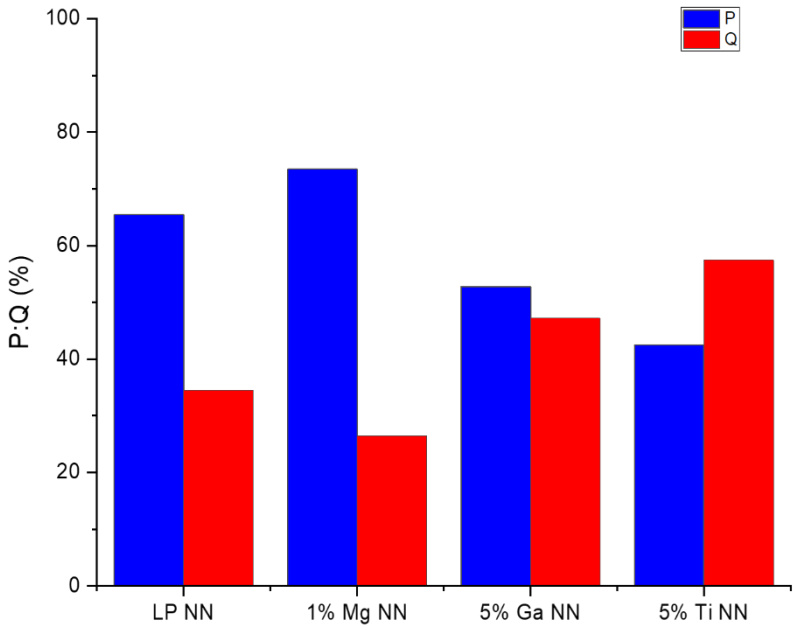

Figure 5.8: Ratio of P:Q Phases in Acceptor Doped NN Obtained from Rietveld Refinement

Doping with gallium and titanium caused a slight increase in the amount of Q phase present in the system compared to 'LP NN'. Doping with magnesium causes the amount of Q phase to decrease compared to 'LP NN'.

5.1.2. Microstructure

The microstructure of acceptor doped NN has been investigated *via* SEM-EDS. Grain sizes have been evaluated and distributions are shown in Figure 5.9.

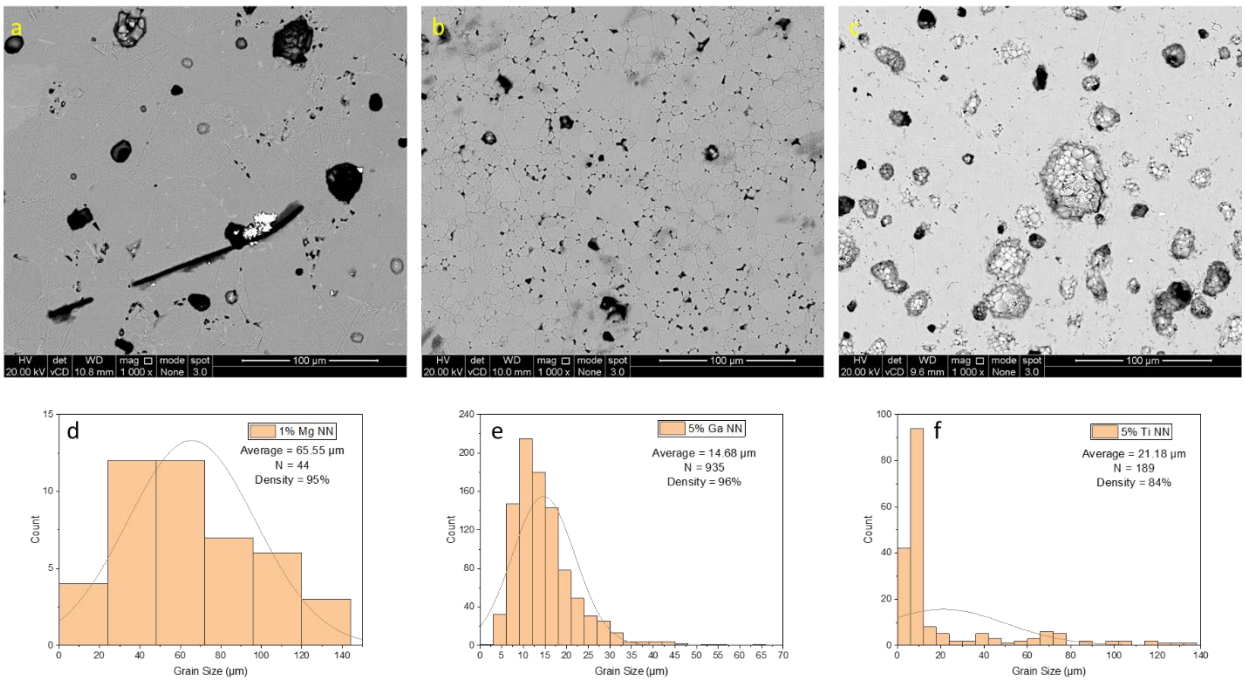

Figure 5.9: BSE Images of a) 1% Mg NN b) 5% Ga NN c) 5% Ti NN and Associated Grain Size Evaluations d) 1% Mg NN e) 5% Ga NN and f) 5% Ti NN

Doping with gallium does not yield a significant increase in average grain size compared to 'LP NN'. Use of an equivalent concentration of titanium caused the average grain size to approximately double. Use of magnesium as an acceptor dopant caused the grain size to increase significantly, up to 6.5x the average grain size of 'LP NN'.

The elemental distribution through the ceramics has been evaluated *via* EDS maps and are shown in Figures 5.10-5.12.

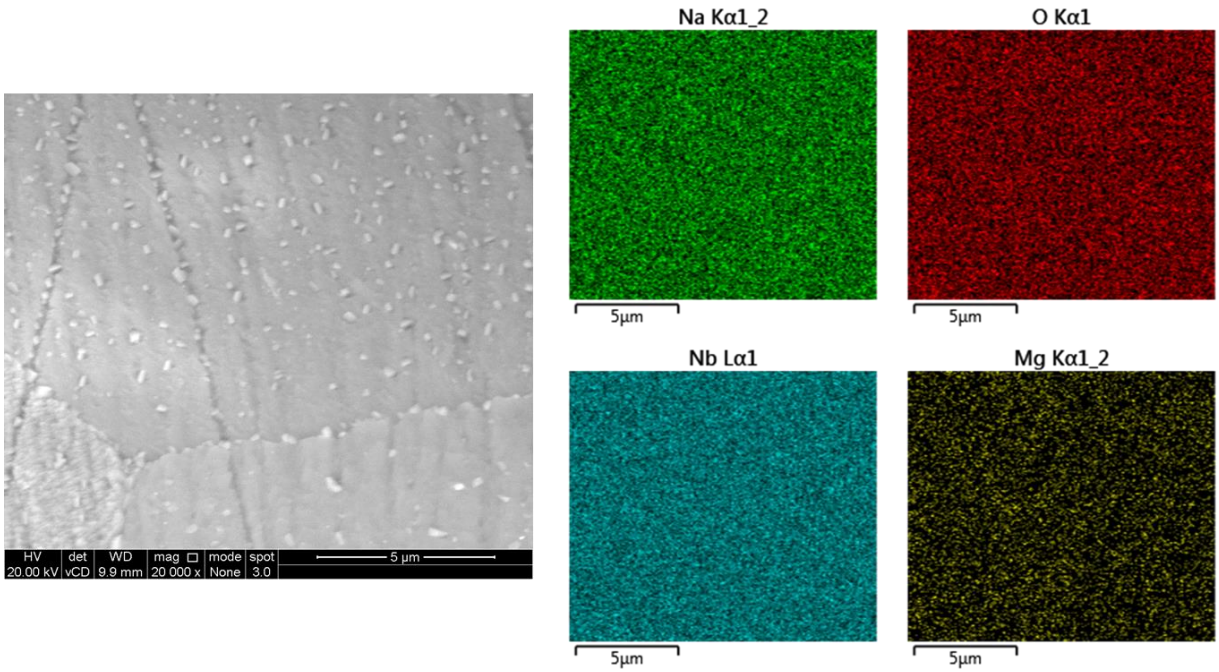

Figure 5.10: EDS Map of 1% Mg NN

At greater magnification it becomes clear that small amounts of a lighter secondary phase appear as ‘flecks’ across the surface of the grains and along the grain boundaries. However, the elemental distribution throughout the magnesium doped ceramic appears to be consistent throughout grains and grain boundaries with the flecks not appearing to impact the elemental distribution.

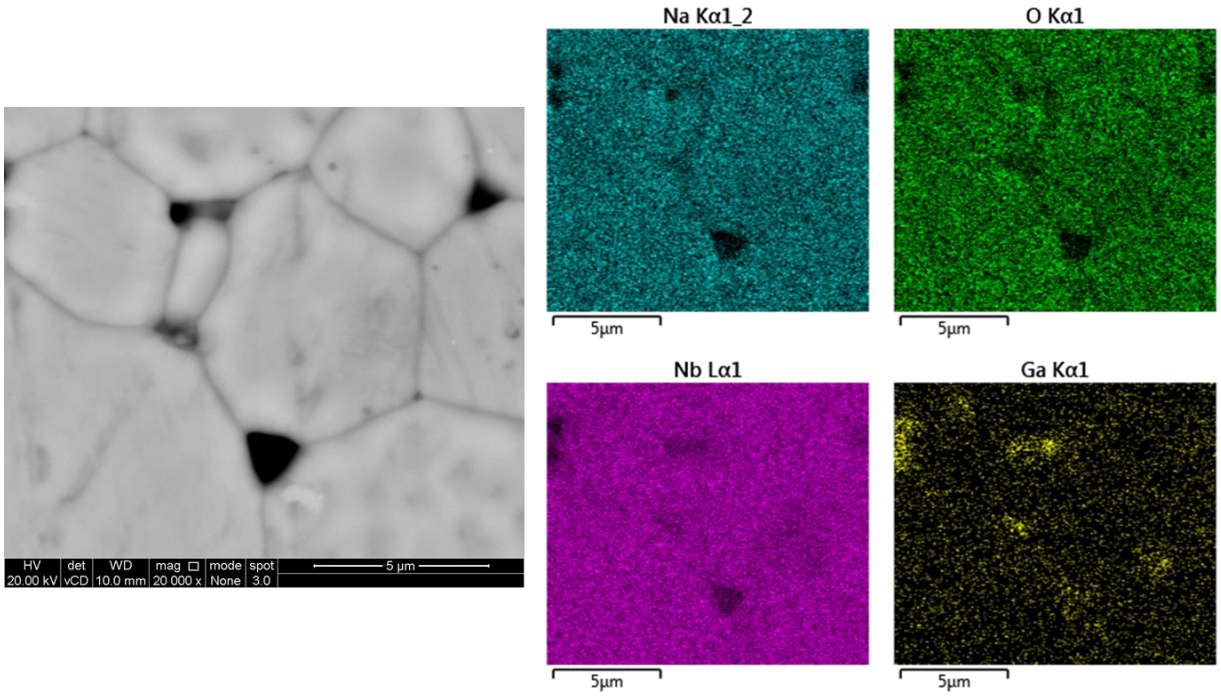

Figure 5.11: EDS Map of 5% Ga NN

The EDS map of the 5% Ga NN shows slight sodium deficiencies along the grain boundaries. Some gallium-rich regions appear in the EDS map although they are associated with the pore regions in the ceramic surface and are a consequence of the measurement, rather than a real effect. Discounting this the gallium content appears to be consistent throughout the ceramic.

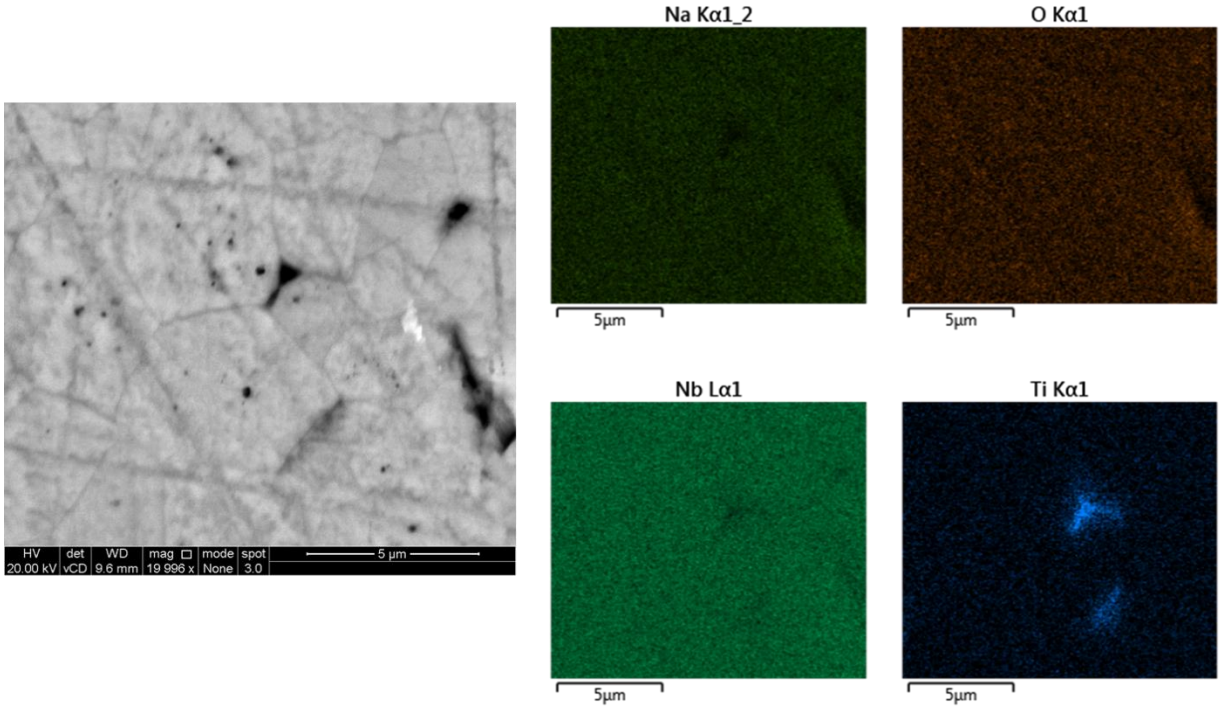

Figure 5.12: EDS Map of 5% Ti NN

The elemental distribution of 5% Ti NN appears to be consistent throughout the ceramic, with apparent titanium-rich regions being related to porosity in the ceramic.

The spot analysis of acceptor doped ceramics is shown below in table 5.4.

	Theoretical				Grain				Grain Boundary			
Composition	**Na / wt%**	**Nb / wt%**	**X / wt%**	**O / wt%**	**Na / wt%**	**Nb / wt%**	**X / wt%**	**O / wt%**	**Na / wt%**	**Nb / wt%**	**X / wt%**	**O / wt%**
1% Mg NN	14.11	56.44	0.15	29.31	14.37 ± 0.01	51.94 ± 0.01	0.49 ± 0.14	33.26 ± 0.01	14.93 ± 0.01	50.95 ± 0.01	0.21 ± 0.33	33.91 ± 0.01
5% Ga NN	14.20	54.50	2.15	29.15	13.70 ± 0.10	59.20 ± 0.20	0.10 ± 0.10	26.90 ± 0.20	11.66 ± 0.10	58.62 ± 0.20	0.66 ± 0.10	29.06 ± 0.20
5% Ti NN	14.26	54.74	1.48	29.52	13.08 ± 0.04	58.67 ± 0.02	1.22 ± 0.24	27.02 ± 0.03	12.71 ± 0.03	59.85 ± 0.01	0.90 ± 0.19	26.55 ± 0.03

Table 5.4: Average Grain and Grain Boundary Compositions of Acceptor Doped NN Ceramics

The 5% Ga NN ceramic showcases gallium concentrations far below the theoretical wt% for the dopant level. Grains showcase the lowest concentration of gallium, and grain boundaries showcase an ~6x increase in gallium content.

The opposite effect is observed in magnesium and titanium doped ceramics, although it is worth noting that the errors associated with magnesium and titanium wt% are large and are potentially not fully representative of the real stoichiometries.

Gallium and titanium doped NN exhibit lower concentrations of sodium in the grain boundaries compared to the grains, whereas the sodium content in the magnesium doped ceramic appears reasonably consistent throughout.

In order to more accurately quantify the elemental content of the 1% Mg and 5% Ga NN ceramics, electron probe microanalysis (EPMA) has been utilised with wavelength dispersive spectroscopy (WDS). The obtained WDS maps are shown below in Figures 5.13 and 5.14.

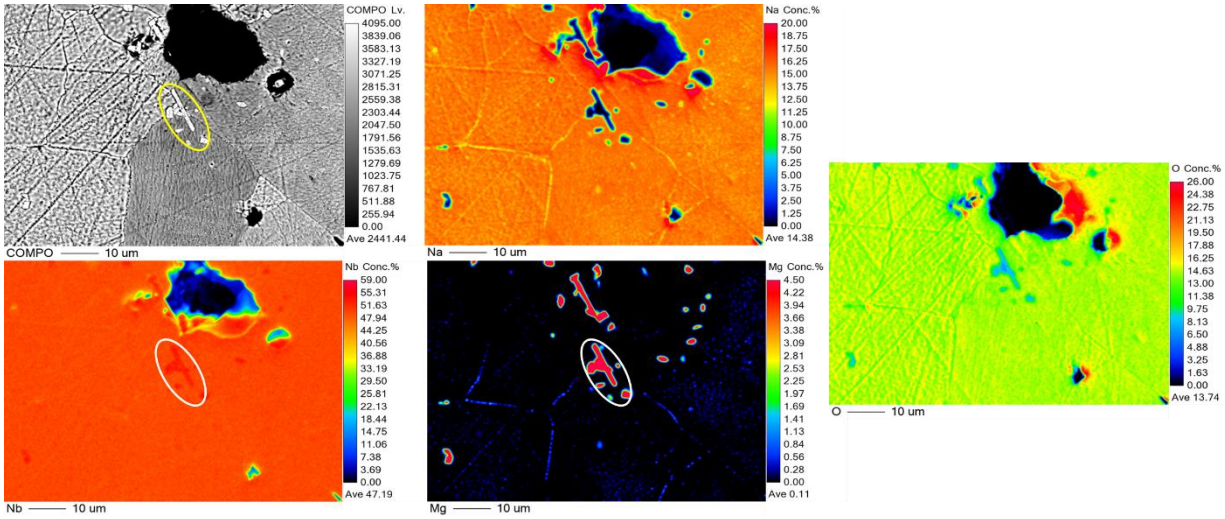

Figure 5.13: WDS Maps of 1% Mg NN

The WDS analysis showcases a sodium deficiency along the grain boundary of the 1% Mg NN ceramic; this sodium deficiency is accompanied by an increase in the concentration of magnesium. Additionally, the circled regions in Figure 5.13 are areas within the ceramic that have high concentrations of magnesium and niobium.

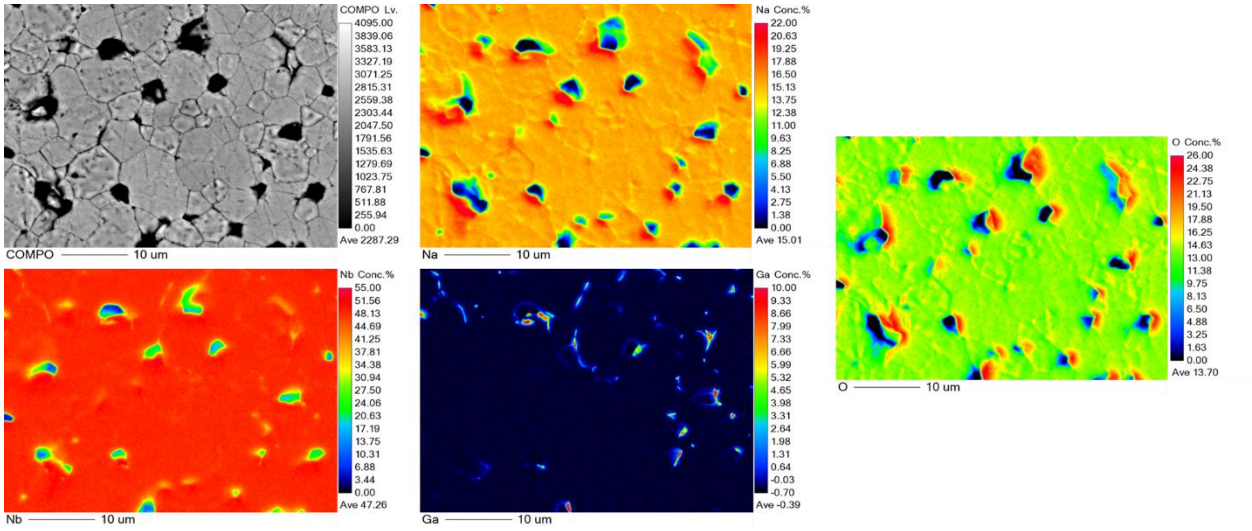

Figure 5.14: WDS Maps of 5% Ga NN

The WDS analysis of the 5% Ga NN ceramic showcase a notable sodium deficiency along grain boundaries and very low concentrations of gallium throughout. The regions where gallium appears to be abundant are associated with geometric effects and 'shadowing' around pores in the ceramic and are unlikely to be representative of the true stoichiometry.

Spot analysis of the 1% Mg and 5% Ga NN ceramics has been utilised to accurately quantify the elemental composition throughout the ceramic. The results are shown in table 5.5.

	Theoretical				Grain				Grain Boundary			
Composition	**Na / wt%**	**Nb / wt%**	**X / wt%**	**O / wt%**	**Na / wt%**	**Nb / wt%**	**X / wt%**	**O / wt%**	**Na / wt%**	**Nb / wt%**	**X / wt%**	**O / wt%**
1% Mg NN	14.11	56.44	0.15	29.31	14.698 ± 0.191	49.856 ± 0.996	0.065 ± 0.001	35.382 ± 0.603	13.988 ± 0.011	50.860 ± 0.031	0.437 ± 0.001	34.714 ± 0.028
5% Ga NN	14.20	54.50	2.15	29.15	15.913 ± 0.230	53.836 ± 1.408	0.108 ± 0.001	30.373 ± 0.584	15.694 ± 0.204	56.415 ± 1.200	0.547 ± 0.013	27.344 ± 0.420

Table 5.5: Average Grain and Grain Boundary Compositions of 1% Mg and 5% Ga NN Ceramics from WDS Quantitative Analysis

WDS analysis of the acceptor doped NN ceramics shows dopant concentrations in the grains and grain boundaries to be significantly different than targeted. In both cases the concentration of the dopant ion increases along grain boundaries compared to the grains. Concentrations of other elements appear to be generally consistent between grains and grain boundaries.

In the case of the 1% Mg NN ceramic, this observation differs from the EDS spot analysis, where concentrations of magnesium appear to decrease in grain boundaries, although the large errors associated with the tabulated values are likely responsible for this discrepancy. The 5% Ga NN ceramic consistently showcases an increase in gallium concentration in grain boundaries, however, as WDS utilises standards in order to determine elemental

concentrations, the concentrations shown in table 5.5 are more representative of the ceramic.

WDS quantitative analysis of the magnesium rich region identified in Figure 5.13 has been conducted and the results are shown in table 5.6.

	Na / wt%	Nb / wt%	Mg / wt%	O / wt%
Unknown Mg Rich Phase	0.637 ± 0.004	60.870 ± 0.037	6.936 ± 0.004	31.558 ± 0.032

Table 5.6: Elemental Composition of Unknown Mg Rich Phase in Figure 5.13

There is very little sodium detected in the magnesium rich region of the WDS map. Conversion to at% shows an approximate 2:1 Nb:Mg ratio, indicating the columbite phase $MgNb_2O_6$ phase is preferentially forming along grain boundaries of the 1% Mg NN ceramic. This phase is also likely responsible for the light 'flecks' in Figure 5.10.

5.1.3. Relative Permittivity and Dielectric Losses

The temperature dependence of permittivity and dielectric losses have been assessed for each of the acceptor doped NN variants. The ε'-T plots are shown in Figure 5.15.

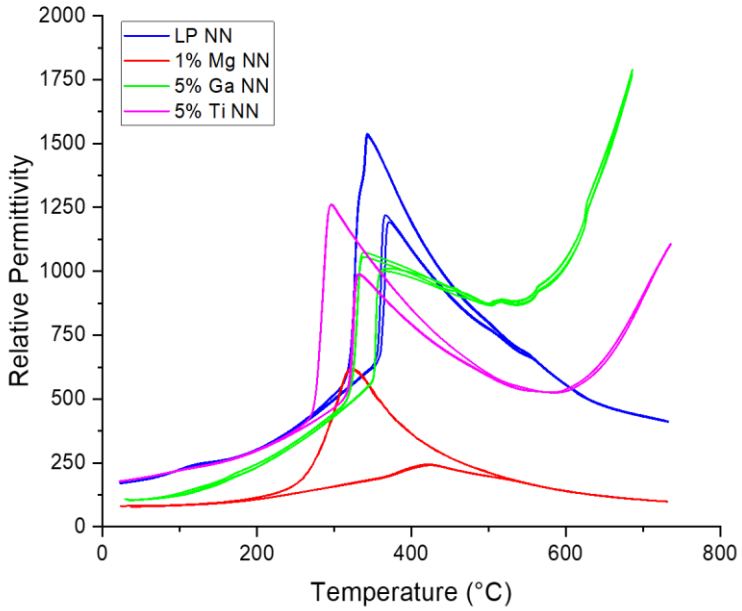

Figure 5.15: Relative Permittivity versus Temperature of Acceptor Doped NN Ceramics Compared to 'LP NN' at 100 kHz

The ε'-T plots of acceptor doped NN vary significantly according to dopant ion. 1% Mg NN has the greatest deviation from LP NN with a significantly lower maximum permittivity *vs* any

other ceramic, and a notable broadening of the hysteresis on thermal cycling. On heating the P-R phase transition occurs at ~400 °C, the highest temperature of any of the acceptor doped variants.

5% Ga NN shows the closest agreement with LP NN in terms of hysteresis and stability around the P-R phase transition.

5% Ti NN shows the size of the hysteresis is consistent, however, the P-R phase transition has shifted to significantly lower temperatures (~ 250-300 °C).

All acceptor doped ceramics are stable over subsequent heating/cooling cycles with no significant changes occurring to permittivity or the P-R phase transition temperature.

The associated dielectric losses for acceptor doped NN ceramics are shown in Figure 5.16.

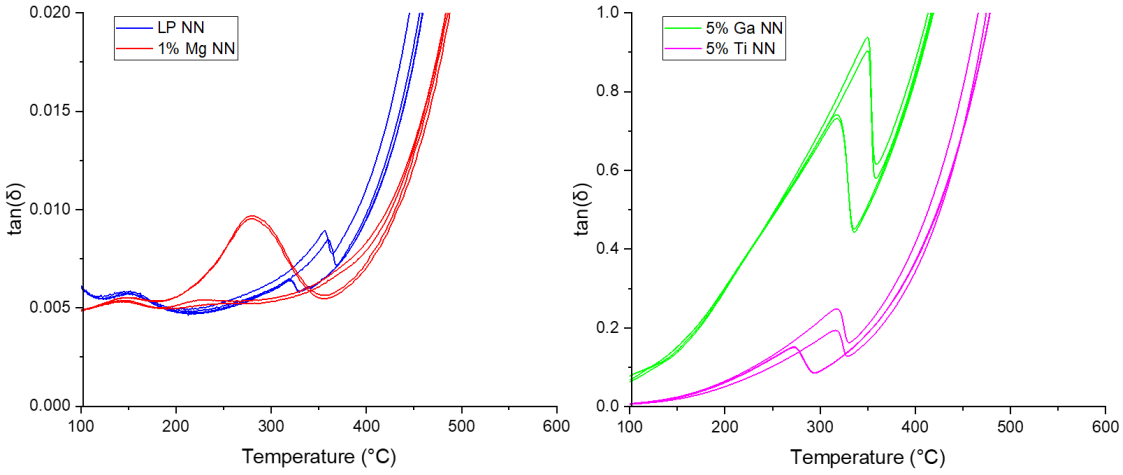

Figure 5.16: Dielectric Losses of Acceptor Doped NN Ceramics at 100 kHz

As previously observed in chapters 3 and 4, the dielectric losses of NN acceptor doped ceramics increase significantly after ~400-450 °C due to large space charge effects suggesting losses of greater than 100%.

Below 450 °C losses in 5% Ga and 5% Ti NN remain high. 5% Ga NN showcases greater losses with a maximum of 94% on heating cycles around the P-R phase transition. 5% Ti NN showcases some hysteresis on heating with losses ranging 20-30% around the P-R phase transition. No significant peaks are observable in the tan δ – Temperature plot below the P-R phase transition.

Conversely, the 1% Mg NN showcases similar losses to the LP NN ceramic with losses of ~1% around the P-R phase transition although it is worth noting that this peak exhibits its

maximum loss on cooling, all other NN ceramics showcase this on heating; additionally, it is slightly shifted to lower temperatures with a slight divergence from the permittivity plot in Figure 5.15. At ~150 °C there is an additional, smaller peak with no significant change between heating/cooling cycles. In 1% Mg NN this peak is identical to LP NN with maximum losses of ~0.5%; this peak corresponds to conversion of the ferroelectric Q phase into the antiferroelectric P phase.

5.1.4. Impedance Spectroscopy

The electrical properties of acceptor doped NN ceramics have been tested *via* impedance spectroscopy to determine bulk conductivity, electrical homogeneity and identify the presence of ionic conductivity. The overlaid M''/Z'' plots are shown below in Figure 5.17.

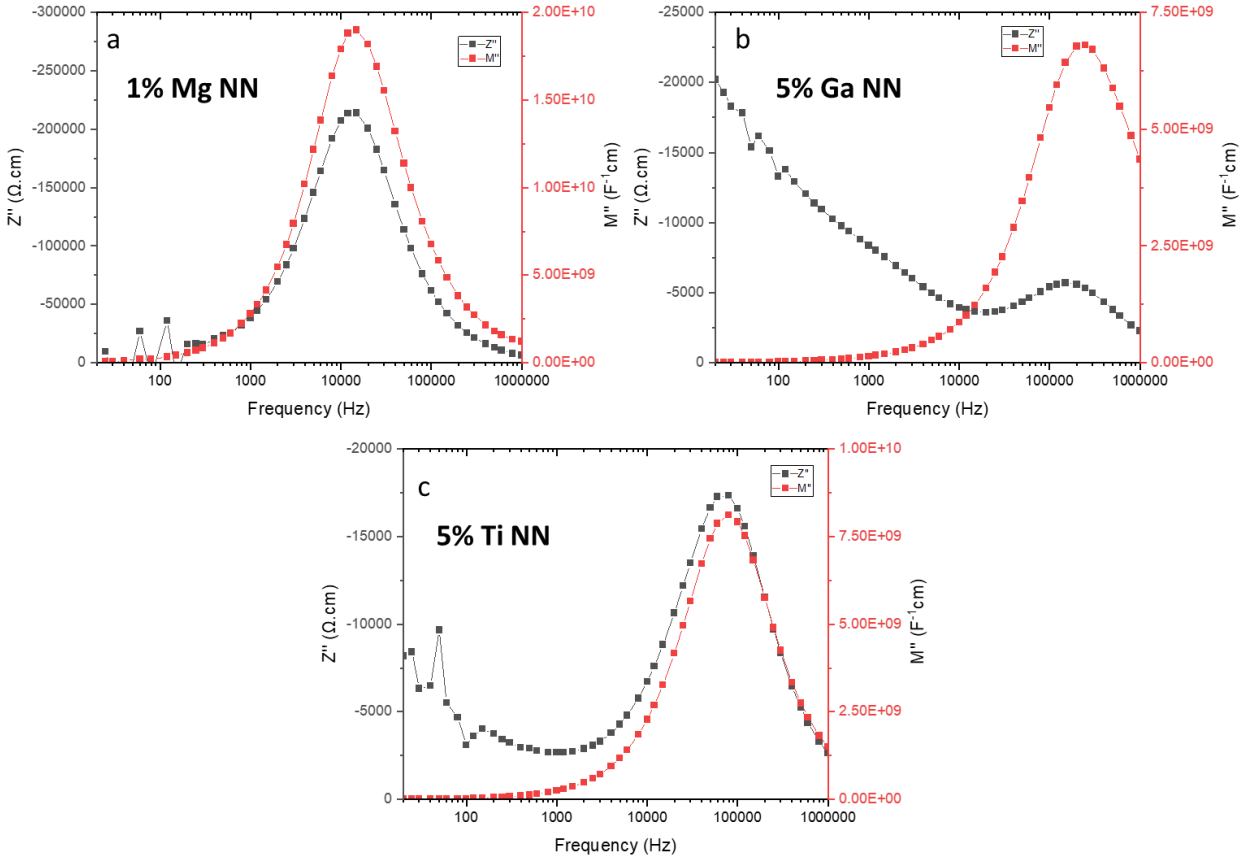

Figure 5.17: M'' Z'' Plots of a) 1% Mg NN at 630 °C b) 5% Ga NN and c) 5% Ti NN both at 460 °C

	Capacitance (Z'') / F cm^{-1}	Capacitance (M'') / F cm^{-1}	Corresponding Response
1% Mg NN	$2.5(1) \times 10^{-11}$	$2.6(1) \times 10^{-11}$	Bulk
5% Ga NN	$9(2) \times 10^{-11}$	$7.4(4) \times 10^{-11}$	Bulk
5% Ti NN	$6(6) \times 10^{-11}$	$6.1(3) \times 10^{-11}$	Bulk

Table 5.7: Tabulated Capacitances from M'' and Z'' Extracted from Figure 5.17

All acceptor doped ceramics show good electrical homogeneity between M'' and Z'' spectra with a single peak in each plot corresponding to a single RC element identified as the bulk electrical response. 1% Mg NN does not show a Warburg response in the Z'' plane, additionally the ceramic appears to be significantly more insulating than either of the other acceptor doped variants.

5% Ga NN and 5% Ti NN ceramics both showcase a clear Warburg response in the Z'' spectra indicating the presence of ionic conductivity, most likely corresponding to oxide ions arising from the increased concentration of oxygen vacancies.

The Arrhenius plots of bulk conductivity for acceptor doped NN ceramics are shown below in Figure 5.18.

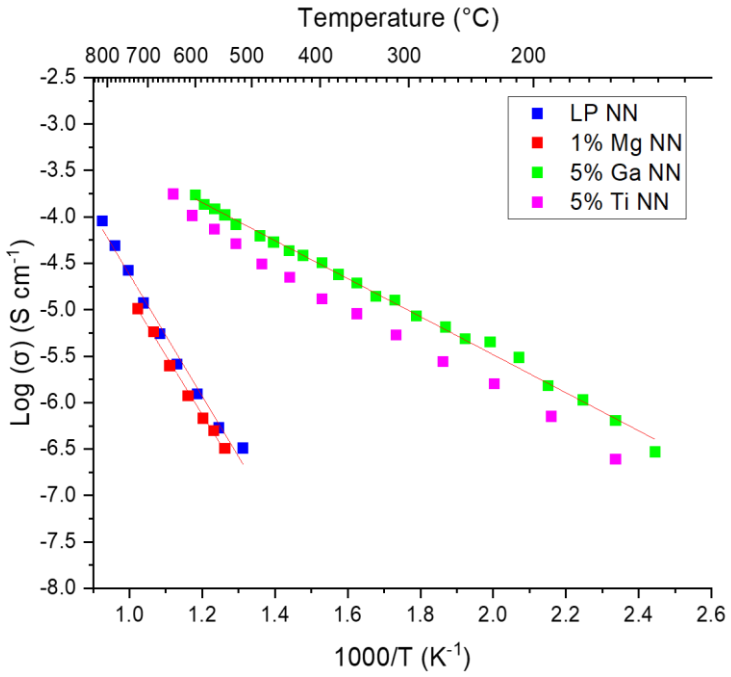

Figure 5.18: Arrhenius Plots of Bulk Conductivity for Acceptor Doped NN Ceramics

Each Arrhenius plot showcases a slightly different gradient at higher temperatures to what is observed at lower temperatures, indicating slight changes in conduction mechanism as temperature increases. The activation energy of the bulk conduction of each ceramic has been extracted and tabulated below.

Composition	Low Temperature Ea / eV	High Temperature Ea / eV
LP NN	1.01 ± 0.10	1.52 ± 0.02
1% Mg NN	1.26 ± 0.04	-
5% Ga NN	0.51 ± 0.02	0.40 ± 0.00
5% Ti NN	0.43 ± 0.01	0.53 ± 0.02

Table 5.8: Activation Energies of B-Site Acceptor Doped NN Variants Extracted from Figure 5.18

The bulk conductivity of 5% Ga NN and 5% Ti NN are in reasonable agreement with each other, with bulk conductivity occurring within half an order of magnitude at all temperatures. The bulk conductivity of 5% Ga and 5% Ti NN ceramics show a significant improvement at lower temperatures compared to LP NN. The activation energies of 5% Ga and 5% Ti are also within good agreement of each other and are significantly lower than the activation energy of LP NN, indicating that the conduction mechanism is different from undoped NN variants but likely shared with each other.

The outlier for acceptor doped NN is 1% Mg NN. This ceramic showcases more insulating bulk conductivity at all temperatures compared to LP NN with a greater activation energy.

The pO_2 dependence of 1% Mg, 5% Ga and 5% Ti NN ceramics has been assessed and are shown below in Figures 5.19 and 5.20.

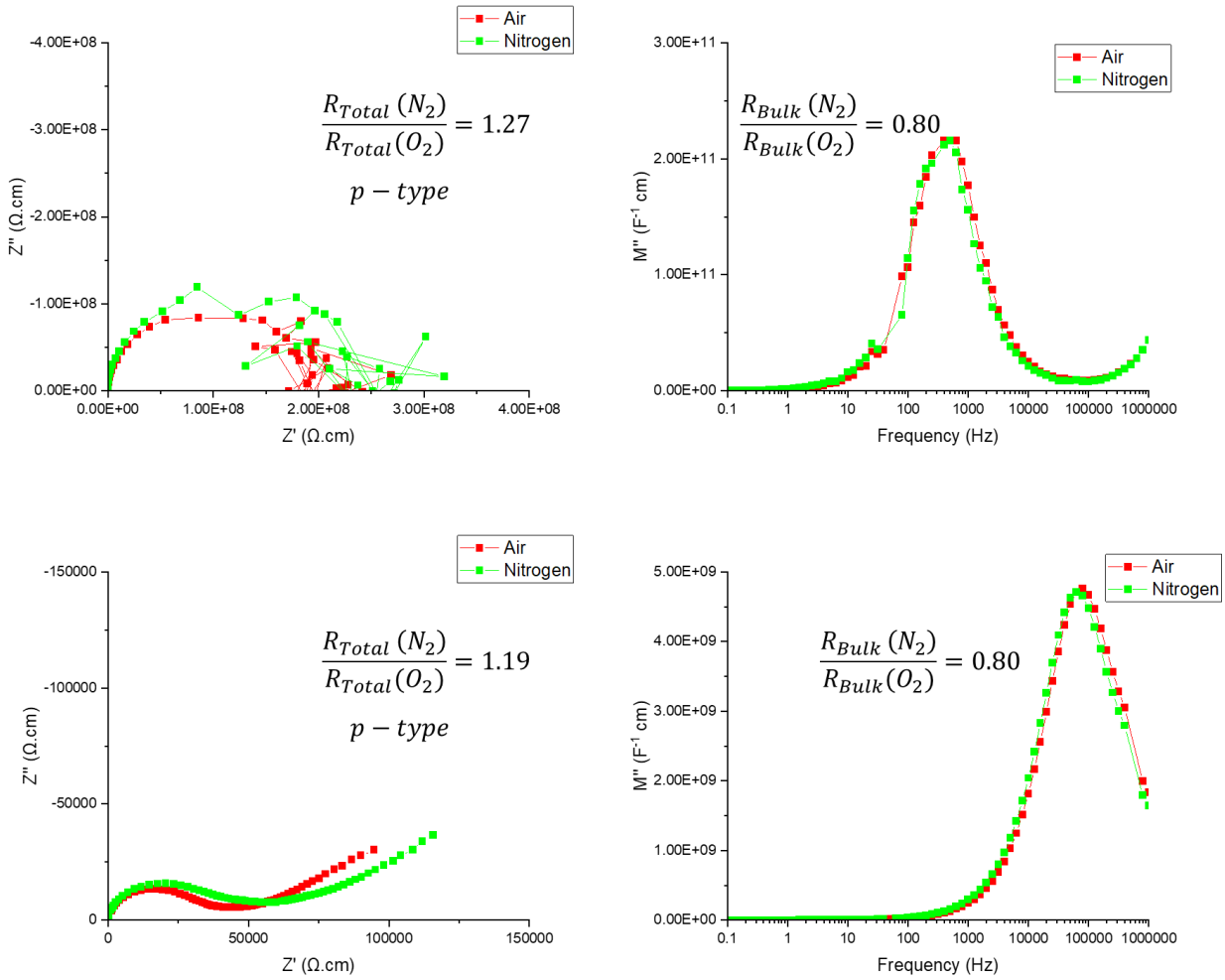

Figure 5.19: pO_2 Dependence of 1% Mg NN at 600 °C (Top) and 5% Ga NN at 440 °C (Bottom)

The 1% Mg NN ceramic exhibits the same pO_2 dependence as the 5% Ga NN ceramic. There is an additional increase in capacitance at high frequencies, however this is attributed to a jig effect and may be disregarded.

The 5% Ga NN ceramic shows an increase in total resistivity in the Z* plane as pO_2 decreases indicating the presence of p-type conductivity, however the bulk resistivity based on the M'' spectra showcases slightly n-type behaviour, indicating that as observed with non-stoichiometric NN some extrinsic effects are influencing the pO_2 dependence of the ceramic.

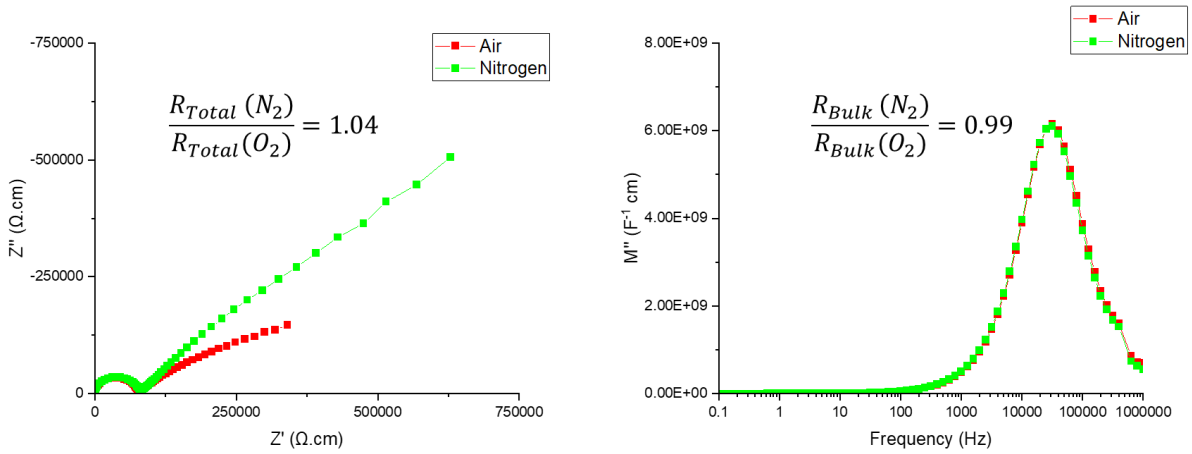

Figure 5.20: pO_2 Dependence of 5% Ti NN Ceramic at 400 °C

The 5% Ti NN ceramic showcases slight p-type pO_2 dependence in total resistivity, however, the bulk response is pO_2 independent. Indicating any pO_2 dependence is attributed to extrinsic effects. Additionally, the electrode response is affected, with a more ideal Warburg spike showcased in the lower pO_2 measurement. This may be indicative of oxide ion conductivity in the ceramic.

5.1.5. Band Gap Determination

The UV-Vis spectrum of 5% Ga NN has been acquired and converted into a tauc-plot to determine the electronic band gap. Figure 5.21 shows the raw data and associated tauc-plot compared to LP NN.

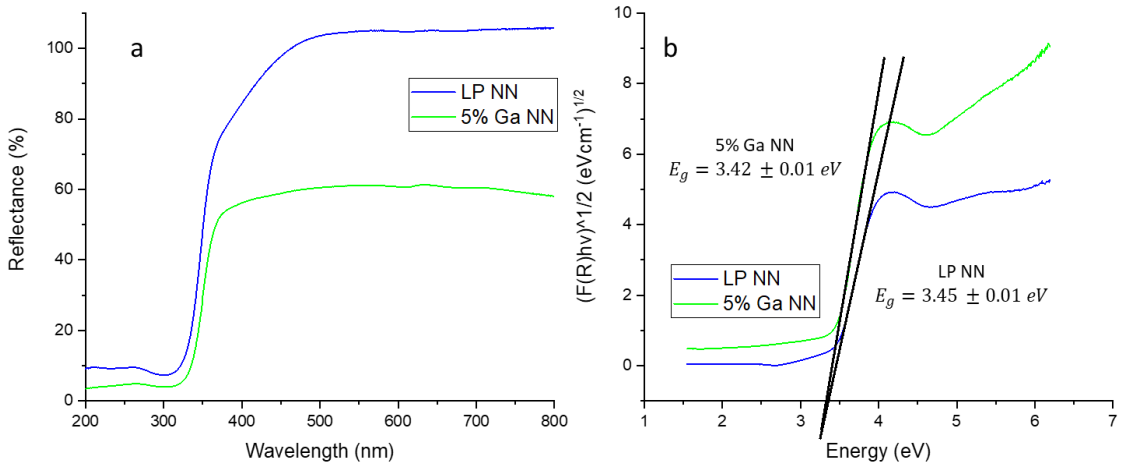

Figure 5.21: a) UV-Vis Spectrum of 5% Ga NN and LP NN Powder Using a $BaSO_4$ Standard and b) Associated Tauc-Plots Showcasing X-Intercept of Linear Region

The UV-Vis spectrum of 5% Ga NN showcases a sharp increase in reflectance at ~350 nm. Extrapolating the linear region of the tauc-plot in Figure 5.21b to the x-axis allows for determination of the electronic band gap in electron volts. The band gap of 5% Ga NN showcases an almost negligible reduction compared to LP NN.

5.1.6. Oxygen Transport Number

The oxygen transport numbers of B-site acceptor doped NN ceramics have been determined and are shown below in Figure 5.22 as a function of temperature.

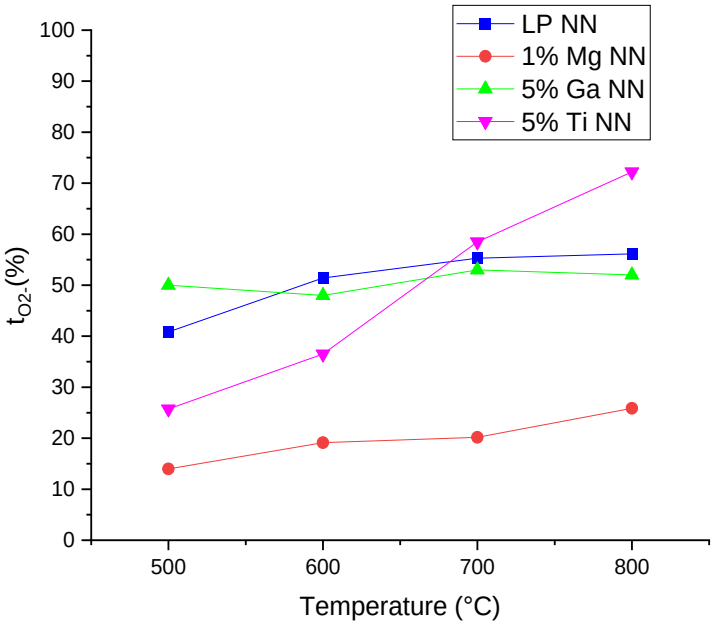

Figure 5.22: Oxygen Transport Number for Acceptor Doped NN Ceramics

The 5% Ga NN ceramic and LP NN both exhibit oxide ion transport numbers of approximately 50% indicating that 50% of the charge is carried by oxide ions and 50% of the charge is carried by electrons. Conversely, the 1% Mg NN ceramic showcases a significantly lower charge transport number of ~20% indicating that oxide ion conductivity has been suppressed.

5% Ti NN initially showcases a transport number of ~72% at 800 °C, however, this value decreases with temperature, to a minimum of ~25%. As the total pO_2 response showcases slight p-type conductivity this indicates that there is an increasing electronic contribution and conduction is not exclusively ionic.

5.2. B-Site Donor Doped Sodium Niobate

As discussed in the introduction to this chapter, DFT calculations show that donor doping of the B-site with tungsten and molybdenum should be possible although experimental work has not been conducted.[3] This section evaluates the properties of B-site donor doped NN.

Both molybdenum and tungsten were doped onto the B-site according to the following mechanism:

$$Nb^{5+} = M^{6+} + \frac{1}{2}O^{2-} \qquad (5.4)$$

1. x% W NN - $NaNb_{0.99}W_{0.01}O_{3.005}$
2. x% Mo NN - $NaNb_{0.99}Mo_{0.01}O_{3.005}$

1, 5, and 10% dopant levels of each were successfully synthesized, although for the purposes of this chapter only 1% variants underwent in-depth analysis.

The reagents used and associated processing conditions for the B-site donor doped ceramics discussed are shown in table 5.9.

Composition	Reagents	Conditions Required for Single Phase Powders
1% Mo NN	Na_2CO_3 (99.98%) Nb_2O_5 (99.85%) MoO_3 (>99.99%)	Calcined 900 °C 2 Hours Sintered 1330 °C 4 Hours
1% W NN	Na_2CO_3 (99.98%) Nb_2O_5 (99.85%) WO_3 (>99.99%)	Calcined 900 °C 2 Hours Sintered 1300 °C 4 Hours

Table 5.9: Compositions of B-Site Donor Doped NN Variants with Reagents and Processing Conditions

Donor doping of the B-site showcases minimal changes to the tolerance factor of NN due to the relatively small amount of dopants used as shown in table 5.10.

Ion	Ionic Radii / pm	Adjusted Tolerance Factor
Nb^{5+}	64	NN-0.967
Mo^{6+}	59	1% Mo NN – 0.967
W^{6+}	60	1% W NN – 0.967

Table 5.10: Ionic Radii of Investigated Ions Extracted from R.D. Shannon[9] and Associated Tolerance Factors for NN Variants

Table 5.10 shows how doping with molybdenum and tungsten has no effect on the tolerance factor of NN. This suggests that the observed P:Q ratios for LP NN, 1% Mo NN, and 1% W NN should be consistent.[8]

5.2.1. Phase Purity and Crystal Structure

The phase purity and crystal structure of the B-site donor doped NN variants has been investigated *via* x-ray diffraction. The resultant diffraction patterns are shown below in Figure 5.23.

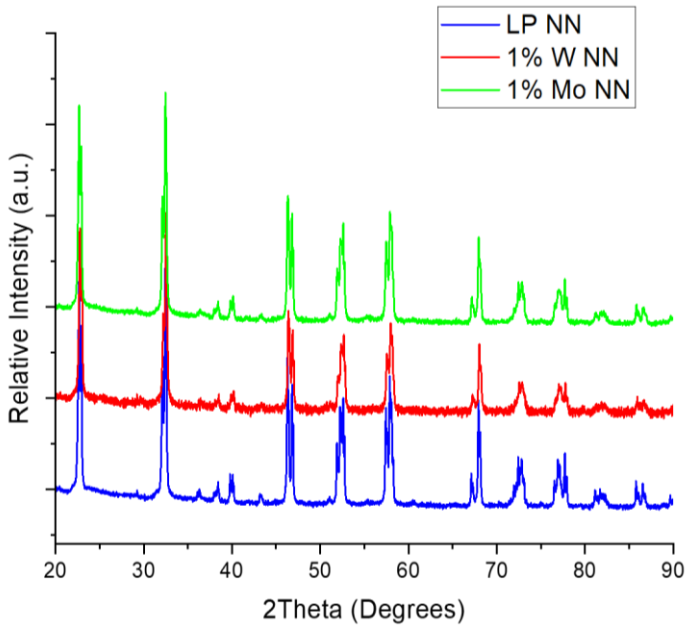

Figure 5.23: X-Ray Diffraction Patterns of B-Site Donor Doped NN Variants Compared to 'LP NN'

After a single calcination the 1% W and 1% Mo powders appear to be a mixture of the P (Pbma) and Q ($Pmc2_1$) phases of NN. No additional secondary phases are detected in the powder XRD patterns.

The diffraction patterns shown in Figure 5.23 have undergone Rietveld refinement and the results are summarised in table 5.11.

	Parameters	LP NN	1% W NN	1% Mo NN
P Phase (Pbma)	a / Å	5.57450(6)	5.56915(14)	5.57167(11)
	b / Å	15.51670(17)	15.5206(3)	15.51765(31)
	c / Å	5.51674(7)	5.51133(15)	5.51328(13)
	Cell Volume / Å^3	477.18611(2)	476.38035(4)	476.67392(4)
	Phase Fraction	0.655(9)	0.715(15)	0.502(8)
Q Phase (Pmc21)	a / Å	7.75949(26)	7.7817(11)	7.75729(15)
	b / Å	5.56788(22)	5.5775(11)	5.56767(10)
	c / Å	5.51122(22)	5.5204(9)	5.50510(12)
	Cell Volume / Å^3	238.1062(7)	239.5988(3)	237.76543(3)
	Phase Fraction	0.345(9)	0.285(15)	0.498(8)
Residuals	R_w / %	2.935	3.284	2.435
	χ^2	8.95	2.73	6.19

Table 5.11: Summary of Rietveld Refinements of B-Site Acceptor Doped NN Powders

The P and Q ratios determined *via* Rietveld refinements are shown below in Figure 5.24 compared to LP NN.

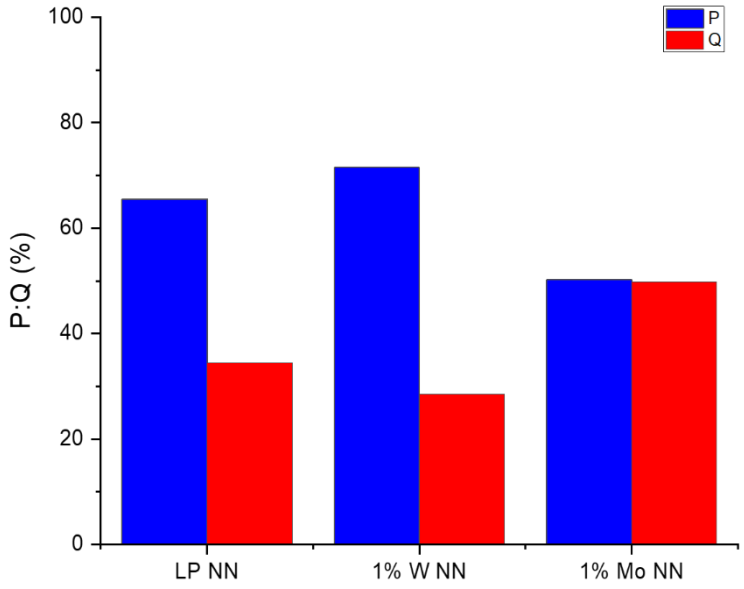

Figure 5.24: P:Q Ratios of B-Site Donor Doped NN Variants

1% W NN shows a similar P:Q ratio as LP NN indicating that tungsten has no significant effect on polymorphism preference. 1% Mo NN on the other hand showcases an approximately 50:50 ratio of the room temperature phases, as observed in other B-site doped variants. As W^{6+} and Mo^{6+} are both smaller than Nb^{5+} it would be expected that the tolerance factor would increase, and in turn stabilise the Q phase. However, as shown in table 5.10 the tolerance factor is unaffected at 1% doping.

To identify limits of the solid solution the XRD patterns of 5% and 10% dopant concentrations for W and Mo powders are shown in Figure 5.25.

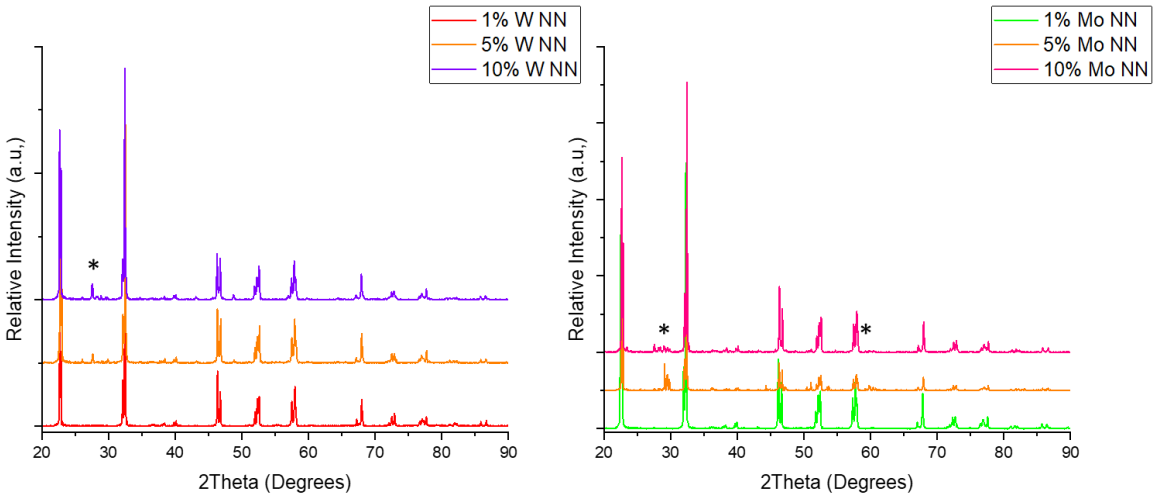

Figure 5.25: X-Ray Diffraction Patterns of Donor Doped NN Variants

The solid solution limits for donor doped NN variants appear generally very low. Both tungsten and molybdenum variants indicate the presence of secondary phases in both 5% and 10% variants indicated by a *. The secondary phases have been identified *via* phase analysis to be Na_2WO_4 and Na_2MoO_4.

5.2.2. Microstructure

The microstructure of 5, and 10% W and 1% Mo NN ceramics has been investigated *via* SEM-EDS analysis. The microstructure of the ceramics is shown below in Figure 5.26.

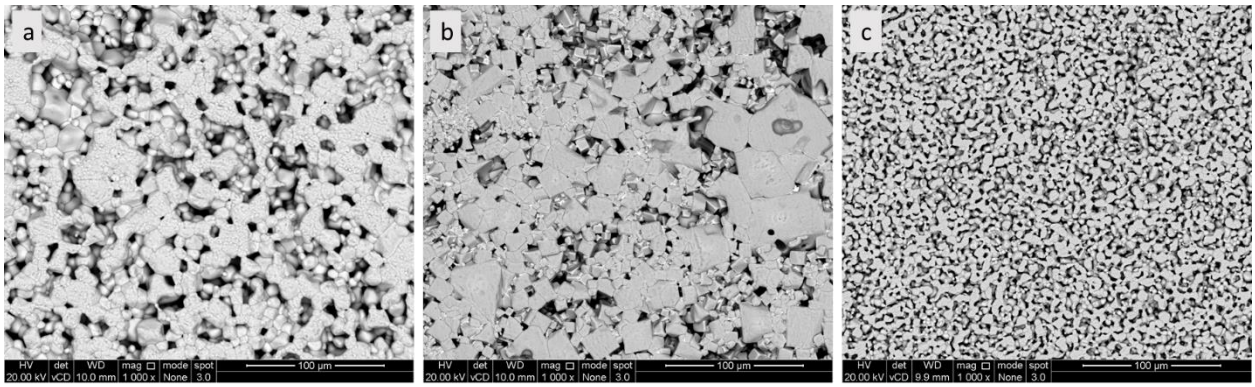

Figure 5.26: BSE Images of a) 5% W NN b) 10% W NN and c) 1% Mo NN Ceramics

The B-site donor doped ceramics suffer from extreme porosity. The 5% W NN ceramic appears to have a larger grain size than the 1% Mo NN counterpart, however as the samples are porous any grain size analysis may not be consistent with a less porous,

densified ceramic. At 10% W doping there is a slight improvement to density with a notable change in grain morphology appearing as a matrix of geometric cuboids (Figure 5.26b).

Elemental distribution throughout the ceramics has been assessed *via* EDS. The obtained EDS maps are shown below in Figures 5.27 – 5.29.

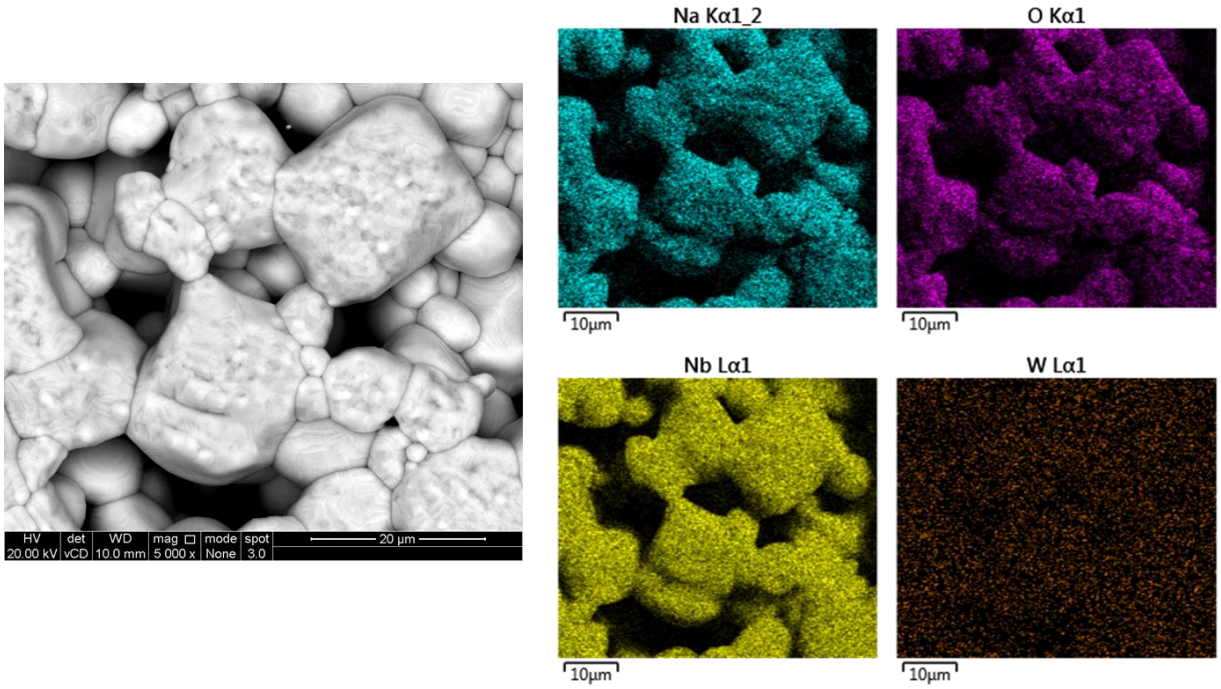

Figure 5.27: EDS Maps of 5% W NN Ceramic

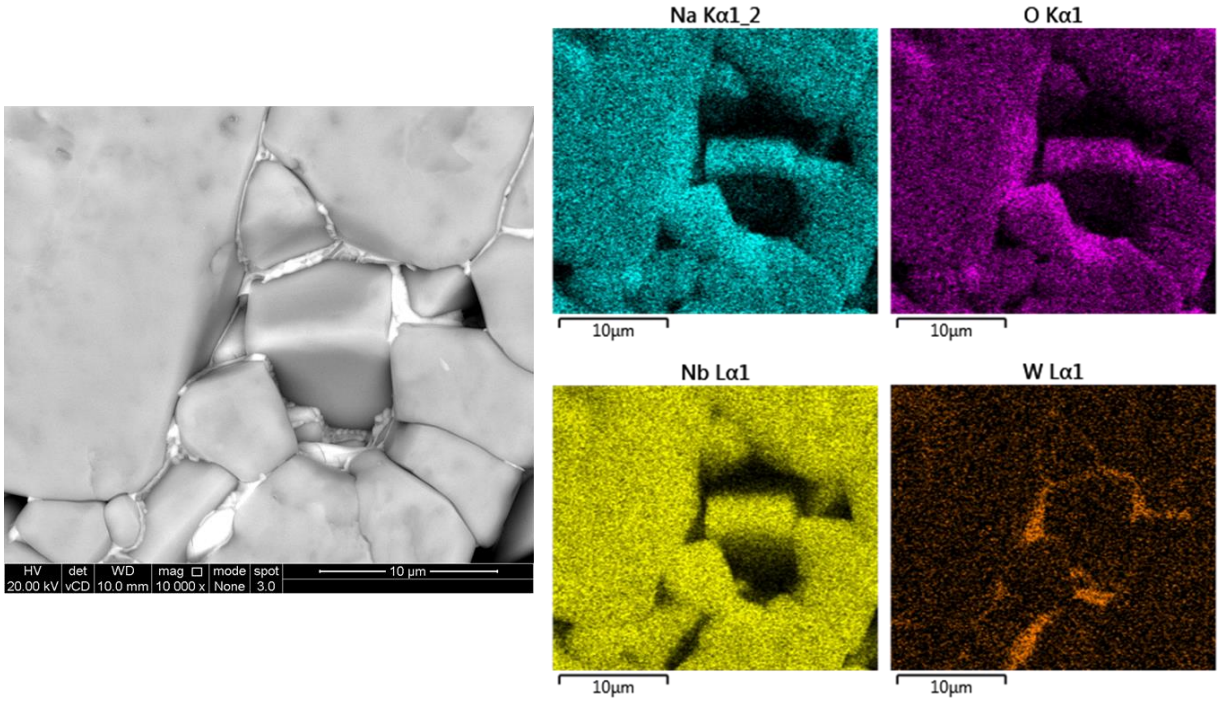

Figure 5.28: EDS Maps of 10% W NN Ceramic

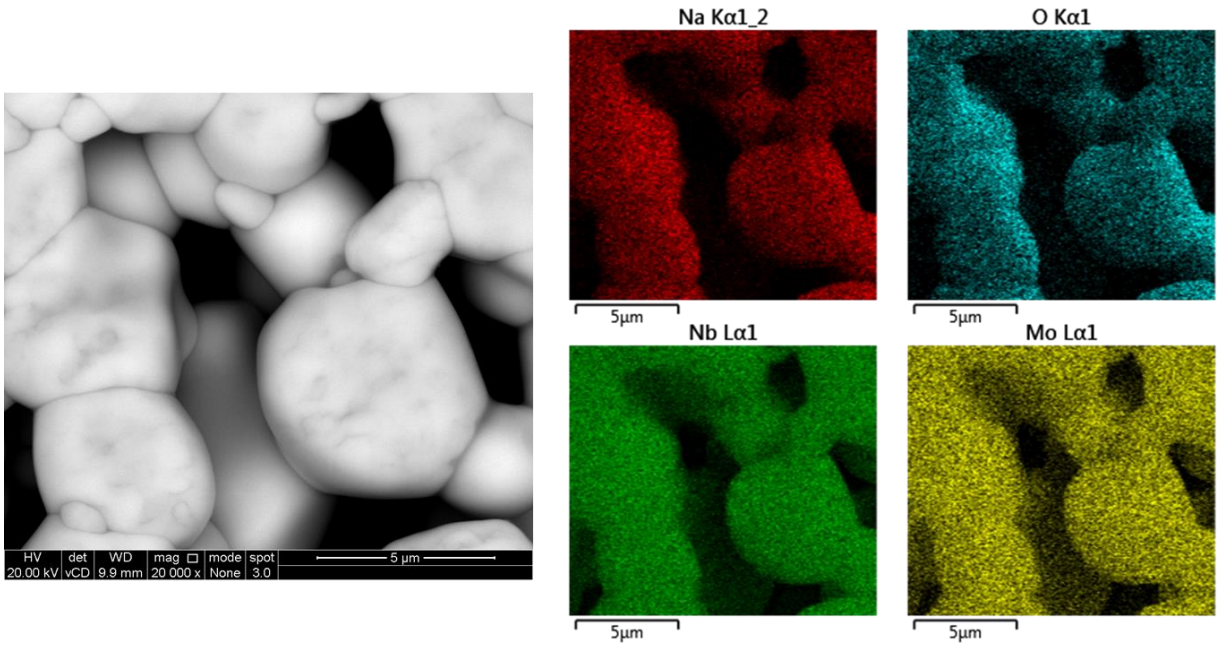

Figure 5.29: EDS Maps of 1% Mo NN Ceramic

No significant difference is observed between the grains and grain boundaries of the 5% W NN or 1% Mo NN ceramics. The 10% W NN ceramic showcases a clear increase in tungsten content in the lighter secondary phase observed along grain boundaries/in the voids between cubes. In order to quantify the elemental distribution throughout the ceramic, spot analysis has been conducted, the results are shown in table 5.12.

	Theoretical				Grain				Grain Boundary			
Composition	**Na / wt%**	**Nb / wt%**	**X / wt%**	**O / wt%**	**Na / wt%**	**Nb / wt%**	**X / wt%**	**O / wt%**	**Na / wt%**	**Nb / wt%**	**X / wt%**	**O / wt%**
5% W NN	13.94	55.78	5.44	29.16	12.50 ± 0.01	58.45 ± 0.01	3.70 ± 0.11	25.25 ± 0.02	11.80 ± 0.10	60.90 ± 0.30	4.10 ± 0.30	23.20 ± 0.30
10% W NN	13.29	48.34	10.63	27.75	12.20 ± 0.01	56.23 ± 0.01	6.23 ± 0.08	25.33 ± 0.02	8.77 ± 0.03	33.57 ± 0.02	41.17 ± 0.05	17.17 ± 0.03
1% Mo NN	14.02	56.08	0.59	29.32	13.97 ± 0.01	54.21 ± 0.01	0.00 ± 0.00	31.70 ± 0.01	11.70 ± 0.10	62.90 ± 0.30	0.50 ± 0.30	24.80 ± 0.30

Table 5.12: Average Composition of Grains and Grain Boundaries of 5% W, 10% W and 1% Mo NN Ceramics

The 5% W NN ceramic appears to be consistent in composition between grains and grain boundaries. The observed tungsten content is slightly lower than expected. In contrast, the 1% Mo NN ceramic only has molybdenum concentrated at the grain boundaries, although the associated errors are large, and it is possible that the molybdenum concentration falls below the detection limits of the spectrometer.

The 10% W NN ceramic showcases lower than expected tungsten concentrations in the grains, corresponding to an ~6% W doped bulk ceramic. The grain boundary regions showcase significant concentrations of tungsten as observed in Figure 5.28; this likely

corresponds to formation of a secondary phase. Table 5.13 shows the converted at% concentrations of the 10% W NN grain boundary.

	Theoretical				Secondary Phase			
Composition	**Na / at%**	**Nb / at%**	**W / at%**	**O / at%**	**Na / at%**	**Nb / at%**	**W / at%**	**O / at%**
10% W NN	20.04	17.97	2.00	59.99	18.79 ± 0.10	17.71± 0.30	10.76 ± 0.30	52.74 ± 0.30
Ratio	1	0.9	0.1	2.99	1.75	1.65	1	4.90

Table 5.13: Composition of Tungsten Rich Secondary Phase Identified in Figure 5.28

The determined at% indicate the secondary phase may be either Na_2WO_4, or the tungsten bronzes $NaWO_3$, $Na(W,Nb)O_3$.[6] In particular, the Nb:W ratio appears to be in line with the 8:5 phase shown in Figure 5.4

5.2.3. Relative Permittivity and Dielectric Losses

The relative permittivity and associated dielectric losses of the B-site donor doped NN ceramics has been assessed. The ε_r-T plots for the ceramics are shown below in Figure 5.30 and compared to LP NN.

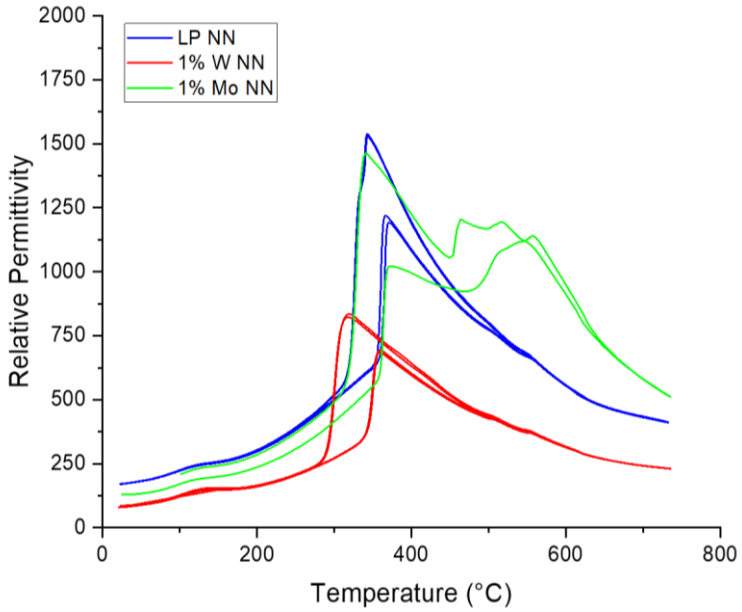

Figure 5.30: Temperature Dependence of Relative Permittivity of B-Site Donor Doped NN Variants at 100 kHz

The P-R phase transition in the 1% W NN ceramic shifts to slightly lower temperatures on cooling compared to LP NN. This may indicate a stabilisation of the higher temperature R phase. The 1% Mo NN ceramic exhibits permittivity in line with LP NN up to the P-R phase transition. After the transition the permittivity increases around 500 °C this effect is likely caused by increased space charge effects or a more pronounced impact of the R-S phase transition not typically pronounced in the permittivity plots of NN.[10]

The associated dielectric losses for the ceramics are shown in Figure 5.31.

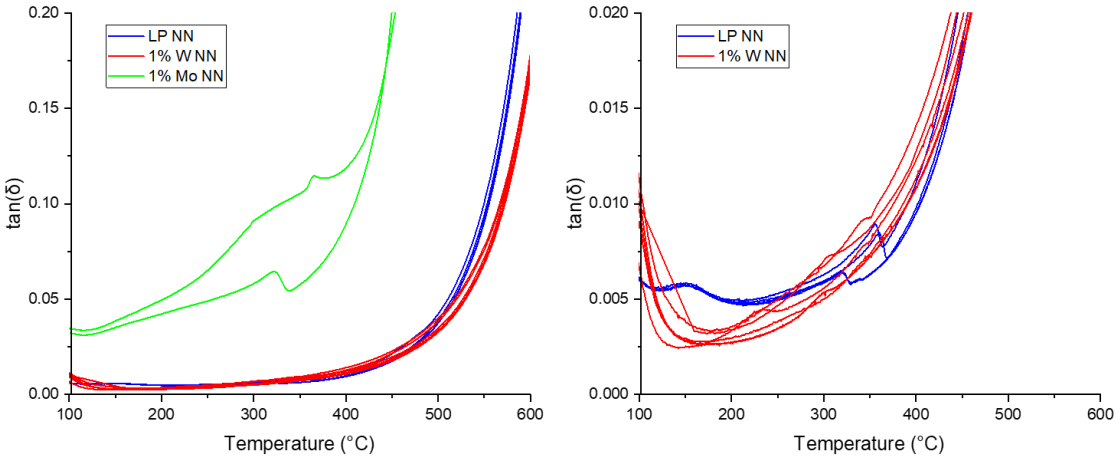

Figure 5.31: Dielectric Losses of B-Site Donor Doped NN Variants at 100 kHz

The dielectric losses of the 1% W NN ceramic are in line with LP NN with maximum losses around the P-R phase transition of ~1%. Conversely, the 1% Mo NN ceramic showcases more significant losses of ~12% around the P-R phase transition. Beyond 450 °C the dielectric losses for all NN ceramics rapidly increases due to increased space charge effects.

5.2.4. Impedance Spectroscopy

The electrical properties of B-site donor doped NN materials have undergone investigation *via* impedance spectroscopy. The overlaid M'' Z'' spectra of the tested ceramics have been used to extract conductivities and assess electrical homogeneity. The overlaid plots are shown below in Figure 5.32.

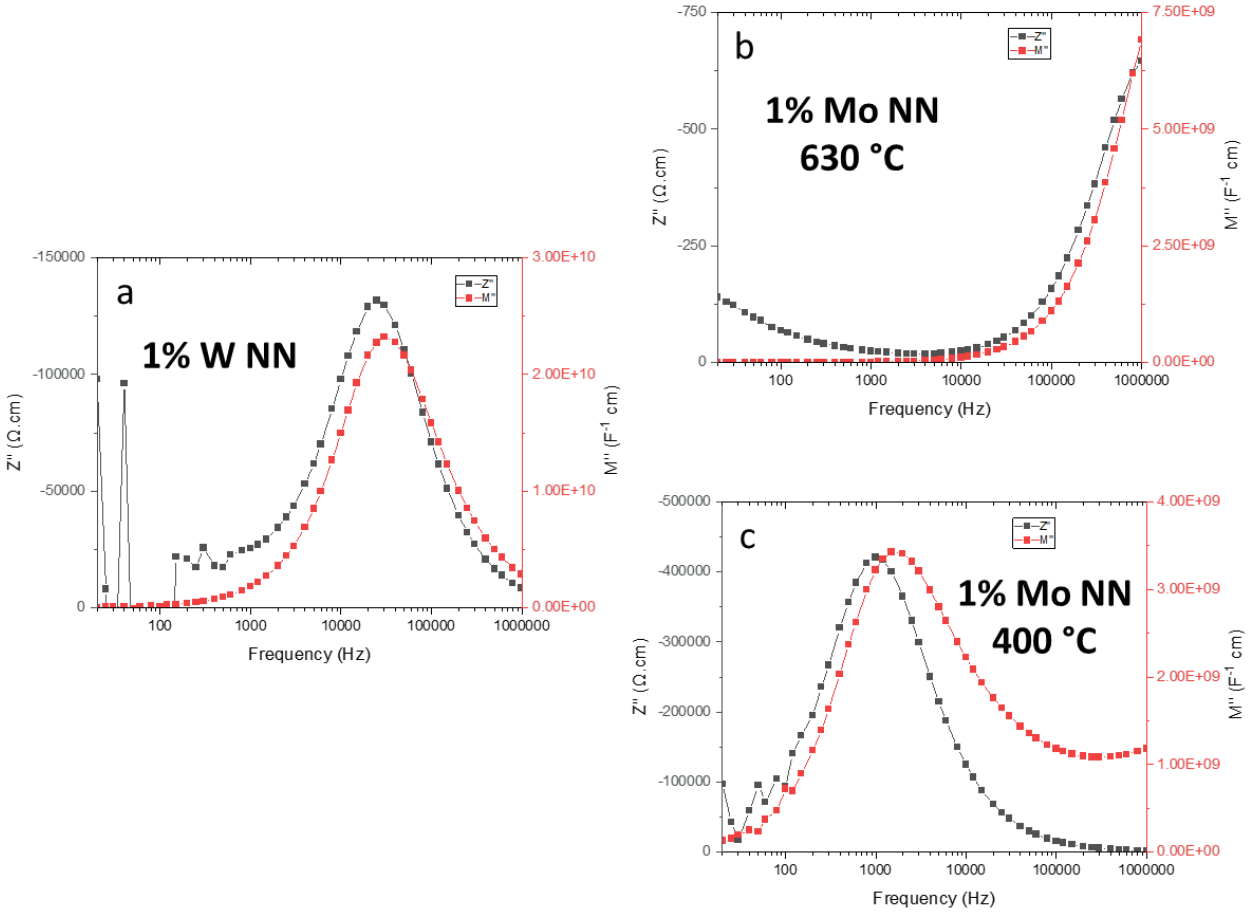

Figure 5.32: Overlaid M'' Z'' Plots of a) 1% W NN at 630 °C b) 1% Mo NN at 630 °C and c) 1% Mo NN at 400 °C

	Capacitance (Z'') / F cm^{-1}	Capacitance (M'') / F cm^{-1}	Corresponding Response
1% W NN	$5(5) \times 10^{-10}$	$2.2(1) \times 10^{-11}$	Bulk
1% Mo NN (400 °C)	$1.9(4) \times 10^{-10}$	$1.46(7) \times 10^{-10}$	Bulk

Table 5.14: Tabulated Capacitances from M'' and Z'' Spectra Extracted from Figure 5.32

The 1% W NN ceramic showcases good electrical homogeneity between M'' and Z'' responses showing a single peak in each plot corresponding to 1 RC element identified as the bulk electrical response. There is no significant increase in the low frequency response suggesting no ionic conductivity is present in the ceramic. At 630 °C the 1% Mo NN ceramic is significantly more conductive than 1% W NN with the bulk electrical response becoming too conductive to measure, there is a notable spike in the Z'' spectrum at low frequencies indicating the presence of ionic conductivity. At lower temperatures (400 °C) it becomes apparent that there is significant electrical heterogeneity. At higher frequencies there is an increase in M'' indicating a more complex equivalent circuit as opposed to a single, parallel RC element. Additionally, the distorted M'' and broad Z'' peaks shown in Figure 5.32c,

suggests multiple contributions to the response. Conversion of the capacitance extracted from the M'' of 1% Mo NN into relative permittivity shows ε_r=1649. This is greater than the permittivity reported in Figure 5.30, further indicating the contribution of an additional component to the M'' peak.

The conductivity of B-site donor doped NN variants has been extracted from the M'' peak when possible. In region 3 of 1% Mo NN, due to the high frequency of the peak in Figure 5.32b, the conductivity was extracted from the low intercept of the Z* as an approximation of the M'' response. The extracted conductivities are shown in the Arrhenius plot in Figure 5.33.

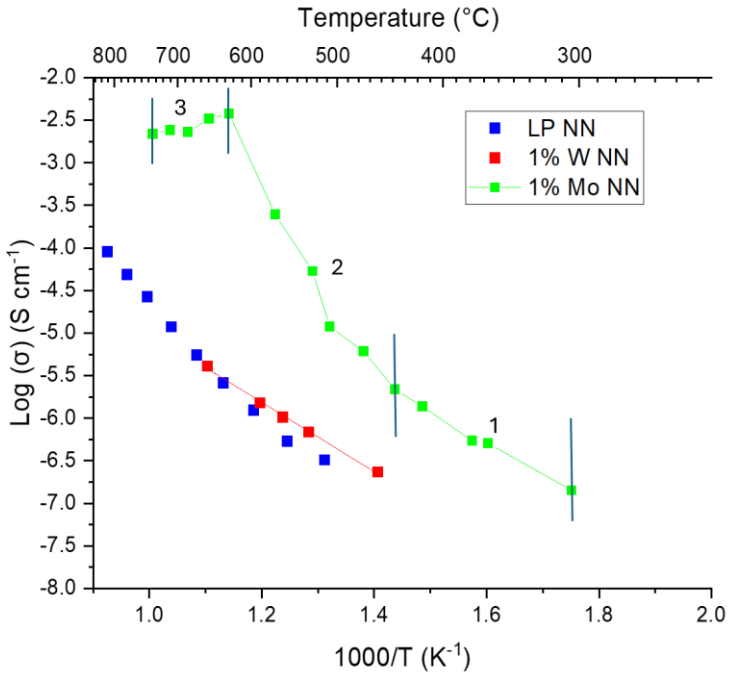

Figure 5.33: Arrhenius Plots of Extracted Conductivity of B-Site Donor Doped NN Variants

Composition	Low Temperature Ea / eV	High Temperature Ea / eV
LP NN	1.01 ± 0.10	1.52 ± 0.02
1% Mo NN	0.75 ± 0.03	N/A
1% W NN	0.81 ± 0.02	-

Table 5.15: Activation Energies of B-Site Donor Doped NN Variants Extracted from Figure 5.33

The 1% W NN ceramic showcases similar conductivity to LP NN with a notable decrease in the activation energy indicating a change in conduction mechanism. As there is no significant change in gradient as the Arrhenius moves to higher temperatures, the determined activation energy likely has extrinsic contributions.

The extracted conductivity of the 1% Mo NN ceramic has 3 distinct regions indicated in Figure 5.33:

1. Low temperature non-ionic region
2. Intermediate temperature transitionary region
3. High temperature region showcasing Warburg diffusion.

Figure 5.34 shows the Z* response of 1% Mo NN at 400 °C and 630 °C to showcase the emergence of Warburg diffusion in region 3.

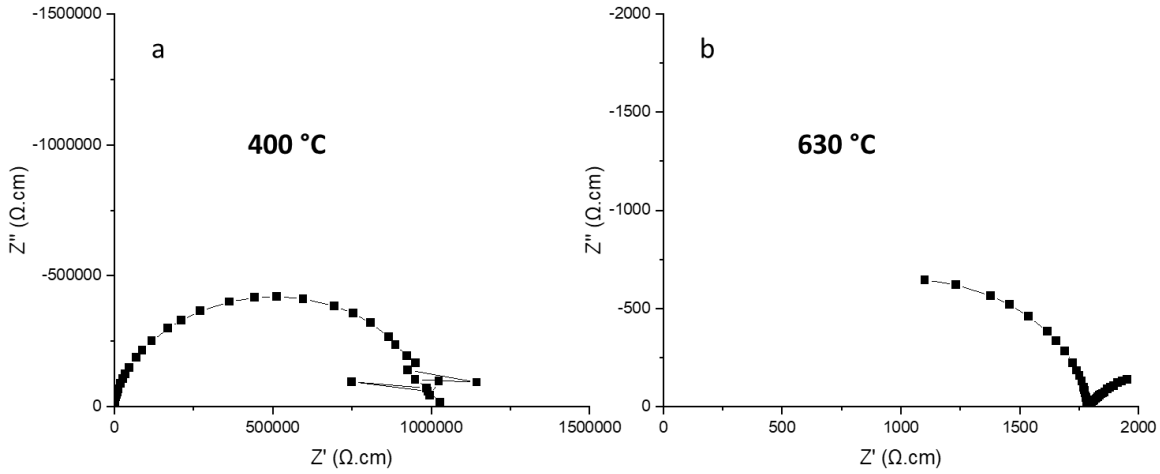

Figure 5.34: Z Spectra of 1% Mo NN at a) 400 °C and b) 630 °C*

In region 1 the observed conductivity is notably higher than the LP NN ceramic while showcasing no evidence of ionic conductivity. The activation energy is in line with the tungsten doped variant which may indicate a similar conduction mechanism but with a higher carrier concentration. As temperatures increase ionic conductivity is introduced to the ceramic and conductivity increases rapidly up to region 3 where the conductivity plateaus.

To further investigate the high conductivity of molybdenum doped NN, the total conductivity of 1, 5, and 10% Mo NN ceramics has been extracted from Z* and plotted in the Arrhenius plot shown in Figure 5.35.

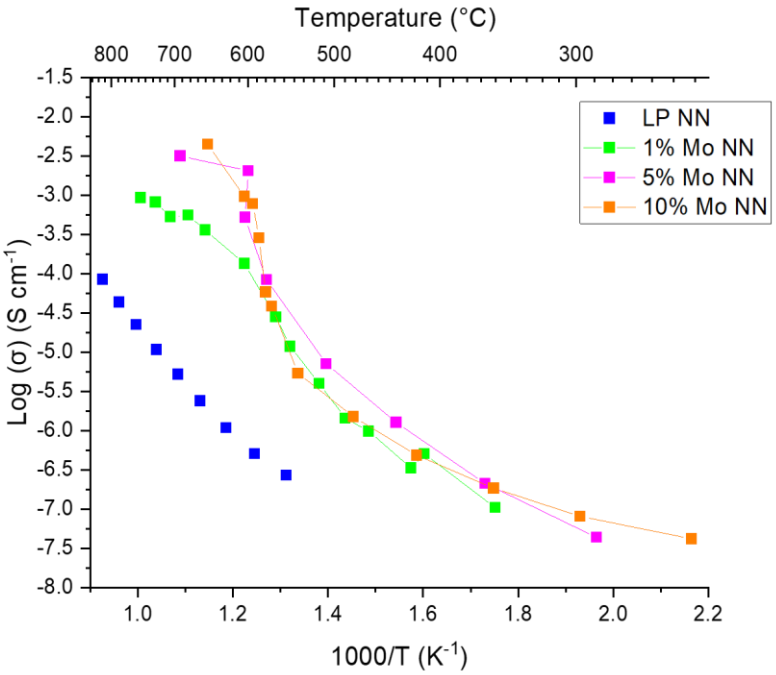

Figure 5.35: Arrhenius Plots of Total Conductivity of Mo Doped NN Variants

All molybdenum doped NN variants showcase a similar total conductivity at low temperatures, and all showcase the 3 distinct regions discussed above. However, 5% and 10% Mo NN showcase greater conductivity in the high temperature domain compared to 1% Mo. This may indicate that a maximum conductivity is achieved in the region of 1-5% Mo doping. Alternatively, the apparent maximum conductivity may be a consequence of parallel conduction pathways through the grain boundaries leading to shorting and therefore an additional (low) resistive element in the equivalent circuit. The electrical heterogeneity and apparent contribution of bulk and grain boundaries to the Z'' and M'' responses in Figure 5.32c is also showcased in the 5% Mo and 10% Mo NN ceramics.

This effect of increased conductivity is observed in 5 and 10% W NN ceramics as shown in Figure 5.36.

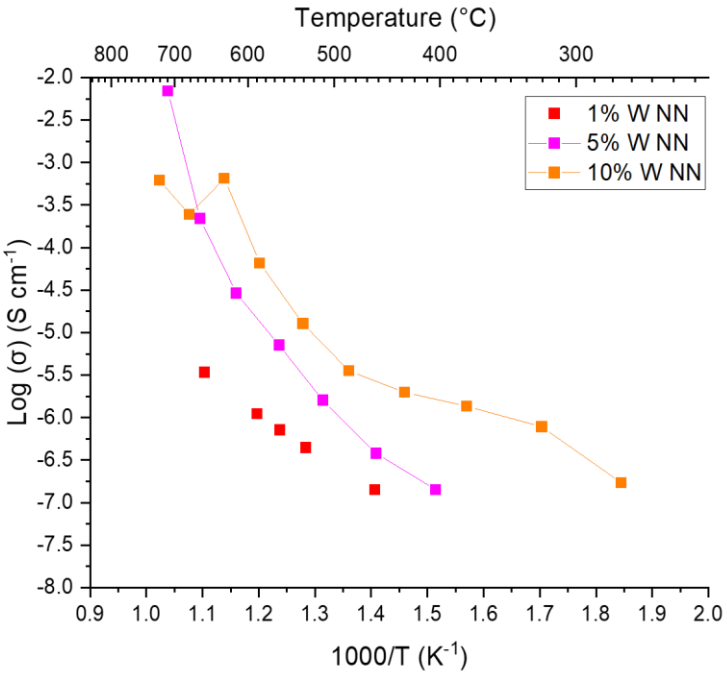

Figure 5.36: Arrhenius Plots of Total Conductivity of W Doped NN Variants Extracted from M''
N.B: High Temperature Bulk Conductivity for 5% and 10% W Determined via Low Z Intercept*

The 5% W NN ceramic showcases comparable bulk conductivity to 1% W NN at low temperatures before rapidly increasing, 10% W NN exhibits consistently higher total conductivity. The shapes of the Arrhenius plots and significant conductivity indicates that as with Mo doped NN ceramics, parallel pathways through grain boundaries are likely leading to short circuiting and artificially enhancing the conductivity.

The ceramics have had their pO_2 dependence assessed and the resultant impedance plots are shown below in Figures 5.37-5.39.

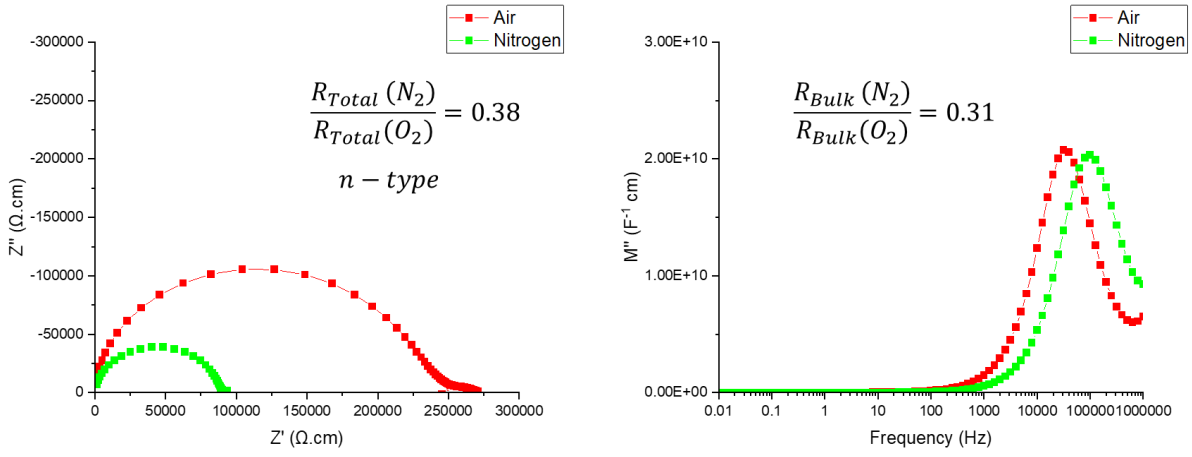

Figure 5.37: pO_2 Dependence of 1% W NN Ceramic at 650 °C

The 1% W NN ceramic showcases a significant drop in total resistance as pO_2 decreases indicating the presence of n-type conductivity. This drop in conductivity is mostly attributed to the bulk electrical response in which f_{max} is shifted to higher frequencies in low pO_2.

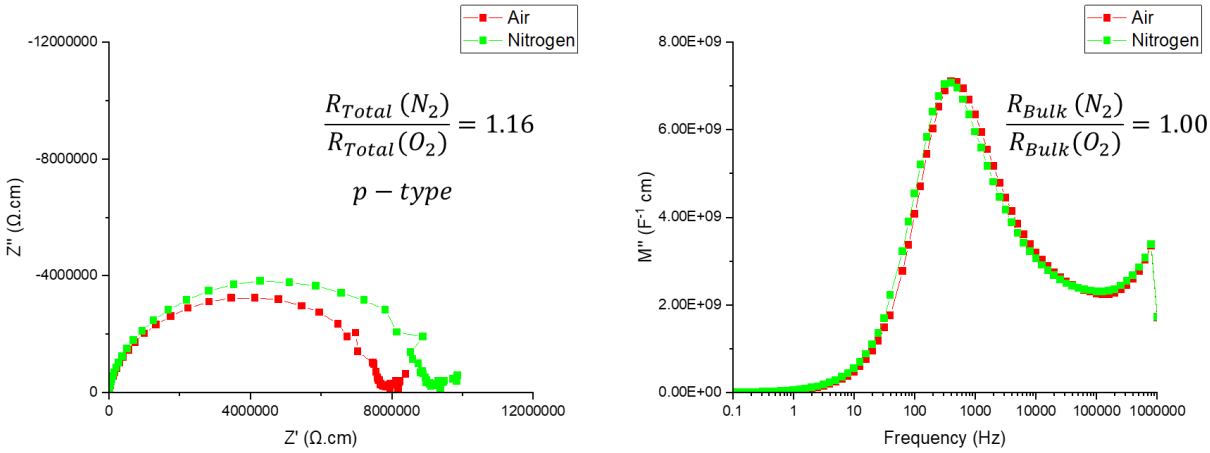

Figure 5.38: pO_2 Dependence of 1% Mo NN Ceramic at 360 °C

At 360 °C the 1% Mo NN ceramic exhibits an increase in total resistance as pO_2 decreases indicating the presence of p-type conductivity, however, the conductivity of the M'' response does not show any pO_2 dependence indicating that the p-type conductivity observed is due to additional extrinsic effects.

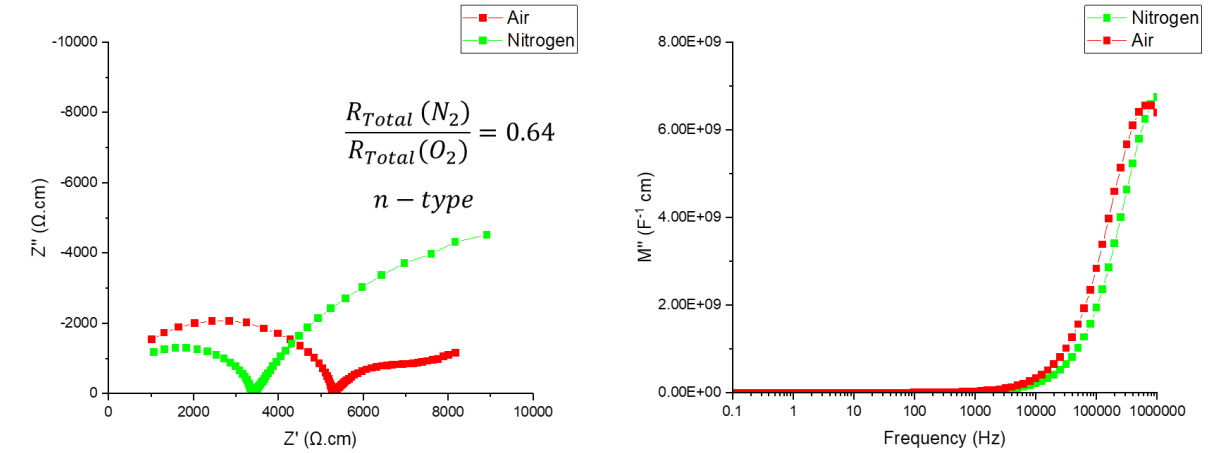

Figure 5.39: pO_2 Dependence of 1% Mo NN Ceramic at 600 °C

At 600 °C the 1% Mo NN ceramic is now in the high temperature region of the Arrhenius plot where a Warburg spike is observed. The total resistance decreases with pO_2 indicating a switch from p to n-type conductivity. This corresponds to an n-type response in the M'' associated with the phase responsible for the short circuit *via* the grain boundaries.

This confirms as with all other ionically conductive NN ceramics discussed in this thesis that the high conductivity region is attributed to mixed ionic-electronic conduction. Additionally, the observed pO_2 dependence of the electrode response may indicate that the observed ionic contribution is due to oxide ions.

Unfortunately, due to the poor densities and subsequent poor mechanical properties, the oxygen transport number for B-site donor doped NN ceramics could not be investigated *via* probostat measurements.

5.3. Discussion

5.3.1. Effects of B-Site Acceptor Doping on Polymorphism and Microstructure

Figure 5.8 showcases that gallium and titanium doping of NN leads to an increase in the concentration of the Q-phase of NN. Whereas magnesium doping showcases a slight decrease in Q-phase concentration compared to LP NN. As established in table 5.2, the influence of B-site doping in NN on the tolerance factor is minimal, indicating that the increase in concentration of the Q-phase is likely a consequence of increased oxide ion concentrations caused by the acceptor doping mechanism.[8,11]

Acceptor doping of the B-site generally shows a notable increase in density at sintering temperatures ~100 °C lower than undoped NN variants. Figure 5.9d shows that 1% Mg NN showcases a notable increase in the average grain size up to ~66 μm giving comparable grain sizes to the sodium-rich 51:49 and 55:45 NN variants discussed in chapter 3 (45-47 μm). Figures 5.9e and f show 5% Ga and 5% Ti NN variants showcase similar grain sizes to undoped conventionally processed NN variants.

The elemental distributions of all acceptor doped NN variants appears to be consistent throughout the grains and grain boundaries, of each material according to SEM maps (Figures 5.10-5.12). Table 5.4 shows the 1% Mg NN appears to showcase greater than expected concentrations of magnesium in grains and grain boundaries from EDS spot analysis, whereas gallium and titanium concentrations appear lower than expected.

Further investigation of the 1% Mg and 5% Ga NN ceramics *via* EPMA WDS analysis confirms notably lower concentrations of gallium in grains and grain boundaries suggesting that the solid solution of gallium in NN is generally low; greater concentrations at grain boundaries may be indicative of gallium volatility through grain boundaries, although further investigation would be needed to confirm this suggestion.

The 1% Mg NN ceramic showcases regions of the ceramic identified to be the columbite phase $MgNb_2O_6$ (Figure 5.13 and table 5.6), combined with the decrease in Q-phase concentration from the Rietveld refinements and it is likely that doping of the B-site with magnesium is minimal, and the niobium-rich columbite phase is preferentially forming.[12] This differs from the observed result with A-site doping where the apparent low solid solution limit is indicated by unreacted MgO on the surface of the ceramic (chapter 4).

5.3.2. Effects of B-Site Donor Doping on Polymorphism and Microstructure

Donor doping of the B-site has notably less of an impact on polymorphism in NN compared to acceptor doping. Figure 5.24 shows Q-phase concentrations slightly decrease when doping with tungsten yet increase when doped with molybdenum. Neither dopant ion causes a significant change in tolerance factor indicating that stabilisation/destabilisation is likely due to changes in oxygen vacancy concentrations.[11] 5% and 10% W/Mo variants show evidence of secondary phases present, indicating the limits of B-site donor doping concentrations are very low.

The B-site donor doped NN ceramics showcase very poor densities and as a result suffer from poor mechanical strength. Figures 5.27, 5.28 and 5.29 show that all donor doped ceramics show sodium deficiencies along grain boundaries. The 5% W NN ceramic appears to have consistent tungsten concentrations between grains and grain boundaries. As tungsten content increases, the grain structure changes significantly and appears as a matrix of geometric cuboids. This effect is observed in the sodium rich 55:45 NN ceramic, additionally, the determined tungsten concentration in the grains is indicative of up to 6% W doping. Any additional tungsten in the ceramic is incorporated into a secondary phases Na_2WO_4/$NaWO_3$/$Na(Nb,W)O_3$ along the grain boundaries.[6] This is supported in the XRD patterns where Na_2WO_4 is identified. This significant difference in observed stoichiometry *vs* expected suggests that the change in grain structure is a consequence of Na:Nb non-stoichiometry as discussed in chapter 3.

The molybdenum doped NN ceramic appears to have molybdenum exclusively along grain boundaries from EDS spot analysis. There is no significant evidence of molybdenum successfully incorporating into the structure of NN, it is therefore likely that a similar effect as discussed in the 10% W NN ceramic is occurring in molybdenum doped variants. It is therefore suggested that the increased concentration of the Q-phase in 1% Mo NN is a consequence of the Na:Nb non-stoichiometry increasing the tolerance factor to 0.970, and destabilising the P-phase.[8]

5.3.3. Effects of B-Site Doping on Permittivity

The variance of permittivity with B-site doping is significantly less than observed in A-site doping of NN and is more in line with undoped and non-stoichiometric NN. Figure 5.40 and table 5.16 show the change in temperature where ε_r is at a maximum (T_{Max}) on heating and cooling on B-site dopant species.

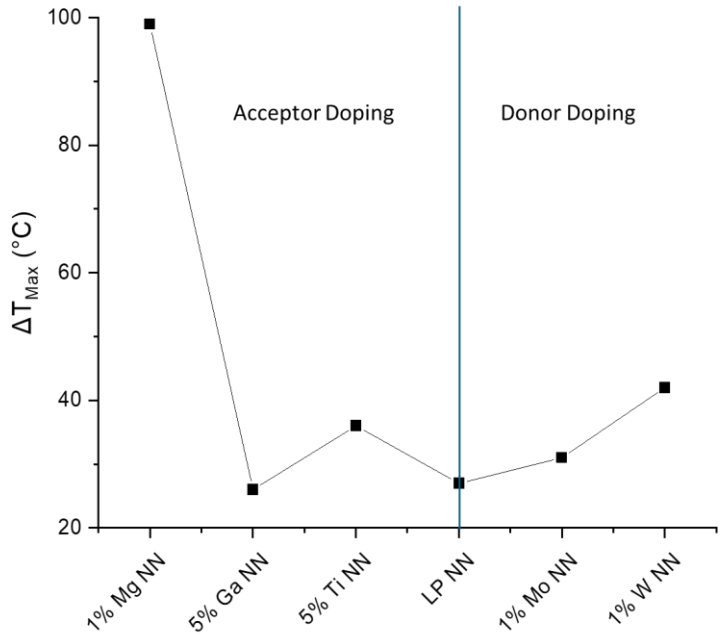

Figure 5.40: Change in ΔT_{Max} of B-Site Doped NN Ceramics

Composition	T_{max} (Heating) / °C	T_{max} (Cooling) / °C	ΔT_{Max} / °C	P-Phase / %	Q-Phase / %
1% Mg NN	423	324	99	74	26
5% Ga NN	364	338	26	53	47
5% Ti NN	332	296	36	43	57
LP NN	371	344	27	66	34
1% Mo NN	372	341	31	50	50
1% W NN	359	317	42	72	28

Table 5.16: Comparison of T_{Max} on Heating and Cooling in B-Site Doped NN Ceramics (σ_T = ±0.5°C)

ΔT_{Max} in B-site doped NN does not showcase significant variance with the exception of 1% Mg NN. The magnesium doped ceramic showcases generally low permittivity with a very large ΔT_{Max}. In chapter 4 it was shown that A-site doping, and A-site metal vacancies may cause a broadening of the hysteresis compared to LP NN. The broadening of the hysteresis in 1% Mg NN is primarily caused by an apparent stabilisation of the lower temperature P-phase on heating.

5% Ti NN showcases a ΔT_{Max} consistent with other B-site doped materials, however, the P-R phase transition is shifted to lower temperatures (~30 °C) indicating a stabilisation of the higher temperature R-phase on both heating and cooling.

The magnitude of ε_r in B-site doped NN is generally consistent with LP NN, with the exceptions of; 1% Mg NN which both showcase very low permittivity's more in line with 2.5% Ca NN discussed in chapter 4.

5.3.4. Effects of B-Site Doping on Conductivity

Acceptor doping of the B-site was utilised in an attempt to increase oxide ion conductivity through NN. The dopant ions used have decreasing ionic charge, it was hoped that decreasing the charge of the dopant ion would lead to a greater concentration of oxygen vacancies forming in NN, and in turn greater levels of oxide ion conduction.

Figure 5.18 shows that this is not the case as titanium and gallium doping exhibit the same bulk conductivity despite the expected stoichiometries indicating 5% Ga NN contains double the concentration of oxygen vacancies of 5% Ti NN. Acceptor doping with gallium and titanium lead to an increase in bulk conductivity and lowering of the activation energy in both the high and low temperature domains. However, the conductivity is comparable between the two, where according to the expected doping mechanism gallium would be notably more conductive. This may indicate that either:

1. Maximum vacancy concentrations are established at low doping concentrations.
2. More oxygen vacancies are forming in 5% Ga NN, but the conductivity is supressed due to pinning of the oxygen vacancies as acceptor dopants attract and form defect complexes limiting the mobility of oxygen vacancies:[13]

$$(Ti'_{Nb} - V_O^{\cdot\cdot})^{\cdot}$$

$$(Ga''_{Nb} - V_O^{\cdot\cdot})$$

While magnesium would be expected to showcase the highest conductivity, it exhibits no notable increase compared to LP NN. Figure 5.41 shows the C' vs frequency plot of the acceptor doped NN ceramics at 460 °C.

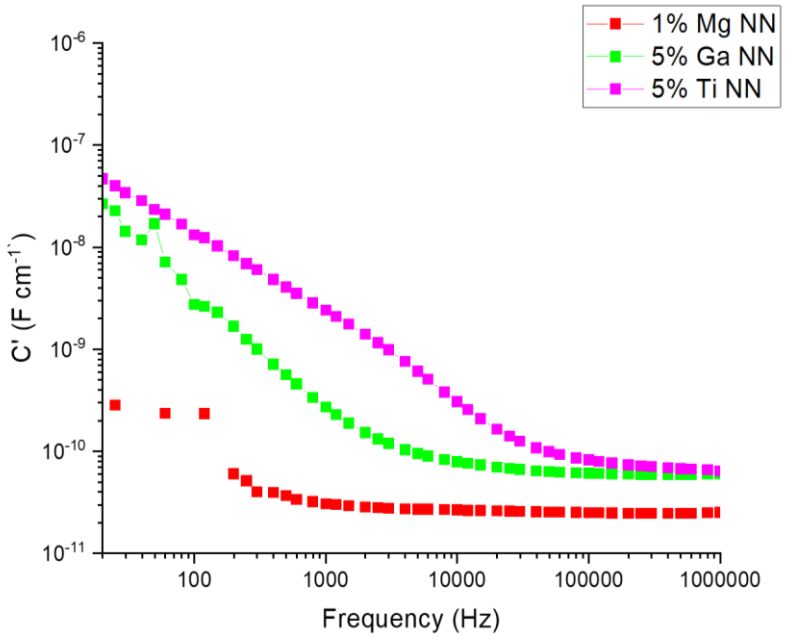

Figure 5.41: C' vs Frequency Plot of Acceptor Doped NN Ceramics at 460 °C.

Figure 5.41 shows that in 5% Ga and 5% Ti NN there is a notable increase in capacitance at lower frequencies giving rise to a Warburg spike, indicating the presence of ionic conductivity. In all cases the ionic conductivity presented is confirmed as oxide ions, *via* oxygen transport number measurements shown in Figure 5.22. All measured NN ceramics showcase mixed electronic-oxide ion conduction, indicated by transport numbers less than 1. 5% Ti NN showcases the greatest proportion of oxide ion conduction at 800 °C although this decreases with temperature, this differs from the work presented by Gouget *et. al.* discussed in the literature review, and the introduction of this chapter, where it is claimed that titanium acceptor doped NN is a pure oxide ion conductor at high temperatures.[2] This work has shown that 5% Ti NN is a mixed oxide ion-electronic conductor.

1% Mg NN does not show any notable increase in capacitance. Paired with the low oxygen transport number shown in Figure 5.22, there is strong evidence that ionic conductivity in the 1% Mg NN ceramic has been supressed. Paired with the preferential formation of $MgNb_2O_6$ previously discussed and the low Mg concentrations within grains it is suggested that Magnesium (as MgO) preferentially dopes the A-site of the perovskite and partially fills the sodium and oxygen vacancies.

$$4Na_{Na}^{x} + 2O_{O}^{x} \rightarrow 4V'_{Na} + 2V_{O}^{\cdot\cdot} + 2Na_2O_{(g)} \qquad (5.5)$$

$$4V'_{Na} + 2V_{O}^{\cdot\cdot} \rightarrow Mg_{Na}^{\cdot} + O_{O}^{x} + 3V'_{Na} + V_{O}^{\cdot\cdot} \qquad (5.6)$$

This mechanism would lead to an effective decrease in oxygen vacancies compared to LP NN, supressing ionic conductivity. Once the oxygen vacancies are filled the columbite phase may form. This leads to the nominally B-site magnesium doped NN exhibiting comparable conductivity to the A-site doped magnesium discussed in chapter 4. This is shown in the Arrhenius plot in Figure 5.42. This infers that there is negligible B-site doping of Mg in NN.

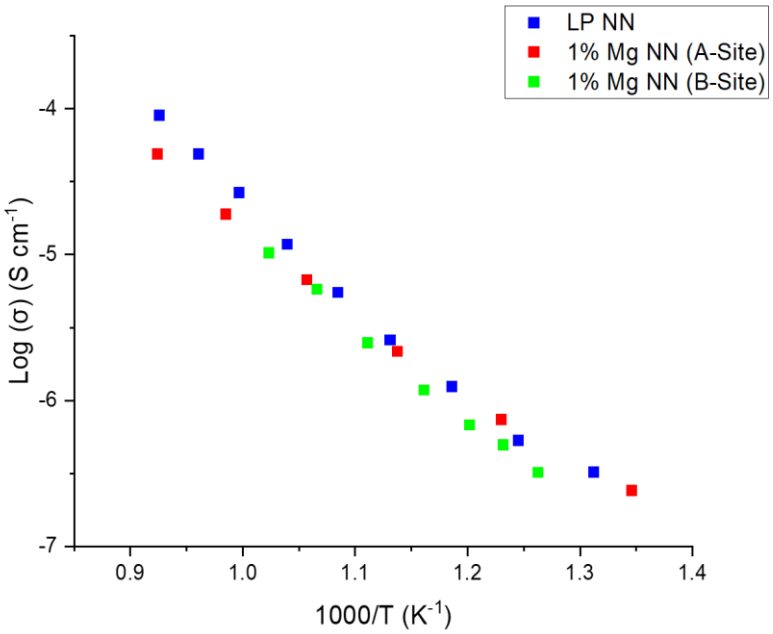

Figure 5.42: Comparison of A-Site vs B-Site Magnesium Doping Compared to LP NN

B-Site donor doped NN leads to differing electrical properties between W^{6+} and Mo^{6+}. The 1% W NN variant showcases comparable conductivity to LP NN, and both magnesium variants, with no significant evidence of ionic conduction, suggesting filling of oxygen vacancies according to the mechanism:

$$Nb^{5+} + \frac{1}{2}O^{2-} = W^{6+} \qquad (5.7)$$

Whereas the molybdenum doped variant showcases greater conductivity, before increasing further into the mixed conduction region at high temperatures. This is showcased in the summary Arrhenius plot in Figure 5.43.

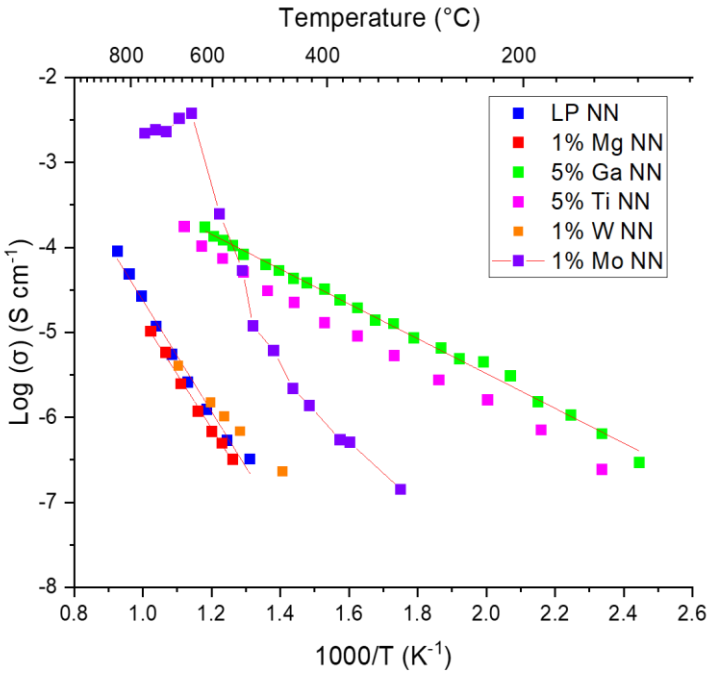

Figure 5.43: Summary Arrhenius of B-Site Doped NN Variants

The molybdenum doped NN ceramic at high temperatures showcases the greatest conductivity of any doped NN ceramic discussed in this thesis. The rapid increase in conductivity and electrical heterogeneity showcased in the Mo doped NN ceramics paired with the exclusive molybdenum occupation along grain boundaries may suggest that this abnormal behaviour showcased is a result of multiple parallel conduction pathways through the grain boundaries leading to a short circuit artificially enhancing the conductivity.

5% and 10% W NN showcases a similar trend attributed to the formation of secondary phases along the grain boundaries. The initial increase in bulk conductivity observed at lower temperatures may be due to Na:Nb non-stoichiometry arising from low solid solution limits for B-site doping. Tungsten doped NN variants are shown in the Arrhenius plot in Figure 5.44 compared to non-stoichiometric 51:49 NN (discussed in chapter 3).

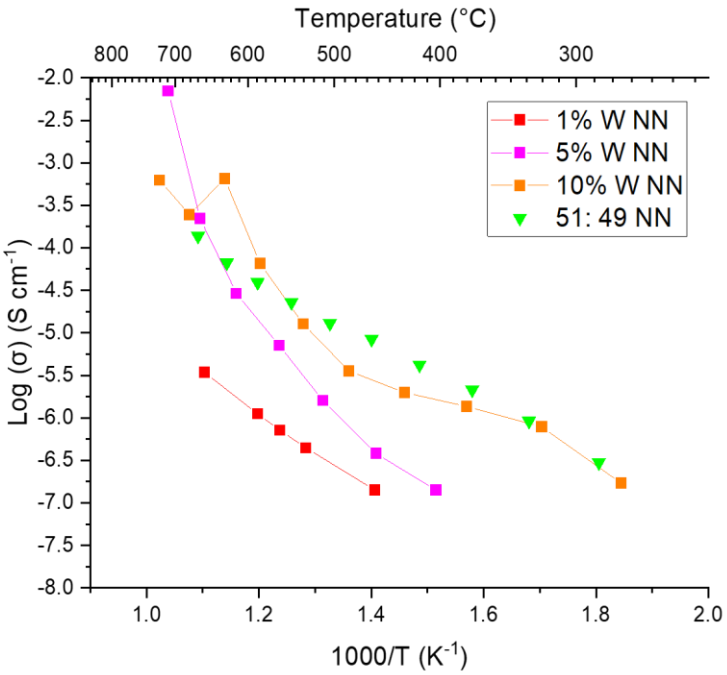

Figure 5.44: Arrhenius Plots of Bulk Conductivity Comparing Tungsten Doped NN to 51:49 NN

10% W NN showcases comparable conductivity to the bulk conductivity of 51:49 NN at lower temperatures, additionally the suggested stoichiometry of the grains from EDS indicated a maximum W dopant concentration of ~6%. Assuming this dopant concentration and a final stoichiometry of ~ABO_3 in the grains the 10% W NN ceramic bulk is more representative of $NaNb_{0.94}W_{0.06}O_{3.03}$ where the Na:Nb ratio is equal to 51:49.

The increased conductivity caused by shorting through the grain boundaries may be attributed to the conductive tungsten bronze secondary phases, and the spinel Na_2WO_4. The introduced ionic conductivity in the high temperature domain of 5 and 10% W NN ceramics may be attributed to the spinel secondary phase where t_{Na+}=1;[14] although additional investigation may be required for confirmation.

The comparable conductivities of the donor doped 1% Mg (A-site), acceptor targeted 1% Mg (B-Site) and the donor doped 1% W NN ceramics, may further indicate that the donor doping mechanism is preferentially targeted when doping with Mg^{2+}, although the conduction mechanisms differ as indicated by the activation energies (1% Mg NN-1.26 eV, 1% W NN – 0.81 eV ± 0.02). This difference may be a consequence of MgO compensating for soda loss and effectively maintaining ABO_3 stoichiometry *vs* W^{6+} doping directly onto the B-site. Both mechanisms lead to the reduction of oxygen vacancies, however, 1% W NN may still contain A-site metal vacancies and associated oxygen vacancies.

5.3.5. pO_2 Dependence of B-Site Doped NN

The pO_2 dependence of B-site doped NN ceramics is summarised in table 5.17.

Composition	$\frac{R_{Total}(N_2)}{R_{Total}(O_2)}$	Total Observed Response	$\frac{R_{Bulk}(N_2)}{R_{Bulk}(O_2)}$	Observed M'' Response
1% Mg NN	1.27	p	0.80	n
5% Ga NN	1.19	p	0.80	n
5% Ti NN	1.04	p	0.99	Independent
LP NN	0.96	n	0.99	Independent
1% W NN	0.38	n	0.31	n
1% Mo NN (Low T)	1.16	p	1.00	Independent
1% Mo NN (High T)	0.64	n	-	n

Table 5.17: Summarised pO_2 Dependence of B-Site Doped NN Ceramics

1% Mg and 5% Ga NN ceramics showcase p-type conductivity in the total response. The bulk response for the ceramics is n-type, as shown before this is likely a consequence of oxygen loss and reduction of the niobium ion:

$$O_O^x \rightarrow \frac{1}{2}O_{2(g)} + V_O^{\cdot\cdot} + 2e' \qquad (5.8)$$

$$2Nb_{Nb}^x + 2e' \rightarrow 2Nb'_{Nb} \qquad (5.9)$$

The p-type conductivity likely arises due to extrinsic effects caused by secondary phases arising from the low solid solution.

This effect is not observed in 5% Ti NN where the bulk response is pO_2 independent, as observed in LP NN. This would indicate that the conductivity in 5% Ti NN is 100% ionic, this contrasts the obtained oxygen transport number shown in Figure 5.22, which indicates mixed oxide ion-electronic conduction. This is a consequence of the slight p-type conductivity exhibited in the total response (table 5.17/Figure 5.20), as the probostat measurement cannot differentiate between grains and grain boundaries the obtained transport number corresponds to the overall ceramic.

Donor doping of the B-site using tungsten showcases notable n-type conductivity, likely according to the mechanism shown above. Conversely, donor doping with molybdenum at low temperatures showcase pO_2 independence before moving more in line with tungsten in the high temperature domain showcasing n-type conduction. However, as previously

discussed due to the electrical heterogeneity observed in 1% Mo NN, this behaviour is not fully attributed to the bulk electrical response of the ceramic.

5.4. Conclusions

The B-site of NN has been successfully doped according to acceptor and donor doping mechanisms. Although solid solution limits appear generally low. Acceptor doping typically leads to improvements in microstructure and ceramic density. In contrast, donor doping leads to very porous microstructures and low ceramic density. This trend may indicate that the generation of oxygen vacancies *via* dopant, or potentially *via* soda volatility, may be favourable to the sintering process in NN. Large Na:Nb non-stoichiometry in 10% W NN contributes to the formation of cuboidal grains.

No significant difference in relative stabilisation of phases occurred with the exception of titanium doping, where the higher temperature R-phase is stabilised on heating and cooling.

Acceptor doping of the B-site with either gallium or titanium leads to a notable increase in bulk conductivity; however, the oxygen transport number of both ceramics continue to showcase mixed electronic-oxide ion conductivity as observed in undoped NN variants, indicating that they are unsuitable for use as an ITSOFC electrolyte material.

Donor doping of the B-site showcases a difference between comparable concentrations of tungsten and molybdenum. No significant change in conductivity is observed with 1% tungsten doping. In contrast, 1% molybdenum doping showcases a notable increase in conductivity with no change in conduction mechanism. However, at higher temperatures molybdenum doped NN showcases ionic conduction, and the conductivity increases significantly. 5 and 10% W/Mo doping showcase greater conductivities across all temperatures, it is suggested that this is due to Na:Nb non-stoichiometry and the formation of tungsten/molybdenum bronzes at grain boundaries, leading to parallel conduction pathways and ‘shorting’ through the grain boundaries.

Targeted magnesium acceptor doping of the B-site generally appears to be unsuccessful. Poor conductivity and decreased oxygen transport number indicate magnesium may have preferentially doped onto the A-site of NN with excess magnesium preferentially forming the $MgNb_2O_6$ columbite phase.

The tolerance factor for all acceptor doped NN variants are similar with all chosen dopants having good size agreement with the Nb^{5+} cation. However, only magnesium appears to preferentially dope onto the A-site, the reasons for this are explored further in chapter 6; gallium doping of NN.

5.5. References

1. Gouget, G. *et al.* High Ionic Conductivity in Oxygen-Deficient Ti-Substituted Sodium Niobates and the Key Role of Structural Features. *Chem. Mater.* **31**, 2828–2841 (2019).

2. Gouget, G. *et al.* Associating and Tuning Sodium and Oxygen Mixed-Ion Conduction in Niobium-Based Perovskites. *Adv. Funct. Mater.* **30**, 1–12 (2020).

3. Shi, H., Lu, M., Lan, B. & Zhang, C. Effects of (Mo/W, N) codoping on electronic structures of $NaNbO_3$ based on hybrid density functional calculations. *Mod. Phys. Lett. B* **32**, 1–10 (2018).

4. Roth, R. S. & Waring, J. L. Phase equilibria as related to crystal structure in the system niobium pentoxide-tungsten trioxide. *J. Res. Natl. Bur. Stand. Sect. A Phys. Chem.* **70A**, 281 (1966).

5. West, A. R. *Basic Solid State Chemistry*. (John Wiley & Sons, Ltd, 1999).

6. Dickens, P. G. & Whittingham, M. S. The tungsten bronzes and related compounds. *Q. Rev. Chem. Soc.* **22**, 30–44 (1968).

7. Wold, A., Kunnmann, W., Arnott, R. J. & Ferretti, A. Preparation and Properties of Sodium and Potassium Molybdenum Bronze Crystals. *Inorg. Chem.* **3**, 545–547 (1964).

8. Guo, H., Shimizu, H., Mizuno, Y. & Randall, C. A. Strategy for stabilization of the antiferroelectric phase (Pbma) over the metastable ferroelectric phase (P21ma) to establish double loop hysteresis in lead-free (1-x)$NaNbO_3$ -x $SrZrO_3$ solid solution. *J. Appl. Phys.* **117**, 214103 (2015).

9. Shannon, R. D. Revised effective ionic radii and systematic studies of interatomic distances in halides and chalcogenides. *Acta Crystallogr. Sect. A Cryst. physics, diffraction, Theor. Gen. Crystallogr.* **32**, 751–767 (1976).

10. Megaw, H. D. The Seven Phases of Sodium Niobate. *Ferroelectrics* **7**, 87–89 (1974).

11. Shakhovoy, R. A. *et al.* Ferroelectric Q and antiferroelectric P phases' coexistence and local phase transitions in oxygen-deficient $NaNbO_3$ single crystal: Micro-Raman, dielectric and dilatometric studies. *J. Raman Spectrosc.* **43**, 1141–1145 (2012).

12. Ananta, S., Brydson, R. & Thomas, N. W. Synthesis, formation and Characterisation of $MgNb_2O_6$ Powder in a Columbite-like Phase. *J. Eur. Ceram. Soc.* **19**, 355–362

(1999).

13. Yang, F., Wu, P. & Sinclair, D. C. Electrical conductivity and conduction mechanisms in $(Na_{0.5}Bi_{0.5}TiO_3)_{1-x}(BiScO_3)_x$ ($0.00 \leq x \leq 0.25$) solid solutions. *J. Mater. Chem. C* **6**, 11598–11607 (2018).

14. Bottelberghs, P. H. & Everts, E. Charge carriers and dc polarization phenomena in solid Na_2WO_4. *J. Solid State Chem.* **14**, 342–348 (1975).

Chapter 6. Gallium Doping of $NaNbO_3$

The apparent preference for A-site donor doping expressed by magnesium doped NN is not shown in 5% Ga or 5% Ti NN ceramics, where bulk conductivities and oxygen transport numbers increase significantly. All acceptor dopants selected in chapter 5, have comparable ionic radii with the Nb^{5+} ion.[1] Therefore, showcased preferences for doping would either apply to all 3 dopants if ionic size and associated tolerance factor are the primary limitations for B-site doping. Alternatively, the apparent preference may be due to charge concerns as Mg^{2+} is notably lower than Nb^{5+}.

This phenomenon of doping preference has not been previously reported in respect to NN. However, a similar phenomenon is showcased in aluminium doped $(Na,K)_{0.5}Bi_{0.5}TiO_3$ (NKBT) where at sufficient concentrations of aluminium dopant a 12 coordinate site emerges in the ^{27}Al MAS NMR spectra, shown in Figure 6.1.[2]

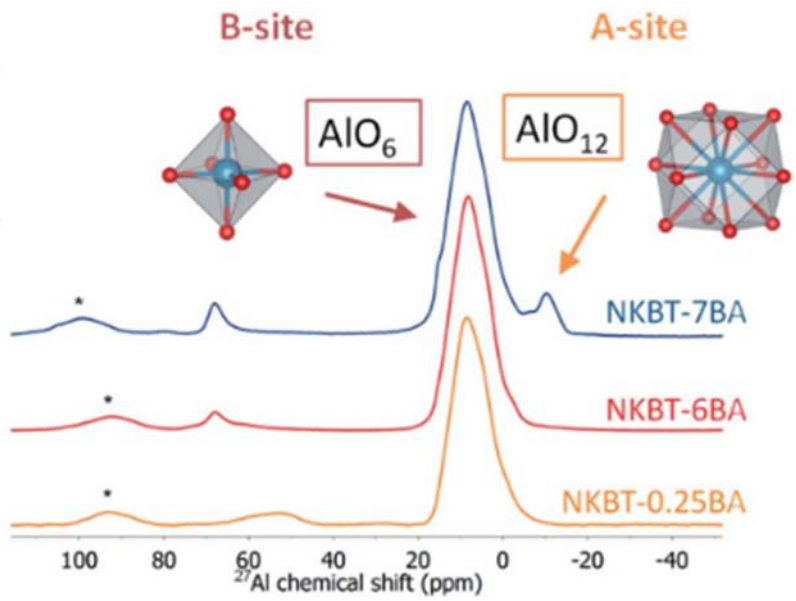

Figure 6.1: ^{27}Al MAS NMR Spectra of Al-doped NBT (Taken from Groszewicz, P et. al.)[2]

As previously discussed in chapter 4, aluminium, like magnesium and gallium may typically be considered too small to dope onto the A-site of a perovskite and does not formally have an agreed 12 coordinate ionic radius.[1] The NMR study of Al-NKBT showcases that intermediate size cations may, under certain circumstances, dope onto the A-site of a perovskite. In this case, up to 5% of Al^{3+} cations may substitute on the A-site in NKBT-7BA with any excess going towards the formation of secondary phases.[2]

In gallium doped NN, $NaGaO_2$ may form as a secondary phase. $NaGaO_2$ exists in 2 forms. α-$NaGaO_2$ which has a layered-rocksalt structure, with hexagonal symmetry; and β-$NaGaO_2$

which has wurtzite structure with orthorhombic symmetry. These 2 phases of $NaGaO_2$ interchange with each other, at high pressures (0.5-5.0 GPa) the $\beta \rightarrow \alpha$ phase transition is observed, and above 200 °C the $\alpha \rightarrow \beta$ phase transition is observed.[3] Given the relatively low pressures involved in conventional solid state synthesis used for all gallium doped NN variants, it is therefore unlikely that the metastable α-$NaGaO_2$ would form. β-$NaGaO_2$ is commonly used as a precursor for ion exchange reactions used to produce semiconducting materials, although electrical characterisation of β-$NaGaO_2$ appears to be limited.[4]

This chapter focuses exclusively on gallium doping, in an attempt to elucidate the potentially competing doping mechanisms in B-site targeted NN.

6.1. Gallium Doping of NN

In order to further investigate the doping mechanisms of NN, and to attempt further increases in the bulk conductivity, the 0-10% Ga range of doped NN was synthesised. Low level gallium doping (0.1 and 0.5% Ga) was utilised to try and understand the doping mechanisms at play, while the range 1-10% Ga was utilised to understand the influence of increasing dopant concentration and determine the limits of the solid solution. The samples tested and associated tolerance factors are listed in table 6.1:

Composition	Abbreviation	Tolerance Factor	Reagents and Conditions Required for Single Phase Powders
$NaNb_{0.999}Ga_{0.001}O_{2.999}$	0.1% Ga NN	0.967	Na_2CO_3 (99.98%) Nb_2O_5 (99.85%) Ga_2O_3 (>99.99%) Calcined 900 °C 2 Hours Sintered 1240 °C 4 Hours
$NaNb_{0.995}Ga_{0.005}O_{2.995}$	0.5% Ga NN	0.967	
$NaNb_{0.99}Ga_{0.01}O_{2.99}$	1% Ga NN	0.967	
$NaNb_{0.98}Ga_{0.02}O_{2.98}$	2% Ga NN	0.967	
$NaNb_{0.97}Ga_{0.03}O_{2.97}$	3% Ga NN	0.967	
$NaNb_{0.96}Ga_{0.04}O_{2.96}$	4% Ga NN	0.967	
$NaNb_{0.95}Ga_{0.05}O_{2.95}$	5% Ga NN	0.968	
$NaNb_{0.94}Ga_{0.06}O_{2.94}$	6% Ga NN	0.968	
$NaNb_{0.93}Ga_{0.07}O_{2.93}$	7% Ga NN	0.968	
$NaNb_{0.92}Ga_{0.08}O_{2.92}$	8% Ga NN	0.968	
$NaNb_{0.91}Ga_{0.09}O_{2.91}$	9% Ga NN	0.968	
$NaNb_{0.90}Ga_{0.10}O_{2.90}$	10% Ga NN	0.968	

Table 6.1: Compositions of Gallium Doped NN Variants with Reagents and Processing Conditions

Doping with gallium up to 10% B-site occupation has no significant effect on the tolerance factor of NN.

For clarity, the 0.1, 0.5 and 1% Ga NN ceramics are primarily discussed in this chapter and compared to LP NN and the 5% Ga NN ceramic discussed in chapter 5.

6.1.1. Phase Purity and Polymorphic Assemblage

The phase purity and polymorphic assemblage of gallium doped NN variants have been investigated *via* x-ray diffraction. The obtained diffraction patterns are shown in Figure 6.2.

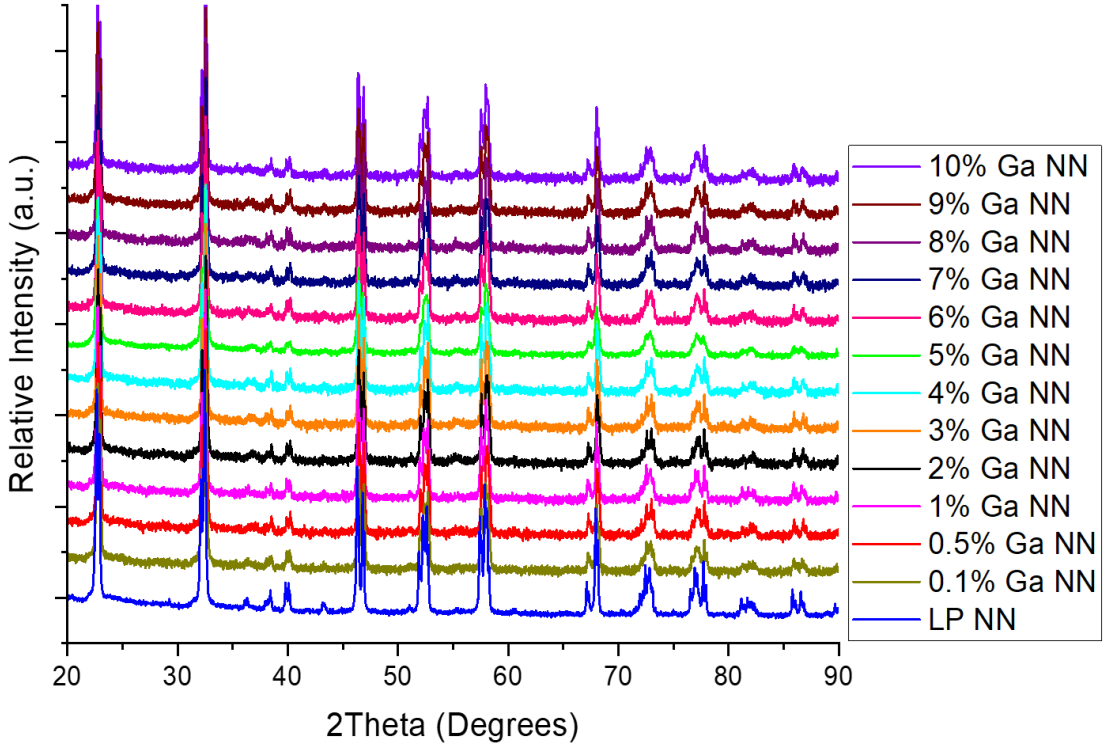

Figure 6.2: X-Ray Diffraction Patterns of Gallium Doped NN Powders Compared to 'LP NN'

As gallium concentration increases no obvious additional phases form, and the system remains a mixture of P and Q phases. The XRD patterns in Figure 6.2 have undergone Rietveld refinements, and the determined parameters are shown in table 6.2

	Parameters	LP NN	0.1% Ga NN	0.5% Ga NN	1% Ga NN	2% Ga NN	3% Ga NN	4% Ga NN	5% Ga NN	6% Ga NN	7% Ga NN	8% Ga NN	9% Ga NN	10% Ga NN
P Phase (Pbma)	a / Å	5.57450(6)	5.56503(24)	5.56871(10)	5.57000(15)	5.56713(10)	5.56805(9)	5.56727(13)	5.56278(23)	5.56635(20)	5.56650(15)	5.56777(13)	5.56625(17)	5.56717(16)
	b / Å	15.51670(17)	15.5154(9)	15.51648(27)	15.5147(4)	15.51435(28)	15.51632(26)	15.5134(3)	15.5292(6)	15.5158(7)	15.5134(4)	15.5142(4)	15.5140(5)	15.5132(4)
	c / Å	5.51674(7)	5.50591(30)	5.50494(10)	5.51184(16)	5.50387(10)	5.50480(9)	5.50419(13)	5.50785(24)	5.50583(23)	5.50417(15)	5.50456(14)	5.50489(18)	5.50630(16)
	Cell Volume / $Å^3$	477.18611(2)	475.40046(9)	475.66412(3)	476.31601(5)	475.37147(3)	475.59075(3)	475.38195(4)	475.79850(7)	475.51857(7)	475.31448(5)	475.48113(4)	475.37369(6)	475.54952(5)
	Phase Fraction	0.655(9)	0.512(15)	0.716(15)	0.495(14)	0.489(10)	0.545(10)	0.56(15)	0.528(21)	0.526(12)	0.567(13)	0.578(10)	0.547(13)	0.517(11)
Q Phase (Pmc21)	a / Å	7.75949(26)	7.7563(4)	7.7698(6)	7.76125(24)	7.7633(4)	7.7655(4)	7.7609(4)	7.7727(5)	7.7570(4)	7.7603(3)	7.75627(28)	7.7588(4)	7.75949(22)
	b / Å	5.56788(22)	5.51561(27)	5.5756(5)	5.57446(21)	5.57198(27)	5.5733(3)	5.57283(27)	5.5700(4)	5.57265(20)	5.57246(24)	5.57345(17)	5.57254(23)	5.57264(16)
	c / Å	5.51122(22)	5.57149(21)	5.5163(5)	5.51754(24)	5.51196(29)	5.5146(4)	5.51454(30)	5.5167(5)	5.51658(27)	5.51459(26)	5.51557(20)	5.51560(26)	5.51570(19)
	Cell Volume / $Å^3$	238.1062(7)	238.35239(8)	238.9732(1)	238.71514(7)	238.43059(9)	238.6689(1)	238.50483(9)	238.8397(1)	238.46546(8)	238.47272(7)	238.43359(6)	238.47371(8)	238.50353(5)
	Phase Fraction	0.345(9)	0.488(15)	0.284(15)	0.505(14)	0.511(10)	0.455(10)	0.44(15)	0.472(21)	0.474(12)	0.433(13)	0.422(10)	0.453(13)	0.483(11)
Residuals	R_w / %	2.935	3.935	3.429	3.425	3.407	3.384	3.473	2.033	3.975	3.474	3.984	3.522	3.553
	χ^2	8.95	4.11	3.10	3.05	3.01	2.93	3.10	2.61	3.97	3.01	3.88	3.05	3.03

Table 6.2: Summary of Rietveld Refinements for Gallium Doped NN Powders

The determined P:Q ratios of gallium doped NN are shown in Figure 6.3 and compared to LP NN (x=0).

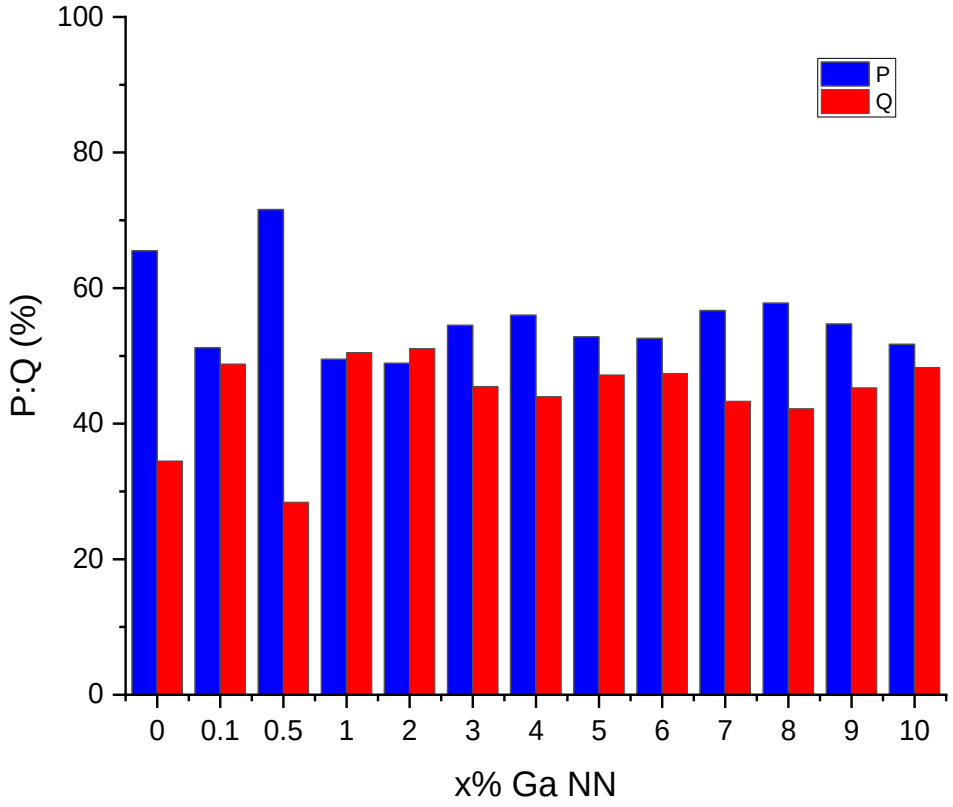

Figure 6.3: Ratio of P:Q Phases in Gallium Doped NN Powders Obtained from Rietveld Refinement

The P:Q ratio remains reasonably consistent as gallium concentration increases, with the amount of Q-phase increasing *vs* 'LP NN'. The only exception to this is the 0.5% Ga NN sample, where Q-phase decreased slightly compared to 'LP NN'.

The determined cell parameters of the P and Q phases has been determined *via* Rietveld refinement and the variance is show below in Figure 6.4.

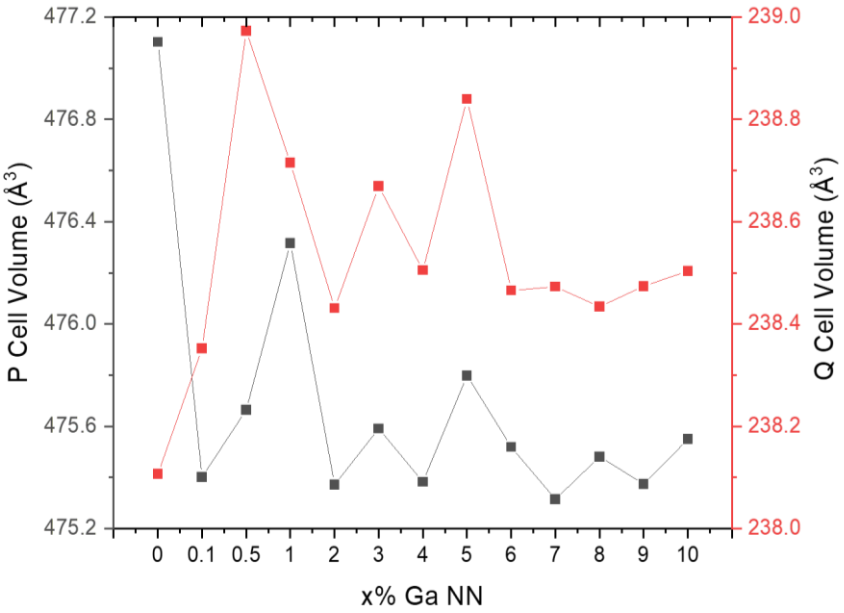

Figure 6.4: Variance of P and Q Phase Cell Volumes in Gallium Doped NN

On addition of 0.1% Ga the P-phase unit cell contracts by ~2 Å^3. As the concentration increases from 0.1 to 0.5% Ga a slight expansion of the cell is observed. This continues up to 1% Ga prior to a final contraction of the P-phase unit cell, beyond 2% Ga the variance in the unit cell is minimal (~0.4 Å^3).

Initially, the Q-phase unit cell expands as small concentrations of gallium dopant increase, up to a total expansion of ~1 Å^3 at 0.5% Ga. Beyond this concentration the Q-phase varies minimally (~0.4 Å^3), before fully stabilising around 238.5 Å^3.

6.1.2. Microstructure

The microstructure of 0.1, 0.5, and 1% Ga NN ceramics has been investigated *via* SEM-EDS to assess grain sizes and elemental distribution. The microstructure and the associated grain size distribution for 0.1, 0.5, and 1% Ga NN ceramics are shown below in Figure 6.5.

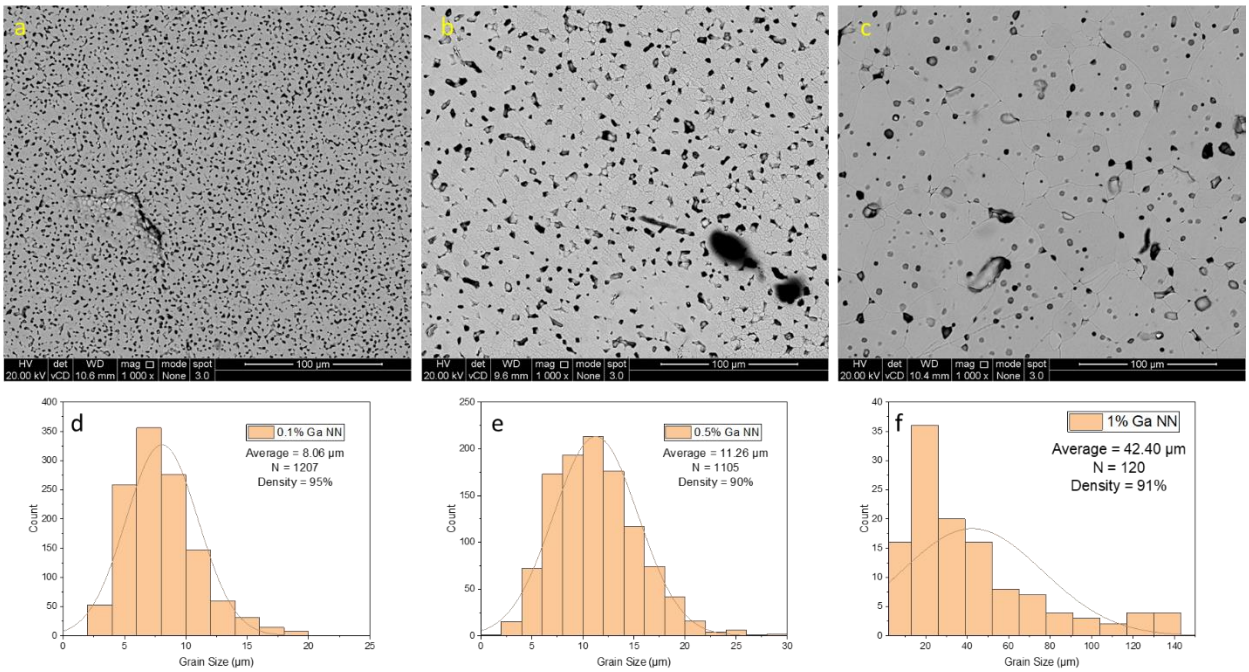

Figure 6.5: BSE Images of a) 0.1% Ga NN b) 0.5% Ga NN Ceramics and c) 1% Ga NN and Associated Grain Size Distribution d) 0.1% Ga NN e) 0.5% Ga NN and f) 1% Ga NN

The 0.1% Ga and 0.5% Ga NN ceramics showcase comparable densities to LP NN and other acceptor doped variants. 0.1% Ga showcases the smallest grain size of 8.06 µm, a reduction of ~40% compared to LP NN. 0.5% Ga NN showcases a grain size similar to LP NN. 1% Ga NN showcases a significant increase in grain size of ~4x compared to 0.5% Ga NN and LP NN.

In order to determine the elemental distribution within the 0.1, 0.5 and 1% Ga NN ceramics, EDS maps have been used in conjunction with spot analysis. The EDS maps are shown below in Figures 6.6-6.8.

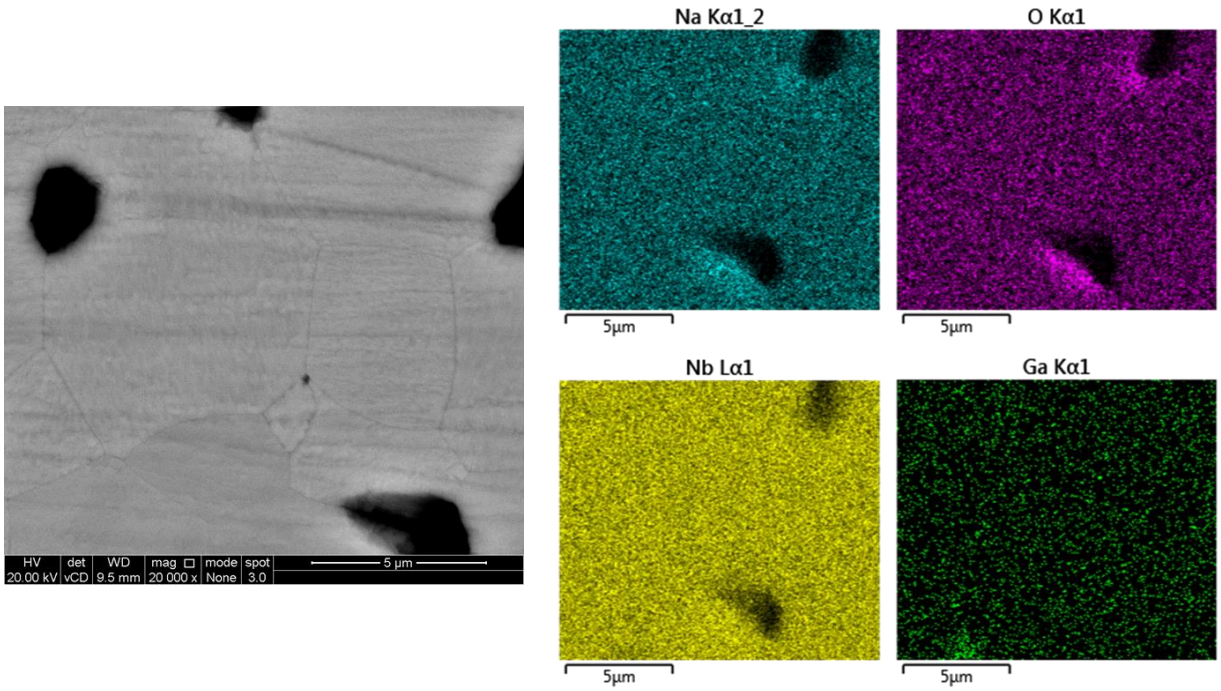

Figure 6.6: EDS Maps of 0.1% Ga NN

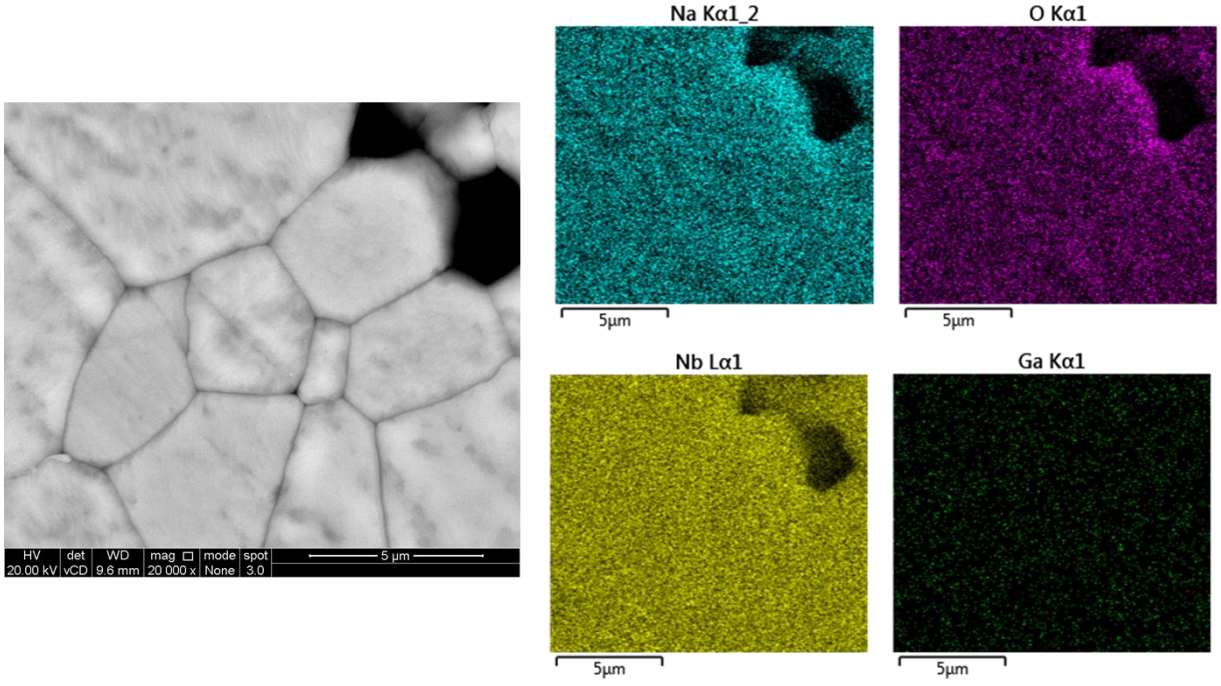

Figure 6.7: EDS Maps of 0.5% Ga NN

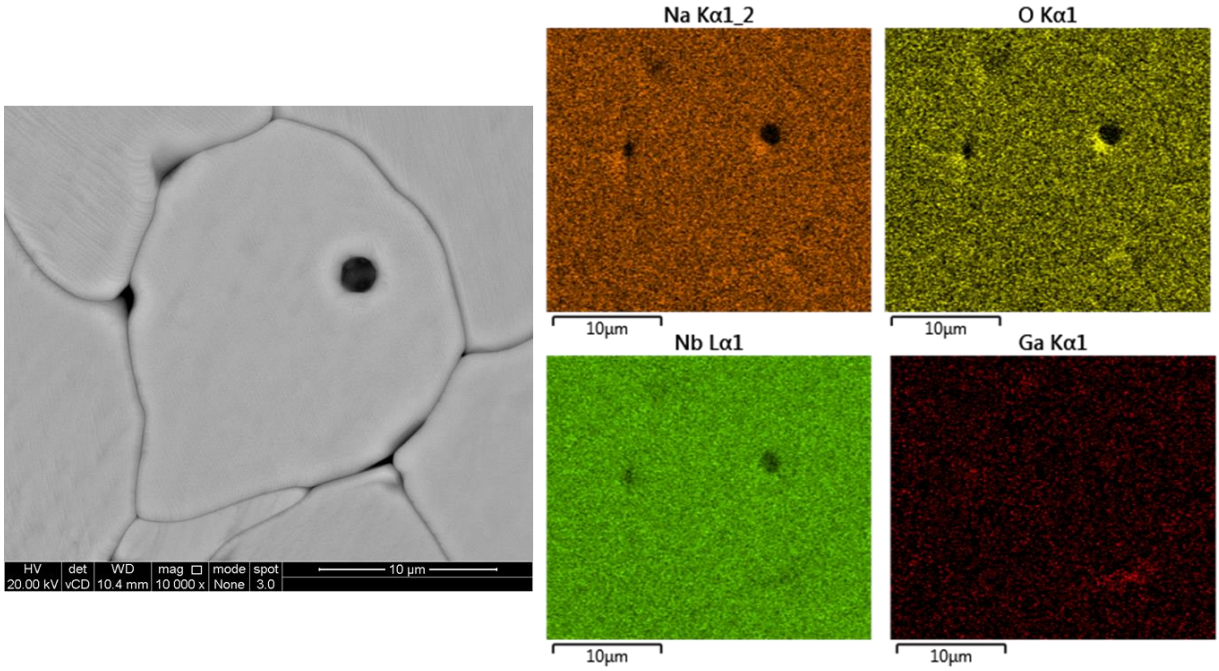

Figure 6.8: EDS Maps of 1% Ga NN

0.1, 0.5 and 1% Ga NN ceramics show no significant differences between the grains and grain boundaries in the EDS maps. Gallium concentrations appear very low throughout.

The spot analysis of gallium doped NN ceramics is shown below in table 6.3.

	Theoretical				Grain				Grain Boundary			
Composition	**Na / wt%**	**Nb / wt%**	**Ga / wt%**	**O / wt%**	**Na / wt%**	**Nb / wt%**	**Ga / wt%**	**O / wt%**	**Na / wt%**	**Nb / wt%**	**Ga / wt%**	**O / wt%**
0.1% Ga NN	14.03	56.64	0.04	29.28	12.51 ± 0.02	61.93 ± 0.01	0.00 ± 0.00	25.56 ± 0.02	12.80 ± 0.02	61.83 ± 0.01	0.03 ± 0.50	25.27 ± 0.02
0.5% Ga NN	14.04	56.44	0.21	29.26	13.30 ± 0.01	59.95 ± 0.01	0.00 ± 0.00	26.80 ± 0.02	12.77 ± 0.01	62.00 ± 0.01	0.17 ± 1.20	25.00 ± 0.02
1% Ga NN	14.05	56.20	0.43	29.33	12.64 ± 0.02	58.88 ± 0.01	0.08 ± 1.73	28.35 ± 0.02	12.52 ± 0.02	58.87 ± 0.01	0.13 ± 1.73	28.47 ± 0.02
5% Ga NN	14.20	54.50	2.15	29.15	13.70 ± 0.10	59.20 ± 0.20	0.10 ± 0.10	26.90 ± 0.20	11.66 ± 0.10	58.62 ± 0.20	0.66 ± 0.10	29.06 ± 0.20

Table 6.3: Average Grain and Grain Boundary Compositions of Ga Doped NN Ceramics

As observed with the EDS maps, elemental composition appears mostly consistent between grains and grain boundaries. The analysis suggests that grain boundaries have increased gallium concentrations, however the associated errors in this measurement are large and most likely a consequence of gallium concentrations in the ceramic being below the detection limit of the spectrometer.

6.1.3. Relative Permittivity and Dielectric Losses

The temperature dependence of permittivity and dielectric losses for the 0.1 and 0.5% Ga NN ceramics has been investigated. The ε_r-T plots are shown below in Figure 6.9 and compared to LP NN and 5% Ga NN.

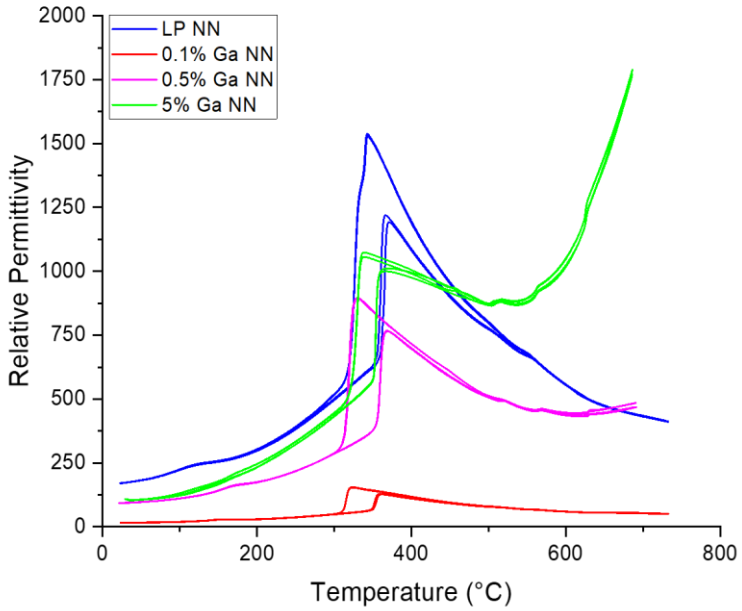

Figure 6.9: Relative Permittivity of 0.1% Ga and 0.5% Ga NN Ceramics Compared to 5% Ga and LP NN at 100 kHz

The relative permittivity decreases significantly when doped with 0.1% Ga showing the lowest observed permittivity of all NN ceramics, while the P-R phase transition remains unaffected. With the slight increase in dopant concentration up to 0.5% Ga the permittivity increases to be more in line with 5% Ga NN.

The associated dielectric losses of 0.1 and 0.5% Ga NN ceramics are shown below in Figure 6.10.

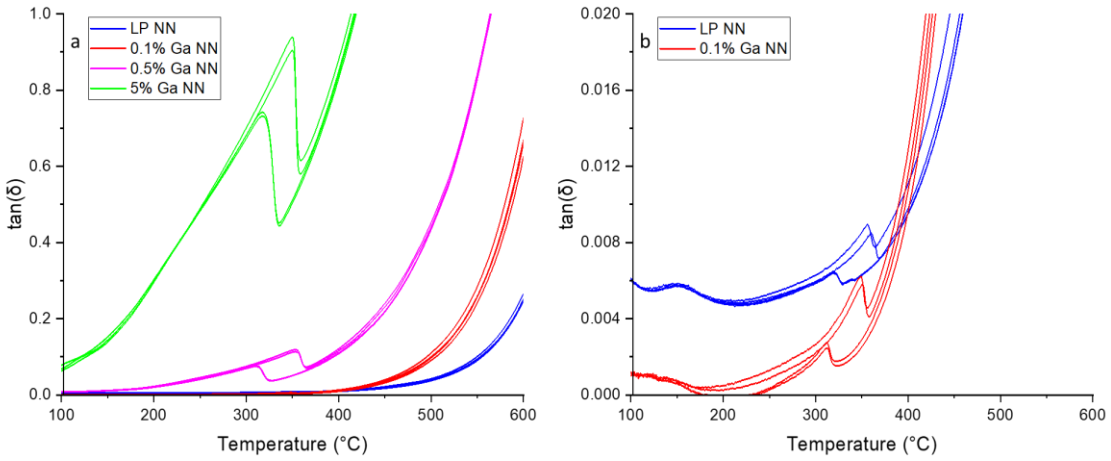

Figure 6.10: a) Dielectric Losses of 0.1% Ga and 0.5% Ga NN Ceramics Compared to '5% Ga NN' and 'LP NN' at 100 kHz b) Adjusted Scale for LP NN and 0.1% Ga NN

Figure 6.10a) shows that dielectric losses increase significantly beyond 400 °C due to increased contributions from space charge effects, as observed with all NN variants.

At temperatures less than 400 °C a hysteresis is observed around the P-R phase transition in line with the permittivity increase shown in Figure 6.9 where maximum losses are observed on heating. Figure 6.10b) shows that 0.1% Ga NN showcases dielectric losses slightly lower than LP NN with maximum losses occurring around the P-R phase transition of 0.6%. Figure 6.10a) shows that 0.5% Ga NN losses increase significantly up to ~12%, although this does not reach the same levels of 5% Ga NN, where ~93% losses are observed.

6.1.4. Impedance Spectroscopy

The electrical properties of 0.1 and 0.5% Ga NN ceramics have been investigated *via* impedance spectroscopy. The overlaid M''/Z'' plots for the ceramics are shown in Figure 6.11.

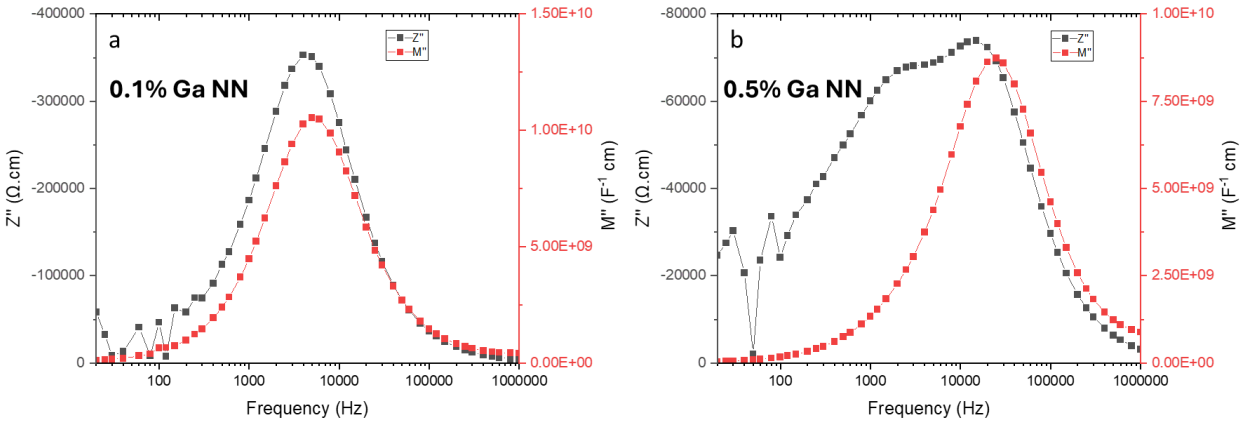

Figure 6.11: Overlaid M'' Z'' Plots of a) 0.1% Ga NN and b) 0.5% Ga NN Ceramics at 460 °C

	Capacitance (Z'') / F cm^{-1}	Capacitance (M'') / F cm^{-1}	Corresponding Response
0.1% Ga NN	$5.6(9) \times 10^{-11}$	$4.7(2) \times 10^{-11}$	Bulk
0.5% Ga NN 1	$2(6) \times 10^{-11}$	$2.6(1) \times 10^{-11}$	Bulk
0.5% Ga NN 2	$4(3) \times 10^{-10}$	-	Grain Boundary

Table 6.4: Tabulated Capacitances Extracted from M'' and Z'' Responses in Figure 6.11

The 0.1% Ga NN ceramic showcases a single response in M'' and Z'' with good electrical homogeneity indicating a single RC element corresponding to a bulk electrical response; at low frequencies there is no significant spike in Z'' indicating no significant ionic conduction is present in the ceramic. The 0.5% Ga NN ceramic appears to be significantly more conductive at a comparable temperature and showcases a single peak in the M'' spectra, corresponding to the bulk electrical response. In the Z'' spectra there are 2, poorly resolved, yet observable peaks indicating the presence of 2 RC elements connected in parallel. The high frequency peak corresponds to the bulk electrical response observed in M'' spectra, the lower frequency Z'' peak corresponds to a slightly resistive grain boundary element. Figure 6.11 does not appear to show an increase in Z'' data at low frequencies, however, an associated low frequency increase in capacitance is observed in the C' *vs* frequency plot shown below in Figure 6.12.

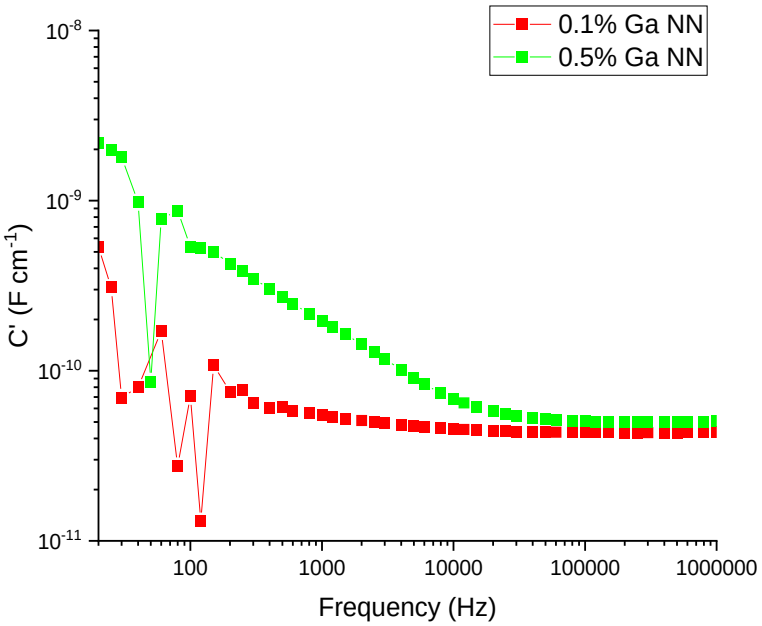

Figure 6.12: C' vs Frequency Plot of 0.1 and 0.5% Ga NN Ceramics at 460 °C

The capacitance of the 0.1% Ga NN ceramic does not feature any notable increase at lower frequencies, whereas the 0.5% Ga NN ceramic shows a clear and continuous increase in capacitance below 10 kHz indicating the presence of ionic conduction.

The Arrhenius plots of bulk conductivity for 0.1 and 0.5% Ga NN ceramics are shown below in Figure 6.13 and compared against LP NN and 5% Ga NN ceramics.

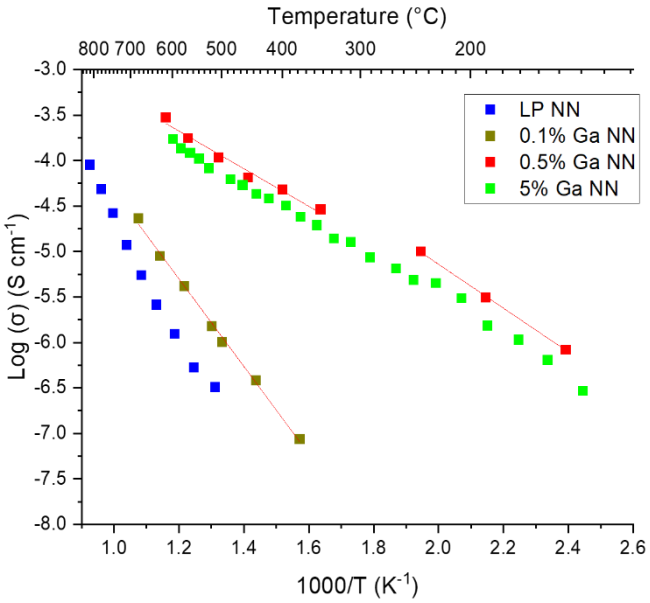

Figure 6.13: Arrhenius Plots of Bulk Conductivity of 0.1 and 0.5% Ga NN Ceramics Compared to 'LP NN' and 5% Ga NN

Composition	Low Temperature Ea / eV	High Temperature Ea / eV
LP NN	1.01 ± 0.10	1.52 ± 0.02
0.1% Ga NN	1.26 ± 0.04	-
0.5% Ga NN	0.48 ± 0.01	0.41 ± 0.03
5% Ga NN	0.51 ± 0.02	0.40 ± 0.00

Table 6.5: Activation Energies of Bulk Conductivity Extracted from the Arrhenius Plots in Figure 6.13.

0.1% Ga NN showcases a slight increase in bulk conductivity compared to the LP NN ceramic, the activation energy remains constant throughout, showcasing a slight decrease compared to the high temperature domain of LP NN. The 0.5% Ga NN ceramic showcases a significant increase in bulk conductivity compared to LP NN, matching the increase in conductivity shown in the 5% Ga NN ceramic as well as the lower activation energies at all temperatures.

The series of gallium doped NN ceramics have also been electrically tested and the bulk conductivities extracted from M'' spectra are shown in the Arrhenius plots in Figure 6.14.

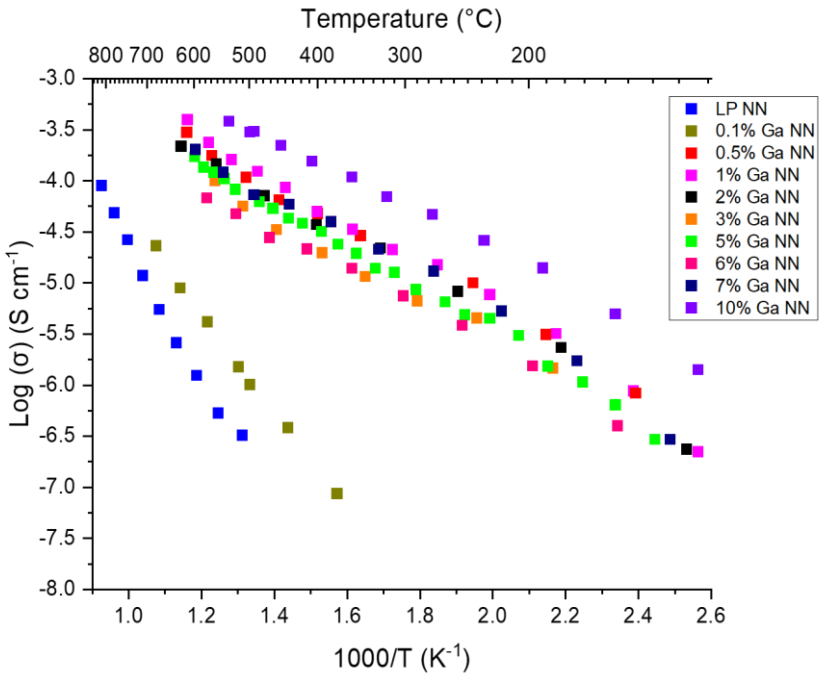

Figure 6.14: Arrhenius Plots of Bulk Conductivity for Gallium Doped NN Ceramics

The conductivity of gallium doped NN appears consistent across most of the range 1-10%, with 10% gallium showcasing the only notable increase in conductivity compared to 1%. This suggests a plateau of maximum conductivity is established at very low dopant concentrations before rising again at higher concentrations. Activation energies remain consistent across the entire range as shown in table 6.6.

Composition	Low Temperature Ea / eV	High Temperature Ea / eV
LP NN	1.01 ± 0.10	1.52 ± 0.02
0.1% Ga NN	1.26 ± 0.04	-
0.5% Ga NN	0.48 ± 0.01	0.41 ± 0.03
1% Ga NN	0.50 ± 0.03	0.44 ± 0.02
2% Ga NN	0.46 ± 0.03	0.42 ± 0.01
3% Ga NN	0.47 ± 0.00	0.41 ± 0.02
5% Ga NN	0.51 ± 0.02	0.40 ± 0.00
6% Ga NN	0.50 ± 0.02	0.33 ± 0.02
7% Ga NN	0.50 ± 0.02	0.33 ± 0.02
10% Ga NN	0.40 ± 0.01	0.33 ± 0.01

Table 6.6: Activation Energies of Gallium Doped NN Variants Extracted from Figure 6.14

Beyond 0.5 at% gallium doping activation energies are consistently low. Beyond 5 at% gallium doping the activation temperature in the high temperature domain decreases slightly and remains consistent up to 10% Ga NN.

The apparent increase in low temperature conductivity for 10% Ga NN compared to other Ga-NN variants may be a result of electrical heterogeneity, similar to the observation in B-site donor doped NN ceramics discussed in chapter 5. The M'' Z'' spectra of 10% Ga NN at 270 °C and 470 °C are shown in Figure 6.15a and b, respectively.

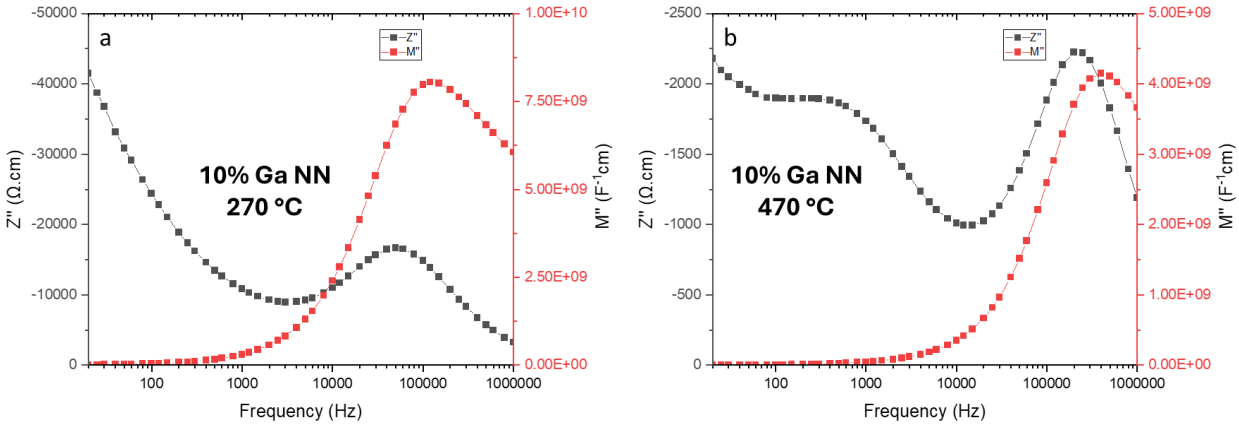

Figure 6.15: Overlaid M'' Z'' Spectra of 10% Ga NN at a) 270 °C and b) 470 °C

10% Ga NN	Capacitance (Z'') / F cm^{-1}	Capacitance (M'') / F cm^{-1}	$w_{\frac{1}{2}h}$ (M'') / Hz
270 °C	$10(3) \times 10^{-11}$	$6.2(3) \times 10^{-11}$	1.56
470 °C 1	$2(1) \times 10^{-10}$	$1.21(6) \times 10^{-10}$	1.40
470 °C 2	$2.1(6) \times 10^{-7}$	-	-

Table 6.7: Tabulated Capacitances Extracted from M'' and Z'' Responses in Figure 6.15
N.B.: $w_{1/2h}$ (M'') is the Half Height Peak Width of the M'' peak and is the Calculated Minimum for a Fully Symmetrical Peak. The Real Width of the Peak is Likely Greater Although this Cannot be Accurately Determined due to Frequency Limits of the Impedance Analyser.

At 270 °C the M'' peak from which the bulk conductivity is extracted, and the Z'' peak appear very broad. This indicates that more than 1 RC element is contributing to the response. As temperature increases to 470 °C into the high temperature domain of the Arrhenius plot the M'' and Z'' peaks appear to narrow as the response becomes more indicative of the intrinsic conduction mechanism and a grain boundary response emerges in the Z'' spectra.

It is suggested that the increased conductivity of the M'' response at lower temperatures is a consequence of this apparent heterogeneity and is overcome at higher temperatures where the conductivity is in line with other Ga-NN variants.

Table 6.8 compares the relative permittivity extracted *via* LCR to the relative permittivity determined from the capacitances extracted from M'' spectra, table 6.7.

Temperature / °C	Relative Permittivity (100 kHz LCR)	Relative Permittivity (M'' Capacitance)	% Difference
270	530	700	24
470	1424	1370	4

Table 6.8: Variance of Relative Permittivity in 10% Ga NN Determined via LCR and Impedance

At lower temperatures, there is a large variation in capacitance between LCR and impedance, as temperatures increase the variance decreases significantly. Additionally, the M'' extracted permittivity is greater than the LCR at low temperatures, and less than the LCR at high temperatures. The relative permittivity of M'' if it corresponds to a bulk response would be less than the permittivity determined *via* LCR which would showcase the total permittivity of the ceramic. The greater permittivity at low temperatures further indicates that an additional component is contributing to the response.

The pO_2 dependence of the ceramics has also been evaluated and is shown below in Figures 6.16-6.18.

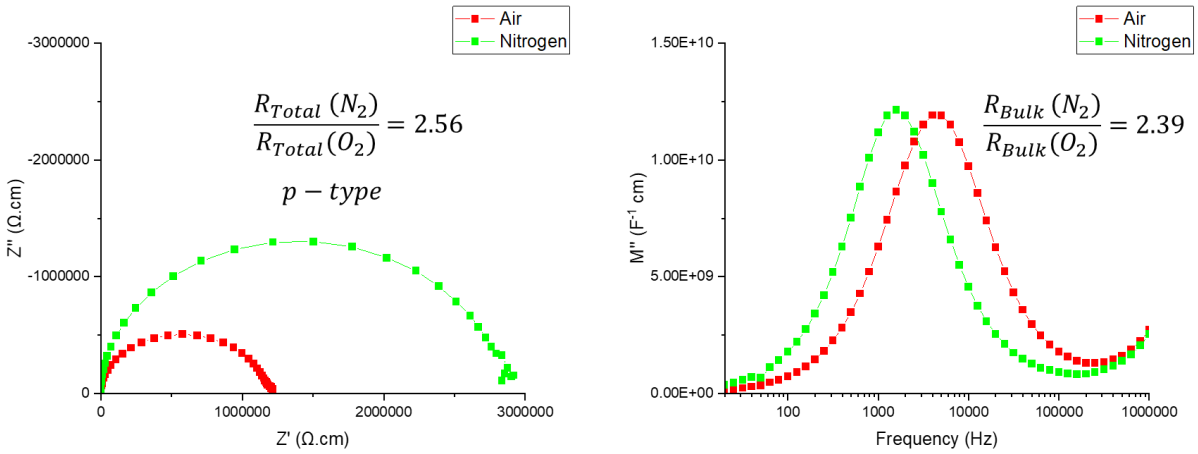

Figure 6.16: pO_2 Dependence of 0.1% Ga NN Ceramic at 470 °C

The 0.1% Ga NN ceramic showcases a significant increase in total resistance as pO_2 decreases, indicating the presence of p-type conductivity. This effect is attributed to the bulk electrical response as the M'' peak shifts to lower frequency when in low pO_2 environments. The increase in M'' at high frequencies is attributed to a jig effect and may be disregarded.

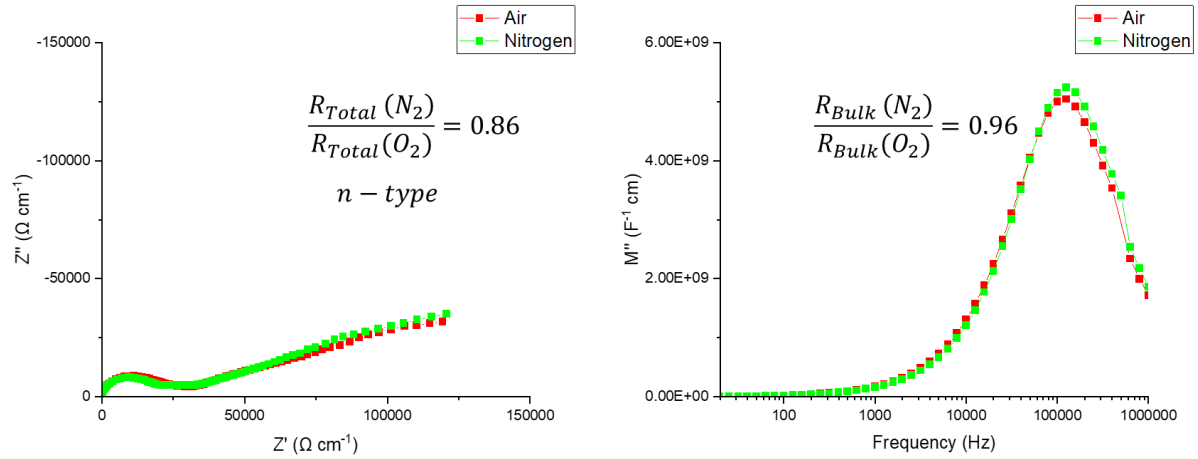

Figure 6.17: pO_2 Dependence of 0.5% Ga NN Ceramic at 470 °C

The 0.5% Ga NN ceramic exhibits a drop in total resistance observed in the Z* plane indicating the presence of n-type conductivity. However, the bulk electrical response in M'' remains relatively unchanged indicating that the n-type conductivity present arises due to extrinsic electrical effects in the sample.

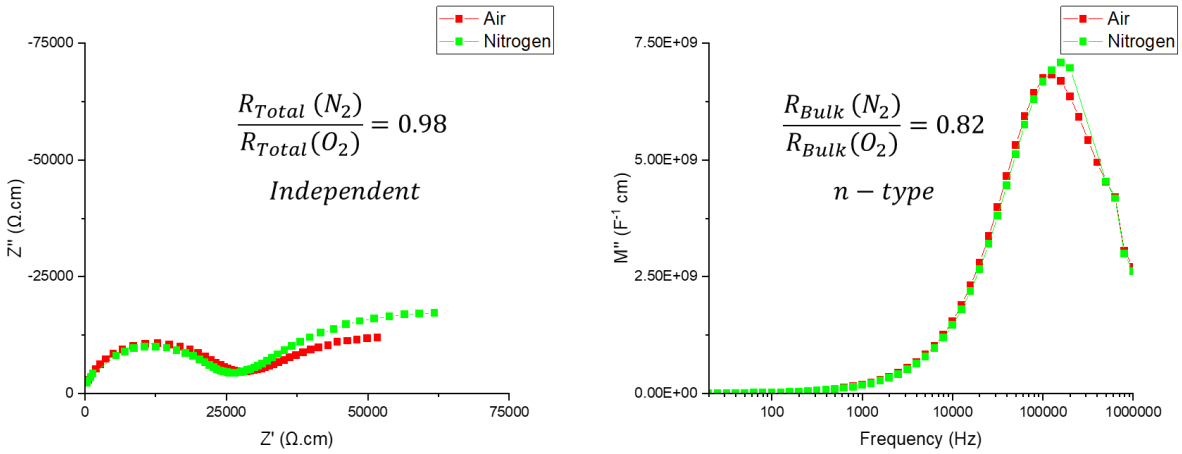

Figure 6.18: pO_2 Dependence of 1% Ga NN Ceramic at 470 °C

The 1% Ga NN ceramic appears pO_2 independent in the Z* plane, however, the bulk electrical response in M'' showcases slight n-type behaviour.

6.1.5. Transport Number

The oxygen transport number of 0.1 and 5% Ga NN have been determined *via* probostat measurements and are shown in Figure 6.19 compared to LP NN.

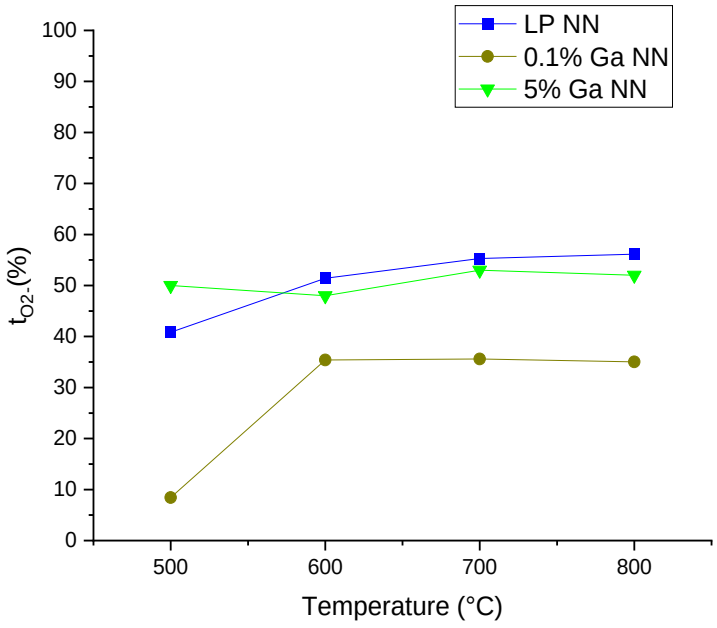

Figure 6.19: Oxygen Transport Number for Gallium Doped NN Ceramics

The 0.1% Ga NN ceramic showcases a notably lower oxygen transport number compared to LP NN and 5% Ga NN, indicating a greater contribution from electronic conductivity, or

suppression of oxide ion conduction. The transport number rapidly decreases below 600 °C although this may be a consequence of the measurement rather than a true representation of the ceramic, potentially due to poor electrode contact.

6.1.6. Gallium NMR

In order to understand the local distribution of gallium within the NN lattice, gallium NMR has been utilised.

The ^{71}Ga NMR spectra of Ga-doped NN according to the mechanisms shown in equations 6.1-6.4 were simulated and compared to the experimentally collected spectra of 1 and 5% Ga NN shown in Figure 6.20.

$$Na^{+} + Nb^{5+} = 2Ga^{3+} \quad (6.1)$$

$$3Na^{+} = Ga^{3+} \quad (6.2)$$

$$Nb^{5+} + O^{2-} = Ga^{3+} \quad (6.3)$$

$$2Nb^{5+} + 2O^{2-} = 2Ga^{3+} \quad (6.4)$$

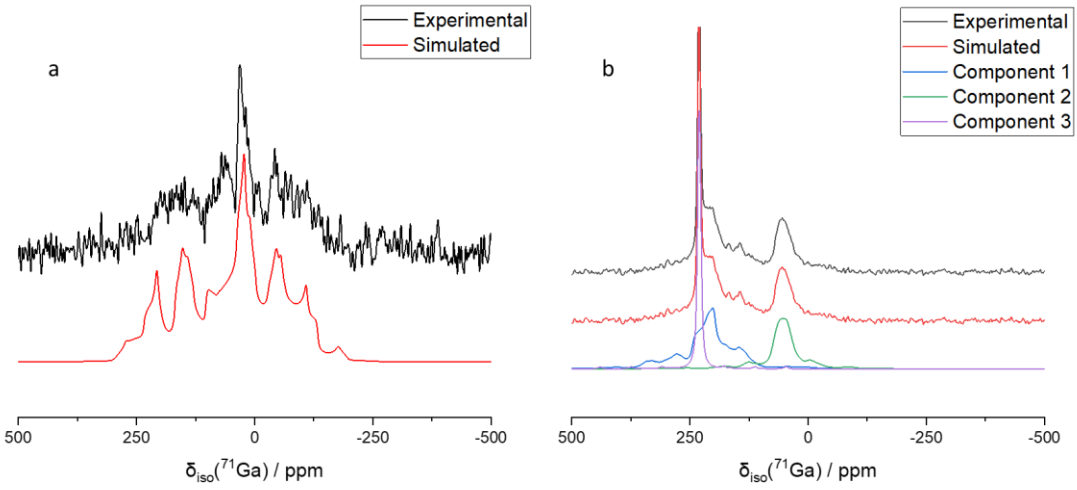

Figure 6.20: ^{71}Ga NMR Spectra of a) 1% Ga NN and b) 5% Ga NN

The experimentally obtained ^{71}Ga NMR spectrum of 1% Ga NN has shown good agreement with the mechanism shown in equation 4 where 2 adjacent B-sites are doped with gallium giving rise to the highly disordered spectrum in Figure 6.20a.

The ^{71}Ga NMR spectrum of 5% Ga NN in Figure 6.20b is in good agreement with a simulation comprised of 3 components. Component 1 corresponds to equation 3, where a single B-site is occupied by a gallium nucleus giving rise to the peak $\delta_{iso}(^{71}Ga)$ =78 ppm.

Table 6.9 shows the agreement between calculated and experimental parameters for the doping mechanisms assigned.

	1% Ga NN ($2Nb^{5+}+2O^{2-}=2Ga^{3+}$)			5% Ga NN ($Nb^{5+}+O^{2-}=Ga^{3+}$)		
	δ_{iso} / ppm	C_Q / MHz	η	δ_{iso} / ppm	C_Q / MHz	η
Calculated Parameters	100	15	Disordered	80	10	0.2
Experimental Parameters	115	15.5	0.3	78	9.5	0.4

Table 6.9: Calculated NMR Parameters Compared to Experimentally Determined Parameters
δ_{iso}=Chemical Shift
C_Q=Nuclear Quadrupolar Coupling Constant
η=Asymmetry Parameter

The remaining components in Figure 6.20b were assigned according to parameters reported in existing literature. Component 2 showcases good agreement to the secondary phase $NaGaO_2$ or a similar phase to give rise to the peak $\delta_{iso}(^{71}Ga)$ =235 ppm.[5]

Component 3 showcases good agreement to a tetrahedral β-Ga_2O_3 like environment to give rise to the peak $\delta_{iso}(^{71}Ga)$ =240 ppm.[6]

The results of the ^{71}Ga NMR confirm that gallium doping of the B-site is occurring, however, the additional components present in the 5% Ga NN spectrum indicates that competing doping mechanisms or secondary phases may be present.

6.2. Discussion

6.2.1. Polymorphic Assemblage and Microstructure

Acceptor doping of the B-site with gallium leads to an increase in the concentration of the Q-phase in NN, in all ceramics with the exception of 0.5% Ga NN. Table 6.1 shows the effect of gallium doping on the tolerance factor of NN is minimal indicating that any changes to the P:Q ratio are a consequence of changing oxygen vacancy concentrations.[7,8] For the range of 1-10% Ga NN the P:Q ratio is generally consistent with no significant deviation from an approximately 50:50 ratio which may indicate a maximum concentration of oxygen vacancies may form at relatively low doping concentrations.

The 0.1% Ga NN ceramic may further indicate that maximum vacancy concentrations are achieved at low dopant concentrations, however, the 0.5% Ga NN showcases a decrease in the P:Q ratio compared to other Ga doped NN variants and LP NN, which may indicate that vacancy concentrations have decreased, leading to a relative stabilisation of the P-phase.

Acceptor doping with gallium leads to an initial contraction of the P-phase unit cell, as gallium content increases the unit cell expands slightly before a second contraction at 2% Ga doping, beyond which cell volumes remain consistent. The opposite trend is observed with the Q-phase unit cell. However, as with all NN variants the variation in P and Q phase unit cells are very small (P - <2 $Å^3$, Q - <1 $Å^3$). The initial contraction of the P-phase unit cell may be due to elimination of oxygen vacancies due to donor doping of the A-site. As vacancy concentrations increase and oxygen vacancies are reintroduced the cell may expand, up to 2% Ga NN where the slightly smaller Ga^{3+} ion occupying the Nb^{5+} causes contraction of the cell.[1,9] The minimal variance beyond 2% Ga doping may indicate that the solid solution limit has been reached and no further doping of the B-site occurs.

0.1% Ga NN showcases a notable increase in the density of the sintered ceramic compared to other NN variants. Additionally, the grain size decreases significantly compared to other variants of NN. 0.5% Ga NN showcases a similar density to undoped NN variants with a comparable grain size. EDS analysis indicates that low level gallium doping occurs primarily along the grain boundaries, with no significant amount of gallium detected in the grains *via* spot analysis. However, as the concentrations are very low, it is likely that any accepted gallium is at concentrations below the detection limit for the technique.

6.2.2. Effects of Low-Level Gallium Doping on Permittivity

The variance in permittivity caused by low level gallium doping is significant, as shown in Figure 6.9. B-site targeted acceptor doping with 0.1% Ga led to a significant decrease in permittivity, showcasing the lowest permittivity of any measured NN variant. In contrast, 0.5% Ga doping showcases a comparable permittivity plot to 1 and 5% Ga NN variants.

Figure 6.21 shows the variance in T_{max} on heating and cooling where permittivity is at a maximum for gallium doped NN variants.

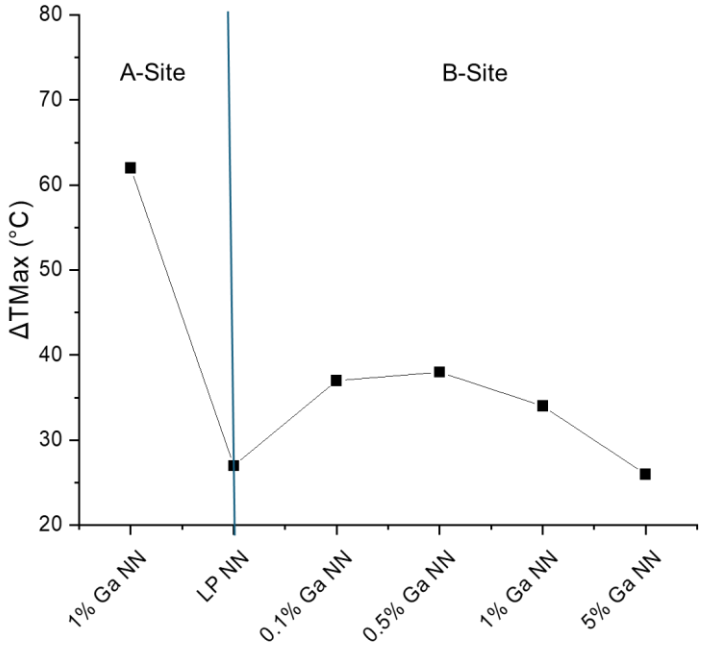

Figure 6.21: Change in ΔT_{Max} of Gallium Doped NN Ceramics

Composition	T_{max} (Heating) / °C	T_{max} (Cooling) / °C	ΔT_{Max} / °C	P-Phase / %	Q-Phase / %
1% Ga NN (A-Site)	399	337	62	91	9
LP NN	371	344	27	66	34
0.1% Ga NN	359	322	37	51	49
0.5% Ga NN	368	330	38	72	28
1% Ga NN	367	333	34	50	50
5% Ga NN	364	338	26	53	47

Table 6.10: Comparison of T_{Max} on Heating and Cooling in Gallium Doped NN Ceramics (σT = ±0.5°C)

As discussed in chapter 4, donor doping of the A-site leads to broadening of the hysteresis around the P-R phase transition. Low level gallium doping appears to slightly broaden the hysteresis, although the reasons for this alternate between 0.1 and 0.5% Ga, where 0.1% Ga NN appears to stabilise the higher temperature R phase on heating and cooling, whereas the 0.5% Ga NN appears to only stabilise on cooling. As doping concentrations increase the hysteresis narrows and becomes more consistent with LP NN.

6.2.3. Effects of Gallium Doping on Conductivity

Figures 6.13 and 6.14 showcase that doping with 0.1% Ga NN leads to a slight increase in bulk conductivity compared to the LP NN ceramic. Slightly increasing dopant concentration to 0.5% Ga showcases comparable bulk conductivity to all other gallium doped NN variants in the range of 1-10% Ga. Additionally, Figures 6.11 and 6.12 show that there is no notable increase in the low frequency capacitance of the 0.1% Ga NN ceramic, compared to the

notable incline observed in 0.5% Ga NN and all other gallium doped NN ceramics indicative of ionic conductivity.

The apparent maximum bulk conductivity achieved by gallium doping occurs between 0.1-0.5% Ga NN suggesting, as suggested in chapter 5, either:

1. Maximum concentrations of oxygen vacancies form at low concentrations of gallium.
2. Beyond a critical concentration the oxygen vacancies are pinned limiting conductivity
3. Doping is initially targeting the A-site (as observed with 1% Mg NN)
4. A combination of the above

Therefore, the small increase in conductivity with 0.1at% Ga doping may be attributed to either, partial progress towards the solid solution limit, or initial doping of the A-site. In chapter 4 A-site gallium doped NN was investigated. Figure 6.22 compares the Arrhenius plots of LP NN, 0.1% Ga NN, 0.5% Ga NN, 1% Ga NN and 1% Ga (A-Site) NN.

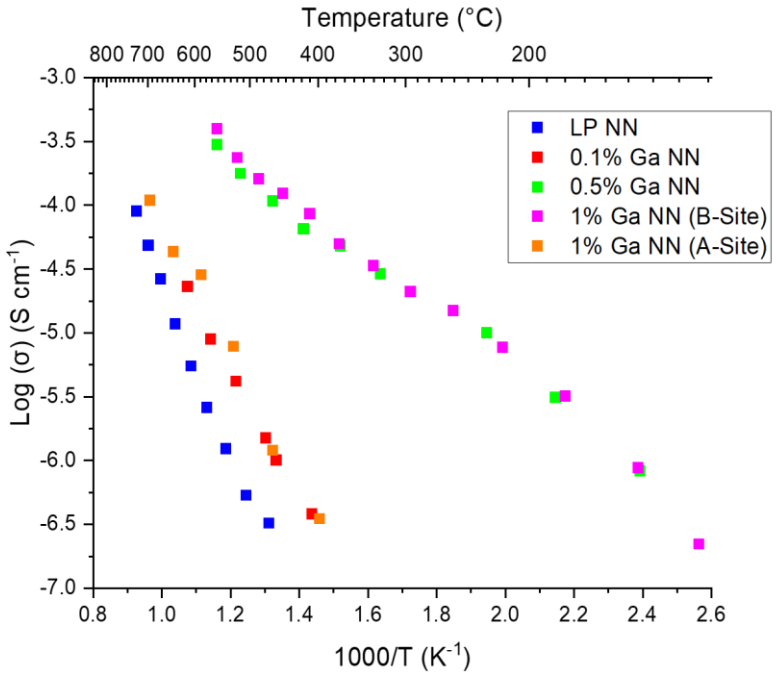

Figure 6.22: Arrhenius Plot of Bulk Conductivity for Gallium Doped NN Variants

The 0.1% Ga NN showcases the same bulk conductivity as the 1% Ga NN (A-site variant) whereas the 0.5% Ga NN showcases the same bulk conductivity as the 1% Ga NN (B-site variant). Chapter 4 discusses how the A-site targeted gallium doping suggests very low concentrations of gallium are successfully incorporated into the structure of NN. Both A-site and B-site magnesium doped NN variants showcase the same bulk conductivity, this has been attributed to a preferential doping of only the A-site (chapter 5). While the same preference is not observed at higher doping levels of gallium NN (≥0.5% Ga), the 0.1% Ga

NN suggests there may be a preference for A-site donor doping across multiple dopant ions; indicating that initial doping of NN preferentially targets A-site metal vacancies that are formed during calcination/sintering due to soda loss (Na_2O), filling oxygen vacancies and targeting a nominally stoichiometric NN.

$$4Na_{Na}^{x} + 2O_{O}^{x} \rightarrow 4V_{Na}^{\prime} + 2V_{O}^{\cdot\cdot} + 2Na_2O \qquad (6.5)$$

$$4V_{Na}^{\prime} + 2V_{O}^{\cdot\cdot} \rightarrow Ga_{Na}^{\cdot\cdot} + \frac{3}{2}O_{O}^{x} + 3V_{Na}^{\prime} + \frac{1}{2}V_{O}^{\cdot\cdot} \qquad (6.6)$$

This initial filling of oxygen vacancies may be observed *via* the initial reduction in oxygen transport number shown in Figure 6.19, where 0.1% Ga NN showcases t_{O2-} of ~35% compared to ~50% for LP NN.

Once oxygen vacancies have been filled according to the A-site donor doping mechanism (or the limit of doping the intermediate sized Ga on the A-site has been reached), the B-site is targeted as intended and oxygen vacancies are created, promoting oxide ion conduction, and increasing bulk conductivity.

$$Nb_{Nb}^{x} + \frac{5}{2}O_{O}^{x} \rightarrow Ga_{Nb}^{\prime\prime} + \frac{3}{2}O_{O}^{x} + V_{O}^{\cdot\cdot} \qquad (6.7)$$

This increase in oxygen vacancies may be observed as t_{O2-} increases to ~50% in 5% Ga NN.

The ^{71}Ga NMR spectra of 5% Ga NN appears to support this hypothesis, as multiple gallium sites are present. An octahedral environment corresponding to the B-site targeted dopant mechanism, and 2 additional sites corresponding to phases similar to $NaGaO_2$ and β-Ga_2O_3.[5,6] As there is not significant evidence of secondary phases in the XRD and SEM of the 5% Ga NN ceramic the components in the NMR may correspond to gallium nuclei occupying a 4 coordinate site ($NaGaO_2$) or 2 coordinate site (β-Ga_2O_3). The presence of these sites may suggest that gallium is incorporated into the A-site in 2 or 4 coordinate environments. As the Ga^{3+} ion is significantly smaller than the sodium sites in NN, doping onto the A-site may form a 4-coordinate environment facilitated by increased tilting of the NbO_6 octahedra, similar to the regular sublattice formed in $CaCu_3Ti_4O_{12}$ where Cu^{2+} occupies 4-coordinate square planar environments, and Ca^{2+} occupies a typical 8-coordinate site associated with the octahedral tilting of the TiO_6 units.[10] In order to facilitate a 2-coordinate A-site environment further tilting of the NbO_6 octahedra would be required, there are no examples of 2-coordinate sites in perovskites currently reported. It is therefore more likely that the 2-coordinate environments observed in the ^{71}Ga NMR correspond to unreacted β-Ga_2O_3 at concentrations below the detection limits of XRD and EDS.

Ideally, 0.1 and 0.5% Ga NN samples would be investigated *via* ^{71}Ga NMR to confirm the hypothesis that this preferential doping mechanism occurs at very low dopant concentrations. However, due to the relatively low abundance of the NMR active ^{71}Ga nucleus and the low concentrations of gallium in the samples it is not possible to collect the spectra under any reasonable timeframe. The key to confirming this likely lies with an investigation of aluminium doped NN, as the ^{27}Al nucleus (100%) is significantly more abundant than ^{71}Ga (39.9%).

6.2.4. pO_2 Dependence of Gallium Doped NN

The pO_2 dependence of gallium doped NN ceramics is summarised in table 6.11.

Composition	$\frac{R_{Total}(N_2)}{R_{Total}(O_2)}$	Total Observed Response	$\frac{R_{Bulk}(N_2)}{R_{Bulk}(O_2)}$	Bulk Observed Response
LP NN	0.96	n	0.99	Independent
0.1% Ga NN	2.56	p	2.39	p
0.5% Ga NN	0.86	n	0.96	Independent
1% Ga NN	0.98	Independent	0.82	n
1% Ga NN (A-Site)	1.43	p	1.78	p
5% Ga NN	1.19	p	0.80	n

Table 6.11: Summarised pO_2 Dependence of Ga-Doped NN Ceramics

The pO_2 dependence of gallium doped NN ceramics varies significantly. Higher gallium concentrations (≥1%) in acceptor doped NN showcase comparable n-type conductivity in the bulk electrical response, attributable to reduction of the niobium ion as previously discussed:

$$O_O^x \rightarrow \frac{1}{2}O_{2_{(g)}} + V_O^{\cdot\cdot} + 2e' \qquad (6.8)$$

$$2Nb_{Nb}^x + 2e' \rightarrow 2Nb'_{Nb} \qquad (6.9)$$

The 0.5% Ga NN ceramic bulk response appears pO_2 independent. As the solid solution limits in NN appear low, this initial pO_2 independence of the bulk and consistent n-type conductivity at higher gallium concentrations may indicate that the pO_2 dependence of ≥1% Ga NN ceramics is a consequence of Na:Nb non-stoichiometry. As both LP NN and 0.5% Ga NN appear pO_2 independent it is suggested that NN when close to stoichiometric ABO_3 exhibits pO_2 independence. When the solid solution limits are exceeded the Na:Nb non-stoichiometry introduces n-type conductivity *via* promotion of oxygen loss.

The 0.1% Ga NN and 1% Ga NN (A-site) ceramics showcase p-type conductivity attributed to holes on oxygen sites:[11]

$$V_O^{\cdot\cdot} + \frac{1}{2}O_{2_{(g)}} \rightarrow O_O^x + 2h^{\cdot} \qquad (6.10)$$

$$2h^{\cdot} + 2O_O^x \rightarrow 2O_O^{\cdot} \qquad (6.11)$$

As previously suggested the 0.1% Ga NN ceramic showcases that gallium preferentially donor dopes onto the A-site of the perovskite. As A-site vacancies and in turn oxygen vacancies are filled according to the mechanism in equations 6.5 and 6.6, holes may be introduced to the oxygen sites for charge balance.

The shared pO_2 dependence of 0.1% Ga NN and 1% Ga NN (A-Site) is a further indication of the proposed A-site preference.

6.3. Conclusions

Use of low-level gallium doping of the B-site has indicated that an A-site donor doping preference exists in NN. Acceptor doping the B-site using gallium generally leads to high bulk conductivities and strong evidence of oxide ion conductivity, however, maximum conductivities are achieved at low concentrations of gallium (<0.5% Ga), most likely due to an apparent low solid solution limit for B-site doped NN.

0.1% Ga NN showcases properties more in line with donor doped materials with low conductivity, a lower oxygen transport number, p-type pO_2 dependence and very low permittivity. 0.5% Ga NN showcases properties in line with acceptor doped NN variants with high conductivity, and evidence of ionic conductivity.

^{71}Ga NMR indicates 3 distinct environments in 5% Ga NN attributed to B-site doping, and gallium environments similar to $NaGaO_2$ and β-Ga_2O_3, it has been suggested that the $NaGaO_2$ site may be indicative of A-site doping, similar to the observed A-B aluminium co-doping showcased in NBT.[2]

It is suggested that gallium preferentially targets the A-site of NN to compensate for soda loss. Once the A-site solid solution limit has been exceeded remaining gallium fills the vacant B-sites as targeted, up to the B-site solid solution limit leading to enhanced oxide ion conductivity. Any gallium in excess of the B-site solid solution remains as unreacted β-Ga_2O_3 finely distributed throughout the ceramic.

The pO_2 dependence of NN ceramics may be primarily influenced by Na:Nb non-stoichiometry, specifically, n-type conductivity may indicate that the targeted B-site

stoichiometry has not been achieved and an effective increase in the Na:Nb ratio promotes oxygen loss and reduction of the niobium ion.

6.4. References

1. Shannon, R. D. Revised effective ionic radii and systematic studies of interatomic distances in halides and chalcogenides. Acta Crystallogr. Sect. A Cryst. physics, diffraction, Theor. Gen. Crystallogr. 32, 751–767 (1976).

2. Groszewicz, P. B. et al. The fate of aluminium in (Na,Bi)TiO_3-based ionic conductors. J. Mater. Chem. A 8, 18188–18197 (2020).

3. Wang, K. et al. Phase transition of $NaGaO_2$ at high pressure and high temperature. Solid State Commun. 152, 540–544 (2012).

4. Omata, T., Nagatani, H., Suzuki, I. & Kita, M. Wurtzite-derived ternary I-III-O_2 semiconductors. Sci. Technol. Adv. Mater. 16, (2015).

5. Ash, J. T. & Grandinetti, P. J. Solid-state NMR characterization of ^{69}Ga and ^{71}Ga in crystalline solids. Magn. Reson. Chem. 44, 823–831 (2006).

6. Massiot, D. et al. ^{71}Ga and ^{69}Ga nuclear magnetic resonance study of β-Ga_2O_3: resolution of four- and six-fold coordinated Ga sites in static conditions. Solid State Nucl. Magn. Reson. 4, 241–248 (1995).

7. Guo, H., Shimizu, H., Mizuno, Y. & Randall, C. A. Strategy for stabilization of the antiferroelectric phase (Pbma) over the metastable ferroelectric phase (P21ma) to establish double loop hysteresis in lead-free (1-x)$NaNbO_3$ - x $SrZrO_3$ solid solution. J. Appl. Phys. 117, 214103 (2015).

8. Shakhovoy, R. A. et al. Ferroelectric Q and antiferroelectric P phases' coexistence and local phase transitions in oxygen-deficient $NaNbO_3$ single crystal: Micro-Raman, dielectric and dilatometric studies. J. Raman Spectrosc. 43, 1141–1145 (2012).

9. Tsvetkov, D. S., Sereda, V. V., Malyshkin, D. A., Ivanov, I. L. & Zuev, A. Y. Chemical lattice strain in nonstoichiometric oxides: an overview. J. Mater. Chem. A 10, 6351–6375 (2022).

10. Božin, E. S. et al. Temperature dependent total scattering structural study of $CaCu_3Ti_4O_{12}$. J. Phys. Condens. Matter 16, (2004).

11. Ren, P. et al. Mixed oxide ion and proton conduction and p-type semiconduction in $BaTi_{0.98}Ca_{0.02}O_{2.98}$ ceramics. J. Mater. Chem. C 1, 2426–2432 (2013).

Chapter 7. Conclusions and Further Work

7.1. Conclusions

The goal of this thesis was to investigate the suitability of $NaNbO_3$ (NN) as a material for use as an ITSOFC electrolyte. Some criteria for ITSOFC electrolyte suitability are as follows:

1. Stability in oxidising and reducing environments at operating temperatures between 400 and 700 ºC.
2. Conductivity in excess of 1 mS cm^{-1} at operating temperatures.
3. Exclusive oxide ion conductivity/minimal contributions from electronic conduction.

It has been shown that no NN variant discussed in this thesis fulfils all 3 criteria. Fundamentally, it appears that all NN variants are mixed oxide ion-electronic conductors evidenced by the consistent pO_2 dependence of NN ceramics showcasing Warburg diffusion.

The use of impedance spectroscopy throughout this work while assessing pO_2 dependence has showcased an advantage of the technique. By allowing extraction of the bulk electrical response, it has been possible to identify when pO_2 dependence is attributed to the bulk ceramic, or if it is due to extrinsic properties such as grain boundary effects and/or secondary phase impurities in the ceramics. Typical techniques used to assess resistivity, and in turn pO_2 dependence, such as 4 probe measurements fail to make this distinction and only showcase the total pO_2 dependence.[1]

All NN ceramics that have undergone probostat measurements to determine their associated oxide ion transport number showcase mixed conduction, the greatest measured transport number has been shown to be ~72% in 5% Ti NN, although this is still too low to be used as an effective solid oxide electrolyte. The mixed contribution to 5% Ti NN may be attributed to electronic conduction as the slight p-type conductivity in the total pO_2 resistivity will influence the probostat measurement.

It has been suggested that the origin and type of pO_2 dependence of NN is primarily linked to the Na:Nb ratio and associated processing conditions. As the Na:Nb ratio changes from 1:1 n-type conductivity arises due to oxygen loss and consequent reduction of the Nb^{5+} ion:

$$O^{2-} \rightarrow \frac{1}{2}O_{2_{(g)}} + 2e^- \qquad (7.1)$$

$$2Nb^{5+} + 2e^- \rightarrow 2Nb^{4+} \qquad (7.2)$$

Although NN appears to be generally unsuitable as a solid oxide electrolyte, the doping mechanisms have been studied, and suggested that acceptor doping of the B-site is challenging due to a preference for A-site donor doping.

The A-site deficient Ca-doped NN has been investigated and it is indicated that sodium ion conduction is present. This work explores up to 5% Ca doping, however, existing literature shows that calcium and bismuth may dope up to 20% of the A-site according to the mechanism:[2,3]

$$xNa^{+} = M^{x+} \qquad (7.3)$$

The bismuth doping mechanism suggests that up to 40% A-site vacancies may be generated in NN, however, a purely non-stoichiometric approach has shown that this may be pushed slightly further to ~43% in $Na_{0.57}NbO_{2.785}$.[3,4]

This work has shown that the donor doping mechanism shown in equation 7.4 is possible and leads to a reduction in ionic conductivity, presumably due to the elimination of oxygen vacancies.

$$Na^{+} = Mg^{2+} + \frac{1}{2}O^{2-} \qquad (7.4)$$

B-site doping of NN appears to have significantly lower solid solution limits than A-site doping. Acceptor doping of the B-site leads to a significant increase in bulk conductivity attributed to mixed oxide ion-electronic conduction. However, this increase is achieved at very low dopant concentrations (≤0.5at % Ga NN). This may be showcasing a trend among oxide ion conducting perovskite materials where the limits of a solid solution, or maximum conductivities may be linked to the type of perovskite used.

In $LaGaO_3$ a +3:+3 perovskite, the solid solution limits are reported to up to 50% A-site doping;[5] with maximum conductivities achieved *via* codoping of the A and B sites in $La_{0.8}Sr_{0.2}Ga_{0.85}Mg_{0.15}O_{2.825}$.[6] In $Na_{0.5}Bi_{0.5}TiO_3$, a +2:+4 perovskite, much of the oxide ion conductivity may arise due to non-stoichiometry in $Na_{0.5}Bi_{0.49}TiO_{2.985}$ (1% A-site vacancies), doping has been shown to increases conductivity with up to 2% of the B-site acceptor doped in $Na_{0.5}Bi_{0.49}Ti_{0.98}Mg_{0.02}O_{2.965}$.[7] The suggestion in $NaNbO_3$, a +1:+5 perovskite, that maximum conductivities and solid solution limits are achieved at concentrations ≤0.5at% Ga NN may indicate acceptor dopant limits for perovskite materials are heavily reliant on the charges of A and B ions in the base material.

Although the room temperature P:Q ratio may be influenced by the associated tolerance factor of an NN ceramic, B-site doped NN has very little effect on the tolerance factor due to

the low solid solution limits. Therefore, the primary cause in the change of P:Q ratio in B-site doped NN is a result of the formation of oxygen vacancies.[8] The greatest concentration of the Q-phase was 58% in 5% Ti NN, which may indicate a greater concentration of oxygen vacancies compared to the acceptor doped gallium variants in the region of 1-10% Ga where the P:Q ratio is approximately 50:50. As the conductivities of the 5% Ti NN and 1-10% Ga NN ceramics are consistent in this region, in spite of the increased oxygen vacancy content in 5% Ti NN. It indicates that some pinning of the oxygen vacancies occurs as acceptor dopants attract and form defect complexes and limit the mobility of oxygen vacancies, this is shown in equations 7.5 and 7.6.[9]

$$(Ti'_{Nb} - V_O^{\cdot\cdot})^{\cdot} \qquad (7.5)$$

$$(Ga''_{Nb} - V_O^{\cdot\cdot}) \qquad (7.6)$$

Doping of NN also has a significant effect on the stability of the P-Q phase transition around 360 °C. As previously demonstrated, calcium doping leads to significant stabilisation of the higher temperature R-phase on heating and destabilisation of the P-phase on cooling shifting the phase transition to lower temperatures. This effect leads to a broadening of the hysteresis ΔT_{Max}. It has been suggested that the primary reason for broadening of this hysteresis is due to increasing A-site vacancy concentrations as materials processed in sodium rich environments/Na:Nb ratios >1 showcase a relative reduction of ΔT_{Max}. Therefore, the broadening of ΔT_{Max} in acceptor doped NN; and the variance observed in stoichiometric NN, is attributed to the formation of A-site vacancies due to soda (Na_2O) volatility during calcination and sintering.

The generation of A-site vacancies due to processing conditions allows for the A-site donor doping mechanism to be favoured in all compatible NN variants (Mg/Ga). It is suggested that the reason for this preference is for NN to resist the formation of oxygen vacancies and maintain a stoichiometry near to ABO_3.

$$4Na_{Na}^{x} + 2O_O^{x} \rightarrow 4V'_{Na} + 2V_O^{\cdot\cdot} + 2Na_2O \qquad (7.7)$$

$$4V'_{Na} + 2V_O^{\cdot\cdot} \rightarrow Ga_{Na}^{\cdot\cdot} + \frac{3}{2}O_O^{x} + 3V'_{Na} + \frac{1}{2}V_O^{\cdot\cdot} \qquad (7.8)$$

With sufficient concentration of dopant, the B-site is then targeted, and a greater concentration of oxygen vacancies is reintroduced to the system.

$$Nb_{Nb}^{x} + \frac{5}{2}O_O^{x} \rightarrow Ga''_{Nb} + \frac{3}{2}O_O^{x} + V_O^{\cdot\cdot} \qquad (7.9)$$

In the case of acceptor doped 1%Mg NN, equation 7.9 is less favourable than the formation of the columbite secondary phase $MgNb_2O_6$.

Donor doping of the B-site exhibits similar limitations. However, W^{6+}/Mo^{6+} do not appear to target the A-site. Instead, the Na:Nb non-stoichiometry appears to dominate the system leading to any excess dopant not incorporated forming a conductive phase such as a tungsten bronze along the grain boundaries of the ceramics. This leads to the emergence of heterogeneity in electrical data due to a short circuit through the conductive $Na(Nb,W/Mo)O_3$ secondary phase along grain boundaries.

7.2. Further Work

The suggested doping mechanisms and associated donor doping preferences of B-site doped NN ceramics is primarily supported by electrical measurements (impedance spectroscopy/LCR). XRD and Rietveld refinement have been somewhat useful in identifying any secondary phases and determining the P:Q ratio; however, the changes in the unit cells appear to be minimal. As X-rays primarily interact with the electron cloud of each atom, in the case of NN, niobium will disproportionately influence the diffraction pattern. As the proposed doping mechanisms describe changes to the sodium and oxygen sites in the perovskite any subtle changes to the crystal structure may be hidden. Utilising neutron diffraction may allow for a greater understanding of the overall changes to the structure of NN in regard to sodium and/or oxygen vacancy distributions.[10]

In several NN variants it is suggested that electrical heterogeneity is present due to grain boundary effects. NN ceramics that have had their pO_2 dependence assessed indicate that extrinsic effects such as grain boundary contributions influence the total pO_2 dependence of the ceramics. In order to explore this TEM would be useful in a full characterisation of the grain boundaries in NN, and identification of any potential secondary phases that may be influencing the system but cannot be detected by SEM or XRD.

The ^{71}Ga NMR spectra of 1 and 5% Ga NN have been useful in confirming the presence of gallium on the B-site according to equation 7.9. However, the evidence of multiple sites within the unit cell is tenuous, and the results obtained in 5% Ga NN may simply be indicative of secondary phases within the sample, rather than A-B codoping. Additionally, the 0.1% Ga and 0.5% Ga NN samples were unable to be tested under any reasonable timeframe. An investigation of aluminium doped NN would allow for an ^{27}Al NMR study to be conducted under a more reasonable timeframe even using <1% Al dopant due to the significantly more abundant nucleus. A full investigation utilising the methodology discussed

in this thesis would likely be required to confirm the Al-NN system behaves in line with Ga-NN at similar dopant levels, or if differences arise as observed with W^{6+} and Mo^{6+}.

A study of doped NN using low temperature processing techniques, such as hydrothermal synthesis may be useful in an attempt to limit the proposed initial A-site donor doping by limiting soda volatility.[11]

Finally, a study of alternative +1: +5 perovskites such as $KTaO_3$ may be useful in assessing doping limits of perovskite materials for oxide ion conduction. $KTaO_3$ has already shown promise as an oxide ion conductor, although the dopant limits suggested in the literature are significantly greater than what is suggested in this thesis. This may be due to the use of multiple dopant ions on the tantalum site allowing up to 60% doping of the B-site.[12] This is a methodology that has not been considered in this thesis and may well allow for expansion of doping limits in NN.

7.3. References

1. Tucker, M. C., Cheng, L. & Dejonghe, L. C. Selection of cathode contact materials for solid oxide fuel cells. *J. Power Sources* **196**, 8313–8322 (2011).

2. Aso, S., Matsuo, H. & Noguchi, Y. Reversible electric-field-induced phase transition in Ca-modified $NaNbO_3$ perovskites for energy storage applications. *Sci. Rep.* **13**, 1–10 (2023).

3. Lei, X. *et al.* Realizing oxygen ion conduction in perovskite structure $NaNbO_3$ by A-site Bismuth doping. *J. Alloys Compd.* **924**, 2–6 (2022).

4. López, M. L. *et al.* New dielectric anomalies in the A-site highly deficient Na_xNbO_3 electroceramics. *Ceram. Int.* **46**, 16770–16780 (2020).

5. Vasylechko, L., Matkovski, A., Suchocki, A., Savytskii, D. & Syvorotka, I. Crystal structure of $LaGaO_3$ and $(La,Gd)GaO_3$ solid solutions. *J. Alloys Compd.* **286**, 213–218 (1999).

6. Huang, P. Superior Oxygen Ion Conductivity of Lanthanum Gallate Doped with Strontium and Magnesium. *J. Electrochem. Soc.* **143**, 1644 (1996).

7. Li, M. *et al.* A family of oxide ion conductors based on the ferroelectric perovskite $Na_{0.5}Bi_{0.5}TiO_3$. *Nat. Mater.* **13**, 31–35 (2014).

8. Shakhovoy, R. A. *et al.* Ferroelectric Q and antiferroelectric P phases' coexistence and local phase transitions in oxygen-deficient $NaNbO_3$ single crystal: Micro-Raman,

dielectric and dilatometric studies. *J. Raman Spectrosc.* **43**, 1141–1145 (2012).

9. Yang, F., Wu, P. & Sinclair, D. C. Electrical conductivity and conduction mechanisms in $(Na_{0.5}Bi_{0.5}TiO_3)_{1-x}(BiScO_3)_x$ ($0.00 \leq x \leq 0.25$) solid solutions. *J. Mater. Chem. C* **6**, 11598–11607 (2018).

10. Knight, K. S. Structural phase transitions, oxygen vacancy ordering and protonation in doped $BaCeO_3$: Results from time-of-flight neutron powder diffraction investigations. *Solid State Ionics* **145**, 275–294 (2001).

11. Handoko, A. D. & Goh, G. K. L. Hydrothermal synthesis of sodium potassium niobate solid solutions at 200 °C. *Green Chem.* **12**, 680–68 (2010).

12. Yadav, A., Pyare, R., Goodenough, J. B. & Singh, P. $KTa_{1-x-y}Ti_xGe_yO_{3-\delta}$: A High κ Relaxor Dielectric and Superior Oxide-Ion Electrolyte for IT-SOFC. *ACS Appl. Energy Mater.* **3**, 3205–3211 (2020).